Volume 27   Number 3   JULY – SEPTEMBER 2025

OBRABOTKA METALLOV

METAL WORKING & MATERIAL SCIENCE

NOVOSIBIRSK

НГТУ НЭТИ

Технологии, которые работают.

1950 ⟶ 2025

ИНЖЕНЕРНОЕ СЕРДЦЕ СИБИРИ: НГТУ НЭТИ ОТМЕЧАЕТ 75-ЛЕТИЕ

В 2025 году один из крупнейших технических вузов страны – Новосибирский государственный технический университет НЭТИ празднует 75-летний юбилей. Вуз под названием НЭТИ (Новосибирский электротехнический институт) был создан под задачи индустриального прорыва в Сибири после окончания Великой Отечественной войны в 1950 году.

РЕКТОР НГТУ НЭТИ ДОКТОР ТЕХНИЧЕСКИХ НАУК, ПРОФЕССОР АНАТОЛИЙ АНДРЕЕВИЧ БАТАЕВ:

Спустя 75 лет НГТУ НЭТИ остается центром прикладной науки, производя новые знания в виде результатов фундаментальных исследований и технологических решений.

Университет обеспечивает подготовку инженерных кадров для важнейших отраслей, определяющих специфику промышленного развития региона, в том числе для машино-, самолето- и приборостроения, энергетики, электроники, IT-отрасли, для предприятий оборонно-промышленного комплекса страны. За 75 лет вуз выпустил более 200 тысяч профессионалов.

В настоящее время в НГТУ НЭТИ 11 факультетов дневного отделения, Институт социальных технологий, народный факультет. Общее число студентов превышает 15 тысяч человек. Сегодня в университете осуществляется подготовка по более чем 130 направлениям.

Профессорско-преподавательский состав — это коллектив выдающихся ученых и инженеров, сохраняющих традиции академических знаний и технической школы, в содружестве с молодыми преподавателями, готовыми совершать прорыв в постиндустриальной экономике вместе со студентами.

В НГТУ НЭТИ учебный процесс осуществляют более 1500 преподавателей, в их числе два академика и пять членов-корреспондентов РАН, более 200 докторов наук. Ежегодно ученые и инженеры НГТУ НЭТИ создают около 200 разработок в области новых материалов, электроники, энергетики и ИТ для предприятий России.

Ознакомиться с годовой программой празднования юбилея:
www.nstu.ru/university/university_events_people/NETI75

The journal is issued since 1999

Publication frequency – 4 numbers a year

Data on the journal are published in
«Ulrich's Periodical Directory»

Journal "Obrabotka Metallov" ("Metal Working and Material Science") has been Indexed in Clarivate Analytics Services.

Journal "Obrabotka Metallov – Metal Working and Material Science" is indexed in the world's largest abstracting bibliographic and scientometric databases Web of Science and Scopus.

Journal "Obrabotka Metallov" ("Metal Working & Material Science") has entered into an electronic licensing relationship with EBSCO Publishing, the world's leading aggregator of full text journals, magazines and eBooks. The full text of JOURNAL can be found in the EBSCOhost™ databases.

CONTENTS

Obrabotka metallov –
Metal Working and Material Science

Journal homepage: http://journals.nstu.ru/obrabotka_metallov

Determination of the main parameters of resistance spot welding of Al-5 Mg aluminum alloy

Viktor Kondratiev [1, 2, a], Valeriy Gozbenko [3, 4, b, *], Roman Kononenko [5, c],
Marina Konstantinova [5, d], Elena Guseva [5, e]

[1] A.P. Vinogradov Institute of Geochemistry of the Siberian Branch of the Russian Academy of Sciences, 1A Favorsky str., Irkutsk, 664033, Russian Federation
[2] Cherepovets State University, 5 Lunacharsky pr., Cherepovets, 162600, Russian Federation
[3] Irkutsk State Transport University, 15 Chernyshevskogo str., Irkutsk, 664074, Russian Federation
[4] Angarsk State Technical University, 60 Tchaikovskogo str., Angarsk, 665835, Russian Federation
[5] Irkutsk National Research Technical University, 83 Lermontova str., Irkutsk, 664074, Russian Federation

[a] https://orcid.org/0000-0002-7437-2291, imz@mail.ru; [b] https://orcid.org/0000-0001-8394-0054, vgozbenko@inbox.ru;
[c] https://orcid.org/0009-0001-5900-065X, istu_politeh@mail.ru; [d] https://orcid.org/0000-0002-8533-0214, mavikonst@mail.ru;
[e] https://orcid.org/0000-0002-8719-7728, el.guseva@rambler.ru

ARTICLE INFO

ABSTRACT

Introduction. The resistance spot welding (*RSW*) process has proven to be widely applicable across various industrial sectors, especially for mass production. Typical fields of application include aerospace, automotive, furniture manufacturing, and other industries. However, the *RSW* process presents certain challenges when welding aluminum and its alloys. Generally, aluminum alloys produce poor welds due to their physical and metallurgical properties such as oxide formation, thermal expansion and contraction, lower weldability, and the formation of intermetallic compounds. This study aims to evaluate the feasibility and mechanical characteristics of *RSW* joints in *Al-5 Mg* aluminum alloys. **The purpose** is to assess the potential of resistance spot welding for aluminum alloys and to determine the influence of key *RSW* parameters on the microstructure and properties of the weld. **Research methods.** *Al-5 Mg* aluminum alloy sheets in as-received condition were used. Spot welding was performed using a stationary resistance spot welding machine *MT-4240*. Samples for analysis were cut, polished, and subsequently examined under an optical microscope. Hardness measurements were carried out using a microhardness tester along two directions: radially across the nugget and through the sheet thickness, employing a 100 g load. An *Instron* electromechanical testing machine was utilized for shear testing at a constant traverse speed of 1 mm/min until complete joint failure at room temperature. The nugget diameter was measured on the fracture surface after shear tensile testing. **Results and Discussion.** Optimal input parameters for welding 2.5 mm thick aluminum sheets were identified, and three output variables were analyzed: tensile strength, joint hardness, and nugget diameter. It was observed that joint strength improved significantly with increased process parameters (welding current and welding period). Nugget diameter showed a clear correlation with input parameters related to current and welding period. An increase in process parameters, i.e., weld cycle time, electrode force, and welding current, led to an increase in nugget size. The ratio of weld strength to base metal strength reached approximately 0.9. It is demonstrated that resistance spot welding of 2.5 mm thick *Al-5 Mg* aluminum sheets is feasible and can be employed in various industrial applications.

* Corresponding author
Gozbenko Valeriy E., D.Sc. (Engineering), Professor
Irkutsk State Transport University,
15 Chernyshevskogo str.,
664074, Irkutsk, Russian Federation
Tel: +7 914 951-60-21, **e-mail**: vgozvenko@inbox.ru

Introduction

Resistance spot welding (*RSW*) is widely used in the automotive, aerospace, construction, and energy industries for joining sheet metal components made of steel and aluminum alloys, as well as for creating dissimilar joints between steel and aluminum, aluminum and magnesium, and aluminum and titanium [1–10]. For example, the productivity of modern automated automotive assembly lines reaches up to 7 million spot welds per day [8, 9]. Aluminum alloys are extensively employed in the aerospace industry due to a combination of properties such as low density, high specific strength, good machinability, and corrosion resistance. Another significant advantage of aluminum alloys is their wide availability. The density of aluminum alloys is approximately one-third that of steel, which allows for a reduction in aircraft structural weight, improved fuel efficiency, and increased payload capacity.

For manufacturing critical load-bearing structural components of supersonic aircraft, where high strength is crucial, steel remains the preferred material [11–15]. However, aluminum alloys are widely used for wing panels, fuselage sections, empennage components, exhaust system parts, interior components, and engine turbine parts of modern aircraft. Aluminum alloys constitute between 50 % and 90 % of the mass of modern spacecraft. They have been extensively used in spacecraft such as *Soyuz*, *Progress*, space shuttles, satellites, and others [11–15]. Aluminum alloys are classified based on alloying systems such as *Al–Mg*, *Al–Mg–Li*, *Al–Cu–Li*, among others, which are the most common types applied in aerospace and automotive industries for high-strength engineering applications [14–18].

One of the key trends in the automotive industry is the reduction of vehicle weight. This goal is achieved by using materials with low specific weight, such as aluminum and its alloys, which in turn contributes to optimizing production costs [7–9]. Aluminum alloys are suitable metals for automotive applications because they can be easily cast and formed into required shapes and offer promising weight reduction compared to steel. The use of aluminum alloys in manufacturing body parts, cabin panels, wheel rims, and interior trim can reduce vehicle mass by more than 50 % [10, 11]. Owing to their combination of casting and deformation properties along with low specific weight, aluminum alloys stand out favorably compared to steels and are widely applied in the automotive sector.

For resistance spot welding of aluminum and its alloys, high-power welding guns are required due to the need for welding currents 2 to 3 times higher than those used for steel. This is caused by aluminum's higher electrical and thermal conductivity. Meanwhile, the welding period must be reduced to approximately one-third of that used for steel welding [1, 2].

Resistance spot welding (*RSW*) is a process of joining contacting metallic surfaces through heating generated by the electrical resistance to the current flowing through the parts being welded [1]. The welding process is controlled by three main parameters: *mechanical* (electrode force), *electrical* (welding current), and *temporal* (welding period). An electric current supplied to two overlapping sheets via coaxial electrodes is maintained for a sufficient duration to achieve localized fusion at the interface of the metal sheets. After the current is switched off, pressure is applied to form a strong joint along the fusion line. Subsequently, the molten metal cools down, forming a cast weld nugget within a confined volume.

The current density and applied pressure must be sufficient to form a solidified nugget but not so high as to expel molten metal from the weld zone. The welding current duration should be short enough to prevent excessive heating of the electrode surfaces. Electrode force, welding current magnitude, and welding period play a decisive role in the quality of the resistance spot weld. An electronic control unit is used in welding machines to monitor and regulate these welding parameters.

The quality and strength of welds produced by *RSW* are determined by the shape and size of the weld nuggets. Nugget size is a critical parameter that dictates the load-bearing capacity of the joint. There exists a direct correlation between heat generation and the size of the weld nugget during the *RSW* process. Heat generation, and consequently nugget size, is influenced by the following primary factors: contact resistance between the welded surfaces, welding current density, welding period, and thickness of the sheets being joined.

A key feature of *RSW* is the absence of the need for filler materials or fluxes. The competitive advantages of *RSW* over alternative metal joining methods, such as gas metal arc welding (*GMAW*), gas tungsten

arc welding (*GTAW*), and riveting, include the possibility for full process automation and integration into robotic production lines.

The main challenges limiting the application of *RSW* for aluminum alloys are:

1) *limited service life of contact electrodes*. The surface of aluminum alloys is characterized by the presence of an oxide film (Al_2O_3) with high electrical resistance and non-uniform thickness [1, 2, 12–16]. When the sheets are compressed by the electrodes, the oxide film deforms unevenly, resulting in current concentration at localized contact points. The high current density in these areas causes intense heating, localized melting, and fusion between the copper electrode and aluminum, leading to erosive wear of the electrode's working surface [1, 2]. Changes in the geometry and composition of the electrode surface during operation cause instability in welding parameters and reduce weld strength [12–15].

2) *high welding current requirements*. To ensure the formation of high-quality welds in aluminum alloys by *RSW*, significantly higher welding currents are required compared to steels. This factor diminishes the potential energy efficiency advantages of aluminum alloys related to their lower density compared to steels [3, 4, 17, 18].

Existing studies on resistance spot welding (*RSW*) of aluminum alloys are predominantly focused on thick materials [19–21]. Thin-sheet aluminum alloys require separate consideration because differences in contact areas, thermal regimes, and electrical characteristics necessitate adjustments in welding parameters, including electrode force and current density [1, 2, 20–22]. Both alternating current (*AC*) and direct current (*DC*) power sources with varying frequencies are used for *RSW* [1, 2, 23–29], affecting energy transfer modes and optimal welding period for both stationary and portable equipment [1–3, 22, 28, 30, 31, 31–36]. Welding quality is also significantly influenced by external factors such as surface condition (roughness, contamination) [2–8], assembly accuracy [9], electrode condition (wear) [9–14], and the precision of positioning the welded parts (axial and angular misalignment) [20–22].

Aluminum alloys are highly sensitive to oxidation under environmental exposure. The oxide film formed on the surface (Al_2O_3) exhibits high electrical resistance, which leads to increased heat generation at the contact zone during welding. Insufficient surface preparation aimed at oxide film removal can cause aluminum adhesion to the electrode material, accelerated electrode degradation, and poor-quality welds [1–5, 36–38]. Some studies have investigated the surface characteristics of aluminum alloy welds produced by *RSW* [3–8]; however, only a few reports document a significant decrease in hardness within the weld zone [1–4] for various aluminum alloy grades. Several works address the reduction in weld joint strength relative to the base metal and analyze the fracture behavior in the central weld nugget zone [29, 39].

This study aims to investigate the influence of resistance spot welding (*RSW*) parameters on the microstructure and mechanical properties of weld joints made from *Al-5 Mg* aluminum alloy.

The objectives of this work are:

1) to evaluate the applicability of resistance spot welding (*RSW*) for joining *Al-5 Mg* aluminum alloy;

2) to determine the effect of key *RSW* parameters on the microstructure and mechanical properties of the weld joint.

Materials and experimental procedure

The *RSW* process cycle diagram and the lap joint configuration used for tensile shear testing are shown in Figs. 1 and 2, respectively.

For welding, 2.5 mm thick sheets of *Al-5 Mg* aluminum alloy (*GOST 21631-2023*) were used. Surface preparation of the sheets included the following steps: preliminary degreasing, followed by etching in a 4 % sodium hydroxide (*NaOH*) solution for 10 minutes, and subsequent treatment in a 2 % nitric acid (*HNO₃*) solution for 5 minutes to remove the oxide film. Welding was performed on a stationary resistance spot welding machine *MTN-100.01*. The *RSW* process scheme and cycle diagram are presented in Fig. 2.

Shear tensile tests were conducted on a universal electromechanical testing machine *Instron* at room temperature, with a constant traverse speed of 1 mm/min until complete joint failure. The weld nugget diameter was measured on the fracture surface after the shear tensile test. Load values at shear and nugget diameter were calculated as the arithmetic mean of five measurements for each test series.
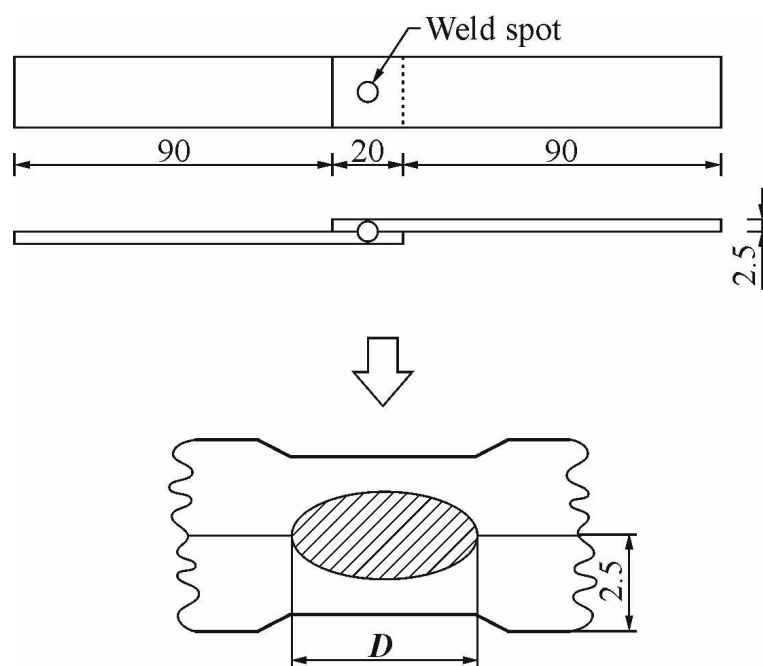
Fig. 1. Dimensions of the lap joint specimen produced by
resistance spot welding (*RSW*) for tensile testing
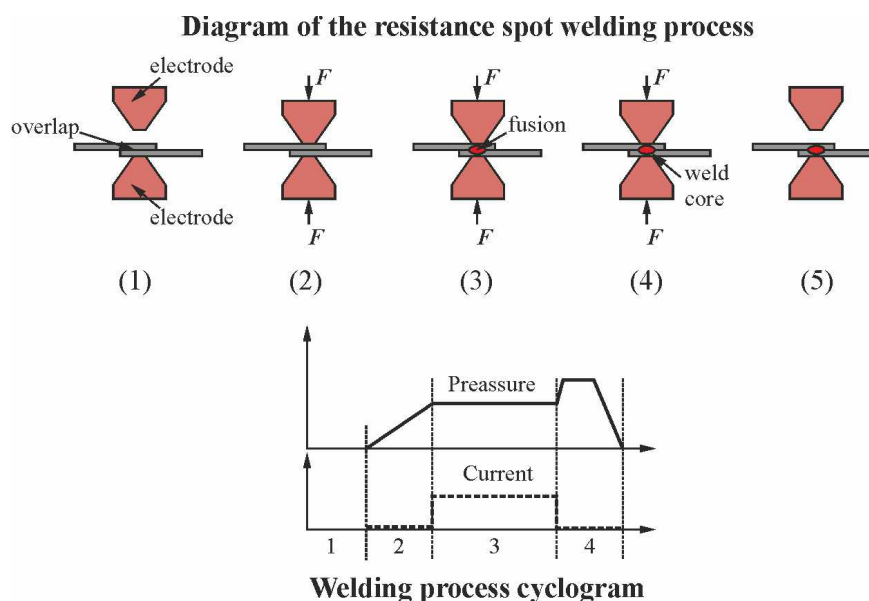
Fig. 2. Process scheme and cycle diagram of resistance spot welding (*RSW*)

For resistance spot welding (*RSW*) of 2.5 mm thick aluminum alloys, three variable parameters were used: welding current (ranging from 5 to 30 kA), welding period (from 1 to 5 seconds), and electrode force (from 2,000 to 5,000 N). The experiment consisted of thirteen series, each including welding of five samples: four for static shear tensile testing and one for metallographic analysis and hardness measurement.

Samples for metallographic analysis and hardness testing were cut perpendicular to the longitudinal direction of the welded specimens from the central region of the joint. Preparation of metallographic specimens involved cutting samples into 12×12 mm blanks, grinding, polishing, and etching to reveal the microstructure. Microstructure examination was performed using an optical microscope *Mikromed 2*. Hardness measurements were carried out in two directions (along the nugget radius and through the sheet thickness) using a microhardness tester with a 100 g load.

Results and Discussion

The welds produced by resistance spot welding (*RSW*) demonstrated satisfactory surface quality across the entire range of tested parameters. Changes in the diameter and depth of electrode indentation were observed depending on the welding mode. Metallographic analysis revealed no internal defects such as porosity or shrinkage cavities within the cast structure of the weld nugget.

Fig. 3 shows the general microstructure of the weld joint, illustrating characteristic structural zones including the fusion zone and the heat-affected zone (*HAZ*). In the cast structure region (Fig. 3, *a*, *b*), a fine-grained recrystallized microstructure with equiaxed grains is observed, along with insoluble $FeAl_3$ intermetallic inclusions (black) and a narrow zone of columnar crystals oriented along the heat dissipation direction during solidification. The heat-affected zone (*HAZ*), adjacent to the fusion zone (Fig. 3, *c*), is characterized by a dendritic structure. The base metal microstructure (Fig. 3, *d*) consists of grains elongated in the rolling direction.

a

b

c

d
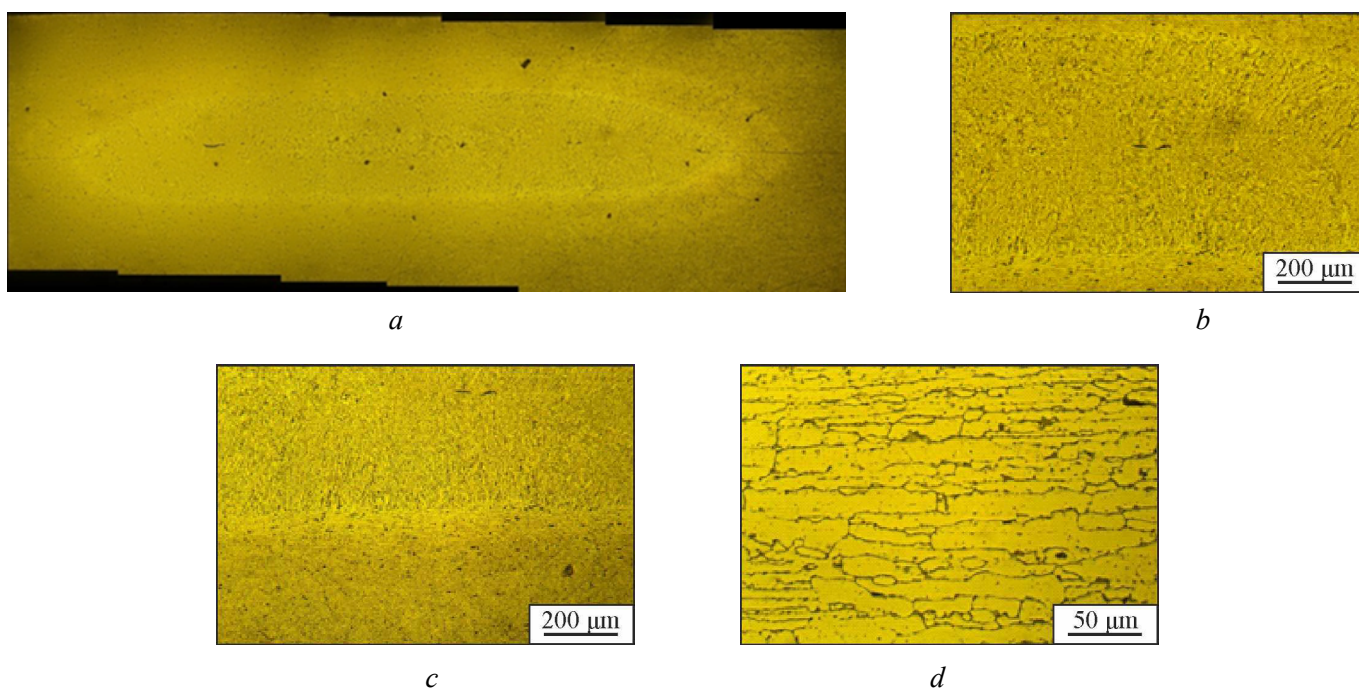
Fig. 3. Microstructure of a welded joint obtained by resistance spot welding (*RSW*):

a – general view of the welded joint; *b* – microstructure of the cast zone of the weld core; *c*) transition zone from the weld core to the heat-affected zone (*HAZ*); *d* – microstructure of the base material

To study the effect of welding period on the weld microstructure, metallographic analyses were performed on samples welded at various welding periods (from 33.4 ms to 167.0 ms) at a fixed welding current of 12 kA. It was found that increasing the welding period in this range leads to growth in grain size of equiaxed, dendritic, and columnar structures within the fusion zone. No significant changes in grain size or microstructure were detected in the *HAZ* compared to the base metal. However, welding periods exceeding 167.0 ms caused grain growth in the *HAZ* adjacent to the fusion zone relative to the base material, attributed to increased heat input during welding.

In the fusion zones of welds produced at the minimum welding current, a columnar grain structure with a pronounced liquation zone at the fusion boundary was observed (Fig. 3, *b*). The extent of the liquation zone increased at lower welding currents. Increasing the welding current resulted in a significant enlargement of the columnar grains in the fusion zone. Additionally, equiaxed grain regions formed in the central part of the fusion zone, indicating decreased cooling rates and thermal gradients. Grain coarsening was also noted in the *HAZ* of welds produced at higher welding currents.

Raising the welding current to 17 kA led to the formation of finer equiaxed grains in the fusion zone. The increase in welding current from 12 kA to 17 kA caused deeper electrode indentation into the sheets, reducing the distance between the cooled electrode and the center of the fusion zone. Consequently, the thermal gradient (G) in the fusion zone increased. The diameter of the fusion zone was largely determined by welding current and welding period. A higher thermal gradient in the weld metal promotes the formation of a fine-grained microstructure during solidification, which is consistent with findings reported in references [1–7].
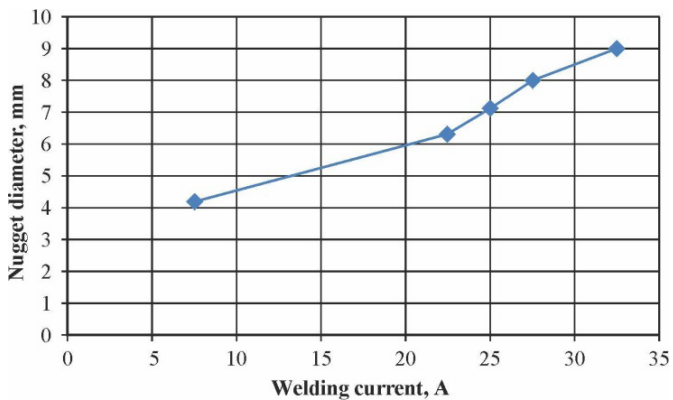
Fig. 4. Dependence of the nugget diameter on the welding current (*RSW*)

The dependence of the fusion zone diameter on welding current and welding period is presented in Figs. 4 and 5. A monotonic increase in the fusion zone diameter is observed with increasing welding current up to the maximum value achievable by the equipment used (Fig. 4). This trend is attributed to the increased heat input with rising welding current and is consistent with findings reported for carbon steels [1]. The results indicate that the applied electrode force was insufficient to cause the expulsion effect and the subsequent reduction in fusion zone diameter, since despite a small amount of expulsion occurring at 28.7 kA, no decrease in fusion zone diameter was observed (Fig. 4).

Several researchers have noted the possibility of increasing welding current without metal expulsion by increasing electrode force [2–5]. Metallographic analysis of samples welded at high current values revealed incomplete metal expulsion. Furthermore, welding current affects the depth of electrode indentation on the metal surface. All welds exhibited electrode indentations, the depth of which was largely determined by the welding current magnitude.

Electrode force has a minor effect on the fusion zone diameter for values up to 4,000 N. However, when the force exceeds this value, a slight decrease in fusion zone diameter is observed (Fig. 6). This effect can be explained by improved contact between the welded surfaces, resulting in reduced electrical resistance and heat input at higher electrode forces. The influence of the contact interface between the sheets on changes in fusion zone size depending on electrode compression force is also reported in studies [19–22].

The effect of electrode force on indentation depth was negligible within the investigated range. For detailed analysis of the electrode force effect on thickness reduction of the welded sheets, measurements were conducted at an intermediate welding current of 26.4 kA and welding period of cycle over a load range from 2,354 to 4,709 N. It was found that electrode force does not significantly affect indentation depth, while all welds showed an approximate 10% reduction in sheet thickness.

To evaluate the strength and load-bearing capacity of the welds, tensile tests were performed (Table 1).
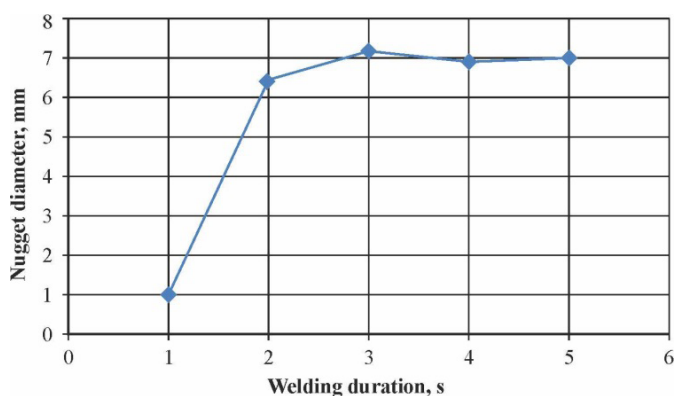
Fig. 5. Effect of welding period on the nugget size
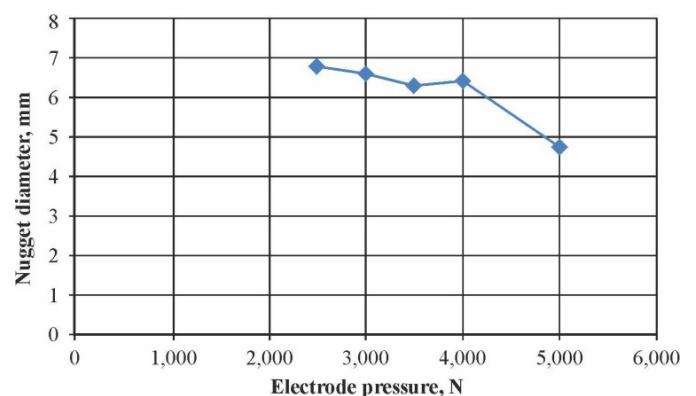
Fig. 6. Effect of the electrode force on the nugget

Values of ultimate strength, nugget diameter, and average microhardness

Exp. No.	Tensile strength, MPa	Nugget diameter, mm	Average microhardness, HV
Base metal	272	–	94
1	231	7.91	110
2	220	7.68	105
3	228	7.62	103
4	218	7.59	98
5	198	6.94	103
6	187	6.85	101
7	210	7.20	106
8	203	6.87	101
9	189	7.12	106

Table 1 also presents results reflecting the influence of welding parameters on joint strength, fusion zone diameter, and hardness. It was found that increasing electrode force from 2 kN to 3 kN and welding current from 7 kA to 8 kA leads to a significant increase in tensile strength. Changes in welding period from 15 ms to 25 ms had little effect on joint strength.

To characterize the mechanical properties of the weld joint, *Vickers* microhardness was measured in the weld zone (Fig. 7). It was found that microhardness in the fusion zone increases with rising welding current and welding period. Maximum hardness values reached 110 HV and 107 HV. Average hardness values in the fusion zone exceeded that of the base metal (Fig. 7, red line), indicating a reduction in weld ductility compared to the base material.

Fig. 7. Values of microhardness of the weld versus experiment number

Resistance spot welding (*RSW*) is a thermo-mechanical joining process in which heat plays a central role in forming a bond between the welded components. According to the *Joule-Lenz* law, the amount of heat generated during *RSW* is determined by the welding current, welding period, and the electrical resistance of the materials involved. Therefore, welding current, welding period, and electrode force are the primary parameters governing the welding process and, consequently, the quality of the weld joint (see Fig. 2). The *RSW* process cycle diagram typically reflects the variation of these three parameters over time and helps identify optimal ranges to achieve the desired weld characteristics [1–7].

It is well known that insufficient welding current can result in cold welding, whereas excessive welding current may cause metal expulsion from the fusion zone, as well as the formation of internal porosity or cracks within the cast microstructure. Insufficient electrode force may lead to molten metal spreading along the fusion boundary, while excessive force can reduce heat generation efficiency due to lowered contact resistance [1].

During welding, as the metal temperature rises, its electrical resistance also increases. The total resistance in the welding circuit (including the resistance of the welding machine, electrodes, and welded parts) determines the welding current magnitude. To form a molten zone in *RSW*, a certain value of total electrical resistance in the circuit must be ensured, which is the sum of resistances at each current path section through the welded workpieces [1, 2]. Higher total resistance improves weldability [1]. The total resistance depends

on the surface condition of the welded materials and electrodes, electrode surface geometry, and electrode force. Maximum heat generation occurs at the contact interface between the welded parts, where the main electrical resistance is concentrated. Meanwhile, the high thermal conductivity of copper electrodes and their intensive water cooling prevent the base metal surface from reaching melting temperature.

As the temperature rises in the zone of maximum electrical resistance, metal melting and molten zone (weld nugget) formation occur. Simultaneously, the welded sheets thin, and the distance between electrodes decreases under electrode force, reducing the overall dynamic resistance. If the molten metal volume becomes too large for the surrounding solid metal to contain under the applied force, molten metal expulsion from the weld zone occurs. Increasing electrode force reduces electrical resistance by improving the contact between sheets and smoothing surface irregularities.

The efficiency of energy absorption and the growth rate of the fusion zone depend on the geometrical dimensions of the welded parts [10–15]. However, classical *RSW* studies [1, 2] often overlooked this factor, and most *RSW* control systems are optimized for welding parts of identical dimensions. Many researchers [1–12] aim to optimize *RSW* parameters to achieve a stable process and produce welds with specified properties. The significant influence of welding current and welding period on the quality of spot welds is consistently emphasized.

Authors [1–5] identify welding current, welding period, and electrode force as the main parameters of the resistance spot welding (*RSW*) process. To achieve an optimal fusion nugget diameter, increased values of welding current and welding period are recommended [1–3]. At the same time, other studies demonstrate a direct correlation of the fusion zone diameter with welding current and welding period, and an inverse correlation with electrode force [5–8].

The morphology of *RSW* joints in metal-to-metal connections is characterized by three distinct zones: the fusion zone (*FZ*), the heat-affected zone (H*AZ*), and the base metal (*BM*) (Fig. 3). The fusion zone represents the cast nugget formed due to melting and subsequent solidification of the welded metals. The heat-affected zone is the region that does not melt but undergoes microstructural changes due to heat transfer from the fusion zone. Microstructural analysis of samples obtained in this work also revealed these three characteristic zones (Fig. 3), with significant differences in microstructure within each zone. Both *FZ* and *HAZ* exhibit columnar dendrites oriented in a specific direction. Porosity formation in the cast structure is typically associated with surface contamination and possible hydrogen saturation of the metal. The absence of porosity in the fusion zone in this study indicates sufficient heat input to ensure quality melting of the base metal and formation of a strong joint.

Comparison of the microstructure between the *HAZ* and *FZ* shows larger columnar dendrite grains forming at the fusion boundary. The formation of columnar dendrites in both zones is driven by a high solidification rate (R) and a steep thermal gradient (G) between the molten metal (approximately 600 °C) and the base metal (at room temperature). Under these conditions, the undercooling criterion required for planar solidification at the solid-liquid interface is not met [1–7], meaning the G/R ratio is insufficient to suppress dendritic growth. The smaller size of columnar dendrites in the fusion zone is related to a higher cooling rate (i.e., faster solidification), attributed to the high thermal conductivity of aluminum alloys (120–180 W/m·K) [1, 5, 9, 12–15].

The cooling rate decreases from the fusion zone through the *HAZ* to the base metal, which acts as a heat sink. This is because thermal conductivity is the primary factor controlling cooling rate. Consequently, the $G \times R$ value in the *HAZ* is lower compared to the fusion zone, resulting in coarser grains.

The size and shape of the fusion zone are key criteria for assessing *RSW* joint quality (Fig. 3, *a*) [1, 2, 5, 16–19]. In this study, the fusion zone diameter (D_{FZ}) ranged from 1.33 to 7.61 mm. Each value represents an average of at least three measurements. A fusion zone diameter exceeding 7 mm is considered critical by several authors [1, 2] regarding its influence on the joint's mechanical strength. The increase in fusion zone size is attributed to the high heat input under the applied welding conditions.

Shear tensile strength is another important criterion used to evaluate the quality of resistance spot welded joints. In the conducted experiments, the shear tensile strength of nine welded samples ranged from 179 to 231 MPa (Table 1). The maximum shear tensile strength was achieved at a fusion zone diameter of 7.91 mm.

In conclusion, the *RSW* process is characterized by a complex interaction of multiple factors. However, the primary controllable parameters are welding current, electrode force, and welding period, all of which significantly affect the quality of the welded joint. Table 2 presents a summary of the influence of these parameters on the *RSW* process and weld quality, along with corresponding optimization measures based on a review of the literature [1–23].

T a b l e 2

Recommendations for optimizing the basic parameters of contact spot welding

Process variables	Effect on the welding point	Optimization measures
Welding current	Size and shape of the weld; Occurrence of expulsion; Shear and tensile strength form the microstructure of the weld	It is necessary to use a process modeling and experimentation to find the optimal combination for a specific process
Weld period	Tensile strength, peeling, and shear strength of welded joints	It is necessary to apply variation rather than a constant value during the process
Electrode force	Energy efficiency of the process; Occurrence of molten metal expulsion; Specific features of weld core solidification during spot welding	It is necessary to apply variation rather than a constant value during the process

TIn conclusion, it should be noted that achieving high-quality welds of aluminum alloys by resistance spot welding (*RSW*) requires careful selection of an optimal combination of welding cycle parameters. Specifically, to attain high shear tensile strength and welds with a large fusion zone diameter, it is essential to consider the potential occurrence of undesirable phenomena such as metal expulsion, spatter, cold welding, or formation of an insufficiently sized fusion zone. A review of the literature [1–23] indicates that welding current is the key parameter determining heat input during welding and is also the most easily adjustable parameter. Additionally, the application of variable electrode force, implemented via an electric servomechanism, can improve process stability and enhance weld quality [14–23].

Future research will focus on optimizing resistance spot welding parameters for aluminum alloys of various thicknesses.

Conclusions

1. In resistance spot welding (*RSW*) of *Al-5 Mg* aluminum alloy, an increase in welding current and welding period leads to higher heat input and, consequently, an increase in the fusion zone diameter. The shear tensile strength of the welded joint also increases with rising welding current and welding period, which is attributed to the enlargement of the fusion zone diameter — a key factor determining joint strength.

2. For resistance spot welding (*RSW*) of 2.5 mm thick lap joints of *Al-5 Mg* aluminum alloy, the optimal parameters ensuring a shear tensile strength of 238 MPa are: electrode force of 3,000 N, welding current of 12 kA, and welding period of 25 ms.

References

1. Kochergin K.A. *Kontaktnaya svarka* [Contact welding]. Leningrad, Mashinostroenie Publ., 1987. 240 p.

2. Orlov B.D. *Tekhnologiya i oborudovanie kontaktnoi svarki* [Technology and equipment of contact welding]. Moscow, Mashinostroenie Publ., 1986. 352 p.

3. Zhou K., Yao P. Overview of recent advances of process analysis and quality control in resistance spot welding. *Mechanical Systems and Signal Processing*, 2019, vol. 124, pp. 170–198, DOI: 10.1016/j.ymssp.2019.01.041.

4. Hao M., Osman K.A., Boomer D.R., Newton C.J. Developments in characterization of resistance spot welding of aluminum. *Welding Journal – Including Welding Research Supplement*, 1996, vol. 75 (1), pp. 1–4. Available at:

https://www.scopus.com/record/display.uri?eid=2-s2.0-0029777851&origin=inward&txGid=43eb57982320fc23bd6ff9a0a6c0a142 (accessed 07.08.2025).

5. Manladan S.M., Yusof F., Ramesh S., Fadzil M., Luo Z., Ao S. A review on resistance spot welding of aluminum alloys. *The International Journal of Advanced Manufacturing Technology*, 2017, vol. 90, pp. 605–634. DOI: 10.1007/s00170-016-9225-9.

6. Zhang Y., Li Y., Luo Z., Yuan T., Bi J., Wang Z.M., Wang Z.P., Chao Y.J. Feasibility study of dissimilar joining of aluminum alloy 5052 to pure copper via thermo-compensated resistance spot welding. *Materials & Design*, 2016, vol. 106, pp. 235–246. DOI: 10.1016/j.matdes.2016.05.117.

7. Zhang W., Xu J. Advanced lightweight materials for automobiles: A review. *Materials & Design*, 2022, vol. 221, p. 110994. DOI: 10.1016/j.matdes.2022.110994.

8. Sateesh N., Subbiah R., Nookaraju B.Ch, Nagaraju D. Siva. Achieving safety and weight reduction in automobiles with the application of composite material. *Materials Today: Proceedings*, 2022, vol. 62, pp. 4469–4472. DOI: 10.1016/j.matpr.2022.04.936.

9. Taub A., Moor E. De, Luo A., Matlock D.K., Speer J.G., Vaidya U. Materials for automotive light-weighting. *Annual Review of Materials Research*, 2019, vol. 49 (1), pp. 327–359. DOI: 10.1146/annurev-matsci-070218-010134.

10. Zhang Y., Shan H., Li Y., Guo J., Luo Z., Ma C. Yong. Joining aluminum alloy 5052 sheets via novel hybrid resistance spot clinching process. *Materials & Design*, 2017, vol. 118, pp. 36–43. DOI: 10.1016/j.matdes.2017.01.017.

11. Ambroziak A., Korzeniowski M. Using resistance spot welding for joining aluminium elements in automotive industry. *Archives of Civil and Mechanical Engineering*, 2010, vol. 10 (1), pp. 5–13. DOI: 10.1016/S1644-9665(12)60126-5.

12. Qiu R., Zhang Z., Zhang K., Shi H., Ding G. Influence of welding parameters on the tensile shear strength of aluminum alloy joint welded by resistance spot welding. *Journal of Materials Engineering and Performance*, 2011, vol. 20, pp. 355–358. DOI: 10.1007/s11665-010-9703-4.

13. Li Z., Hao C., Zhang J., Zhang H. Effects of sheet surface conditions on electrode life in resistance welding aluminum. *Welding Journal*, 2007, vol. 86 (4).

14. Qiu R., Li J., Shi H., Yu H. Characterization of resistance spot welded joints between aluminum alloy and mild steel with composite electrodes. *Journal of Materials Research and Technology*, 2023, vol. 24, pp. 1190–1202. DOI: 10.1016/j.jmrt.2023.03.069.

15. Pan B., Sun H., Shang S.-L., Wen W., Banu M., Simmer J.C., Carlson B.E., Chen N., Liu Z.-K., Zheng Z., Wang P., Li J. Corrosion behavior in aluminum/galvanized steel resistance spot welds and self-piercing riveting joints in salt spray environment. *Journal of Manufacturing Processes*, 2021, vol. 70, pp. 608–620. DOI: 10.1016/j.jmapro.2021.08.052.

16. Baek S., Go G.Y., Park J.-W., Song J., Lee H.-c., Lee S.-J., Lee S., Chen C., Kim M.-S., Kim D. Microstructural and interface geometrical influence on the mechanical fatigue property of aluminum/high-strength steel lap joints using resistance element welding for lightweight vehicles: experimental and computational investigation. *Journal of Materials Research and Technology*, 2022, vol. 17, pp. 658–678. DOI: 10.1016/j.jmrt.2022.01.041.

17. Arumugam A., Pramanik A. A review on the recent trends in forming composite joints using spot welding variants. *Journal of Composites Science*, 2024, vol. 8 (4), p. 155. DOI: 10.3390/jcs8040155.

18. Aslanlar S., Ogur A., Ozsarac U., Ilhan E. Welding time effect on mechanical properties of automotive sheets in electrical resistance spot welding. *Materials & Design*, 2008, vol. 29 (7), pp. 1427–1431. DOI: 10.1016/j.matdes.2007.09.004.

19. Matsushita M., Ikeda R., Oi K. Development of a new program control setting of welding current and electrode force for single-side resistance spot welding. *Welding in the World*, 2015, vol. 59, pp. 533–543. DOI: 10.1007/s40194-015-0228-1.

20. Chang B.H., Zhou Y. Numerical study on the effect of electrode force in small-scale resistance spot welding. *Journal of Materials Processing Technology*, 2003, vol. 139 (1–3), pp. 635–641. DOI: 10.1016/S0924-0136(03)00613-7.

21. Podržaj P., Jerman B., Simončič S. Poor fit-up condition in resistance spot welding. *Journal of Materials Processing Technology*, 2016, vol. 230, pp. 21–25. DOI: 10.1016/j.jmatprotec.2015.11.009.

22. Yu J. New methods of resistance spot welding using reference waveforms of welding power. *International Journal of Precision Engineering and Manufacturing*, 2016, vol. 17, pp. 1313–1321. DOI: 10.1007/s12541-016-0156-z.

23. Zhang W., Sun D., Han L., Liu D. Interfacial microstructure and mechanical property of resistance spot welded joint of high strength steel and aluminium alloy with 4047 AlSi12 interlayer. *Materials & Design*, 2014, vol. 57, pp. 186–194. DOI: 10.1016/j.matdes.2013.12.045.

24. Pouranvari M., Marashi S.P.H. Critical review of automotive steels spot welding: process, structure and properties. *Science and Technology of Welding and Joining*, 2013, vol. 18 (5), pp. 361–403. DOI: 10.1179/1362171 813Y.0000000120.

25. Karlina A.I., Kondrat'ev V.V., Kolosov A.D., Balanovskiy A.E., Ivanov N.A. Production of new nanostructures for modification of steels and cast irons. *IOP Conference Series: Materials Science and Engineering*, 2019, vol. 560 (1), p. 012183. DOI: 10.1088/1757-899X/560/1/012183.

26. Balanovsky A.E., Shtayger M.G., Kondrat'ev V.V., Van Huy V., Karlina A.I. Plasma-arc surface modification of metals in a liquid medium. *IOP Conference Series: Materials Science and Engineering*, 2018, vol. 411 (1), p. 012013. DOI: 10.1088/1757-899X/411/1/012013.

27. Konstantinova M.V., Balanovskiy A.E., Gozbenko V.E., Kargapoltsev S.K., Karlina A.I., Shtayger M.G., Guseva E.A., Kuznetsov B.O. Application of plasma surface quenching to reduce rail side wear. *IOP Conference Series: Materials Science and Engineering*, 2019, vol. 560 (1), p. 012146. DOI: 10.1088/1757-899X/560/1/012146.

28. Ivanchik N.N., Balanovsky A.E., Shtayger M.G., Sysoev I.A., Karlina A.I. Capability enhancement of production of activating fluxes for arc welding using ultradispersed products of silicon waste processing. *IOP Conference Series: Materials Science and Engineering*, 2018, vol. 411 (1), p. 012035. DOI: 10.1088/1757-899X/411/1/012035.

29. Yelemessov K., Baskanbayeva D., Martyushev N.V., Skeeba V.Y., Gozbenko V.E., Karlina A.I. Change in the properties of rail steels during operation and reutilization of rails. *Metals*, 2023, vol. 13, p. 1043. DOI: 10.3390/met13061043.

30. Balanovsky A.E., Shtayger M.G., Grechneva M.V., Kondrat'ev V.V., Karlina A.I. Comparative metallographic analysis of the structure of St3 steel after being exposed to different ways of work-hardening. *IOP Conference Series: Materials Science and Engineering*, 2018, vol. 411 (1), p. 012012. DOI: 10.1088/1757-899X/411/1/012012.

31. Balanovsky A.E., Shtayger M.G., Kondrat'ev V.V., Nebogin S.A., Karlina A.I. Complex metallographic researches of 110G13L steel after heat treatment. *IOP Conference Series: Materials Science and Engineering*, 2018, vol. 411 (1), p. 012014. DOI: 10.1088/1757-899X/411/1/012014.

32. Kolosov A.D., Gozbenko V.E., Shtayger M.G., Kargapoltsev S.K., Balanovskiy A.E., Karlina A.I., Sivtsov A.V., Nebogin S.A. Comparative evaluation of austenite grain in high-strength rail steel during welding, thermal processing and plasma surface hardening. *IOP Conference Series: Materials Science and Engineering*, 2019, vol. 560, p. 012185. DOI: 10.1088/1757-899X/560/1/012185.

33. Karlina A.I., Balanovskiy A.E., Kondratiev V.V., Romanova V.V., Batukhtin A.G., Karlina Y.I. An investigation into the behavior of cathode and anode spots in a welding discharge. *Applied Sciences*, 2024, vol. 14 (21), p. 9774. DOI: 10.3390/app14219774.

34. Skeeba V.Yu., Ivancivsky V.V., Kutyshkin A.V., Parts K.A. Hybrid processing: the impact of mechanical and surface thermal treatment integration onto the machine parts quality. *IOP Conference Series: Materials Science and Engineering*, 2016, vol. 126 (1), p. 012016. DOI: 10.1088/1757-899x/126/1/012016.

35. Efremenkov E.A., Martyushev N.V., Skeeba V.Yu., Grechneva M.V., Olisov A.V., Ens A.D. Research on the possibility of lowering the manufacturing accuracy of cycloid transmission wheels with intermediate rolling elements and a free cage. *Applied Sciences*, 2022, vol. 12 (1), vol. 5. DOI: 10.3390/app12010005.

36. Martyushev N.V., Skeeba V.Yu. The method of quantitative automatic metallographic analysis. *Journal of Physics: Conference Series*, 2017, vol. 803 (1), p. 012094. DOI: 10.1088/1742-6596/803/1/012094.

37. Skeeba V.Yu., Ivancivsky V.V. Reliability of quality forecast for hybrid metal-working machinery. *IOP Conference Series: Earth and Environmental Science*, 2018, vol. 194 (2), p. 022037. DOI: 10.1088/1755-1315/194/2/022037.

38. Zverev E.A., Skeeba V.Y., Skeeba P.Y., Khlebova I.V. Defining efficient modes range for plasma spraying coatings. *IOP Conference Series: Earth and Environmental Science*, 2017, 87(8), 082061, DOI: 10.1088/1755-1315/87/8/082061.

39. Skeeba V.Yu. Hybrid process equipment: improving the efficiency of the integrated metalworking machines initial designing. *Obrabotka metallov (tekhnologiya, oborudovanie, instrumenty) = Metal Working and Material Science*, 2019, vol. 21, no. 2, pp. 62–83. DOI: 10.17212/1994-6309-2019-21.2-62-83. (In Russian).

40. Borisov M.A., Lobanov D.V., Yanyushkin A.S., Skeeba V.Yu. Investigation of the process of automatic control of current polarity reversal in the conditions of hybrid technology of electrochemical processing of corrosion-resistant steels. *Obrabotka metallov (tekhnologiya, oborudovanie, instrumenty) = Metal Working and Material Science*, 2020, vol. 22, no. 1, pp. 6–15. DOI: 10.17212/1994-6309-2020-22.1-6-15. (In Russian).

41. Mamadaliev R.A., Bakhmatov P.V., Martyushev N.V., Skeeba V.Y., Karlina A.I. Influence of welding regimes on structure and properties of steel 12KH18N10T weld metal in different spatial positions. *Metallurgist*, 2022, vol. 65 (11–12), pp. 1255–1264. DOI: 10.1007/s11015-022-01271-9.

Conflicts of Interest

The authors declare no conflict of interest.

Obrabotka metallov –
Metal Working and Material Science

Journal homepage: http://journals.nstu.ru/obrabotka_metallov
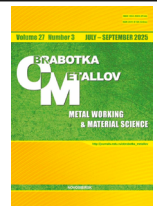
Influence of cutting speed on pulse changes in the temperature of the front cutter surface during turning of heat-resistant steel 0.17 C-Cr-Ni-0.6 Mo-V

Valery Gvindjiliya [a, *], *Evgeny Fominov* [b], *Andrey Marchenko* [c], *Tatiana Lavrenova* [d], *Svetlana Debeeva* [e]

Don State Technical University, 1 Gagarin square, Rostov-on-Don, 344000, Russian Federation

[a] https://orcid.org/0000-0003-1066-4604, ✉ vvgvindjiliya@donstu.ru; [b] https://orcid.org/0000-0002-0165-7536, ✉ fominoff83@mail.ru;
[c] https://orcid.org/0000-0003-4028-6712, ✉ tobago13@yandex.ru; [d] https://orcid.org/0000-0002-8283-7730, ✉ bys_ka87@mail.ru;
[e] https://orcid.org/0000-0002-2796-2424, ✉ sve_tchk@mail.ru

ARTICLE INFO

ABSTRACT

Introduction. This paper is devoted to the evaluation of the influence of periodic fluctuations of machining mode parameters on the change of the maximum temperature of the front surface of the cutter. **Subject of research.** Fluctuations of cutting mode parameters are considered as deviations of their values relative to the nominal ones, resulting in periodic changes in the cross-sectional area of the cut layer and the interaction conditions between the chip and the tool's front surface, which affect temperature changes in the cutting zone. **The purpose of this work** is to evaluate the influence of periodic fluctuations of machining mode parameters at different cutting speeds on the variation of the maximum temperature of the cutting tool's front surface during turning of heat-resistant steel *0.17 C-Cr-Ni-0.6 Mo-V* on a long-life machine without cooling. **Method and methodology.** The finishing longitudinal turning process of heat-resistant steel *0.17 C-Cr-Ni-0.6 Mo-V* on a long-life machine without cooling was investigated. During machining, tool vibrations were measured along three coordinate axes while varying the cutting speed at constant depth of cut and feed. Using digital simulation modeling based on input data obtained from in-situ experiments, the moments in the system dynamics when each cutting mode parameter reaches extreme values due to fluctuations were identified. Deviations of the maximum design temperature from the corresponding nominal value were then determined. **Results and discussion.** It is established that variations in machining speed change the factors destabilizing the thermal state: at low speeds, the main sources of temperature deviations in the investigated cutting system are moments when extreme values of cutting depth and speed are reached; at higher speeds, fluctuations of cutting depth and feed have the greatest effect. It is revealed that when machining parameters reach extreme values, instantaneous temperature generally increases, and cutting speeds at which such deviations are minimal are identified.

Introduction

One of the main factors determining the wear resistance of cutting tools is the temperature in the machining zone. Over the past decades, a significant number of scientific studies have been devoted to the assessment and prediction of maximum temperatures on the surface of cutting tools. Experimental methods for determining this parameter by contact measurement and analysis of heat emission have been proposed [1–3], and various analytical dependencies for predicting temperature have been presented [4–7]. Another relevant area of research is the assessment of the influence of process conditions on the temperature in

* Corresponding author
Gvindjiliya Valery E., Ph.D. (Engineering), Senior Lecturer
Don State Technical University,
1 Gagarin square,
344000, Rostov-on-Don, Russian Federation
Tel.: +7 918 583-23-33, **e-mail:** vvgvindjiliya@donstu.ru

the cutting zone. Most of the works presented in this area are devoted to studying changes in the average temperature when one of the cutting mode parameters varies, but the effect of vibrations generated by the system itself at certain processing modes on the nature of heat dissipation in the contact zone has not been analyzed [8–12]. At the same time, studies show that cutting tool vibrations and the temperature in the cutting zone are highly correlated. For example, *Songyuan Li et al.* show the results of the influence of tool vibrations on temperature for different stages of tool wear [13]. *Qiu Yu et al.* also note the significant influence of cutting modes and tool vibrations on the thermal state in the processing zone, while noting that this relationship is characterized by nonlinear properties and depends on the operating parameters of the cutting system [14].

The temperature in the cutting zone reaches its maximum value at the end boundary of the secondary plastic deformation (*SPD*) zone on the tool rake face. The "tool rake face-chip" interface is a heavily loaded tribological system, in which the cutting edge of the tool heats up as a result of viscous dissipation of friction energy in the surface deformable microvolume of the chip. By applying hydrodynamic analogies to the assessment of deformation processes in the *SPD* layer, *A.V. Chichinadze* and *K.G. Shuchev* obtained an analytical dependence describing the temperature distribution along the rake face and allowing the maximum temperature at this edge to be determined [15]. The parameters of the volumetric heat source in the chip are determined by the specified cutting modes. At the same time, as a result of various vibration disturbances in the cutting system, one or more of the initially specified processing parameters (speed, feed, cutting depth) periodically deviate from their nominal values, changing the set of tribodeformation indicators that determine the maximum instantaneous contact temperature. As a result of the variable nature of the heat sources on the rake face, there will be periodically repeating impulsive changes in the instantaneous temperature associated with mechanical vibrations of the machine's actuators. The specific deviation of this indicator from the nominal value will be determined by a set of values that each of the processing mode parameters takes at the moment of fluctuations. An increase in the amplitude of the variable temperature component leads to an increase in the temperature gradient in the cutting wedge as a whole and to an increase in undesirable heat flows. Temperature fluctuations in areas adjacent to the zone of primary plastic deformation change the characteristics of the material being processed and affect the cutting forces. The unstable thermal state of the cutting zone and the variable nature of the thermal load on the cutter surfaces cause intensification of oxidative and diffusion wear of the working edges of the tool [17–19]. At the same time, thermodynamic processes on the tool face largely determine the thermal state and wear processes on its flank face [20, 21]. Negative temperature effects are particularly acute during dry cutting of heat-resistant materials with low thermal conductivity [22–24]. The use of equipment with a long service life is an additional factor that increases tool vibrations and increases the temperature in the processing area. Such equipment is prone to significant kinematic disturbances originating from the feed drives and the main drive during machining.

The purpose of this work is to evaluate the influence of periodic fluctuations in processing parameters, induced at different cutting speeds, on changes in the maximum temperature of the cutter's rake face when turning heat-resistant *0.17 C-Cr-Ni-0.6 Mo-V* steel on a machine with a long service life without coolant.

Methods

Real-life tests were carried out in production conditions (*Atommash* factory, Volgodonsk) on a *DIP-300* universal turning machine. External longitudinal turning of workpieces with a diameter of 109 mm and a length of 400 mm made of *0.17 C-Cr-Ni-0.6 Mo-V* steel was performed using cemented carbide inserts (*WC* 79 %; *TiC* 15 %, *Co* 6 %) with the following cutting edge geometry: back rake angle $\gamma = 6°$, clearance angle $\alpha = 6°$, major cutting edge angle $\varphi = 95°$, and nose radius $r = 0.5$ mm. Turning was performed at a feed rate of $s = 0.198$ mm/rev, a cutting depth of $t = 0.5$ mm, and a spindle speed of $n = 630$–$1,000$ rpm (cutting speed $V = 215.5$–343.6 m/min). The workpieces were centered and pre-turned. To increase the rigidity of the workpiece subsystem, a reinforced precision rotating tailstock *BISON 8814-5 NC PRECISION 20/30* was used.

Tool vibrations measured in the directions of its mobility were selected as the main information channels about the dynamics of the cutting process, as they have a greater impact on fluctuations in technological

modes. To measure tool vibrations, a stand consisting of three *A603C01* accelerometers, an *LCard E20-10* analog-to-digital converter (*ADC*) with an input signal sampling frequency of up to 10 MHz, and a *BTK-2-010 ICP* converter for amplifying and proportionally converting vibration acceleration signals into alternating voltage with a frequency range of 0.1–50,000 Hz (Fig. 1) was used. The signal sampling frequency was 10 kHz per channel. Signals were recorded using *L-Graph II* software, and experimental data processing and identification of the parameters of the digital model of the cutting process were performed using *Matlab* and *Simulink* software.

a   b
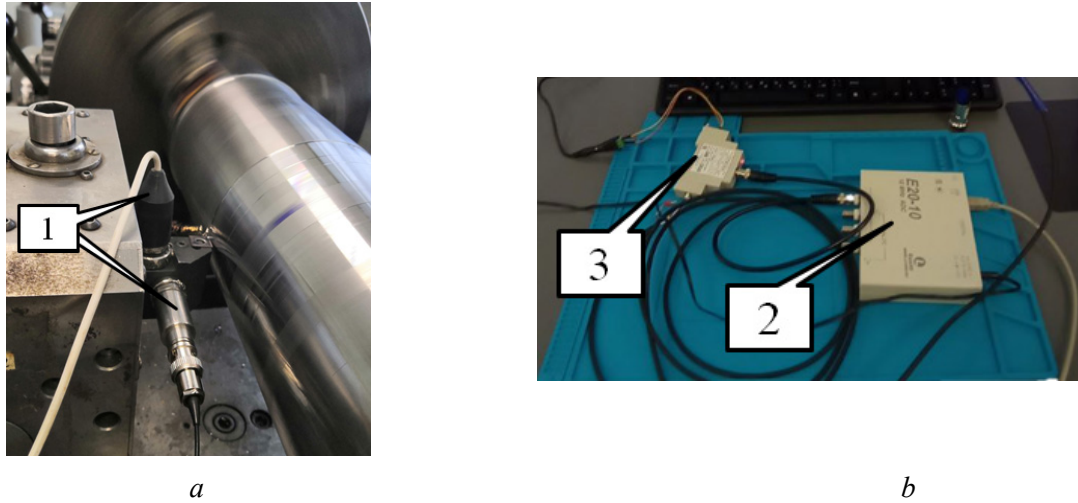
Fig. 1. General view of the equipment for the study:

a – vibration accelerometers (**1**); *b* – continuous vibration monitoring system of the tool: *ADC E20-10* (**2**) and *ICP* transducer *VTK-2-010* (**3**)

The dynamic cutting system model is represented as a set of three interconnected subsystems. The first subsystem controls the movement of the cutting tool relative to the workpiece, i.e., it sets the cutting parameters and the inertial-dissipative properties of the system. The second subsystem models the elastic deformations and cutting forces acting on the tool. The third subsystem implements a block for simulating uncontrolled disturbances, the source of which are kinematic disturbances from the machine's drive system and spindle runout [25].

When modeling the dynamics of the machining process, the values of the cutting speed *V*, feed rate *s*, and cutting depth *t* were determined as follows: for each parameter, the value was determined by the sum of the value set by the control system (V_0, s_0, t_0), deformation displacements $H = \{H_X, H_Y, H_Z\}$, mm, and deformation displacement rates $\eta = dH/d\tau = \{\eta_X, \eta_Y, \eta_Z\}$, mm/s, as well as vibration disturbances $\Delta = \{\Delta_X, \Delta_Y, \Delta_Z\}$, mm. Vibration disturbances are periodic functions of time and can be represented as:

$$\Delta_i(\tau) = \sum_{n=1}^{k} A_n \sin(\omega_n \tau),$$

$$v_i^{\Delta}(\tau) = d\Delta_i / d\tau = \sum_{n=1}^{k} A_n \omega_n \cos(\omega_n \tau),$$

(1)

where A_n, ω_n are the amplitudes and frequencies of the oscillators disturbing the movement of the tool in the directions of movement $i = \{X, Y, Z\}$, determined experimentally.

The final representation of the cutting modes was modeled as follows:

$$V = V_0 - \eta_Z + v_Z^{\Delta};$$

$$s = \int_{\tau-\tau_0}^{\tau} \left(V_x - \eta_X + v_X^{\Delta}\right) d\tau;$$

$$t = t_0 - H_Y + \Delta_Y,$$

(2)

where $\tau_0 = 1/\Omega$ is the time of one rotation of the part, s; Ω is the rotation frequency of the part, Hz; V_x is the feed speed, $V_x = s_0 \cdot \Omega$, mm/s.

The maximum contact temperature on the rake face was calculated for each combination of V, s, and t values that they take at the moments of fluctuations due to tool vibrations using the *Chichinadze-Shucheva* analytical dependence [15]:

$$T = \left(\frac{\omega_{01}}{k_1 + m_1} + \frac{\omega_{02}}{\frac{l_1}{V_C} k_2^3 a_2} \left(\frac{l_1}{V_C} k_2^3 a_2 + 1 - 2k_2 \sqrt{a_2 \cdot \frac{l_1}{V_C}} \cdot \frac{1}{\pi} - \exp\left(\frac{l_1}{V_C} k_2^2 a_2 \right) \cdot rfc\left(k_2 \cdot \sqrt{a_2 \cdot \frac{l_1}{V_C}} \right) \right) \right) \times$$

$$\times \left(\lambda_1 \cdot m_1 + \frac{2\lambda_2}{\pi \cdot a_2 \frac{l_1}{V_C}} \right)^{-1}, \tag{3}$$

where ω_{01} is the maximum volumetric density of the heat source from friction forces in the tool body, W/m³; $\omega_{02} = \dfrac{q_0 k t_H}{t_m h\left(1 - \exp\left(-k\dfrac{T_H}{T_m}\right)\right)}$ is the initial density of the heat source in the material being pro-

cessed, W/m³; q_0 is the specific friction power for the front surface, W/m²; k_1, k_2 are the heat absorption source localization coefficients for the tool and the material being processed, respectively, m⁻¹; a_2 is the thermal conductivity coefficient of the workpiece, m²/s; λ_1, λ_2 are the thermal conductivity coefficient of the solid alloy and the workpiece material, respectively, W/m·°C; V_c is the chip feed rate on the front surface, m/s; τ_k is the average tangential stresses on the front surface, Pa; T_m is the melting point of the workpiece material, °C; k is the temperature coefficient, °C; $k = 7.143 \cdot 10^{-4} \cdot T_m$; h is the average thickness of the plastically deformed layer in the chip, m; T_H is the temperature difference within the plastically deformed layer, °C; l_1 is the length of the *SPD* zone on the rake face, m; $m_1 = \sqrt{\dfrac{\alpha_1}{\lambda_1\left(\dfrac{A_1}{P_1}\right)}}$, A_1 is the tribocontact area on the

SPD zone, m²; P_1 is the perimeter of tribocontact on the SPD zone, m; α_1 is the heat transfer coefficient of the tool material, m²/°C.

The average thickness of the *SPD* zone is determined by the empirical relationship [26]:

$$h = \frac{\tau_k l_1}{\lambda_2 T_m}. \tag{4}$$

To account for the influence of cutting force variations during fluctuations on the values of parameters τ_k and h, the average shear stress on the rake face was determined as $\tau_k = F_{XY}/A_k$, Pa, where *FXY* is the resultant cutting force for the longitudinal (*X*) and radial (*Y*) directions, and A_k is the total contact area between the chip and the rake face, defined as $A_k = 2 \cdot l_1 \cdot b$. The values of the contact length l_1 and the width of the cut layer **b** were determined using the methods [27] and [28], respectively.

Results and Discussion

The data on oscillatory accelerations recorded by vibration sensors were analyzed and processed. The oscillation velocity and displacement of the tool relative to the workpiece were calculated. Fig. 2 shows the vibration characteristics of the cutting process in the longitudinal direction, which is responsible for variations in the area of the cut layer. Based on the spectral characteristics of the data from the measuring system, the dominant frequency components of the system and kinematic disturbances were established.
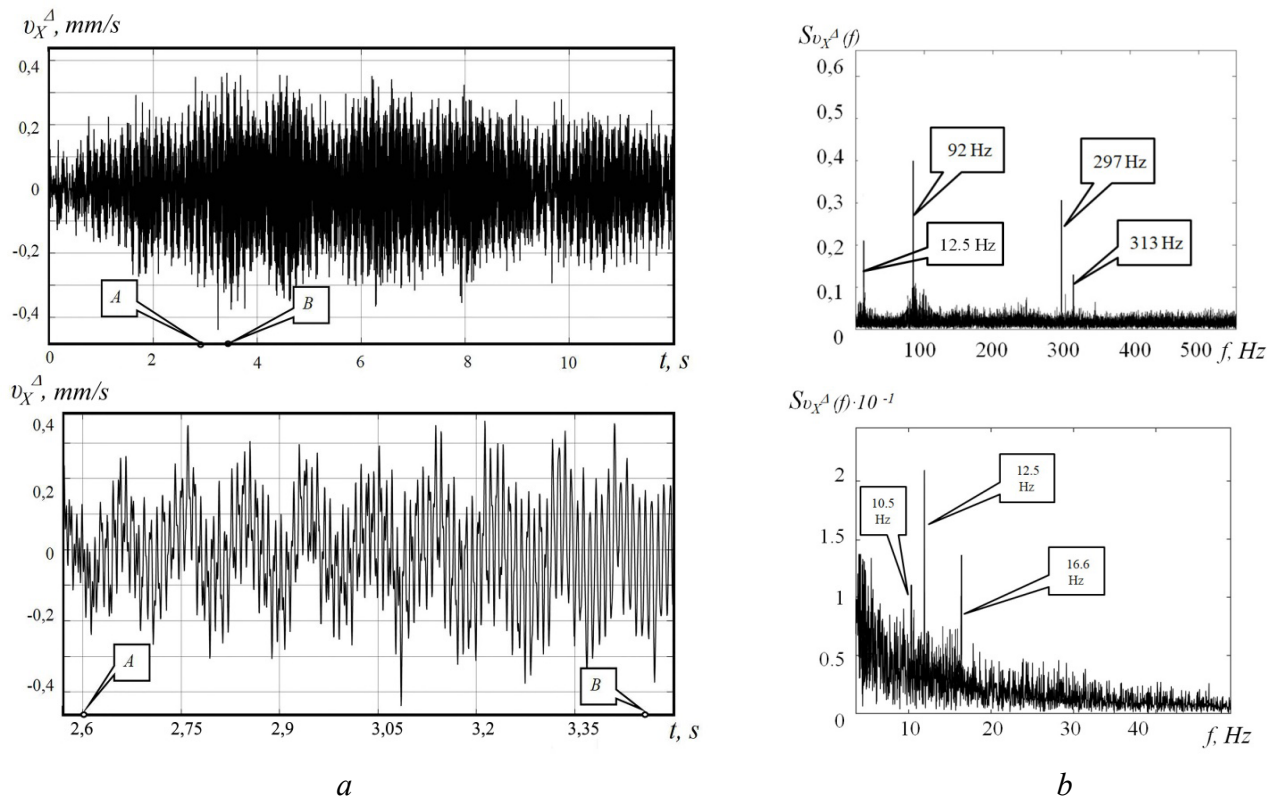
Fig. 2. Example of processed data for tool oscillatory velocity in the longitudinal direction:
a – time-domain signal; *b* – amplitude spectrum of oscillatory velocity in mid-frequency and low-frequency range

Vibration characteristics, as exemplified by the tool holder assembly, exhibit a broadband signal. Analysis of the low-frequency range shows that three main frequencies can be distinguished in the vibration spectrum of the tool holder assembly. The first of these coincides with the frequency of the spindle assembly vibrations. The others, including those in the mid-frequency range, are components of kinematic disturbances.

Based on the data obtained, the dynamics of the cutting process were simulated, taking into account the influence of vibration disturbances (1) [29]. Examples of cutting force dynamics for different cutting speeds are shown in Fig. 3. The range includes both speeds used in full-scale experiments on the machine: $V = 216$ m/min, $V = 270$ m/min, $V = 343$ m/min, and intermediate values obtained by simulation digital modeling.

Regarding the cutting process power indicator dynamics, the upper limit of the optimal workpiece spindle speed range will be values below the first frequency component of kinematic disturbances (12.5 Hz (Fig. 2)), i.e., $n < 700$ rpm or $V < 252$ m/min. Spindle speeds $n = 800$ rpm ($V = 270$ m/min) and $n = 930$ rpm ($V = 318$ m/min) can be used as processing parameters, provided that the part rotation frequency remains constant, since variations in the rotation frequency of the workpiece by 1 Hz can lead to a significant deterioration in the dynamics of the cutting process (Fig. 3). In this case, small variations in the cutting parameters in the quasi-stable parameter zone ($V = 343$ m/min) correspond to significant variations in cutting forces, exceeding the variations of similar parameters at $V = 216$ m/min and $V = 270$ m/min by 1.6 to 2 times.

The results of modeling variations in three cutting parameters using the example of processing speed within the optimal range (216.5 m/min) and beyond it (343.6 m/min) in terms of minimizing variations in the cut-off layer are shown in Fig. 4, *a*, *b*. It is worth noting the effect of suppression of high-frequency components of disturbances from the spindle assembly and the establishment of natural vibrations of the cutting system at $V = 343.6$ m/min, while kinematic disturbances from the tool holder assembly continue to disturb the trajectory of the tool in the longitudinal direction, which leads to variations in the area of the cut-off layer.
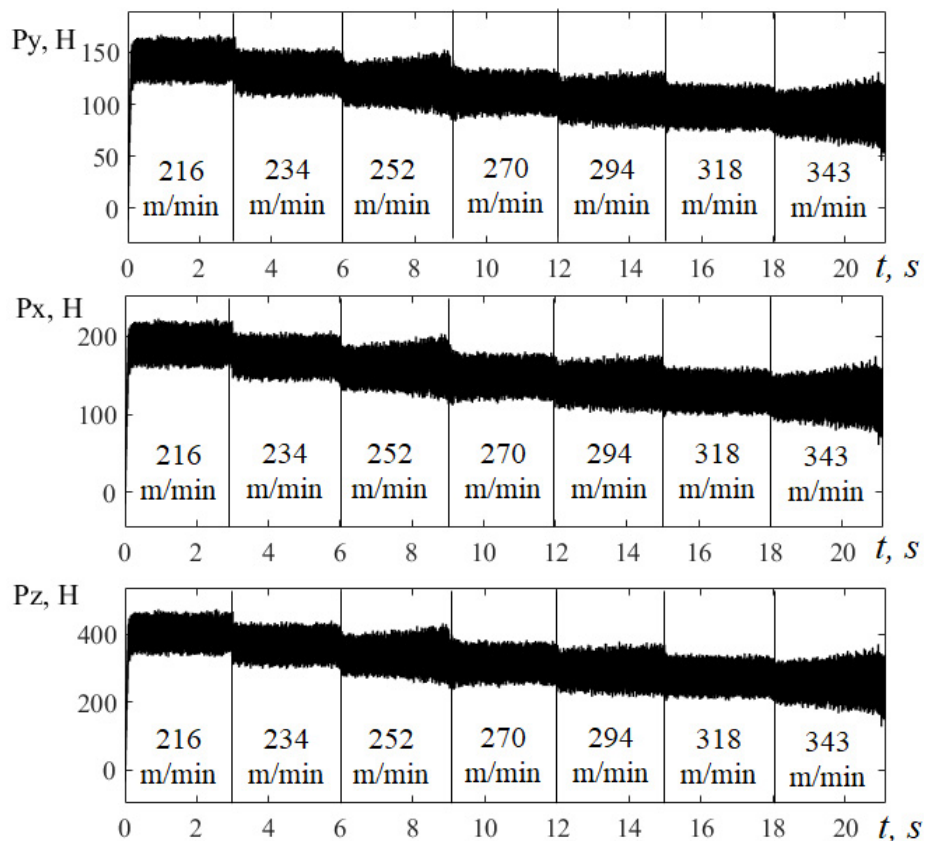
Fig. 3. Modeling of cutting forces along *X*, *Y*, *Z* directions for *s* = 0.198 rpm,
t = 0.5 mm over the spindle speed range *V* = 216–343 m/min

Periodic changes in the area of the cut-off layer due to fluctuations in cutting conditions (*V*, *s*, *t*) relative to their nominal values cause periodic variations in cutting forces, which lead to periodic changes in chip pressure on the tool rake face. In fact, there is a periodic restructuring of the functioning of the "chip-rake face" tribosystem, the characteristics of which directly affect the temperature change in the cutting zone. In this case, a complex relationship is formed between mechanical and thermodynamic processes, which is determined not only by the characteristics of the interacting subsystems of the mechanical part but also by tribophysical phenomena that affect the properties of the environment in the cutting zone. Although the formation of these relationships is caused by external disturbances originating from the mechanical systems of the machine tool, the thermodynamic state of the contact zone is more strongly influenced by the physical and mechanical properties of the tool and workpiece materials, which determine the characteristics of elastic-plastic deformation.

Deformation processes at the points of contact between the chip and the front face of the tool are both a consequence of the dynamics of the cutting process and a source of new nonlinear transformations in the machining zone, including those affecting tool wear and the quality of the machined surface. This necessitates an analysis of the mutual influence of the mechanical and thermodynamic characteristics of the cutting process dynamics based on parameters that can be measured in the system.

To evaluate the temperature change at the tool rake face due to variations in cutting modes and forces characteristic of each spindle speed, we will identify quasi-static instances in the system dynamics when the speed, feed, and cutting depth reach their extreme values as a result of fluctuations. For each of these time points, we will determine the values of the other two parameters of the machining modes and the values of the resultant cutting forces F_{XY} at that moment (Table 1, 2, column 2–5).

Based on the data obtained, the main tribological indicators (3) are calculated using Eq. 3, which determine the maximum temperature of the front edge T_{max}, at the moments of extreme values of the parameters *V*, *s*, and *t* (Tables 1, 2, column 6–10). The deviations of the maximum surface temperature
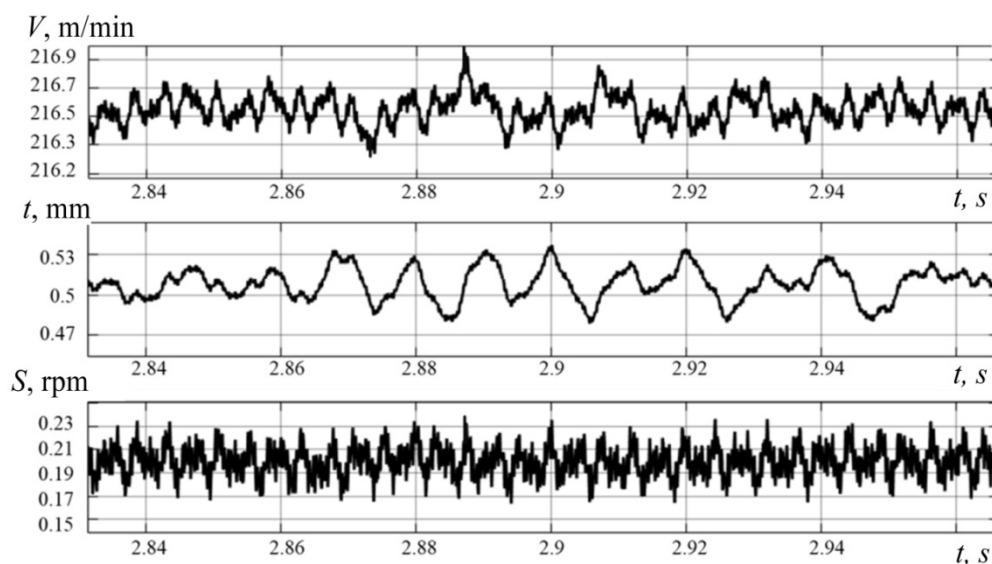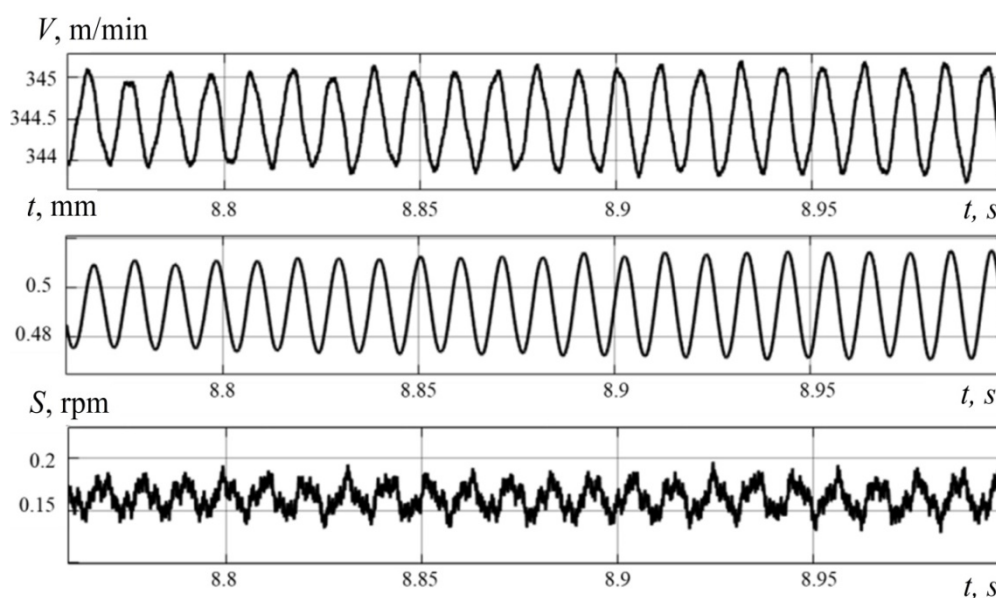
Fig.4. Fluctuations of technological modes:

$a – V$ = 216.5 m/min; $b – V$ = 343.6 m/min

Table 1

Variations of technological modes, cutting forces and main tribological parameters for V = 216.5 m/min

Parameter state at the moment of fluctuation	V, m/min	s, mm/rev	t, mm	F_{XY}, N	$l_{l'}$, mm	h, μm	$\tau_{\kappa'}$, MPa	K_a	$T_{max'}$, °C	ΔT, °C	A_T, °C
(1)	(2)	(3)	(4)	(5)	(6)	(7)	(8)	(9)	(10)	(11)	(12)
nominal	216.5	0.198	0.5	228	0.24	23	508	2.005	1139.2	0	–
$V\rightarrow$max	**217**	0.234	0.51	257	0.28	25	471	1.998	1134.5	−4.7	26.8
$V\rightarrow$min	**216.2**	0.173	0.48	230	0.21	24	619	2.013	1161.2	+22.1	
$s\rightarrow$max	216.8	**0.242**	0.49	271	0.29	27	498	1.998	1149.7	+10.6	10.6
$s\rightarrow$min	216.3	**0.157**	0.47	218	0.19	21	576	2.703	1142.6	+3.4	
$t\rightarrow$max	216.8	0.225	**0.53**	247	0.28	24	460	1.998	1133.1	−6.1	35.9
$t\rightarrow$min	216.3	0.176	**0.46**	235	0.20	25	651	2.014	1168.9	+29.8	

Variations of technological modes, cutting forces and main tribological parameters for V = 343.6 m/min

Parameter state at the moment of fluctuation	V, m/min	s, mm/rev	t, mm	F_{XY}, N	l_p, mm	h, μm	τ_κ, MPa	K_a	T_{max}, °C	ΔT, °C	A_P °C
(1)	(2)	(3)	(4)	(5)	(6)	(7)	(8)	(9)	(10)	(11)	(12)
nominal	343.6	0.198	0.5	142	0.24	14	319	1.962	1092.2	0	–
V→max	**345.4**	0.17	0.507	149	0.21	15	386	1.967	1117.9	+25.8	32.8
V→min	**343.5**	0.158	0.47	139	0.19	15	423	1.974	1124.9	+32.8	
s→max	344.2	**0.207**	0.509	205	0.25	20	430	1.959	1152.8	+60.7	60.7
s→min	344.5	**0.151**	0.47	119	0.17	13	382	1.975	1101.3	+9.1	
t→max	344.7	0.168	**0.519**	194	0.21	19	496	1.966	1162.5	+70.3	70.3
t→min	343.8	0.157	**0.45**	139	0.18	15	447	1.976	1132.6	+40.4	

from the nominal value ΔT and the amplitude of its change at the moments of A_T fluctuations are also presented (Table 1, 2, column 11–12). According to the simulation results, at n = 630 rpm, the greatest increase in instantaneous temperature occurs when the cutting depth reaches its minimum value. At the same time, at the moments of fluctuations, there are combinations of parameters V, s, and t, at which their complex values practically level out the change in instantaneous temperatures (at $V \rightarrow$ max; $s \rightarrow$ min). It should also be noted that, as a result of vibrations under these processing conditions, the maximum instantaneous temperature may decrease relative to the nominal value (at $V \rightarrow$ max; $t \rightarrow$ max). When the cutting speed is increased, negative temperature deviations at moments of fluctuation are less pronounced or cease altogether. Thus, when turning at a speed of V = 343.6 m/min, for any combination of cutting mode parameters, the instantaneous temperature changes only increase (Table 2, column 11).

The amplitudes of temperature spikes generally increase with an increase in spindle speed, and the factors contributing to the generation of positive temperature spikes also change. If at V = 216.5 m/min the main sources of temperature spikes with maximum amplitude are the moments of reaching extreme values of the parameters t and V, then at higher speeds, fluctuations in cutting depth and feed rate have a significant effect. Thus, when turning at V = 343.6 m/min, fluctuations with heating of the tool surface by an additional 61–70 °C occur more frequently, which is due to significant variations in the area of the cut layer due to vibrations characteristic of this machining mode.

Table 3 shows the amplitudes of periodic temperature changes for different spindle speeds n. The highest values of the A_T parameter at each machining speed are underlined, thus highlighting the cutting mode parameters whose fluctuations contribute most to the instability of the thermal state of the cutting zone at each value of n.

The investigated speed range has a pronounced local minimum corresponding to a speed of 270 m/min, for which the lowest values of the A_T parameter are achieved at all extreme values of the turning modes. Increasing the spindle speed above this value leads to a change in the nature of temperature spikes (sources V, t are replaced by s, t) and an increase in A_T amplitudes.

Calculated amplitudes of periodic temperature variations ΔT at moments when parameters V, s, and t reach extreme values

Cutting parameters	Amplitude A_T, °C					
	216.5 m/min	252 m/min	270 m/min	294 m/min	318 m/min	343.6 m/min
V	26.8	31.1	17.8	21.2	24.8	32.8
s	14.1	18.1	12.5	36.1	42.5	60.8
t	35.9	43.2	26.4	41.6	51.4	70.3

Conclusion

Based on the results of digital simulation modeling using data from real-life experiments, deviations of the contact temperature from the nominal value were determined for instances when one of the cutting parameters takes on an extreme value as a result of fluctuations. It was established that the combination of processing parameters at such moments generally leads to an instantaneous increase in the maximum temperature on the tool rake face, characterized by the concept of a thermal flash, but at the same time, for some combinations, a slight decrease in this indicator is possible. Within the range of parameters studied, the optimal cutting speed was identified, at which the output of all three processing parameters to extreme values leads to a minimal change in temperature on the rake face.

It has also been established that this cutting speed is the boundary that divides the studied speed range into two intervals, differing in factors that destabilize the thermal state of the contact zone. When turning a workpiece at a speed below this limit, the greatest temperature deviations occur when the cutting depth and cutting speed reach extreme values. When the processing speed exceeds the optimal value, the main sources of contact temperature changes become the cutting depth and feed rate. Therefore, the factor limiting the productivity of the machining process in terms of minimizing temperature fluctuations is the variation in the area of the cut-off layer due to kinematic disturbances characteristic of the investigated cutting system at higher turning speeds.

The research results presented in this paper can be used to select rational processing parameters, taking into account the kinematic disturbances of the machine tool support group and the thermodynamic state of the contact zone, which depends on their manifestations. The methodology allows evaluating and selecting technological parameters in which force fluctuations minimize possible impulse changes in the temperature of the tool rake face during dry turning. However, it is applicable only for operations that do not use coolant; in the case of the presented work, this was the operation of finishing turning a part of the "Connecting leg" type.

The influence of coolant on pulsed heat release changes will be assessed in further studies. First and foremost, the presented methodology will be effective for machine tool fleets with medium and high degrees of wear, accelerating time-consuming tests to determine optimal operating modes when new tools are delivered. The use of temperature fluctuations caused by kinematic errors as an additional parameter for evaluating the optimality of cutting parameters in vibration monitoring and compensation systems can improve process stability and reduce the overall temperature in the cutting zone. Taking into account temperature changes calculated from the vibration activity signal of the tool is particularly relevant for metal-cutting machines with a long service life, which are characterized by significant periodic disturbances in the cutting system from the feed drives and the main drive.

References

1. Komanduri R., Hou Z.B. A review of the experimental techniques for the measurement of heat and temperatures generated in some manufacturing processes and tribology. *Tribology International*, 2001, vol. 34 (10), pp. 653–682. DOI: 10.1016/S0301-679X(01)00068-8.

2. Grzesik W. Experimental investigation of the cutting temperature when turning with coated indexable inserts. *International Journal of Machine Tools and Manufacture*, 1999, vol. 39 (3), pp. 355–369. DOI: 10.1016/S0890-6955(98)00044-3.

3. Sutter G., Faure L., Molinari A., Ranc N., Pina V. An experimental technique for the measurement of temperature fields for the orthogonal cutting in high speed machining. *International Journal of Machine Tools and Manufacture*, 2003, vol. 43 (7), pp. 671–678. DOI: 10.1016/S0890-6955(03)00037-3.

4. Shan C., Zhang X., Shen B., Zhang D. An improved analytical model of cutting temperature in orthogonal cutting of Ti6Al4V. *Chinese Journal of Aeronautics*, 2019, vol. 32 (3), pp. 759–769. DOI: 10.1016/j.cja.2018.12.001.

5. Barzegar Z., Ozlu E. Analytical prediction of cutting tool temperature distribution in orthogonal cutting including third deformation zone. *Journal of Manufacturing Processes*, 2021, vol. 67, pp. 325–344. DOI: 10.1016/j.jmapro.2021.05.003.

6. Weng J., Saelzer J., Berger S., Zhuang K., Bagherzadeh A., Budak E., Biermann D. Analytical and experimental investigations of rake face temperature considering temperature-dependent thermal properties. *Journal of Materials Processing Technology*, 2023, vol. 314, p. 117905. DOI: 10.1016/j.jmatprotec.2023.117905.

7. Kulkarni A.P., Chinchanikar S., Sargade V.G. Dimensional analysis and ANN simulation of chip-tool interface temperature during turning SS304. *Obrabotka metallov (tekhnologiya, oborudovanie, instrumenty) = Metal Working and Material Science*, 2021, vol. 23, no. 4, pp. 47–64. DOI: 10.17212/1994-6309-2021-23.4-47-64.

8. Ren X.J., Yang Q.X., James R.D., Wang L. Cutting temperatures in hard turning chromium hardfacings with PCBN tooling. *Journal of Materials Processing Technology*, 2004, vol. 147 (1), pp. 38–44. DOI: 10.1016/j.jmatprotec.2003.10.013.

9. Sulaiman S., Roshan A., Borazjani S. Effect of cutting parameters on tool-chip interface temperature in an orthogonal turning process. *Advanced Materials Research*, 2014, vol. 903, pp. 21–26. DOI: 10.4028/www.scientific.net/amr.903.21.

10. Kikuchi M. The use of cutting temperature to evaluate the machinability of titanium alloys. *Acta Biomaterialia*, 2009, vol. 5 (2), pp. 770–775. DOI: 10.1016/j.actbio.2008.08.016.

11. Karaguzel U., Budak E. Investigating effects of milling conditions on cutting temperatures through analytical and experimental methods. *Journal of Materials Processing Technology*, 2018, vol. 262, pp. 532–540. DOI: 10.1016/j.jmatprotec.2018.07.024.

12. Baohai W., Di C., Xiaodong H., Dinghua Z., Kai T. Cutting tool temperature prediction method using analytical model for end milling. *Chinese Journal of Aeronautics*, 2016, vol. 29 (6), pp. 1788–1794. DOI: 10.1016/j.cja.2016.03.011.

13. Li S., Li Sh., Hu Y., Popov E. Experimental study on coupling characteristics of cutting temperature rise and cutting vibration under different tool wear states. *International Journal of Advanced Manufacturing Technology*, 2022, vol. 118, pp. 907–919. DOI: 10.1007/s00170-021-07948-w.

14. Yu Q., Li Sh., Zhang X., Shao M. Experimental study on correlation between turning temperature rise and turning vibration in dry turning on aluminum alloy. *International Journal of Advanced Manufacturing Technology*, 2019, vol. 103, pp. 453–469. DOI: 10.1007/s00170-019-03506-7.

15. Chichinadze A.V., Shuchev K.G., Ryzhkin A.A., Filipchuk A.I., Klimov M.M. Temperaturnyi rezhim pri trenii instrumental'nykh materialov s uchetom ob"emnosti istochnika teplovydeleniya [Temperature regime during friction of tool materials taking into account the volume of heat source]. *Trenie i iznos = Friction and Wear*, 1986, no. 7, pp. 43–51.

16. Lebedev V.A., Aliev M.M., Fominov E.V., Fomenko A.V., Marchenko A.A., Mironenko A.E. Termoelektricheskie kharakteristiki protsessa tocheniya stal'nykh zagotovok tverdosplavnymi plastinami s kombinirovannymi pokrytiyami [Thermoelectric characteristics of the process of turning steel billets by carbide inserts with combined coatings]. *Trenie i iznos = Friction and Wear*, 2023, vol. 44, no. 2, pp. 114–121. DOI: 10.32864/0202-4977-2023-44-2-114-121.

17. Ryzhkin A.A. *Sinergetika iznashivaniya instrumental'nykh materialov pri lezviinoi obrabotke* [Synergetics of tool materials wear during blade machining]. Rostov-on-Don, DSTU Publ., 2019. 289 p.

18. Migranov M.Sh., Shuster L.Sh. *Iznosostoikost' rezhushchego instrumenta s mnogosloinymi pokrytiyami* [Wear resistance of cutting tools with multilayer coatings]. *Trenie i iznos = Friction and Wear*, 2005, vol. 26, no. 3, pp. 304–307.

19. Fominov E.V., Gvindjilia V.E., Marchenko A.A., Shuchev K.G. Effect of periodic fluctuations of cutting mode parameters on the temperature of the front face of a turning tool. *Advanced Engineering Research (Rostov-on-Don)*, 2025, vol. 25 (1), pp. 32–42. DOI: 10.23947/2687-1653-2025-25-1-32-42.

20. Danielyan A.M., Bobrik P.I., Gurevich Ya.L. *Obrabotka rezaniem zharoprochnykh stalei, splavov i tugoplavkikh metallov* [Cutting treatment of heat-resistant steels, alloys and refractory metals]. Moscow, Mashinostroenie Publ., 1965. 308 p.

21. Reznikov A.N. *Teplofizika rezaniya* [Thermophysics of cutting]. Moscow, Mashinostroenie Publ., 1969. 288 p.

22. Abbas A.T., Al-Abduljabbar A.A., El Rayes M.M., Benyahia F., Abdelgaliel I.H., Elkaseer A. Multi-objective optimization of performance indicators in turning of AISI 1045 under dry cutting conditions. *Metals*, 2023, vol. 13 (1), p. 96. DOI: 10.3390/met13010096.

23. Özbek O. Evaluation of nano fluids with minimum quantity lubrication in turning of Ni-base superalloy UDIMET 720. *Lubricants*, 2023, vol. 11 (4), p. 159. DOI: 10.3390/lubricants11040159.

24. Arun K.K., Navaneeth V.R., Prabhu S., Ramesh Kumar M., Giriraj M. Experimental investigation of turning process parameter under several cutting conditions for duplex steels for minimization of cutting temperature. *Materials Today: Proceedings*, 2022, vol. 62 (4), pp. 1917–1920. DOI: 10.1016/j.matpr.2022.01.447.

25. Zakovorotny V.L., Gvindjiliya V.E. The influence of the vibration on the tool shape-generating trajectories when turning. *Obrabotka metallov (tekhnologiya, oborudovanie, instrumenty) = Metal Working and Material Science*, 2019, vol. 21, no. 3, pp. 42–58. DOI: 10.17212/1994-6309-2019-21.3-42-58.

26. Ryzhkin A.A. *Teplofizicheskie protsessy pri iznashivanii instrumental'nykh rezhushchikh materialov* [Thermophysical processes at wear of tool cutting materials]. Rostov-on-Don, DSTU Publ., 2005. 311 p.

27. Bobrov V.F. *Razvitie nauki o rezanii metallov* [Development of science of metal cutting]. Moscow, Mashinostroenie Publ., 1967. 416 p.

28. Silin S.S. *Metody podobiya pri rezanii materialov* [Similarity methods in cutting of materials]. Moscow, Mashinostroenie Publ., 1979. 152 p.

29. Gvindjiliya V.E., Fominov E.V., Moiseev D.V., Gamaleeva E.I. Influence of dynamic characteristics of the turning process on the workpiece surface roughness. *Obrabotka metallov (tekhnologiya, oborudovanie, instrumenty) = Metal Working and Material Science*, 2024, vol. 26, no. 2, pp. 143–157. DOI: 10.17212/1994-6309-2024-26.2-143-157.

Conflicts of Interest

The authors declare no conflict of interest.

NSTU

NETI

Obrabotka metallov -
Metal Working and Material Science

Journal homepage: http://journals.nstu.ru/obrabotka_metallov

Production of rods and sheets from TiNiHf alloy with high-temperature shape memory effect by longitudinal rolling and rotary forging methods

Roman Karelin [a, *], Viktor Komarov [b], Vladimir Cherkasov [c], Artem Osokin [d],
Konstantin Sergienko [e], Vladimir Yusupov [f], Vladimir Andreev [g]

A.A. Baykov Institute of Metallurgy and Materials Science of the Russian Academy of Sciences, 49 Leninsky Ave., Moscow, 119334, Russian Federation

[a] https://orcid.org/0000-0002-4795-8668, ✉ rdkarelin@gmail.com; [b] https://orcid.org/0000-0003-4710-3739, ✉ vickomarov@gmail.com;
[c] https://orcid.org/0000-0002-5450-3565, ✉ cherkasov.vv@misis.ru; [d] https://orcid.org/0009-0008-4945-3648, ✉ art.osokin1201@icloud.com;
[e] https://orcid.org/0000-0003-4018-4599, ✉ shulf@yandex.ru; [f] https://orcid.org/0000-0002-0640-2217, ✉ vsyusupov@mail.ru;
[g] https://orcid.org/0000-0003-3937-1952, ✉ andreev.icmateks@gmail.com

ARTICLE INFO

ABSTRACT

Introduction. *Ti-Ni* based shape memory alloys (*SMAs*) are functional materials that find widespread practical application in engineering and medicine. Functional properties of *Ti-Ni* based alloys are sensitive to the chemical composition. To develop alloys with specific properties, ternary *SMAs* are being actively developed. For example, *TiNiHf* ternary alloys are characterized by a high-temperature shape memory effect. Today, there is a demand for *SMAs* used in the production of functional elements with a response temperature of more than 120 °C. These alloys must also have sufficient ductility to obtain deformed semi-finished products for the subsequent manufacture of heat-sensitive functional elements. Also among the current issues of developing the practical application of *TiNiHf* alloys is the lack of technological schemes for obtaining semi-finished products from *TiNiHf SMAs*. **The purpose of this work** is study the feasibility of conducting deformation processing of the studied *TiNiHf* alloys with a high-temperature shape memory effect and to identify the relationships between phase composition and mechanical characteristics and the applied processing method. **In this work**, the possibility of producing sheets and rods from *TiNiHf* alloys with 5 and 10 at.% *Hf* and 50.0 at.% Ni by longitudinal rolling, caliber rolling, and rotary forging was investigated. **The research methods** were: X-ray analysis, differential scanning calorimetry, and measurement of *Vickers* hardness. **Results and discussion.** It was found that the *TiNiHf* alloy with 10 at.% *Hf* has insufficient ductility. From the alloy with 5 at.% *Hf*, blanks in the form of sheets and rods of various sizes were obtained by using longitudinal rolling and rotary forging processes. It was shown that hot deformation allows increasing the hardness of the studied *TiNiHf* alloy with 5 at.% *Hf* compared to the cast state, from 232 HV to 242–264 HV. Cold deformation leads to a significant increase in hardness values up to 362–394 HV. Characteristic temperatures of the forward and reverse martensitic transformation are quite stable. The obtained results indicate the potential of using longitudinal rolling and rotary forging to obtain semi-finished products of *TiNiHf* alloys with 5 at.% *Hf* and to improve the functional and mechanical properties of the alloy after smelting.

Introduction

Shape memory alloys (*SMAs*) based on titanium nickelide are functional materials that receive widespread practical application in engineering and medicine due to their unique shape memory properties, high mechanical characteristics, corrosion resistance, and biocompatibility [1–7]. In order to regulate their

---

* Corresponding author
Karelin Roman D., Ph.D. (Engineering),
A.A. Baykov Institute of Metallurgy and Materials Science
of the Russian Academy of Sciences,
49 Leninsky ave.,
119334, Moscow, Russian Federation
Tel.: +7 916 590-42-76, **e-mail**: rdkarelin@gmail.com

functional behavior and obtain materials with special properties, the use of ternary titanium nickelide alloys containing *Cu*, *Fe*, *Co*, *Nb*, and *Hf* is being actively developed [8-11]. Among these alloys for high-temperature applications, alloys of the *TiNiHf* system should be highlighted [12–14]. Most scientific research in this field focuses on alloys with 20 at.% *Hf* and 50.3 at.% *Ni*, which provide a temperature range of shape recovery (*TRSR*) of 200–350 °C [15–19]. The high *Hf* (20 at.%) and *Ni* (over 50 at.%) content is attributed to observations from previous studies, which suggest that *TiNiHf* alloys become brittle and difficult to deform when the combined concentration of *Ti* and *Hf* exceeds 49.8 at.%. Embrittlement is attributed to the precipitation of a significant amount of an embrittling $(Ti, Hf)_2Ni$-type phase [20]. To mitigate this, the nickel concentration is typically increased. However, if other elemental contents remain unchanged, the martensitic transformation temperature range will decrease accordingly. Therefore, a higher *Hf* concentration is required to achieve a high-temperature shape memory effect in these alloys. However, high *Hf* content significantly increases the cost, hindering their practical application. Moreover, the application of *TiNiHf SMAs* is also challenged by the limited control over martensitic transformation temperatures. Several industries currently require shape-memory alloys with a *TRSR* ranging from 120 to 200 °C, coupled with sufficient technological plasticity for the production of thermosensitive components. In addition, a significant challenge in expanding the practical applications of *TiNiHf* alloys lies in developing the technology for manufacturing semi-finished products of various grades, a task inextricably linked to the advancement of novel thermomechanical processing methods [21].

Earlier studies showed that rods with high mechanical properties and a shape recovery temperature of 155 °C after 2% bending could be obtained from the $Ti_{49.0}Ni_{49.5}Hf_{1.5}$ alloy using rotary forging [22]. Reference [23] also demonstrated that a pulsed electric current could improve the technological plasticity of the $Ti_{47.4}Ni_{47.6}Hf_{5.0}$ alloy during cold rolling.

Based on the preceding discussion, and as part of our effort to develop methods for creating semi-finished *TiNiHf SMA* products with lower *Hf* and *Ni* content, the first purpose of this study is to explore the application of thermomechanical treatments to *TiNiHf* alloys with 5 and 10 at.% *Hf* and 50 at.% *Ni*, using different deformation methods. The second purpose is to determine how the phase composition and mechanical characteristics of *TiNiHf* alloys change depending on the deformation method used.

This paper investigates the production of semi-finished sheets and rods using longitudinal rolling, caliber rolling, and rotary forging. The alloy's structure and mechanical properties were also analyzed using X-ray analysis, differential scanning calorimetry, and *Vickers* hardness testing. A significant result is the successful production of $Ti_{45.0}Ni_{50.0}Hf_{5.0}$ alloy semi-finished products, including sheets (2.2 and 1.0 mm thick), a rectangular bars (6.9 × 8.5 mm), and a 5.1 mm diameter rods, all demonstrating high hardness and stable phase composition.

Methods

The study used two alloys with compositions $Ti_{45.0}Ni_{50.0}Hf_{5.0}$ and $Ti_{40.0}Ni_{50.0}Hf_{10.0}$. The starting materials were 99.99% pure iodide titanium, 99.99% pure nickel (*H0* grade), and 2.5 mm diameter hafnium wire (*GFI-1* grade). *TiNiHf* ingots containing 5 and 10 at.% *Hf* were produced by vacuum electric arc melting, with eight remelting cycles, and cast into a water-cooled copper mold. Hot deformation was performed by longitudinal flat and bar rolling on a *DUO 300* two-roll rolling mill and by rotary forging at 850 °C. The bar rolling used a square-to-square pass schedule, with the square side changing as follows: 19→17→15→13→11→9→8→7→6 mm. Cold rolling was then performed on a *QUARTO110/300* four-roll rolling mill.

The martensitic transformation temperature range (*TRMT*) in the as-cast alloy was studied by differential scanning calorimetry (*DSC*) using a *Mettler Toledo DSC 3+* calorimeter with a heating and cooling rate of 10 °C/min from 0 to 200 °C.

The martensitic transformation temperature range (*TRMT*) was measured using differential scanning calorimetry (*DSC*) on a *Mettler Toledo DSC 3+* calorimeter, with a heating/cooling rate of 10 °C/min from 0 to 200 °C. The phase composition was analyzed by X-ray diffraction analysis (*XRD*) using a *DRON-3*

diffractometer with *CuKα* radiation at 2θ angles from 35 to 47° [18, 24]. *Vickers* hardness was measured at room temperature using a *LECOM 400-A* hardness tester under a 1 N load to determine mechanical properties.

Result and Discussion

Initial TiNiHf SMA Ingots

Fig. 1 shows the general appearance of the ingots produced by electron beam melting. Table 1 presents the mass, dimensions, and chemical composition of the ingots.

a

b

20 mm

c

Fig. 1. Photographs of ingots **1** (*a*), **2** (*b*), and **3** (*c*) of *TiNiHf SMA* after vacuum arc melting with 8-fold remelting

T a b l e 1

Weight, dimensions and estimated composition of the *TiNiHf* ingots

Ingot No.	Weight, g	Dimensions, ($h \times b \times L$) mm	Chemical composition					
			mass %			at.%		
			Ti	*Ni*	*Hf*	*Ti*	*Ni*	*Hf*
1	148.84	9.5 × 18.1 × 137.5	28.87	44.23	26.90	40.0	50.0	10.0
2	150.15	10.4 × 18.5 × 136.9	36.03	49.06	14.92	45.0	50.0	5.00
3	149.12	9.8 × 17.8 × 137.5	28.87	44.23	26.90	40.0	50.0	10.0

After melting, the martensitic transformation temperature range (*TRMT*) of the ingots was analyzed using differential scanning calorimetry (*DSC*). Characteristic calorimetric curves are shown in Fig. 2.

DSC analysis of samples from ingots **1** and **3** showed no peaks for either forward or reverse transformations within the temperature range studied. Ingot **2**, however, showed a reverse *MT* with starting and finishing temperatures of 63 °C and 124 °C, respectively. This wide temperature range is typical for as-cast ingots due to potential internal stresses and segregation.

To improve homogeneity, ingot **1** was initially subjected to a 12-hour homogenization annealing at 1,100 °C in vacuum. However, the ingot melted during annealing, possibly due to the formation of phases with lower melting temperatures during cooling after melting. Therefore, it was decided not to

Heat flow, mW

Cooling

M_p

M_f M_s

°C

Ingot 1

Ingot 2

A_s A_f

A_p

Heating
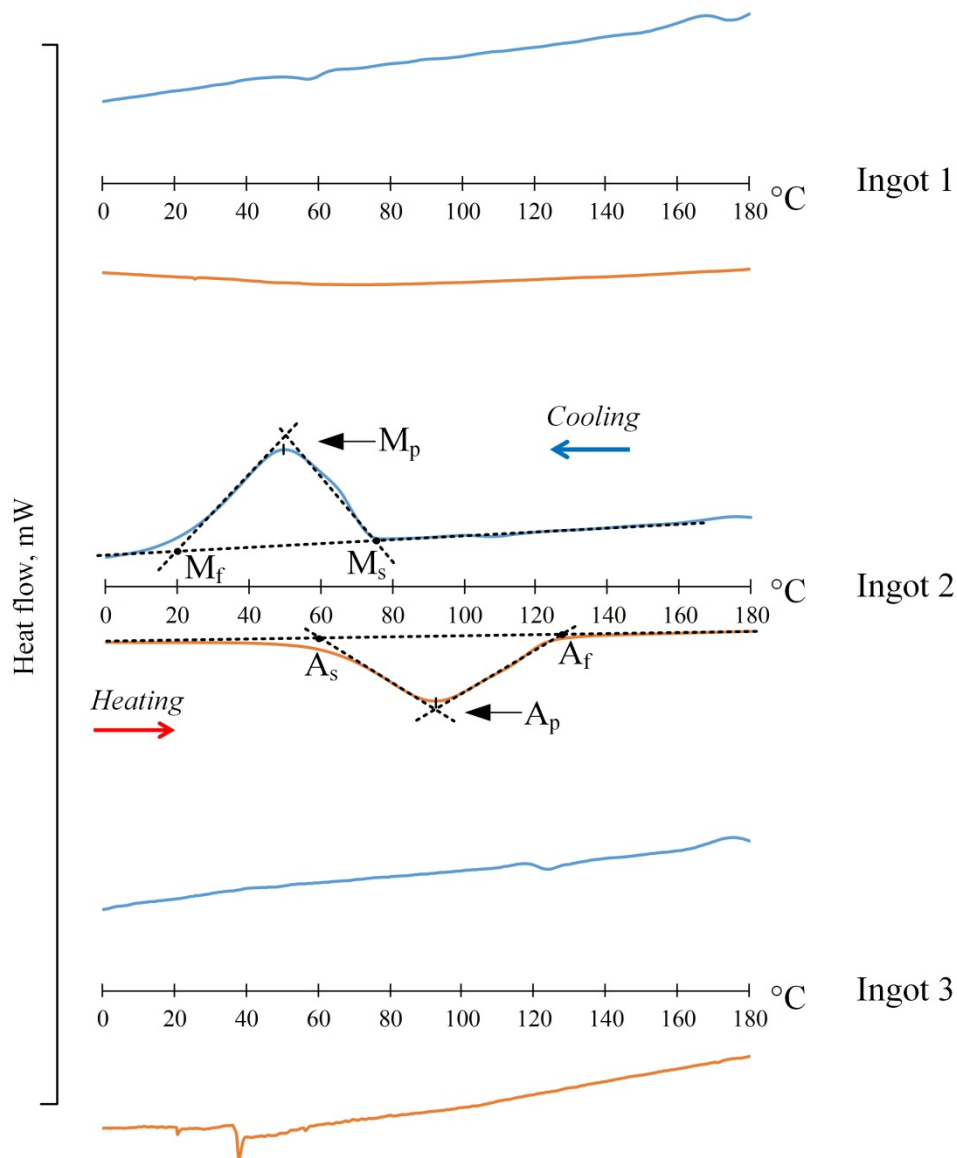
Ingot 3

Fig. 2. Calorimetric curves of ingots **1**, **2**, and **3** of *TiNiHf SMA*

use homogenization annealing, and ingots **2** and **3** were deformed in the as-cast state. Homogenization annealing was therefore excluded from the production process for *TiNiHf SMA* semi-finished products to optimize the technology.

Production of TiNiHf SMA semi-finished products

Before deformation, the ingots were cut into two parts. The resulting ingots had the following dimensions: **2-1** – 10.4 × 18.5 × 53.1 mm and **2-2** – 10.4 × 18.5 × 77.1 mm; **3-1** – 9.8 × 17.8 × 52.1 mm and **3-2** – 9.8 × 17.8 × 76.7 mm.

Hot deformation of ingots **2-1** and **3-1** was first performed by longitudinal rolling at 850 °C. The samples were preheated for 15 minutes without a protective atmosphere to improve rolling workability, unlike previous studies [23] where heating was in a protective argon atmosphere, with 3–5 minute reheating before each pass. The relative strain in one pass was kept below 15%. Hot rolling of ingot **2-1** produced a sheet with dimensions 2.2 × 27.5 × 167.9 mm. However, ingot **3-1** fractured after only 2 passes, accumulating a relative strain of 12%. Considering the lack of distinct peaks on the calorimetric curves, the melting of the similar ingot **1** during homogenization annealing, and the alloy's low workability, it's likely that ingot **3** contained many undesirable secondary phases formed during cooling after melting or during heating for rolling. This suggests that the alloy with 5 at.% *Hf* has better workability than the alloy with 10 at.% *Hf*. Fig. 3 shows photos of the sheet from ingot **2-1** and the fractured ingot **3-1**.

a

b

Fig. 3. Photographs of the obtained sheet from ingot **2-1** (*TiNiHf* alloy) with a thickness of 2.2 mm (*a*)
and ingot **3-1** after fracture (*b*)

Further deformation by hot bar rolling (*HBR*) and rotary forging (*RF*) was only done on ingot **2-2** of the *TiNiHf* alloy with 5 at.% *Hf*. Initially, two passes were rolled in one caliber from a single heating cycle, taking advantage of deformation heating. However, when switching to the second caliber, cracks appeared at the back end of the ingot. This suggests that the alloy has a narrow temperature range for plastic deformation. To prevent the ingot from cooling down, it was reheated after each pass. Changing the rolling pattern and eliminating the second pass without preheating resulted in successful rolling without fracture or new cracks. This produced a rectangular bar measuring 6.9 × 8.5 × 236.4 mm. After bar rolling, a 150 mm long sample was cut from the bar for rotary forging. Rotary forging was carried out at a deformation temperature of 850 °C, with a relative strain per pass below 10%, and the ingot was heated between each pass for 10-15 minutes. This produced a rod with a diameter of 119 mm.

It's worth noting that, unlike the approach in [23], the section of ingot **2** used here was rotary forged after prior deformation rather than in the as-cast state. This highlights the potential for combining hot bar rolling and rotary forging to produce *TiNiHf SMA* rods. Fig. 4 shows a photo of the bars after rolling and rotary forging.

a

b
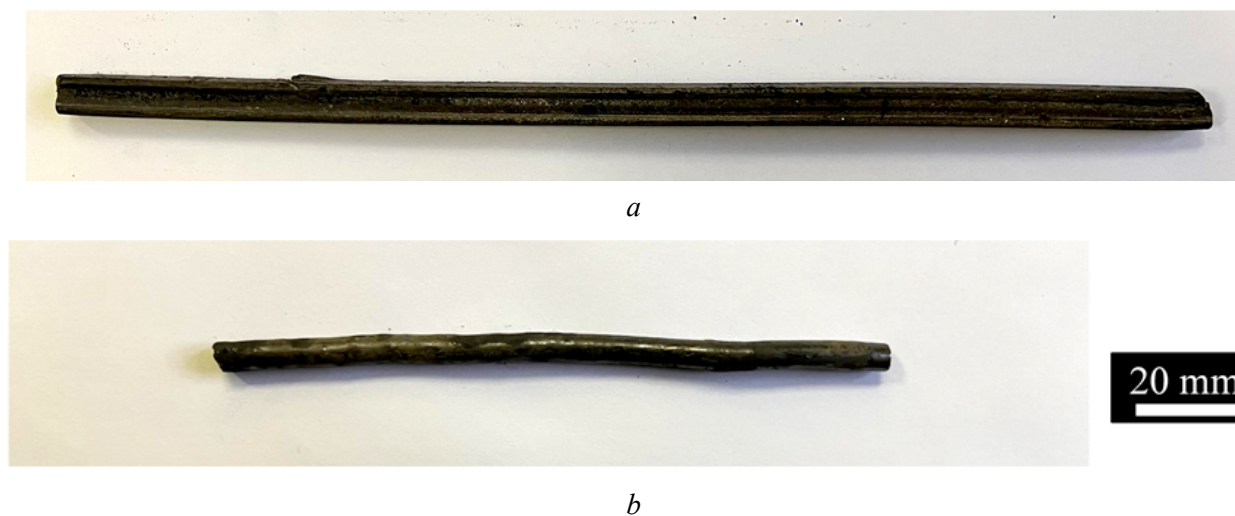
Fig. 4. Photograph of a *TiNiHf* alloy rod after caliber rolling (*a*) and rotary forging (*b*)

It should be noted that rotary forging had difficulties with rod alignment and chipping at the ends, likely due to cooling. Because of this, further rotary forging to smaller diameters (which would cool even faster) wasn't attempted.

Next, a 2.1 × 27.5 × 56 mm sample was cut from the hot-rolled sheet from ingot **2-1** for cold rolling (*CR*). After cutting, the sample was cleaned to remove the surface oxide layer by grinding and chemical etching in a mixture of nitric and hydrofluoric acids. The sheet thickness before rolling was 2.1 mm. Cold rolling was carried out with a relative strain per pass below 10%. Prior work found the critical relative strain for cold rolling *TiNiHf* alloy to be 20% [22]. Therefore, cold rolling was carried out with intermediate annealing at a temperature of 850 °C for 10 minutes upon reaching a relative degree of deformation close to 20%. After cold rolling to 1.04 mm, a sample was cut from the sheet for further cold rolling to fracture to redetermine the critical strain. Fig. 5 shows the sheet before and after cold rolling, thus concluding our description of the cold rolling process.

a   *b*
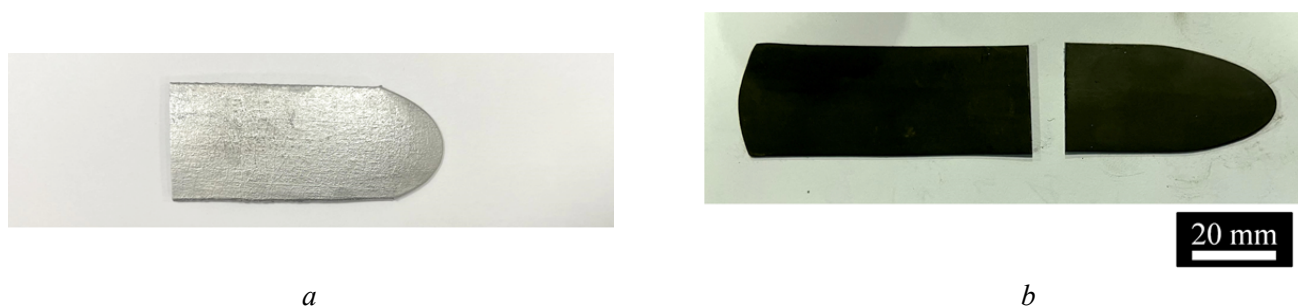
Fig. 5. General view of the *TiNiHf SMA* sheets before (*a*) and after (*b*) cold rolling

Cold rolling the *TiNiHf SMA* sample to its critical strain showed that fracture (a through-crack at the front end) occurred after a total relative strain of 23%, with a final sample thickness of 0.93 mm. This confirms that intermediate annealing is needed during cold rolling of *TiNiHf* alloy samples after a total strain of 20%.

Next, we studied how the phase composition and mechanical properties of the *TiNiHf* + 5 at.% *Hf* alloy changed depending on the processing method.

Investigation of the phase state and mechanical properties of TiNiHf SMA samples following application of various deformation methods

Fig. 6 shows the *Vickers* hardness of alloy **2** after deformation using different methods.
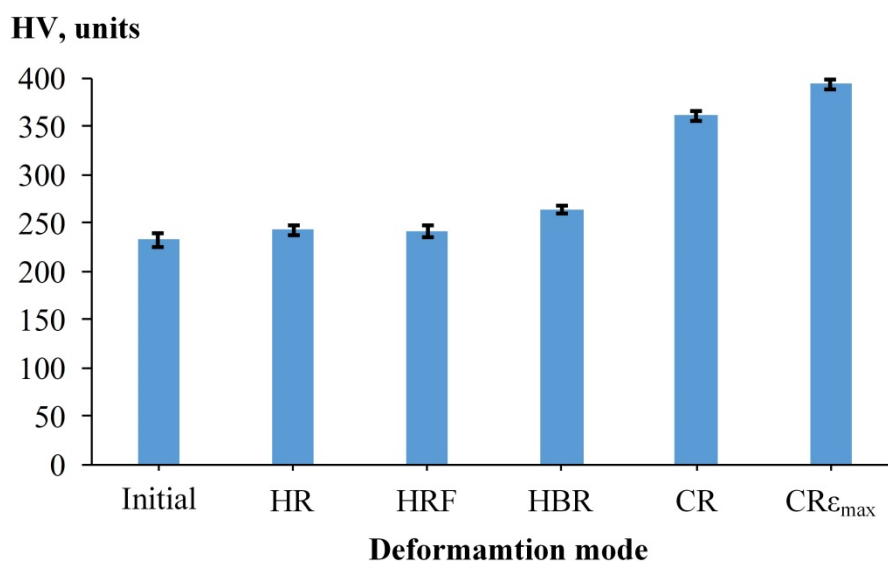
Fig. 6. Hardness of *TiNiHf SMA* samples after various deformation methods

Hot deformation slightly increased the *Vickers* hardness compared to the as-cast ingot **2** (232 HV): hardness after *HR* and *HRF* was about 242 HV, and after *HBR* it was 264 HV. This is typical for high-temperature heat treatment and related to dynamic and static recrystallization. Cold deformation to 1 mm thickness greatly increased hardness to 362 HV, with a maximum of 394 HV after *CR* to the critical strain leading to fracture. This is likely due to the increased crystal lattice defects after *CR*. The hot deformation results suggest that it occurs at a steady stage with dynamic recrystallization and stress relaxation from deformation hardening, unlike *CR*, which results in a heavily deformed structure.

Fig. 7 shows the X-ray analysis results for alloy **2** after various deformation methods.

X-ray analysis showed that martensite was the main phase in alloy **2** samples at room temperature, both before and after deformation. This agrees with the *DSC* data. The absence of *B2*-austenite peaks confirms that the reverse *MT* occurs above room temperature. (*Ti, Hf*)$_2$*Ni* phase lines, formed during cooling after
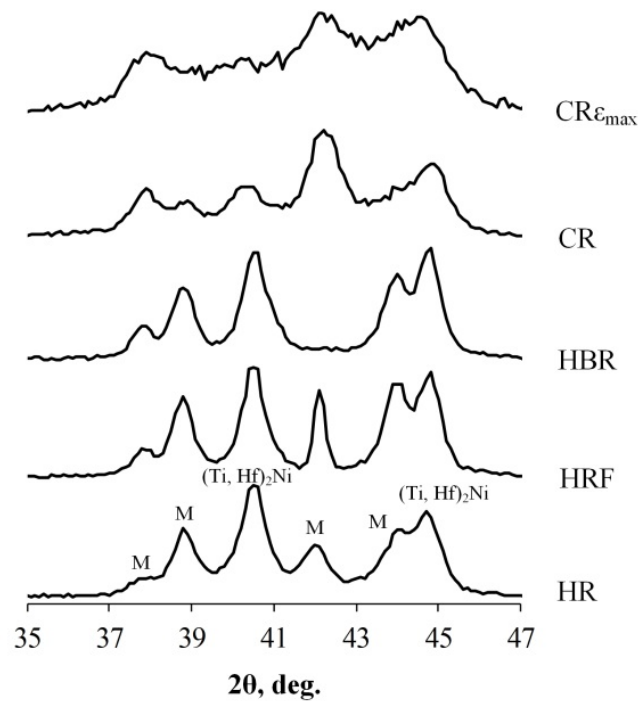
Fig. 7. X-ray diffraction patterns of *TiNiHf SMA*
samples after the studied processing methods

melting, were seen at 2θ angles of 41° and 45°. Hot deformation didn't significantly broaden the X-ray lines, but cold rolling did. The changes in the sample line profile after cold rolling confirm significant deformation hardening and increased crystal structure defects.

Fig. 8 and Table 2 show the martensitic transformation temperature range (*TRMT*) measured by *DSC* after the different processing methods on ingot **2**. Fig. 2 shows the initial *DSC* curves of the *TiNiHf SMA* ingots.
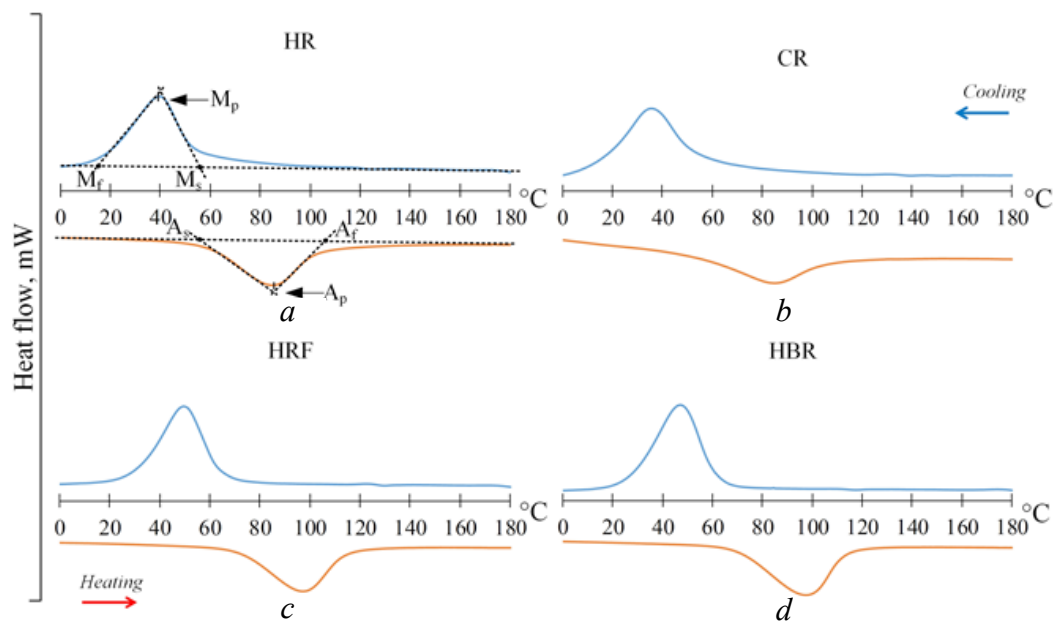
Fig. 8. Calorimetric curves of the samples of ingot 2 (*TiNiHf SMA*) after the studied processing methods: hot rolling (*HR*) (*a*), cold rolling (*CR*) (*b*), hot rotary forging (*HRF*) (*c*), and hot longitudinal rolling (*HLRR*) (*d*)

T a b l e   2

Martensitic transformation temperatures of processed *TiNiHf SMA* (Ingot 2)

Sample	Direct transformation			Reverse transformation		
	M_s, °C	M_f, °C	M_p, °C	A_s, °C	A_f, °C	A_p, °C
Initial	74	50	21	62	92	124
HR	54	40	17	61	85	105
HRF	65	50	31	71	97	115
HBR	62	47	27	70	97	113
CR	54	36	17	52	85	107

The results show that neither hot nor cold deformation significantly changes the martensitic transformation temperatures; they remain relatively stable with fluctuations under 10 °C. However, there's a trend of decreasing forward MT (A_f) temperature compared to the as-cast state of ingot **2**. Even so, this temperature stays above 105 °C in all cases, indicating that the *TiNiHf* alloy maintains its high-temperature shape memory behavior.

Conclusion

A comprehensive investigation was undertaken to assess the feasibility of producing a range of semi-finished products from *TiNiHf* shape memory alloys containing 5 and 10 at.% *Hf* with reduced *Ni* content, utilizing various deformation methods. Based on the findings of this study, the following conclusions can be drawn:

The *TiNiHf SMA* with 10 at.% *Hf* lacks sufficient technological plasticity for thermomechanical treatment by the considered deformation methods.

The *TiNiHf SMA* with 5 at.% *Hf* has sufficient technological plasticity Various deformation methods were applied to the alloy (hot and cold longitudinal rolling, bar rolling, rotary forging). High-quality semi-finished products in the form of sheets and rods of various sizes were obtained.

Hot deformation increases hardness from 232 HV (as-cast) to 242 HV (*HR*/*HRF*) and 264 HV (*HBR*). Cold deformation significantly increases hardness, reaching 362 HV (1 mm thick sheet) and 394 HV (rolling to critical strain).

The characteristic temperatures of the forward and reverse martensitic transformations in the *TiNiHf SMA* with 5 at.% *Hf* remain stable after deformation. Deformation slightly decreases the finishing temperature of the reverse martensitic transformation (A_f) (to 19 °C) compared to the as-cast ingot. However, *Af* remains above 105 °C, confirming their high-temperature shape memory behavior.

Thermomechanical processing using hot and cold rolling and rotary forging is a promising method for producing *TiNiHf SMA* semi-finished products with 5 at.% *Hf* and improving the alloy's functional and mechanical properties after melting.

References

1. Sadashiva M., Sheikh M.Y., Khan N., Kurbet R., Gowda T.D. A review on application of shape memory alloys. *International Journal of Recent Technology and Engineering (IJRTE)*, 2021, vol. 9 (6), pp. 111–120. DOI: 10.35940/ijrte.F5438.039621.

2. Nair V.S., Nachimuthu R. The role of NiTi shape memory alloys in quality of life improvement through medical advancements: A comprehensive review. *Proceedings of the Institution of Mechanical Engineers, Part H: Journal of Engineering in Medicine*, 2022, vol. 236 (7), pp. 923–950. DOI: 10.1177/09544119221093460.

3. Kim M.S., Heo J.K., Rodrigue H., Lee H.T., Pané S., Han M.W., Ahn S.H. Shape memory alloy (SMA) actuators: The role of material, form, and scaling effects. *Advanced Materials*, 2023, vol. 35 (33), p. 2208517. DOI: 10.1002/adma.202208517.

4. Khmelevskaya I., Komarov V., Kawalla R., Prokoshkin S., Korpala G. Features of Ti-Ni alloy structure formation under multi-axial quasi-continuous deformation and post-deformation annealing. *Materials Today: Proceedings*, 2017, vol. 4 (3), pp. 4830–4835. DOI: 10.1016/j.matpr.2017.04.079.

5. Karelin R., Komarov V., Khmelevskaya I., Cherkasov V., Andreev V., Yusupov V., Prokoshkin S. Effect of temperature-deformation regimes of equal channel angular pressing in core-shell mode on the structure and properties of near-equiatomic titanium nickelide shape memory alloy. *Journal of Alloys and Compounds*, 2024, vol. 1005, p. 176071. DOI: 10.1016/j.jallcom.2024.176071.

6. Komarov V., Karelin R., Khmelevskaya I., Yusupov V., Gunderov D. Effect of post-deformation annealing on structure and properties of nickel-enriched Ti-Ni shape memory alloy deformed in various initially deformation-induced structure states. *Crystals*, 2022, vol. 12 (4), p. 506. DOI: 10.3390/cryst12040506.

7. Karelin R., Komarov V., Khmelevskaya I., Andreev V., Yusupov V., Prokoshkin S. Structure and properties of TiNi shape memory alloy after low-temperature ECAP in shells. *Materials Science and Engineering: A*, 2023, vol. 872, p. 144960. DOI: 10.1016/j.msea.2023.144960.

8. Parida J., Mishra S.C. NiTi-based ternary alloys. *Nickel-Titanium Smart Hybrid Materials*. Elsevier, 2022, pp. 191–213. DOI: 10.1016/B978-0-323-91173-3.00020-1.

9. Parvizi S., Hashemi S.M., Moein S. NiTi shape memory alloys: properties. *Nickel-titanium smart hybrid materials*. Elsevier, 2022, pp. 399–426. DOI: 10.1016/B978-0-323-91173-3.00021-3.

10. Ahmad M. Effect of ternary element addition on properties of TiNi-based shape memory alloys for engineering and medical applications. *Journal of Metastable and Nanocrystalline Materials*, 2023, vol. 36, pp. 7–20. DOI: 10.1016/B978-0-323-91173-3.00021-3.

11. Sampath S., Nguyen T.A. NiTi-based ternary shape-memory alloys. *Nickel-titanium smart hybrid materials*. Elsevier, 2022, pp. 123–137. DOI: 10.1016/B978-0-323-91173-3.00006-7.

12. Tong Y., Shuitcev A., Zheng Y. Recent development of TiNi-based shape memory alloys with high cycle stability and high transformation temperature. *Advanced Engineering Materials*, 2020, vol. 22, p. 1900496. DOI: 10.1002/adem.201900496.

13. Karakoc O., Atli K.C., Evirgen A., Pons J., Santamarta R., Benafan O., Noebe R.D., Karaman I. Effects of training on the thermomechanical behavior of NiTiHf and NiTiZr high temperature shape memory alloys. *Materials Science and Engineering: A*, 2020, vol. 794, p. 139857. DOI: 10.1016/j.msea.2020.139857.

14. Tagiltsev A.I., Panchenko E.Y., Timofeeva E.E., Chumlyakov Y.I., Fatkullin I.D., Marchenko E.S., Karaman I. The effect of stress-induced martensite aging in tension and compression on B2-B19′ martensitic transformation in $Ni_{50.3}Ti_{32.2}Hf_{17.5}$ high-temperature shape memory alloy. *Smart Materials and Structures*, 2021, vol. 30 (2), p. 025039. DOI: 10.1088/1361-665X/abdaa8.

15. Shuitcev A., Gunderov D.V., Sun B., Li L., Valiev R.Z., Tong Y.X. Nanostructured $Ti_{29.7}Ni_{50.3}Hf_{20}$ high temperature shape memory alloy processed by high-pressure torsion. *Journal of Materials Science & Technology*, 2020, vol. 52, pp. 218–225. DOI: 10.1016/j.jmst.2020.01.065.

16. Akgul O., Tugrul H.O., Kockar B. Effect of the cooling rate on the thermal and thermomechanical behavior of NiTiHf high-temperature shape memory alloy. *Journal of Materials Research*, 2020, vol. 35, iss. 12, pp. 1572–1581. DOI: 10.1557/jmr.2020.139.

17. Shuitcev A., Vasin R.N., Balagurov A.M., Li L., Bobrikov I.A., Tong Y.X. Thermal expansion of martensite in $Ti_{29.7}Ni_{50.3}Hf_{20}$ shape memory alloy. *Intermetallics*, 2020, vol. 125, p. 106889. DOI: 10.1016/j.intermet.2020.106889.

18. Catal A.A., Bedir E., Yilmaz R., Canadinc D. Design of a NiTiHf shape memory alloy with an austenite finish temperature beyond 400 °C utilizing artificial intelligence. *Journal of Alloys and Compounds*, 2022, vol. 904, p. 164135. DOI: 10.1016/j.jallcom.2022.164135.

19. Kim J.H., Park C.H., Kim S.W., Hong J.K., Oh C.X., Jeon Y.M., Kim K.K., Yeom J.T. Effects of microstructure and deformation conditions on the hot formability of Ni-Ti-Hf shape memory alloys. *Journal of Nanoscience and Nanotechnology*, 2014, vol. 14, pp. 9548–9553. DOI: 10.1166/jnn.2014.10191.

20. Babacan N., Bilal M., Hayrettin C., Liu J., Benafan O., Karaman I. Effects of cold and warm rolling on the shape memory response of $Ni_{50}Ti_{30}Hf_{20}$ high-temperature shape memory alloy. *Acta Materialia*, 2018, vol. 157, pp. 228–244. DOI: 10.1016/j.actamat.2018.07.009.

21. Benafan O., Bigelow G.S., Garg A., Noebe R.D., Gaydosh D.J., Rogers R.B. Processing and scalability of NiTiHf high-temperature shape memory alloys. *Shape Memory and Superelasticity*, 2021, vol. 7, pp. 109–165. DOI: 10.1007/s40830-020-00306-x.

22. Stolyarov V.V., Andreev V.A., Karelin R.D., Ugurchiev U.Kh., Cherkasov V.V., Komarov V.S., Yusupov V.S. Deformability of TiNiHf shape memory alloy under rolling with pulsed current. *Obrabotka metallov*

(tekhnologiya, oborudovanie, instrumenty) = Metal Working and Material Science, 2022, vol. 24, no. 3, pp. 66–75. DOI: 10.17212/1994-6309-2022-24.3-66-75.

23. Karelin R., Komarov V., Cherkasov V., Yusupov V., Prokoshkin S., Andreev V. Production mechanical and functional properties of long-length TiNiHf rods with high-temperature shape memory effect. *Materials*, 2023, vol. 16 (2), p. 615. DOI: 10.3390/ma16020615.

24. Keret-Klainer M., Padan R., Khoptiar Y., Kauffmann Y., Amouyal Y. Tailoring thermal and electrical conductivities of a Ni-Ti-Hf-based shape memory alloy by microstructure design. *Journal of Materials Science*, 2022, vol. 57, iss. 25, pp. 12107–12124. DOI: 10.1007/s10853-022-07383-6.

Conflicts of Interest

The authors declare no conflict of interest.

Obrabotka metallov –
Metal Working and Material Science

Journal homepage: http://journals.nstu.ru/obrabotka_metallov

Information properties of vibroacoustic emission in diagnostic systems for cutting tool wear

Vilor Zakovorotny [a], Valery Gvindjiliya [b, *], Kirill Kislov [c]

Don State Technical University, 1 Gagarin square, Rostov-on-Don, 344000, Russian Federation

[a] https://orcid.org/0000-0003-2187-9897, ✉ vzakovorotny@dstu.edu.ru; [b] https://orcid.org/0000-0003-1066-4604, ✉ vvgvindjiliya@donstu.ru;
[c] https://orcid.org/0000-0002-5770-2519, ✉ kislovk@bk.ru

ARTICLE INFO

ABSTRACT

Introduction. This paper is devoted to the development of a methodology for diagnosing cutting tool wear based on the analysis of vibroacoustic emission signals. Two tasks are addressed. Firstly, the information feature space related to wear is constructed. Secondly, within this space, decision rules are defined that allow division into separate clusters according to wear levels. Since the construction of the information feature space (*IFS*) methods is of primary importance in these procedures, the **purpose of this work** is to determine the regularities of changes in the frequency characteristics of the dynamic cutting system caused by wear development and to construct, on this basis, a rational information space for diagnosing tool wear. **Method and methodology.** The study is based on mathematical modeling results of a perturbed dynamic cutting system to determine the information feature space representing tool wear. Methods for determining the parameters of information signal parameters (*ISPs*) are proposed, which provide high sensitivity to wear changes. All *ISP* parameters should be dimensionless and zeroed at zero wear. They must satisfy additional requirements, including noise immunity conditions. **Results and discussion.** The paper presents results of constructing *ISP* parameters for vibroacoustic emission analysis in two frequency ranges. In the low-frequency range, limited by the first natural frequencies of interacting subsystems (up to 1.0–1.5 kHz), vibration response parameters (*VRP*) are determined based on vibration sequences obtained analytically under power perturbations modeled as "white" noise. In the high-frequency range (above 2.0 kHz), information models based on random pulse sequences are proposed. It is shown that the applicability of a particular information feature depends on the conditions. Thus, the developed methodology, mathematical simulation, and digital and field experiments enabled the formation of a rational information space for wear diagnostics, in which known recognition methods can be used to construct decision rules for classifying information according to wear levels.

Introduction

In recent years (10–15), the global scientific community has been focusing on the construction of virtual digital models (*VDM*) of machining [1–14]. These models are primarily designed to determine the relationship between technological parameters and the output properties of the machining process. Most of the presented works do not reveal the structure of the relationship between state coordinates and output properties [1–7], but use experimentally obtained regression equations that couple technological parameters to the quality parameters of parts and tool wear [5–7]. This information is necessary for constructing a *CNC* program. In many cases, neural network modeling methods are used instead of regression equations [8–11]. The exceptions are studies [2–4, 17–21], in which dynamic cutting system (*DCS*) models are used to construct *VDM*. *VDMs* have been developed that allow the trajectories of form-forming movements to be

* Corresponding author
Gvindjiliya Valery E., Ph.D. (Engineering), Senior Lecturer
Don State Technical University,
1 Gagarin square,
344000, Rostov-on-Don, Russian Federation
Tel.: +7 918 583-23-33, e-mail: vvgvindjiliya@donstu.ru

coupled to the geometric characteristics of the formed surface and wear [17–21]. Most studies are limited to the problem of estimating wear as the main factor affecting the output properties [22–24]. Here, we note the modeling of evolutionary changes in the *DCS* that we proposed earlier [25, 26]. In this system, wear evolution and quality parameters are represented as a *Volterra's* integral equation of the second kind with respect to the phase trajectory of irreversible transformations in terms of work done. Thus, the evolution of properties and parameters reveals the complete *DCS*. However, its use requires significant computing resources. In this paper, we will limit ourselves to the problem of wear diagnosis based on the analysis of vibroacoustic emission (*VAE*) [27–47]. To measure *VAE*, piezoelectric transducers, force sensors, non-contact laser and other measuring systems are used to determine the vibrations of a certain *DCS* coordinate in the frequency range (10 Hz…600 kHz). The measured sequences undergo preliminary processing using integral transformations, primarily *Fourier* transformations [26], *Wavelet* transformations [37], *Hilbert-Huang* transformations [36], *Volterra* transformations [3, 37, 28], etc. Methods of complexing measurable sequences of various physical nature are used [48].

In contrast to previous studies, this paper focuses on the construction of an information sign space (*ISS*), which considers the sensitivity of parameters' variations to wear changes, their noise immunity, and ease of formation in diagnostic systems. Two frequency ranges are considered separately. The low-frequency range is within (1.0–1.5) kHz, and the high-frequency range is above 2.0 kHz. This division is due to the peculiarities of mathematical modeling of the *DCS* as a channel through which information about the force interactions formed during processing is transmitted.

The purpose of the work is to develop a method for diagnosing cutting tool wear by determining the information space of features formed on the basis of studying changes in the frequency characteristics of the dynamic cutting system caused by wear development. To achieve this purpose, the following tasks must be undertaken.

– to develop an analytical method for determining the information space of the low- and high-frequency ranges;

– to perform mathematical modeling and to conduct digital simulations, and full-scale experiments;

– to determine the parameters of the information space within the considered frequency ranges and a method for their evaluation.

Methods

Methodology for experimental wear assessment

A generalized parameter for assessing the tool's condition is the wear on its flank face. Therefore, let us consider an algorithm for the experimental assessment of flank wear, which is defined by the height of the flank wear land (Fig. 1). The configuration of the wear mark on the flank face varies, and only in some cases does it approximate a rectangle, as shown in Fig. 1, *a*. Therefore, we will define the wear assessment as the height of an equivalent rectangle, $w = S_0/(t_p^{(0)} - X_I^*)$, where S_0 is the surface area of the wear trace on the flank face of the tool, and X_I^* is the elastic deformation under equilibrium conditions. The area S_0 is estimated using a grid (Fig. 1, *c*). It has been previously shown [2, 3, 26, 47] that the properties of dynamic contact stiffness (*DCS*) are influenced by dynamic connection parameters, and changes in these parameters are manifested as variations in vibration spectra. The parameters of this connection are dependent on wear, and it is convenient to analyze the interdependence of the vibration spectrum and wear independently within two frequency ranges. In the low-frequency range ($\omega_H \in (0,\omega_0)$), the model can be represented as a finite-dimensional spatial discrete model [47]. This is a frequency range whose upper limit is defined by the natural frequencies of the tool and workpiece subsystems. We will interpret the frequency range above ω_0 as the high-frequency range ($\omega_B \in (\omega_0,\infty)$.

Methodology for analytical determination of the information space in the low-frequency range

The previously derived *DCS* model [47] is considered. We will limit our analysis to the case of machining a non-deformable workpiece. Then, the equation of the perturbed dynamic system response (*DSR*) can be written as:
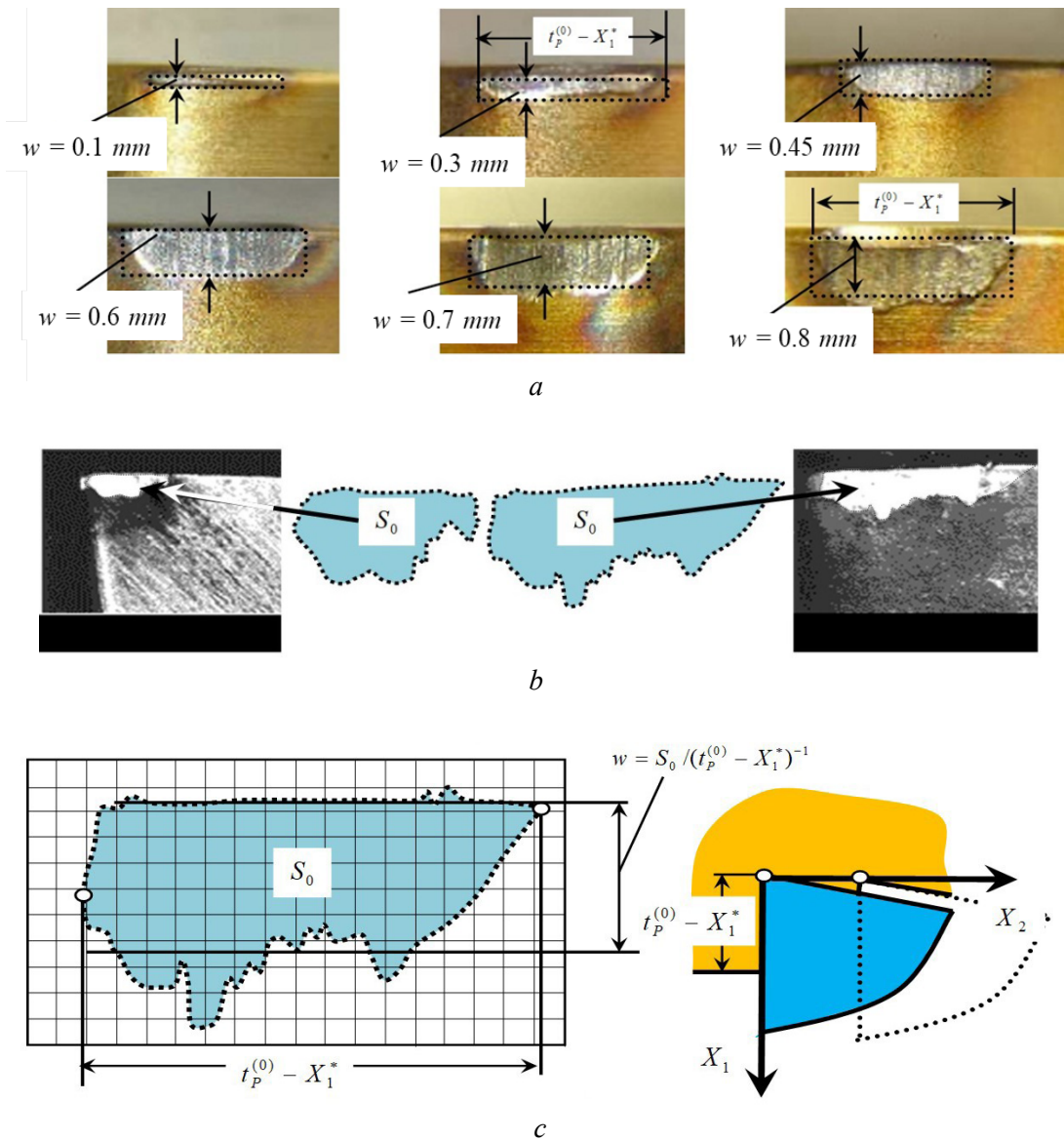
Fig. 1. Examples of photographs of the worn tool part and wear evaluation scheme:

a – flank wear of a *79 WC-15 TiC-6% Co* insert during turning of *AISI 301* steel; *b* – wear development
of a *79 WC-15 TiC-6% Co* insert during turning of steel *0.2 C-Cr*; *c* – schematic of the matrix grid

$$\mathbf{m}\frac{\mathbf{d^2X}}{\mathbf{dt^2}} + \mathbf{h}\frac{\mathbf{dX}}{\mathbf{dt}} + \mathbf{cX} = \mathbf{F_\Sigma(L, V, X, p)} + \mathbf{f(t)} \tag{1}$$

where $\boldsymbol{m} = \mathrm{diag}(m)$, $\boldsymbol{h} = [h_{S,k}]$, $\boldsymbol{c} = [c_{S,k}]$, $\boldsymbol{S}, \boldsymbol{k} = 1, 2, 3$ is positively definite symmetric matrices of inertial, velocity, and elastic coefficients; $\boldsymbol{X} = \{X_1, X_2, X_3\}^T \in \Re_X^{(3)}$ is deformation vector; $\boldsymbol{F_\Sigma} = F + \Phi$ is the vector-function of forces on the rake $\boldsymbol{F}$ and flank $\boldsymbol{\Phi}$ faces; $\boldsymbol{F} = \{F_1, F_2, F_3\}\mathrm{T} \in \Re_X^{(3)}$; $\boldsymbol{\Phi} = \{\Phi_1, \Phi_2, \Phi_3\}\mathrm{T} \in \Re_X^{(3)}$.

Let us also consider deformation velocities $\boldsymbol{V_X} = \mathrm{d}X / \mathrm{d}t = \{V_{X,1}, V_{X,2}, V_{X,3}\}^T \in \Re_X^{(3)}$. We represent forces $\boldsymbol{F}$ in the form $\boldsymbol{F} = \{F_1, F_2, F_3\}^T = F^{(0)}\{\chi_1, \chi_2, \chi_3\}^T$ [47]. Here χ_1, χ_2, χ_3 are angular coefficients satisfying the condition $(\chi_1)^2 + (\chi_2)^2 + (\chi_3)^2 = 1$. The given perturbations $\boldsymbol{f(t)} = f_0(t)\{\chi_1, \chi_2, \chi_3\}^T$ are considered to be reduced to the coordinate system of the forces $\boldsymbol{F}$. Furthermore, $f_0(t)$ is modeled as "white" noise. Based on prior studies, the model of cutting forces acting on the rake face of the tool $F^{(0)}$ is given by [47]:

$$T^{(0)}dF^{(0)} / dt + F^{(0)} = \rho(V_3, V_{X_3})\left\{t_P^{(0)} - [X_1 - k_p X_1(t - T)]\right\} \times \int_{t-T}^{t} \left\{V_2(\xi) - V_{X_2}(\xi)\right\}d\xi, \qquad (2)$$

where $\rho = \rho_0\left\{1 + \mu\exp[-\varsigma(V_3 - V_{X_3})]\right\}$ is the chip pressure, kg/mm^2; $\boldsymbol{\rho_0}$ is the pressure in the area of low cutting speed region on the tool's rake face; $\boldsymbol{\mu}$ is the dimensionless parameter; ς is the steepness coefficient, s/m; $\boldsymbol{T^{(0)}}$ is the chip formation time constant, s; $\boldsymbol{k_p}$ is the dimensionless trail regeneration coefficient ($0\langle k_p\langle\langle 1$).

Forces $\boldsymbol{\Phi_2}$, $\boldsymbol{\Phi_3}$ can be expressed as:

$$\Phi_2 = k_\Phi F_0 + \rho_\Phi\left[t_P^{(0)} - X_1(t)\right]\exp\left[\varsigma(\upsilon - \upsilon^*)\right];$$
$$\Phi_3 = k_\Phi k_T F_0 + k_T\rho_\Phi\left\{\left(t_P^{(0)} - X_1(t)\right)\exp\left[\varsigma(\upsilon - \upsilon^*)\right]\right\}, \qquad (3)$$

where $\boldsymbol{\rho_\Phi}$ is the force per unit contact length on the tool flank face, representing stiffness, kg/mm; ς is a parameter depending on the rear angle á and wear; $\boldsymbol{k_T}$ is the friction coefficient; $\boldsymbol{k_\Phi}$ is the dimensionless coefficient of elastic recovery.

Equations (1)-(3) constitute a numerical model of the *DCS*. The model's adequacy was validated by comparing the results of digital simulations and full-scale experiments, which were conducted using continuous vibration monitoring measurement systems. The parameters of the dynamic connection equation, particularly the chip pressure on the rake face of the tool, were refined using both theoretical material [49] and force measurements during the cutting process [50]. For this purpose, a *STD.201-1* system was used instead of the support to measure the dynamic loads on the tool along the $\{X_1, X_2, X_3\}$ axes. The hardware interface of the test bench consists of a set of electronic units manufactured by National Instruments: *NI-9234*, *NI-9237*, and *NI-9219*, with a sampling frequency of up to 25 kHz. The accuracy of the analytical simulation results is limited by the zone of steady-state tool wear and the onset of accelerated wear, where the influence of random processes in the cutting zone reduces the accuracy of classical analytical nonlinear models.

Here, we leverage previously developed mathematical tools to construct a space of wear characteristics.

It is important to note that the parameters of the dynamic connection $\boldsymbol{p(w)} = \{p_1(w), p_2(w),\dots p_n(w)\}$ formed during cutting depend on wear. Let experimentally determined trajectories be given as $\boldsymbol{p(w)} = \{p_1(w), p_2(w),\dots p_n(w)\}$. For the sequence $\boldsymbol{w} = \{w_1, w_2,\dots w_k\}$, we calculate the spectra $S_{X_1, X_1}(\omega)$, $S_{X_2, X_2}(\grave{u})$ and $S_{X_3, X_3}(\grave{u})$ in the space $\Re_X^{(3)}$ as *Fourier* transforms of the diagonal elements of the correlation matrices of the time series of deformations $\boldsymbol{X^{(i)}(t)} = \{X_1^{(i)}(t), X_2^{(i)}(t), X_3^{(i)}(t)\}^T \in \Re_X^{(3)}$, $i = 1, 2,\dots k$. Consequently, we obtain a set of deformation spectra for each set of parameters corresponding to each wear state $\boldsymbol{w} = \{w_1, w_2,\dots w_k\}$.

Results and Discussion

Example of determining the parameters of the information space in the low-frequency range

If the perturbations $f_0(t)$ are small and the equilibrium is asymptotically stable, then the forces $\boldsymbol{\Phi}$ in Equation (1) can be neglected. In this case, the main parameters influencing the formation of the spectra are the variations in $\boldsymbol{\rho}$ and $\boldsymbol{T^{(0)}}$. Consider the turning of a shaft with a diameter of $\boldsymbol{D} = 84.0$ mm, made of *0.1 C-Mn-2 Ni-Mo-V* steel. The investigations were carried out as part of the implementation of a commercial contract with *Atommash* (Volgodonsk). The machining conditions were based on the technological process for manufacturing a real "blow-off pipe" type detail for rough turning. The technological parameters were as follows: feed rate $\boldsymbol{S_p} = 0.1$ mm; depth of cut $\boldsymbol{t_p} = 2$ mm; and cutting speed $\boldsymbol{V_3} = (0.5\dots3.8)$ m/s. During the investigation, the range of cutting speeds was expanded in order to obtain more complete information

about the diagnostic characteristics in the vibroacoustic emission (*VAE*) signals. Machining was performed on a modernized *1K62* lathe, equipped with adjustable spindle and feed drives. Instead of the carriage, a *STD.201-1* measuring system was installed to determine forces, vibration, and temperature. Parameters are given in Table 1. The total mass is $\boldsymbol{m} = 0.015$ kg·s^2/mm. The dynamic couple parameters are provided in Table 2. The resonant frequencies of the tool subsystem are $\boldsymbol{\Omega_{0,1}} = 130$ Hz, $\boldsymbol{\Omega_{0,1}} = 174$ Hz, $\boldsymbol{\Omega_{0,1}} = 236$ Hz.

T a b l e 1

Matrices of speed coefficients and elasticity of the tool subsystem

$c_{1,1}$ (kg/mm)	$c_{2,2}$ (kg/mm)	$c_{3,3}$ (kg/mm)	$h_{1,1}$ (kg·s/mm)	$h_{2,2}$ (kg·s/mm)	$h_{3,3}$ (kg·s/mm)
4,500	1,500	750	1.3	1.1	0.8
$c_{1,2} = c_{2,1}$ (kg/mm)	$c_{1,3} = c_{3,1}$ (kg/mm)	$c_{2,3} = c_{3,2}$ (kg/mm)	$h_{1,2} = h_{2,1}$ (kg·s/mm)	$h_{1,3} = h_{3,1}$ (kg·s/mm)	$h_{2,3} = h_{3,2}$ (kg·s/mm)
200	150	80	0.6	0.5	0.4

T a b l e 2

Dynamic coupling parameters

ρ (kg/mm^2)	ρ_ϕ (kg/mm^2)	Ω (s^{-1})	T$^{(0)}$ (s)	ς	k_T	$k^{(T)}$ (s /m)	$k^{(S)}$	χ_1	χ_2	χ_3
100–1,000	20	5–50	0.0001	1–7	0.2	5	0.1	0.4	0.51	0.76

The spectra are studied based on numerical modeling in the *Matlab-Simulink* software package, as well as experimentally by direct measurement of the vibroacoustic emission (*VAE*) during the cutting process. Let us consider the spectra of deformation oscillations $X \in \mathfrak{R}_X^{(3)}$ calculated as responses to "white" noise. The spectra in Fig. 2, *a* and *b* differ from the spectrum in Fig. 2, *c* by angular coefficients $\chi = \{\chi_1, \chi_2, \chi_3\}^T$. The examples are selected to illustrate the following properties of the spectra.

1. Resonances (shown as round, unshaded points) and antiresonances (shown as shaded points) can be distinguished in the spectrum. In real systems, they remain virtually unchanged when the parameters of the dynamic connection formed by the cutting process vary.

2. In the case of kinematic disturbances (Fig. 2, *a*), periodic spikes are superimposed on the spectra. The distance between them is equal to the rotation frequency of the workpiece. In the case of force disturbances, the peaks are normalized (Fig. 2, *b*). They are also normalized in the high-frequency range. Therefore, in the actual measured spectrum, significant variations in level are detected as the frequency increases, but resonance frequencies are usually observed.

3. Peaks at all resonances may not appear, or they may appear to a lesser extent (Fig. 2, *c*). This behavior is determined by the structure of the elasticity matrices *c* coefficients χ. It is known that the angular coefficients change as wear increases. For example, forces in the direction normal to the flank face increase faster [51], which is reflected in the redistribution of amplitudes at resonance frequencies.

4. Wear development causes an increase in the parameters ρ and $\boldsymbol{T^{(0)}}$, as well as a change in the angular coefficients χ. An increase in $\boldsymbol{\rho}$ causes a shift in the roots of the characteristic polynomial of the linearized variation equation, such that some roots move toward the imaginary axis, and an increase in $\boldsymbol{\rho}$ always leads to a loss of stability. An increase in $\boldsymbol{T^{(0)}}$ has a contradictory effect. On the one hand, an increase in $\boldsymbol{T^{(0)}}$ contributes to self-excitation, and on the other hand, it leads to additional damping.

5. As wear progresses, due to changes in the parameters of dynamic coupling, the system may lose its equilibrium stability, and various attracting sets of deformations may form in the vicinity of the trajectory,
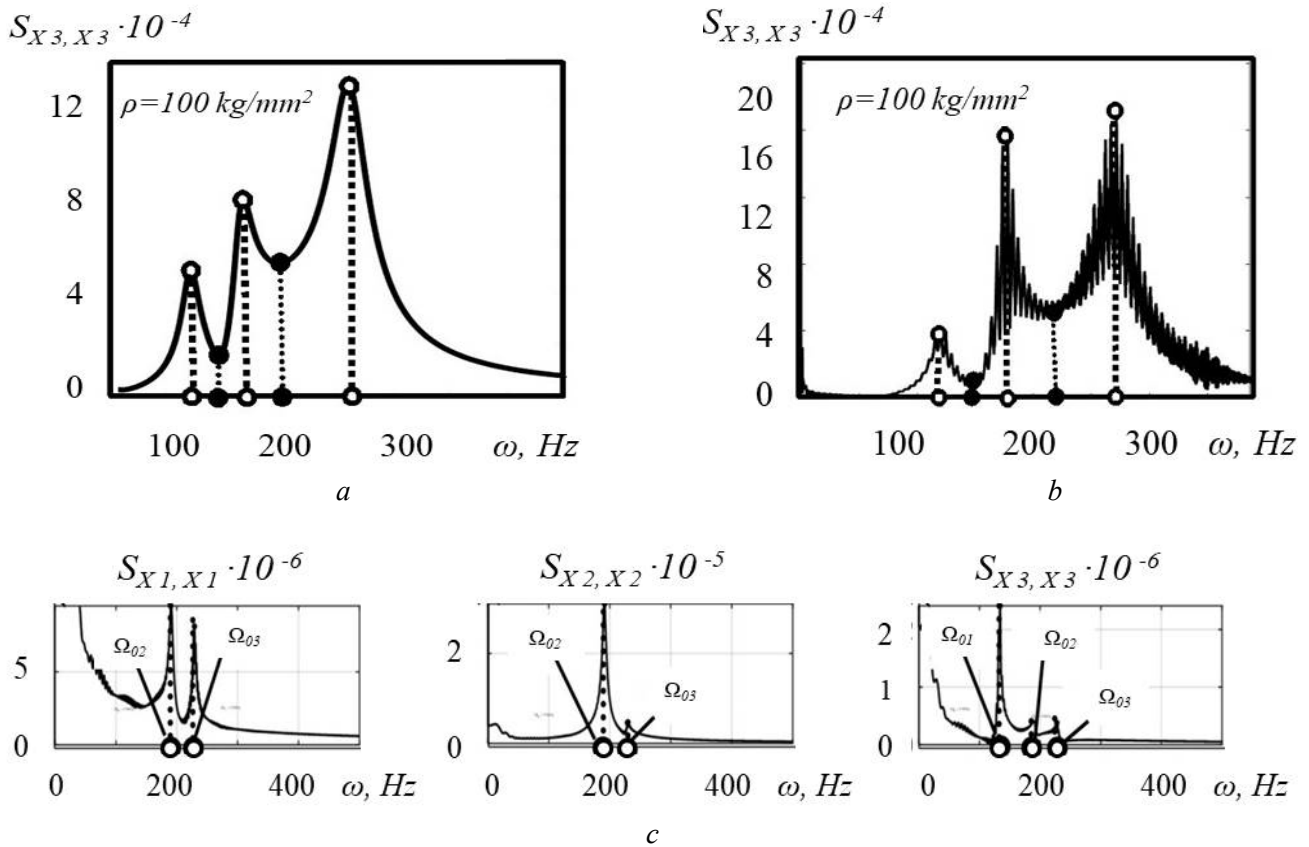
Fig. 2. Typical examples of autospectra:
a – spindle rotation frequency of 10.0 Hz, disturbances applied to feed rate variations; *b* – spindle rotation frequency of 100 Hz, disturbances applied to cutting force module; *c* – spectral changes depending on the direction of deformation displacements in space $\Re_X^{(3)}$

with bifurcations possibly observed along the trajectory. In this case, the normalized vibration spectrum is practically independent of perturbations and is determined by the properties of the *DCS*.

An example of the influence of parameter **ρ** on the dispersion-normalized spectrum for value $X \in \Re_X^{(3)}$ is shown in Fig. 3. Experiments show that for *0.1 C-Mn-2 Ni-Mo-V* steel under conditions of feed rate $S_p^{(0)} = 0.1$ mm, cutting depth $t_p^{(0)} = 1.5$ mm, and cutting speed $V_3^{(0)} = 1.2$ m/s, as wear on the rake face increases to 0.6 mm, a monotonic increase in ρ from 100 kg/mm² to 160 kg/mm² is observed. This corresponds to the transformation of the spectrum shown in Fig. 4.

Note the special features of the spectrum changes. There is a redistribution of the intensity of oscillations in frequency ranges located near the natural frequencies. Let us denote them by $A_{i,s}$, *i, s* = 1, 2, 3. Here, *i* is the resonance number, and *s* is the number of directions of oscillations in space $\Re_X^{(3)}$. As **ρ** increases, not only does the amplitude at frequency Ω_3 increase, but the quality factor of this mode also increases. At **ρ** = 160 kg/mm² a single oscillator with a common frequency Ω_3 is formed. Analysis shows that when **ρ** = 145 kg/mm², the equilibrium loses stability and self-oscillations are formed.

More details on the formation of attracting sets of deformations can be found in our works [2, 3, 25, 26]. As the roots of the characteristic polynomial approach the imaginary axis, the quality factor of the oscillator representing this pair of complex conjugate roots increases. Here are some examples of how the ratio of amplitudes at resonances changes with **ρ** (Fig. 4). The point of instability is marked with a red dotted line, to the right of which a delta-shaped spectrum $\delta(\omega - \Omega_3)$ is formed, so all coefficients increase indefinitely.

A rougher but more interference-resistant estimate is the average frequency of the spectrum $\omega^{(C)}$ in the $X \in \Re_X^{(3)}$ directions. With increasing wear, primarily due to an increase in the parameter $T^{(0)}$, a shift of the
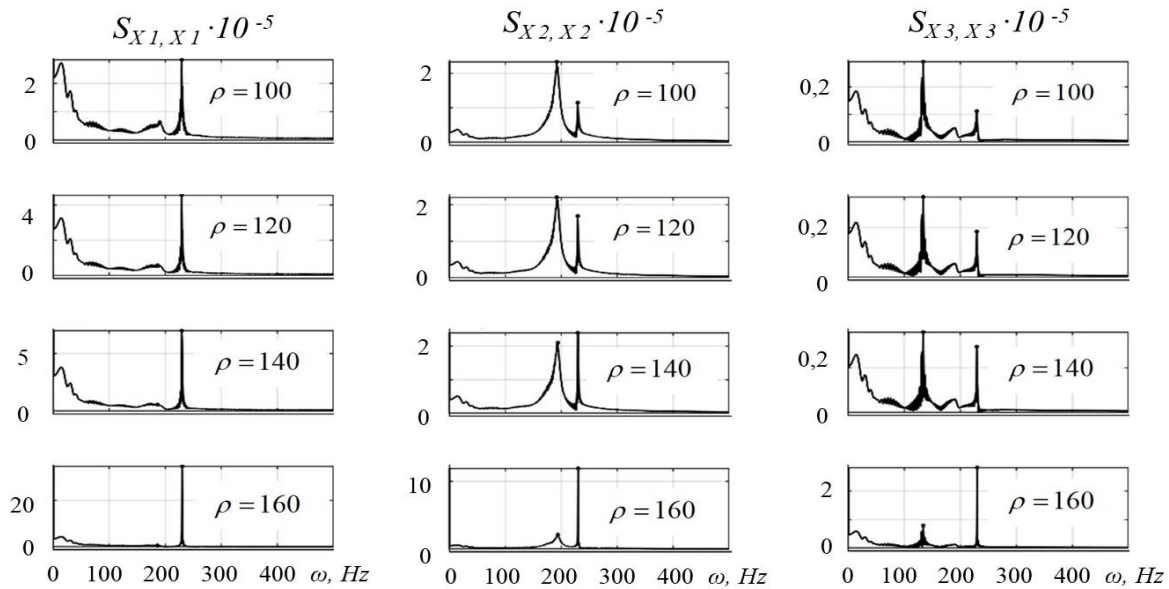
Fig. 3. Example of changes in deformation autospectra depending on chip pressure ρ on the tool's rake face
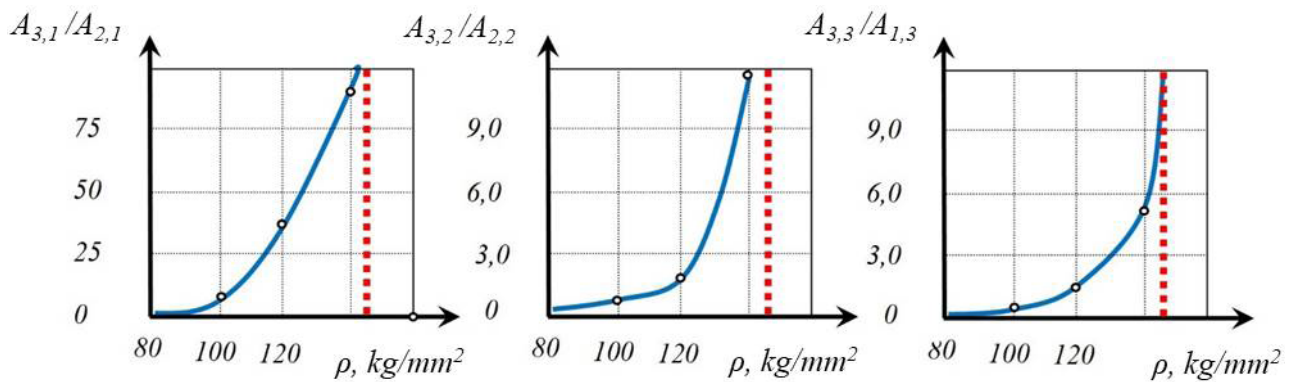
Fig. 4. Sensitivity of amplitudes at resonances to variations ρ

overall vibration spectrum toward the low-frequency range is observed. If $\omega^{(C)}$ is specified, then $\int\limits_{0}^{\omega^{(C)}} S_{X_i X_i}(\omega)d\omega = \int\limits_{\omega^{(C)}}^{\infty} S_{X_i X_i}(\omega)d\omega$ is valid. The increment $\omega^{(C)}$ depends less significantly on variations in the initial parameters, disturbances, and modes.

As wear increases, two interrelated processes can be observed. The first process characterizes the determination of the state (Fig. 5). In this case, the peaks in the spectra become more pronounced and exhibit increased quality factors. The second process characterizes the degradation of properties, manifested in the formation of chaos.

Dispersion estimation is used to evaluate evolution

$$\hat{\sigma}_{X_1,X_1}(\rho_i) = \sigma_{X_1,X_1}(\rho_i)\left[\sigma_{X_1,X_1}(\rho_0)\right]^{-1}, \tag{4}$$

where $\sigma_{X_1,X_1}(\rho_i) = \dfrac{1}{\pi}\int\limits_{0}^{\infty} S_{X_1,X_1}(\omega,\rho_i)d\omega$, $i = 0, 1, 2...k$; $\rho = \{\rho_0, \rho_1,...\rho_r\}$ is sequence of ρ_i values, each of which corresponds to a variance.

In this regard, when considering the total variance, there are two stages (Fig. 5, *b*).
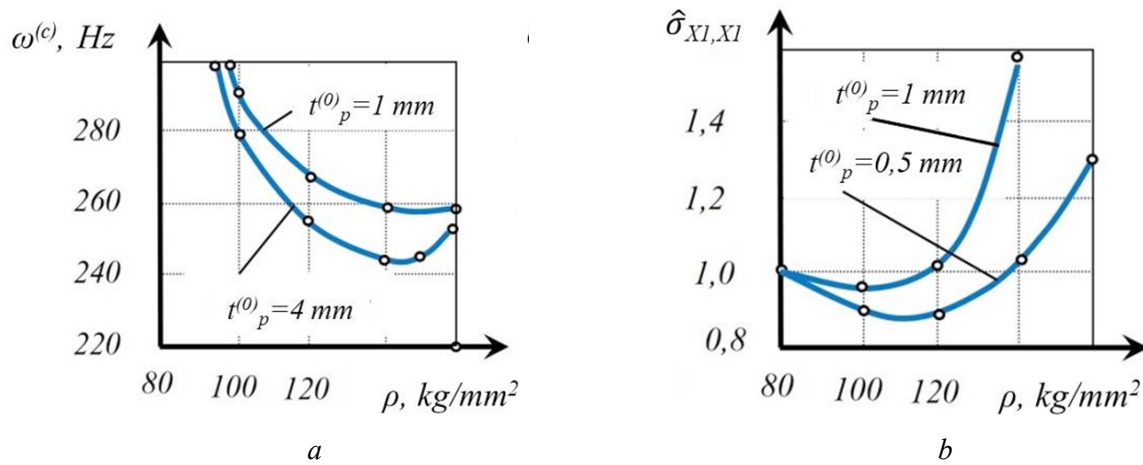
Fig. 5. Sensitivity of average frequency $\omega^{(C)}$ (*a*) and relative dispersion $\sigma_{X1,X2}$ (*b*) during variation at different cutting depths $t_P^{(0)}$

At the initial stage of running-in, the dispersion of oscillations decreases, and then increases. This trend holds true regardless of whether the equilibrium point is stable or whether various attracting sets of deformations form in its vicinity. The analysis allows us to create an *ISS* system. The first assessment $\mathbf{\Pi_1}$ is based on an analysis of changes in relative amplitude $A_{i,s}$, $i, s = 1, 2, 3$ increments in the direction *s*:

$$\Pi_1 = \left[\delta_A(w) - \delta_A(0)\right]\delta_A(0)^{-1}, \tag{5}$$

where $\delta_A(w) = A_{3,1}(w) / A_{2,1}(w)$, $s = 1$.

The second $\mathbf{\Pi_2}$ assessment is based on determining the $\omega^{(C)}$ displacement as *w* wear increases. However, calculating the average frequency requires significant computing resources. Therefore, an equivalent assessment of two signals passing through low- and high-frequency filters can be considered. In this case, it is not necessary for the cutoff frequencies of the filters to coincide exactly with the frequency $\omega^{(C)}$. Then,

$$\Pi_2 = \frac{\sigma_H(w) - \sigma_B(w)}{\sigma(w)}, \tag{6}$$

where $\sigma_H(w)$ is the dispersion of the *VAE* signal in the low-frequency range; $\sigma_B(w)$ is the dispersion of the *VAE* signal in the high-frequency range; $\sigma(w)$ is the general dispersion.

The signal processing is such that when $w = 0$, the assessment $\mathbf{\Pi_2} = 0$. Then, the assessment of $\mathbf{\Pi_3}$ based on (4) is also informative:

$$\Pi_3 = \frac{\hat{\sigma}_{X_1,X_1}(w) - \hat{\sigma}_{X_1,X_1}(0)}{\hat{\sigma}_{X_1,X_1}(0)}, \tag{7}$$

where $\hat{\sigma}_{X_1,X_1}(w)$ is the dispersion assessment calculated using the algorithm in Eq. (4).

Parameters of the high-frequency range information space. In the high-frequency range, it is not possible to analytically determine the response of vibration sequences to changes in wear, since the dynamic model has a limited frequency range of validity. However, the cutting process is a source of waves in the frequency range reaching hundreds of kilohertz [5, 15]. We interpret the measured signal in the high-frequency range as an acoustic emission (*AE*) signal. The source of this signal is the force interactions in the regions (Fig. 6, *a*) of primary (1) and secondary (2) plastic deformation, as well as in the contact area between the flank face of the tool and the workpiece (3). When measuring this signal, the wave properties of the channel connecting the cutting zone with the *AE* measurement point are of fundamental importance. It is necessary to take into account not only the dissipative properties of the channel, but also its geometry, as well as joints that introduce nonlinear distortions and an insensitivity zone caused by butt joints [50, 51].
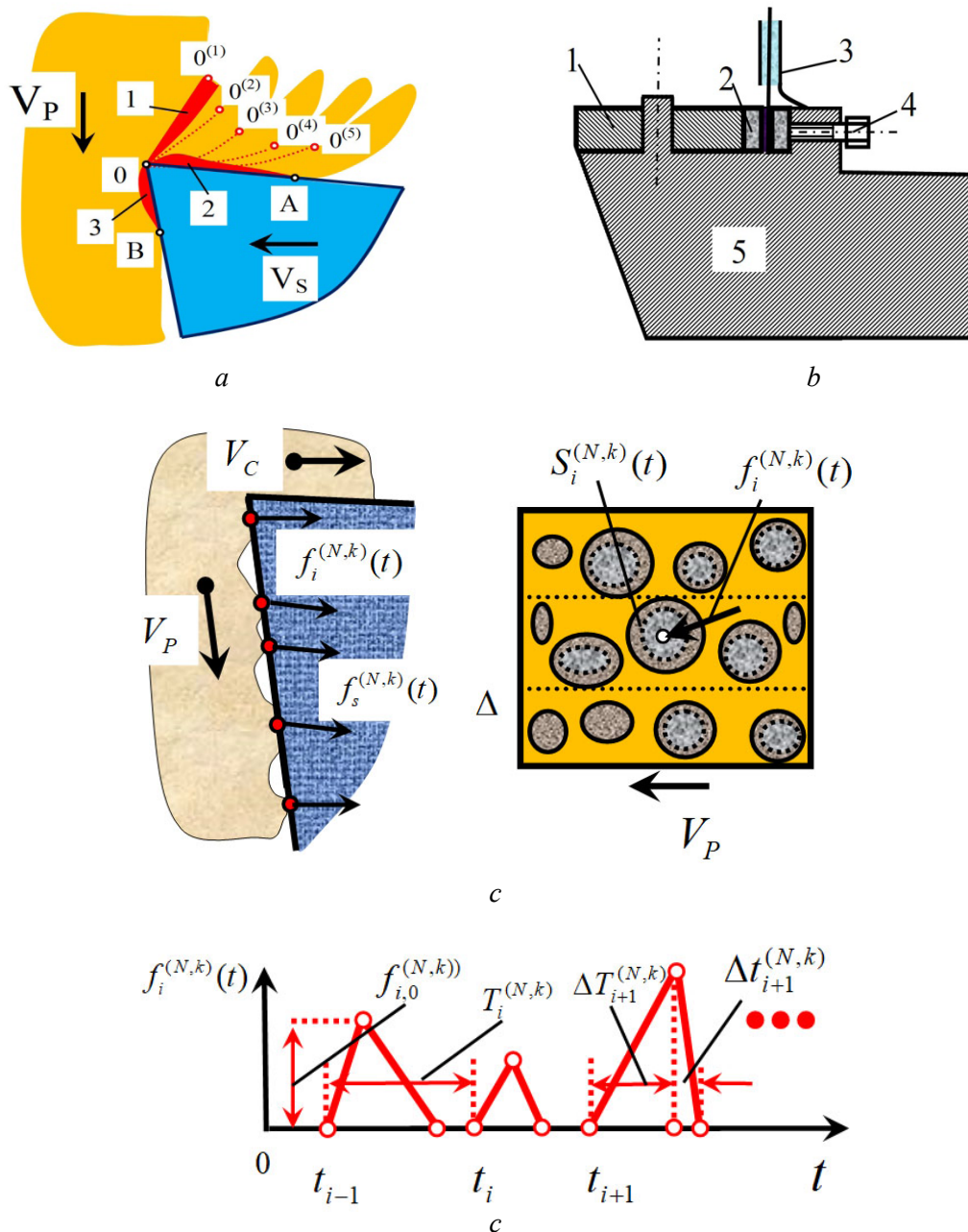
Fig. 6. Scheme of *AE* signal measurement and formation:
a – model of periodic force components formation; *b* – cutter measuring scheme; *c, d* – model
of random pulse sequence formation

A measuring cutter (Fig. 6, *b*) was used for the experimental study of *AE* properties. *AE* was evaluated using a piezoelectric transducer (**2**) installed in contact with a tetrahedral plate (**1**) made of hardmetal (79 % *WC*; 15 % *TiC*) and the body of the cutter (**5**). Two ceramic plates, based on solid solutions of zirconate and lead titanate (*ZLT*), are installed so that their outer surfaces are in electrical contact with the tool body, while the central plates are insulated and connected to a coaxial cable (**3**), the braid of which is connected to the cutter body. The ceramic inserts (**2**) are pressed against the cutting plate with a screw (**4**). The coaxial cable is connected to a computer for information processing via an analog-to-digital converter *E14-440*.

A model of the source of power emission can be proposed. To do this, on the surface of the wearable flank face of the tool, we select the area of $S_i^{(N,k)}(t)$ (Fig. 6, *c*) in which the force $f_i^{(N,k)}(t)$ is formed. In time, it represents a sequence of standard pulses (Fig. 6, *d*), each of which describes the change in forces over a time interval $t \in (t_{i-1}, t_i)$.

$$f_i^{(N,k)}(t) = \begin{cases} f_i^{(N,k)}(t) = k_1^f t, & t \in \left(t_i, t_i + \Delta T_{i+1}^{(N,k)}\right), \ k_1^f = f_{0,i}^{(N,k)} / \Delta T_{i+1}^{(N,k)}; \\ f_{0,i}^{(N,k)} - k_2^f t, & t \in \left(t_i + \Delta T_{i+1}^{(N,k)}, \ t_i + \Delta T_{i+1}^{(N,k)} + \Delta t_{i+1}^{(N,k)}\right), \ k_1^f = f_{0,i}^{(N,k)} / \Delta t_{i+1}^{(N,k)}; \\ f_i^{(N,k)}(t) = 0, & t \in \left(t_i + \Delta T_{i+1}^{(N,k)} + \Delta t_{i+1}^{(N,k)}, t_{i+1}\right). \end{cases} \quad (8)$$

The sequence represents a set of standard pulses (8) $f_i^{(N,k)}(t) =$

$$= \left\{ f_i^{(N,k)}(t), \ t \in \left(0, T_1^{(N,k)}\right); \ f_i^{(N,k)}(t), \ t \in \left(T_1^{(N,k)}, T_2^{(N,k)}\right); \ ...; \ f_i^{(N,k)}(t), t \in \left(T_{s-1}^{(N,k)}, T_s^{(N,k)}\right) \right\}.$$ The

tangential components of elementary forces $f_i^{(T,k)}(t)$ have a similar structure.

In the following, the work is limited to considering the impulse sequence $f_i^{(N,k)}(t)$, which has two stages. In the *first stage*, there is an accumulation of potential energy (time interval $\Delta T_{i+1}^{(N,k)}$). Here, elastic displacement of microcontacts occurs up to values at which the bonds break. This time depends on the cutting speed. In the *second stage*, the energy is released (time interval $\Delta t_{i+1}^{(N,k)}$). The release of energy is accompanied by an impulse of irreversible energy transformations, which generates heat, but also causes other physical interaction effects. The release of energy also forms an elastic wave impulse.

The standard sequence is characterized by the following parameters: the distance between pulses $T_i^{(N,k)}$, rise time $\Delta T_i^{(N,k)}$, fall time $\Delta t_i^{(N,k)}$, and height $f_{i,0}^{(N,k))}$ (Fig. 6, *d*). This impulse can be caused by elastic-plastic interaction or the destruction of adhesive and other bonds.

First, the frequency-domain representations of the sequence are analyzed (Fig. 7). In the illustration, the upper two curves represent the sequence in the time domain, but on different scales. The lower two diagrams correspond to their spectral representations, also shown on two scales. Note the following key properties of these representations.

1. If the distance between pulses is constant $\mathbf{T_i^{(N,k)}} = 0.02 \ s = const$, then the spectrum consists of a discrete set of frequencies depending on the pulse duration relative to the distance $\mathbf{\Delta T_i^{(N,k)}}$. If the pulse width equals the distance between pulses, then in the frequency domain we observe frequency bursts corresponding to a *Fourier* series expansion. In this case, the spectrum contains constant components: the first and third harmonics (Fig. 7, *a*). When $\mathbf{\Delta T_i^{(N,k)}}$ is reduced, additional frequencies appear (Fig. 7, *b*), which eventually transform into a continuous spectrum (Fig. 7, *c*). As $\mathbf{\Delta T_i^{(N,k)}} \rightarrow \mathbf{0}$, the spectrum approaches "white" noise.

2. If uncertainty is introduced in $\mathbf{\Delta T_i^{(N,k)}}$, then the discrete spectrum shown in Fig. 7, *b* transforms into a continuous spectrum (Fig. 7, *d*). A broadening of the spectral lines is observed. The frequency of the spectral maximum corresponds to the mathematical expectation of the distance between pulses, and the variability (spread) of the intervals between pulses is reflected in the broadening of the spectral line.

3. Changes in the ratio between the rising and falling stages of the pulses also affect the spectrum, but modeling shows that these changes are insignificant. Regarding amplitude uncertainty, the spectrum amplifies the components located between the main bursts. If a narrowband filter selects a signal in the frequency window $\mathbf{\Delta\omega}$, an increase in amplitude uncertainty corresponds to an increase in amplitude modulation of the signal within this frequency window $\mathbf{\Delta\omega}$.

In the contact region between the flank face of the tool and the workpiece, numerous interactions occur (Fig. 6, *c*), which generate the emission signal:

$$F^{(N)}(t) = \sum_{i=1}^{i=n} \sum_{k=1}^{k=m} f_i^{(N,k)}(t), \qquad (9)$$

where $\mathbf{k}$ and $\mathbf{i}$ are the numbers of rows and contacts per row on the interaction surface, respectively.

It is necessary to formulate additional hypotheses regarding the influence of the probability distribution of these contacts on the contact surface in order to determine the spectral properties of the set of random sequences.
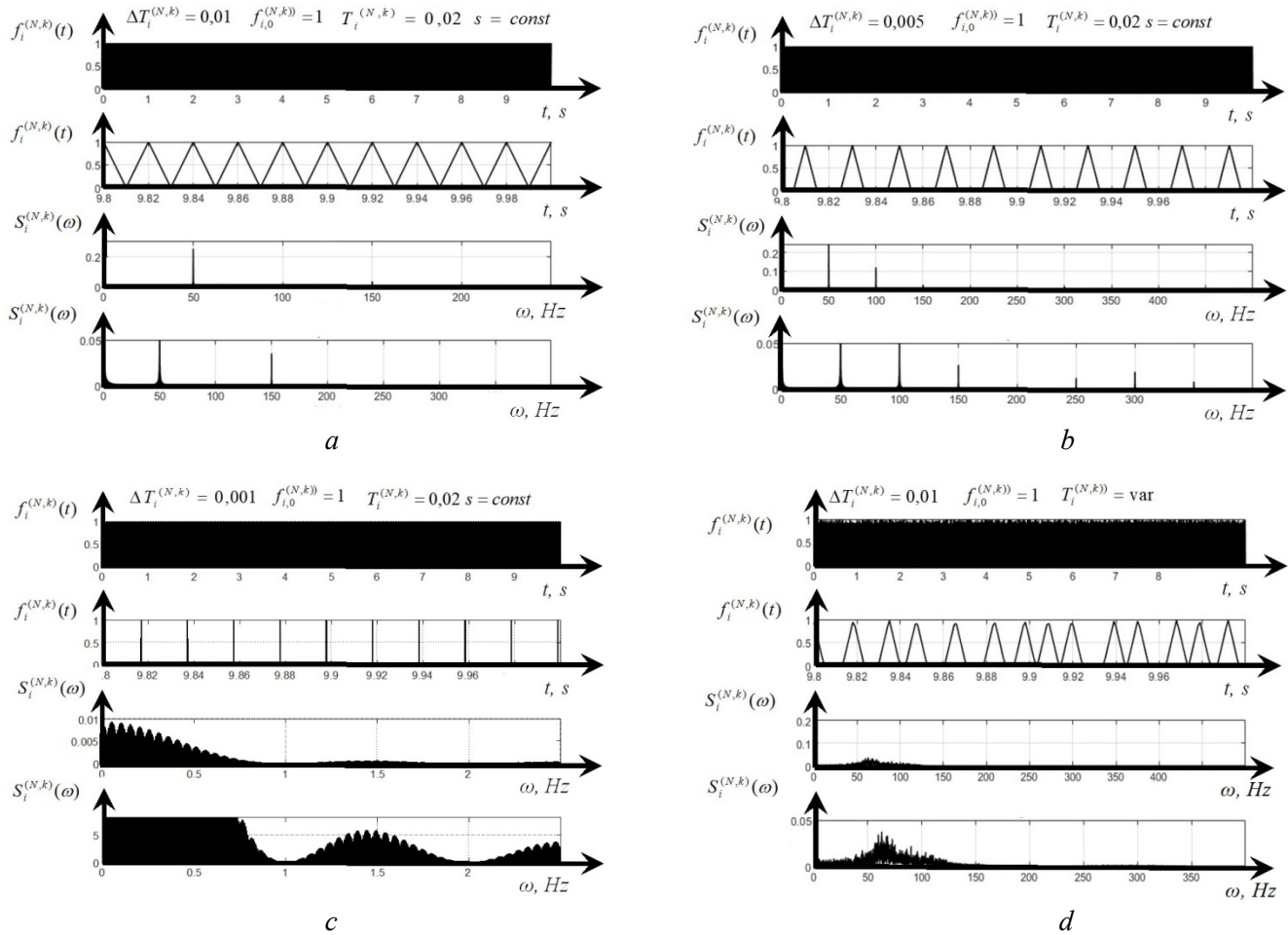
Fig. 7. Examples of spectral changes of a standard pulse sequence

The calculations indicate that increasing the uncertainty in the emission signal over time leads not only to broadening of the emission signal's spectral line but also to a decrease in the intervals between pulses due to regular spatial shifts in the signals. Therefore, as wear increases, the emission signal spectrum becomes blurred and shifts toward the high-frequency region. It is important to note that each individual pulse has risen and fall stages that depend primarily not on time but on the path of relative movements; thus, increasing the cutting speed reduces the parameters $T_i^{(N,k)}$ and $\Delta T_i^{(N,k)}$. As a result, the spectrum becomes dependent on the cutting speed.

If we analyze the frequency range $\Delta\omega_0 \in (\omega_{0,1}, \omega_{0,2})$, we observe that the main changes in the frequency spectra with increasing wear correspond to the features described above. Moreover, the upper frequency $\omega_{0,2}$ in this range is determined by the rule:

$$\omega_{0,2} = \left(\frac{h_0}{V_P}\right)^{-1}$$

where h_0 is the height of the contact between the flank face and the workpiece at the initial stage of wear $w = 0$; it depends on the elastic recovery of the material.

The lower frequency is $\omega_{0,1} = \left(\frac{h_0 + w}{V_P}\right)^{-1}$.

This range must be adjusted experimentally. Here is an example of changes in the spectra obtained from the sequences measured by the cutter shown in Fig. 6, *b* when turning *0.1 C-Mn-2 Ni-Mo-V* steel at the following cutting conditions: feed rate S_p = 0.1 mm, depth of cut t_p = 1.5 mm, and cutting speed V_3 = 1.2 m/s (Fig. 8).
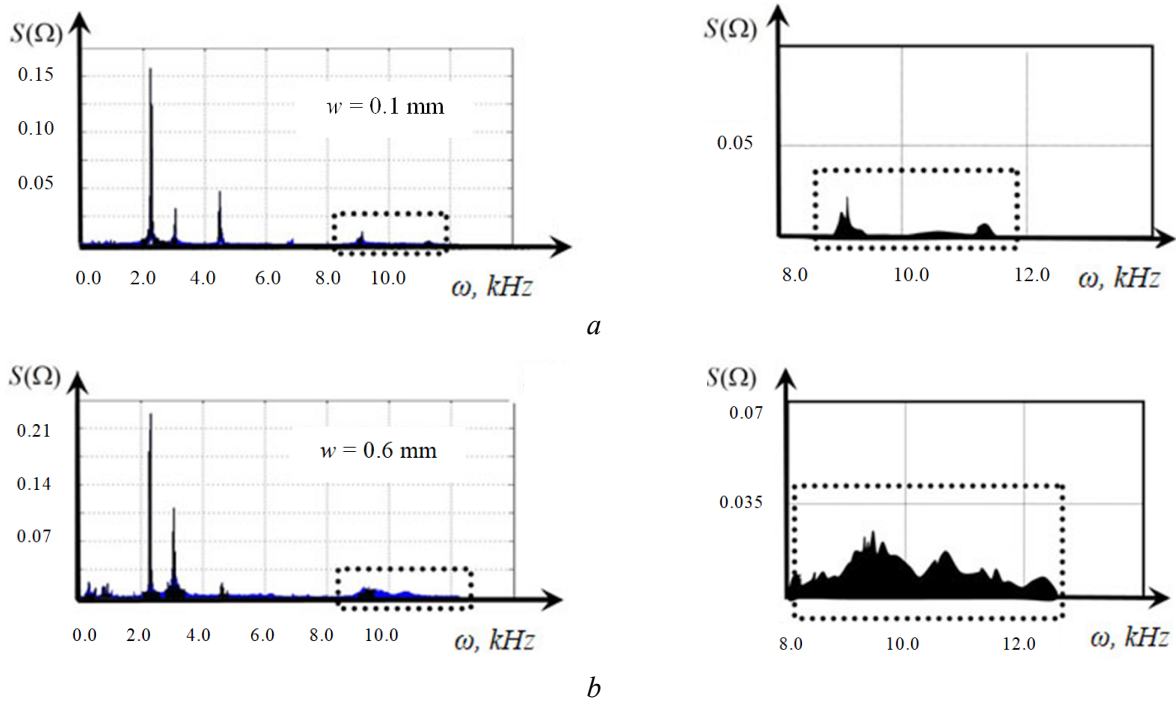
Fig. 8. Example of *AE* spectrum changes depending on wear

The spectra represent the *AE* signal measured after the conversion of forces into acoustic waves. Let the vibration sequence $X(t)$ be defined within the frequency window $\Delta\omega_0 \in (\omega_{0,1}, \omega_{0,2})$. Then, the following information features of the *AE* signal are considered:

$$\Pi_4(w) = \left\{ \int_{\omega_{0,1}}^{\omega_{0,2}} S(\omega, w)\, d\omega - \int_{\omega_{0,1}}^{\omega_{0,2}} S(\omega, 0)\, d\omega \right\} \left\{ \int_{\omega_{0,1}}^{\omega_{0,2}} S(\omega, 0)\, d\omega \right\}^{-1}, \qquad (10)$$

where $S(\omega, w)$ is the *AE* signal spectrum of a worn tool; $S(\omega, 0)$ is the *AE* signal spectrum at the initial stage of wear.

$$\Pi_5(w) = \left\{ \int_{\omega_{0,1}}^{\omega_{0,c}} S(\omega, w)\, d\omega - \int_{\omega_{0,c}}^{\omega_{0,2}} S(\omega, 0)\, d\omega \right\} \left\{ \int_{\omega_{0,1}}^{\omega_{0,2}} S(\omega, 0)\, d\omega \right\}^{-1}, \qquad (11)$$

where $\omega_{0,c}$ is the average frequency of the spectrum within the window $\Delta\omega_0 \in (\omega_{0,1}, \omega_{0,2})$.

Since calculating the frequency within $\Delta\omega_0 \in (\omega_{0,1}, \omega_{0,2})$ can be challenging, it is convenient to select a frequency $\omega_{0,c} = 0.5(\omega_{0,1} + \omega_{0,2})$ and ensure, for $w = 0$, the condition $\int_{\omega_{0,1}}^{\omega_{0,c}} S(\omega, w)\, d\omega = \int_{\omega_{0,c}}^{\omega_{0,2}} S(\omega, 0)\, d\omega$ holds.

Finally, to estimate the irregularity of the pulse sequence amplitude, the amplitude modulation signal of the selected high-frequency signal $X(t)$ can be considered. The modulation level of $x(t)$, determined after detecting the signal $X(t)$ and estimating its dispersion using moving average algorithms $\sigma(t) = \dfrac{1}{T} \int_{t-\Delta T} x\ (\xi)\, d\xi$, is highly informative. Then,

$$\Pi_6(w) = \left\{ \sigma_w(t) - \sigma \right\} \left\{ \sigma \right\}^{-1}. \qquad (12)$$

Depending on the hardware implementation and the vibration sequences available for measurement, all the above-mentioned information features $\Pi = \{\Pi_1, \Pi_2, \dots \Pi_6\}^T \in \Re_{\Pi}^{6}$ can be used.

All formed information feature set (*IFS*) parameters $\mathbf{\Pi} = \{\Pi_1, \Pi_2, \dots \Pi_6\}^T \in \Re_\Pi^6$ have the following properties. First, *IFS* parameters are dimensionless, their values are usually positive, and they change monotonically as wear progresses. Second, wear $\boldsymbol{w} = 0$ in all cases corresponds to the condition $\mathbf{\Pi}_i(\boldsymbol{w}) = 0$, when $\boldsymbol{w} = 0$. Third, from the variety of information features, those highly sensitive to changes in wear have been selected. Their area of application depends on the following.

The information feature $\mathbf{\Pi}_1$ can be used if, as wear progresses, the equilibrium of the dynamic cutting system is asymptotically stable. It suffices to note that the internal amplification factor in the dynamic system depends not only on $\boldsymbol{\rho}$, but also on the cutting depth. It changes to a lesser extent with variations in cutting speed and feed rate. It has been shown earlier that the evolution of the cutting system properties can be highly sensitive to small variations in technological parameters and disturbances. It can be concluded that the redistribution of amplitudes is highly sensitive to wear development. However, this holds true within the range of stable equilibrium, as well as in cases of low sensitivity of the system evolution to variations in initial system parameters and disturbances.

To use the information feature $\mathbf{\Pi}_1$ for diagnosing wear on *CNC* machines, it is necessary to coordinate the diagnosis with the *CNC* program. Information assessments $\mathbf{\Pi}_2$ and $\mathbf{\Pi}_3$ are more universal but less sensitive to variations in the dynamic properties of the system and to changes in operating modes. When constructing diagnostic systems for turning structural steels at constant cutting modes and stable elastic deformation equilibrium, it is possible to divide wear information into 4–5 wear classes [27].

However, all three characteristics depend on the accuracy of the specific machine and its condition. Previous studies of the coherence function between force disturbances and deformations have shown that it increases with increasing frequency [3]. When selecting the space of information features, the features $\mathbf{\Pi}_4$, $\mathbf{\Pi}_5$, and $\mathbf{\Pi}_6$ are more resistant to interference. In this case, the main disturbances are associated with variations in the allowance, spindle group runout, and kinematic disturbances from the feed drives. All disturbances originating from the machine lie within the low-frequency range.

At the same time, when installing the *AE* sensor, it is necessary to take into account the wave properties of the channel connecting the force emission generated in the cutting zone and the measured vibrations (oscillatory deformations, displacements, accelerations, etc.). There is a general rule here: the higher the frequency, the closer the measuring transducer should be to the cutting zone. In our opinion, specialized cutting tools with integrated measurement transducers hold the most promise for *AE* measurement.

The presented method for determining diagnostic signs of tool wear and increased vibration activity of executive elements has practical significance for the creation and development of intelligent algorithms for monitoring systems. Changes in the assessments of diagnostic signs of wear serve as corrective parameters that can be used to build an adaptive control algorithm in the *CNC* unit, capable of extending the tool's service life, but are not limited to this. Within the framework of the presented methodology, the tasks of determining diagnostic signs of degradation of the geometric topology of the part surface and the operational characteristics of the machine tool are of research interest, but these are subjects for future studies. The identified and collected information features in the *VAE* signals allow the creation of "Test Data" and "Training Data" databases for training the assessment of cutting process dynamics in machine learning models of diagnostic systems, which is another step towards the digital transformation of the machine tool industry.

Conclusion

The developed methodology, mathematical modeling, and digital and full-scale experiments have made it possible to form a rational information space for wear diagnosis, in which, based on known recognition methods, decisive rules can be constructed to classify information according to its correspondence to specific wear levels. For the practical application of the methodology in algorithms for monitoring, diagnosing, and controlling the cutting process, it is important to consider the following points.

The basis for constructing tool wear diagnosis systems based on the observation of measurable vibration sequences can be both the dependence of vibrations on changes in the parameters of the dynamic connection

formed by the cutting process and changes in the properties of force emission, represented as a random pulse sequence.

The parameters of the dynamic connection formed by the cutting process depend not only on wear, but also on the technological modes and disturbances originating from the machine itself. Therefore, the use of information parameters based on changes in the vibration spectrum in the low-frequency range is relevant when processing parts in constant modes on equipment with small variations in allowance, spindle group runout, and kinematic disturbances – for example, on automatic production lines. When using these parameters on *CNC* machines, the diagnostic program must be coordinated with the *CNC* program; otherwise, the adequacy of wear representation in the spectral characteristics is significantly reduced.

Force emission, considered in the high-frequency range, firstly causes changes in the intensity of force emission; secondly, shifts the intensity maximum within the frequency range; and finally, the development of wear leads to the formation of uncertainty in all parameters modeling force emission as a random pulse process, which is also an informational feature for wear diagnostic systems.

References

1. Budak E. Machining process improvement through process twins. *Proceedings of the 3rd International Conference on the Industry 4.0 Model for Advanced Manufacturing: AMP 2018*. Springer International Publishing, 2018, pp. 164–179. DOI: 10.1007/978-3-319-89563-5_13.

2. Zakovorotny V., Gvindjiliya V. Process control synergetics for metal-cutting machines. *Journal of Vibroengineering*, 2022, vol. 24 (1), pp. 177–189. DOI: 10.21595/jve.2021.22087.

3. Zakovorotnyi V.L., Gvindjiliya V.E. Influence of speeds of forming movements on the properties of geometric topology of the part in longitudinal turning. *Journal of Manufacturing Processes*, 2024, vol. 112, pp. 202–213. DOI: 10.1016/j.jmapro.2024.01.037.

4. Zakovorotny V.L., Gvindjiliya V.E. The study of vibration disturbance mapping in the geometry of the surface formed by turning. *Obrabotka metallov (tekhnologiya, oborudovanie, instrumenty) = Metal Working and Material Science*, 2024, vol. 26, no. 2, pp. 107–126. DOI: 10.17212/1994-6309-2024-26.2-107-126.

5. Ostaf'ev V.A., Antonyuk V.S., Tymchik G.S. *Diagnostika protsessa metalloobrabotki* [Diagnostics of the metalworking process]. Kiev, Tekhnika Publ., 1991. 152 p. ISBN 5-335-00209-3.

6. Kozochkin M.P. Mnogoparametricheskaya diagnostika tekhnologicheskikh sistem dlya obrabotki materialov rezaniem [Multivariate diagnostics of technological systems for processing materials by cutting]. *Vestnik MGTU «Stankin» = Vestnik MSUT "Stankin"*, 2014, no. 1 (28), pp. 13–19.

7. Grubyi S.V. *Optimizatsiya protsessa mekhanicheskoi obrabotki i upravleniya rezhimnymi parametrami* [Optimization of the process of mechanical processing and control of operating parameters]. Moscow, Bauman MSTU Publ., 2014. 149 p. ISBN 978-5-7038-3935-5.

8. Kabaldin Yu.G., Kuzmishina A.M., Shatagin D.A., Anosov M.S. Neironnosetevoe modelirovanie protsessa iznashivaniya tverdosplavnogo instrumenta [Neural network modeling of the wear process of a carbide cutting tool]. *Avtomatizatsiya. Sovremennye tekhnologii = Automation. Modern Technologies*, 2021, vol. 75, no. 9, pp. 398–402. DOI: 10.36652/0869-4931-2021-75-9-398-402.

9. Kabaldin Yu.G., Shatagin D.A., Anosov M.S., Kuzmishina A.M. Razrabotka tsifrovogo dvoinika stanka s ChPU na osnove metodov mashinnogo obucheniya [Development of digital twin of CNC unit based on machine learning methods]. *Vestnik Donskogo gosudarstvennogo tekhnicheskogo universiteta = Vestnik of Don State Technical University*, 2019, no. 19 (1), pp. 45–55. DOI: 10.23947/1992-5980-2019-19-1-45-55.

10. Kabaldin Yu.G., Shatagin D.A., Kuzmishina A.M. Razrabotka tsifrovogo dvoinika rezhushchego instrumenta dlya mekhanoobrabatyvayushchego proizvodstva [The development of a digital twin of a cutting tool for mechanical production]. *Izvestiya vysshikh uchebnykh zavedenii. Mashinostroenie = Proceedings of Higher Educational Institutions. Machine Building*, 2019, no. 4, pp. 11–17. DOI: 10.18698/0536-1044-2019-4-11-17.

11. Pantyukhin O.V., Vasin S.A. Tsifrovoi dvoinik tekhnologicheskogo protsessa izgotovleniya izdelii spetsial'nogo naznacheniya [Digital double of the technological process of manufacturing special-purpose products]. *Stankoinstrument*, 2021, no. 1 (22), pp. 56–59. DOI: 10.22184/2499-9407.2021.22.1.56.58. (In Russian).

12. Erkorkmaz K., Altintas Y., Yeung C.-H. Virtual computer numerical control system. *CIRP Annals*, 2006, vol. 55 (1), pp. 399–402. DOI: 10.1016/S0007-8506(07)60444-2.

13. Kilic Z.M., Altintas Y. Generalized mechanics and dynamics of metal cutting operations for unified simulations. *International Journal of Machine Tools and Manufacture*, 2016, vol. 104, pp. 1–13. DOI: 10.1016/j.ijmachtools.2016.01.006.

14. Estman L., Merdol D., Brask K.-G., Kalhori V., Altintas Y. Development of machining strategies for aerospace components, using virtual machining tools. *New Production Technologies in Aerospace Industry.* Cham, Springer, 2014, pp. 63–68. DOI: 10.1007/978-3-319-01964-2_9.

15. Kozochkin M.P., Sabirov F.S., Seleznev A.E. Vibroakusticheskii monitoring lezviinoi obrabotki zagotovok iz zakalennoi stali [Vibroacoustic monitoring of cutting edge machining of hardened steel]. *Vestnik MGTU «Stankin» = Vestnik MSUT "Stankin"*, 2018, no. 1 (44), pp. 23–30.

16. Barzov A.A., Gorelov V.A., Igonkin B.A. Akustoelektricheskaya diagnostika protsessa rezaniya polimernykh kompozitsionnykh materialov [Acoustoelectric diagnostics of the cutting process of polymer composite materials]. *Aviatsionnaya promyshlennost' = Aviation Industry*, 1986, no. 12, p. 36.

17. Altintas Y., Kersting P., Biermann D., Budak E., Denkena B. Virtual process systems for part machining operations. *CIRP Annals*, 2014, vol. 63 (2), pp. 585–605. DOI: 10.1016/j.cirp.2014.05.007.

18. Altintas Y., Brecher C., Weck M., Witt S. Virtual machine tool. *CIRP Annals*, 2005, vol. 54 (2), pp. 115–138. DOI: 10.1016/S0007-8506(07)60022-5.

19. Soori M., Arezoo B., Habibi M. Virtual machining considering dimensional, geometrical and tool deflection errors in three-axis CNC milling machines. *Journal of Manufacturing Systems*, 2014, vol. 33 (4), pp. 498–507. DOI: 10.1016/j.jmsy.2014.04.007.

20. Tieng H., Yang H.C., Hung M.H., Cheng F.T. A novel virtual metrology scheme for predicting machining precision of machine tools. *IEEE International Conference on Robotics and Automation*. IEEE, 2013, pp. 264–269. DOI: 10.1109/ICRA.2013.6630586.

21. Astakhov V.P. *Geometry of single-point turning tools and drills: Fundamentals and practical applications*. London, Springer, 2010. 566 p. DOI: 10.1007/978-1-84996-053-3.

22. Konrad H., Isermann R., Oette H.U. Supervision of tool wear and surface quality during end milling operations. *IFAC Proceedings Volumes*, 1994, vol. 27 (4), pp. 507–513. DOI: 10.1016/S1474-6670(17)46074-5.

23. Zakovorotny V.L., Bordachev E.V. Informatsionnoe obespechenie sistemy dinamicheskoi diagnostiki iznosa rezhushchego instrumenta na primere tokarnoi obrabotki [Information support for the system of dynamic diagnostics of cutting tool wear using the example of turning]. *Problemy mashinostroeniya i nadezhnosti mashin = Journal of Machinery Manufacture and Reliability*, 1995, no. 3, pp. 95–103.

24. Grigoriev A.S. Instrumentarii sistemy ChPU dlya diagnostiki i prognozirovaniya iznosa rezhushchego instrumenta v real'nom vremeni pri tokarnoi obrabotke [CNC tool for diagnostic and prediction of cutting tool wear in real time for turning processing]. *Vestnik MGTU «Stankin» = Vestnik MSUT "Stankin"*, 2012, no. 1 (18), pp. 39–43.

25. Zakovorotny V.L., Gvindjiliya V.E. Evolyutsiya dinamicheskoi sistemy rezaniya, obuslovlennaya neobratimymi preobrazovaniyami energii v zone obrabotki [Evolution of the dynamic cutting system caused by irreversible energy transformations in the processing zone]. *STIN = Russian Engineering Research*, 2018, no. 12, pp. 17–25. (In Russian).

26. Zakovorotny V.L., Gvindjiliya V.E. Svyaz' samoorganizatsii dinamicheskoi sistemy rezaniya s iznashivaniem instrumenta [Link between the self-organization of dynamic cutting system and tool wear]. *Izvestiya vuzov. Prikladnaya nelineinaya dinamika = Izvestiya VUZ. Applied Nonlinear Dynamics*, 2020, vol. 28, no. 1, pp. 46–61. DOI: 10.18500/0869-6632-2020-28-1-46-61.

27. Zakovorotny V.L., Gvindjiliya V.E., Kislov K.V. Information properties of frequency characteristics of dynamic cutting systems in the diagnosis of tool wear. *Obrabotka metallov (tekhnologiya, oborudovanie, instrumenty) = Metal Working and Material Science*, 2024, vol. 26, no. 3, pp. 114–134. DOI: 10.17212/1994-6309-2024-26.3-114-134.

28. Rizal M., Ghani J.A., Nuawi M.Z., Haron C.H. A review of sensor system and application in milling process for tool condition monitoring. *Research Journal of Applied Sciences, Engineering and Technology*, 2014, vol. 7 (10), pp. 2083–2097. DOI: 10.19026/rjaset.7.502.

29. Teti R. Advanced IT methods of signal processing and decision making for zero defect manufacturing in machining. *Procedia CIRP*, 2015, vol. 28, pp. 3–15. DOI: 10.1016/ j.procir.2015.04.003.

30. Bhuiyan M., Choudhury I., Nukman Y. An innovative approach to monitor the chip formation effect on tool state using acoustic emission in turning. *International Journal of Machine Tools and Manufacture*, 2012, vol. 58, pp. 19–28. DOI: 10.1016/ j.ijmachtools.2012.02.001.

31. Rehorn A.G., Jiang J., Orban P.E. State-of-the-art methods and results in tool condition monitoring: a review. *International Journal of Advanced Manufacturing Technology*, 2005, vol. 26, pp. 693–710. DOI: 10.1007/s00170-004-2038-2.

32. Jemielniak K., Arrazola P. Application of AE and cutting force signals in tool condition monitoring in micro-milling. *CIRP Journal of Manufacturing Science and Technology*, 2008, vol. 1 (2), pp. 97–102. DOI: 10.1016/ j.cirpj.2008.09.007.

33. Zakovorotny V.L., Ladnik I.V., Dhande S.G. A method for characterization of machine-tools dynamic parameters for diagnostic purposes. *Journal of Materials Processing Technology*, 1995, vol. 53 (3–4), pp. 588–600. DOI: 10.1016/0924-0136(94)01745-M.

34. Zakovorotny V.L., Gvindjiliya V.E. Self-organization and evolution in dynamic friction systems. *Journal of Vibroengineering*, 2021, vol. 23 (6), pp. 1418–1432. DOI: 10.21595/jve.2021.22033.

35. Lee D.E., Hwang I., Valente C.M.O., Oliveira J.F.G., Dornfeld D.A. Precision manufacturing process monitoring with acoustic emission. *International Journal of Machine Tools and Manufacture*, 2006, vol. 46 (2), pp. 176–188. DOI: 10.1016/ j.ijmachtools.2005.04.001.

36. Byrne G., Dornfeld D., Inasaki I., Ketteler G., Konig W., Teti R. Tool condition monitoring (TCM) – the status of research and industrial application. *CIRP Annals*, 1995, vol. 44 (2), pp. 541–567. DOI: 10.1016/S0007-8506(07)60503-4.

37. Dimla D.E. Sensor signals for tool-wear monitoring in metal cutting operations – a review of methods. *International Journal of Machine Tools and Manufacture*, 2000, vol. 40 (8), pp. 1073–1098. DOI: 10.1016/S0890-6955(99)00122-4.

38. Choi Y., Narayanaswami R., Chandra A. Tool wear monitoring in ramp cuts in end milling using the wavelet transform. *International Journal of Advanced Manufacturing Technology*, 2004, vol. 23 (5–6), pp. 419–428. DOI: 10.1007/s00170-003-1898-1.

39. Dolinšek S., Kopac J. Acoustic emission signals for tool wear identification. *Wear*, 1999, vol. 225–229 (1), pp. 295–303. DOI: 10.1016/s0043-1648(98)00363-9.

40. Chiou R.Y., Liang S.Y. Analysis of acoustic emission in chatter vibration with tool wear effect in turning. *International Journal of Machine Tools and Manufacture*, 2000, vol. 40 (7), pp. 927–941. DOI: 10.1016/S0890-6955(99)00093-0.

41. Bhuiyan M.S.H., Choudhury I.A., Dahari M., Nukman Y., Dawal S.Z. Application of acoustic emission sensor to investigate the frequency of tool wear and plastic deformation in tool condition monitoring. *Measurement*, 2016, vol. 92, pp. 208–217. DOI: 10.1016/ j.measurement.2016.06.006.

42. Siddhpura A., Paurobally R. A review of flank wear prediction methods for tool condition monitoring in a turning process. *International Journal of Advanced Manufacturing Technology*, 2013, vol. 65, pp. 371–393. DOI: 10.1007/s00170-012-4177-1.

43. Karandikar J., McLeay T., Turner S., Schmitz T. Tool wear monitoring using naive Bayes classifiers. *International Journal of Advanced Manufacturing Technology*, 2014, vol. 77, pp. 1613–1626. DOI: 10.1007/s00170-014-6560-6.

44. Kene A.P., Choudhury S.K. Analytical modeling of tool health monitoring system using multiple sensor data fusion approach in hard machining. *Measurement*, 2019, vol. 145, pp. 118–129. DOI: 10.1016/j.measurement.2019.05.062.

45. Mohanraj T., Shankar S., Rajasekar R., Sakthivel N., Pramanik A. Tool condition monitoring techniques in milling process – a review. *Journal of Materials Research and Technology*, 2019, vol. 9 (1), pp. 1032–1042. DOI: 10.1016/ j.jmrt.2019.10.031.

46. Kalvoda T., Hwang Y.R. A cutter tool monitoring in machining process using Hilbert–Huang transform. *International Journal of Machine Tool and Manufacture*, 2010, vol. 50 (5), pp. 495–501. DOI: 10.1016/j.ijmachtools.2010.01.006.

47. Zakovorotny V.L., Flek M.B. *Dinamika protsessa rezaniya. Sinergeticheskii podkhod* [The dynamics of the cutting process. Synergistic approach]. Rostov-on-Don, Terra Publ., 2005. 880 p. ISBN 5-98254-055-2.

48. Artobolevskii I.I., Bobrovnitskii Yu.I., Genkin M.D. *Vvedenie v akusticheskuyu dinamiku mashin* [Introduction to the acoustic dynamics of machines]. Moscow, Nauka Publ., 1979. 296 p.

49. Zorev N.N., Granovskii G.I., Larin M.N. *Razvitie nauki o rezanii metallov* [Development of the science of metal cutting]. Moscow, Mashinostroenie Publ., 1967. 416 p.

50. Gvindjiliya V.E., Fominov E.V., Moiseev D.V., Gamaleeva E.I. Influence of dynamic characteristics of the turning process on the workpiece surface roughness. *Obrabotka metallov (tekhnologiya, oborudovanie, instrumenty) = Metal Working and Material Science*, 2024, vol. 26, no. 2, pp. 143–157. DOI: 10.17212/1994-6309-2024-26.2-143-157.

51. Makarov A.D. *Optimizatsiya protsessov rezaniya* [Optimization of cutting processes]. Moscow, Mashinostroenie Publ., 1976. 278 p.

Conflicts of Interest

The authors declare no conflict of interest.

Obrabotka metallov -
Metal Working and Material Science

Journal homepage: http://journals.nstu.ru/obrabotka_metallov

Modal analysis of various grinding wheel types for the evaluation of their integral elastic parameters

Aleksandr Zhukov [a], *, Dmitrii Ardashev [b], Victor Batuev [c], Victor Kulygin [d], Egor Schuleshko [e]

South Ural State University, 76 Prospekt Lenina, Chelyabinsk, 454080, Russian Federation

[a] https://orcid.org/0000-0002-9328-7148, ✉ zhukovas@susu.ru; [b] https://orcid.org/0000-0002-8134-2525, ✉ ardashevdv@susu.ru;
[c] https://orcid.org/0000-0001-9969-4310, ✉ batuevvv@susu.ru; [d] https://orcid.org/0009-0000-8509-1420, ✉ kulyginvl@susu.ru;
[e] https://orcid.org/0000-0002-5709-4285, ✉ schuleshko21@mail.ru

ARTICLE INFO

ABSTRACT

Introduction. In developing a mathematical model for the sound pressure generated by the grinding process, it became necessary to determine the actual values of the integral elastic parameters of grinding wheels to use as inputs in the model. This will expand the applicability of the model and maximize its practical utility. This paper describes an approach to determining *Poisson's* ratios and *Young's* moduli for grinding wheels with different characteristics. The elastic properties of the tool are the **subject** of this study. The **purpose** is to establish the relationship between actual values of integral elastic parameters and grinding wheel characteristics via modal analysis. **The research method** combines experimental investigation of natural frequency spectra and modal analysis, implemented via the finite element method in specialized software. Additionally, regression analysis is employed to derive empirical dependencies of the integral elastic parameters of grinding wheels on abrasive grain size and hardness. **Results and discussion.** The main result of this work is the determination of the actual values of *Poisson's* ratios and *Young's* moduli for grinding wheels with the studied characteristics. The selection of grinding wheel characteristics allowed for the investigation of the influence of abrasive grain size and hardness on its integral elastic properties. The development of a mathematical model for sound pressure generated by the grinding process, along with a methodology for predicting the service life of grinding wheels based on this model, will improve grinding operation efficiency by reducing the machine-setting time, increasing processing time, reducing consumption of manufacturing resources, and optimizing tool lifespan utilization.

Introduction

Predicting the life of a grinding wheel (*GW*) by means of the indirect acoustic criterion naturally implies the need to study its dynamic characteristics. The development of a model for the sound pressure generated by the grinding process requires the values of the elastic moduli of the grinding wheel to correctly calculate the modes and frequencies of the natural vibrations which are the source of the acoustic field. According to

* Corresponding author
Zhukov Aleksandr S., Ph.D. (Engineering) student
South Ural State University,
76 Prospekt Lenina,
454080, Chelyabinsk, Russian Federation
Tel.: +7 351 272-32-94, **e-mail:** zhukovas@susu.ru

the characteristics of such a field, it is possible to predict many output parameters of the grinding process over time: cutting forces, machining quality parameters [1, 2] (roughness, shape deviations of the workpiece, presence of burns, etc.), and stiffness of the technological system. The sequence of manifestation of natural vibration modes of the grinding wheel, inseparably connected with its elastic parameters, determines the nature of the acoustic response of the system during operation, as well as the way it will react to external excitation during grinding.

Modal analysis is a powerful method for determining the dynamic characteristics of a mechanical system. In mechanical engineering, this method is used to solve a wide range of problems, from the design and optimization of machine structures, mechanisms, and parts, to the diagnosis and monitoring of equipment condition. The growing need to improve the design of modern metal-cutting machines and tools with respect to vibration resistance, increasing their reliability and rigidity, has led to the emergence of new and effective applications of modal analysis. In [3–8], parametric optimization of both the design of individual elements of machine tools (spindles, beds, etc.) and complex machine tool assemblies is carried out. In particular, designs of numerically controlled machine tools and multi-axis high-precision machine tools are often optimized by means of modal analysis. In [9–13], cutting tools are designed using modal analysis, and existing designs of turning tools, drills, and milling cutters are improved according to criteria of vibration resistance and enhancement of dynamic balance during machining. Calculating the eigenmodes and vibration frequencies of systems whose operation is associated with dynamic vibration loads is necessary at the design, testing, or modernization stages, regardless of the magnitude of the loads. If the system's operating mode leads to vibrations at the resonance frequency, the design is modified to prevent emergency situations.

The complexity and multi-component structure of a grinding wheel make it difficult to determine its elasticity parameters, which are necessary for calculating its natural vibrations. The elastic parameters of abrasive tools are poorly represented in technical literature. There is no systematization, and no correspondence has been established between these parameters and the characteristics of grinding wheels. Reference books do not provide values for the elastic properties of abrasive tools, such as *Poisson's* ratio and *Young's* modulus. Only isolated experimental references for grinding wheels with specific characteristics can be found.

The variety of existing and emerging grinding wheel formulations is extremely large. Depending on the characteristics of the grinding wheel, the proportions of its components (abrasive, bond, and pores) and their properties vary considerably [14]. Exact calculations of the elastic parameters of grinding wheels are extremely laborious, as they require consideration of the properties of each component and how they interact with each other. To simplify the process, modal analysis is proposed to evaluate the elastic properties of the system as a whole without detailing the components.

The ***objective of this study*** is to determine how the actual values of integral elastic indices depend on grinding wheel characteristics using modal analysis. To achieve this goal, the following tasks must be completed:

1) conduct an experimental study of the frequencies of natural vibrations of grinding wheels with different characteristics;

2) calculate the natural frequencies and mode shapes of grinding wheels for various combinations of elastic and geometric parameters using specialized software and the finite element method;

3) compare and correlate the experimental and calculated natural frequencies of the grinding wheels.

4) determine the actual values of *Poisson's* ratio and *Young's* modulus for all investigated grinding wheels.

Methods

Table 1 shows the list of grinding wheel characteristics included in the study of integral elastic performance.

The grinding wheels were selected for this study to investigate how changes in granularity, hardness, and abrasive material affect the integral elastic properties of the tool (Fig. 1).

Grinding wheels characteristics according to *GOST R 52781-2007*

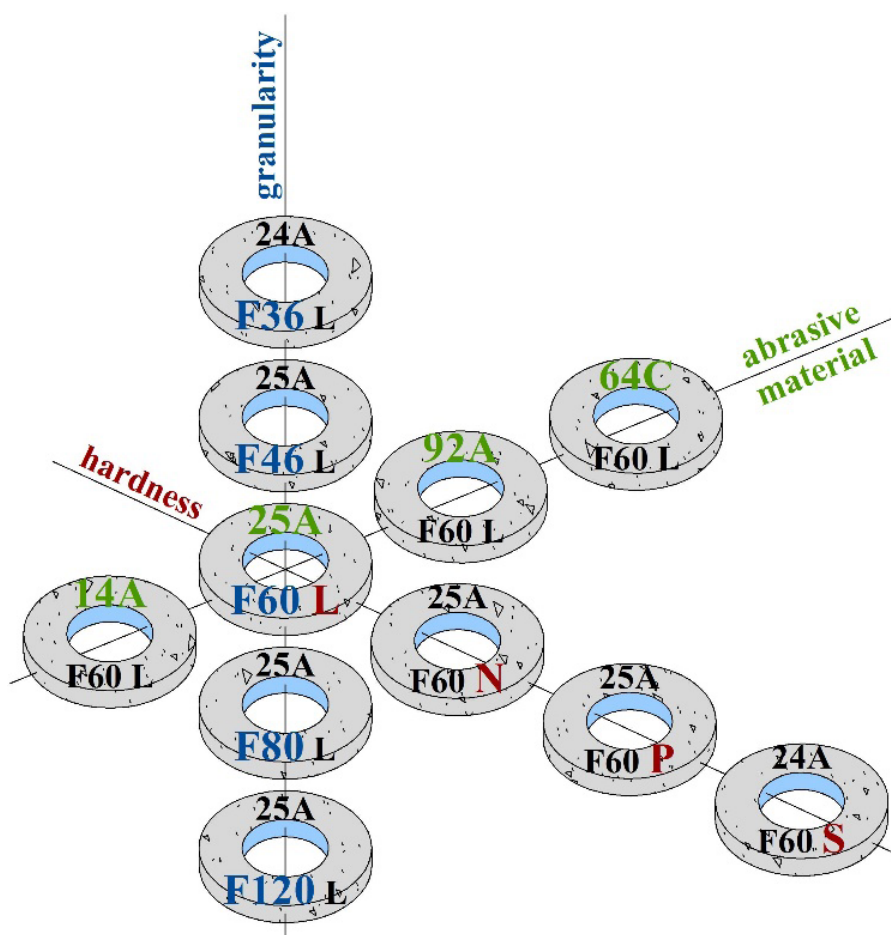| *GW* No.	*GW* dimensions $D \times H \times d$, mm	Abrasive material	Grit	Hardness
1			*F36*	
2			*F46*	
3			*F60*	*L*
4	600×50×305	*25A*	*F80*	
5			*F120*	
6				*N*
7				*P*
8	500×63×305		*F60*	*S*
9	600×50×305	*14A*		
10		*64C*		*L*
11	600×40×305	*92A*		

Fig. 1. Grinding wheels under study

The effect of grain size variation on the elastic properties of grinding wheels No. 1, No. 2, No. 3, No. 4, and No. 5 was studied. The grain size ranged from *F36* to *F120* (*H50* to *H10* according to *GOST 2424-84*), with the average grain size ranging from 0.5 to 0.11 mm. Other properties remained unchanged.

The influence of changes in hardness on the elastic properties of grinding wheels No. 3, No. 6, No. 7, and No. 8 was studied. The hardness varied from *L* to *S* (*CM2* to *T2* according to *GOST 2424-84*). All other formulation characteristics remained unchanged.

To study the influence of different abrasives on the elastic properties of grinding wheels, wheels No. 3, No. 9, No. 10, and No. 11 were considered:

– *25A* white aluminum oxide with 99 % α-Al_2O_3 content. It is used for finishing and profile grinding of hardened steels, as well as sharpening of high-speed tools;

– *14A* normal electrocorundum with 93 % α-Al_2O_3 content. It is used for rough grinding;

– *92A* chromotitanium electrocorundum with 60–75 % α-Al_2O_3 content. It is used for grinding hardened steels, machining with large metal removal, and rough grinding;

– *64C* green silicon carbide with 96–97 % *SiC* content. It is used for final sharpening and finishing of carbide tools, honing, and superfinishing [14, 15].

The structure of the considered grinding wheels is medium (structure numbers **5**, **6**, and **7**), and the bond is ceramic.

Experimental study of natural vibrations of grinding wheels

A full-scale experiment was conducted to record the spectrum of natural frequencies of grinding wheel vibrations. The natural oscillations of the grinding wheel were excited by impact, as shown in Fig. 2. The acoustic signal generated by the wheel's natural vibrations was recorded using the *NFM-2* (natural frequency meter) employing a non-contact method. The grinding wheel (*GW*) was mounted vertically on a carriage. The *ICHSK-2* microphone, which serves as the device's sensitive element, was positioned at an angle of $45° \pm 15°$ relative to the diameter passing through the grinding wheel's support point. A minimum clearance between the cylindrical surface of the grinding wheel and the microphone must be maintained; contact with the surface is not permitted. The striker (hammer) impacts the grinding wheel at an angle of $45° \pm 15°$ relative to the diameter passing through the support point of the grinding wheel, symmetrical to the microphone's position. The striker impacts the cylindrical surface of the tested bearing directed toward its center. The force and area of impact are insignificant since the study focuses on the frequencies, not the amplitudes, of natural vibrations.
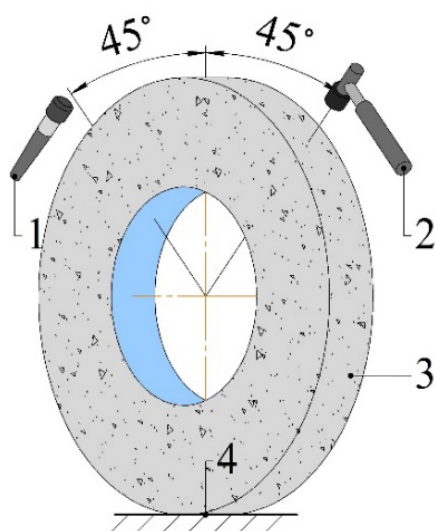
Fig. 2. Scheme of measuring frequencies of *GW* natural vibrations:

1 – microphone, **2** – hammer, **3** – grinding wheel under study, **4** – base

When setting up the device, it is necessary to specify:
– type of product – abrasives / blades / other products;
– type of abrasive – *14A* / *25A* / *92A* / *64C*;
– type of bond – bakelite / vulcanite / ceramic;
– geometric shape and dimensions of the grit (shape coefficient);
– density of the ball;
– frequency range of measurements.

The experiment involved 10 measurements of the eigenfrequencies of each grinding wheel. Then, the average spectral composition of the natural frequencies of each grinding wheel was determined. Fig. 3 shows an example of a spectrogram of ten measurements of natural frequencies of *GW* 1 600×50×305 *25A F60 L* 7 V 50 2kl *GOST R 52781-2007* – grinding wheel No. 3.

Modal analysis of grinding wheel natural vibrations

A computer simulation experiment was conducted using the finite element method in the *COMSOL Multiphysics* software environment to study natural frequencies and vibration modes. This software is widely used for engineering calculations worldwide and has proven effective in solving acoustic and vibration problems [16–20].
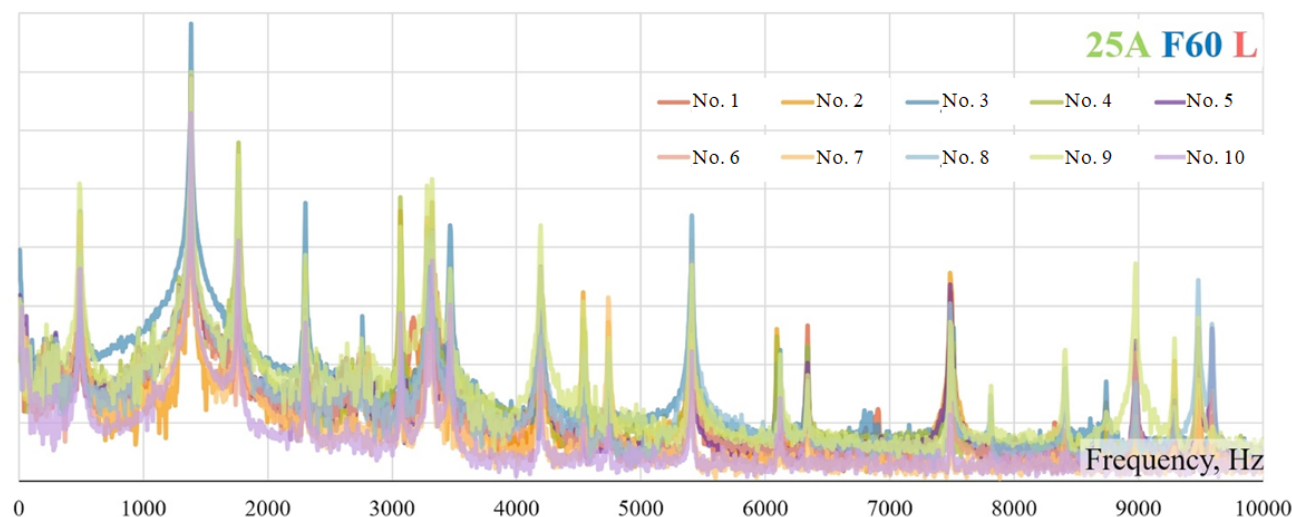
Fig. 3. Spectral composition of grinding wheel No.3 natural vibrations

A model of a grinding wheel was developed that allows parametric control over its geometry and elastic parameters. The following equation expresses the relationship between the natural frequencies of a grinding wheel's vibrations and its geometric dimensions, shape, and elastic parameters:

$$f_i = F_i(a, \nu)\sqrt{\frac{E}{\rho}}$$

where $F_i(a, \nu)$ is the shape factor, which depends on the body's geometrical dimensions and shape ($a = f(D, d, H)$), *Poisson's* ratio (ν), and the mode of oscillation.

The model parameters are summarized in Table 2.

Table 2

Grinding wheel model parameters

Symbol	Description
Geometrical model parameters	
D	*GW* outer diameter
d	*GW* inner diameter
H	*GW* height
Elastic parameters of model material	
ν	*Poisson's* ratio
E	*Young's* modulus
ρ	density

The calculation of eigenmodes and oscillation frequencies was carried out for each variant of the grinding wheel (*GW*) parameters – *D*, *d*, *H*, ν, *E*, and ρ – in order to determine the agreement with the experimentally obtained frequencies. The comparison is presented in the section "*Comparison of experimental and calculated spectral compositions of grinding wheels*".

Results and Discussion
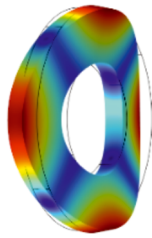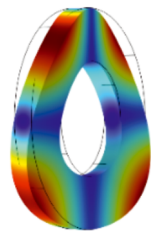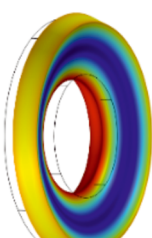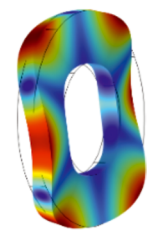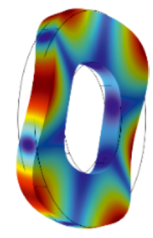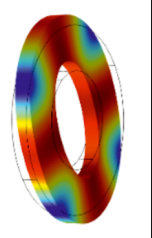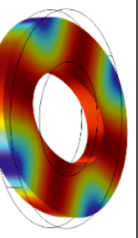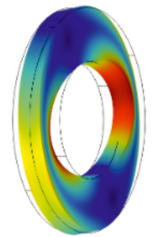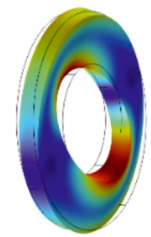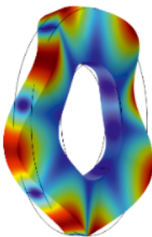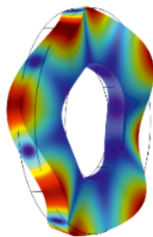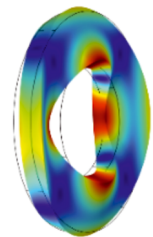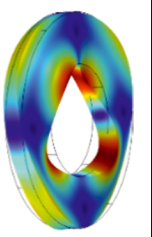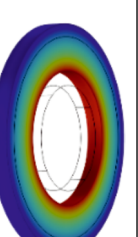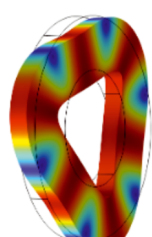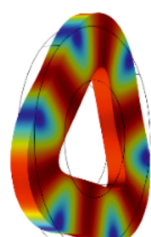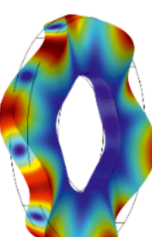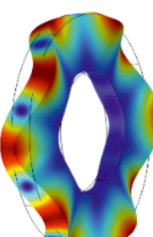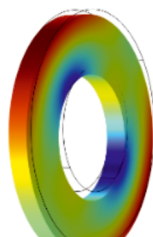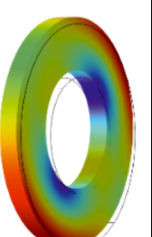
Eigenmodes of Grinding Wheel Vibration

Computer modeling has shown that the order in which eigenmodes of grinding wheel vibrations manifest remains unchanged over a wide range of values of ν, *E*, and ρ. The natural frequency values associated

with each mode vary depending on the values and combinations of the elastic parameters. The geometric parameters of grinding wheels have a decisive influence on the shapes of the modes, the sequence of their manifestation, and the corresponding frequencies. Table 3 summarizes the natural frequencies and their corresponding modes in the order of their manifestation for grinding wheel No. 3 – *GW* 1 600×50×305 *25A F60 L* 7 V 50 2 class *GOST R 52781-2007*.

T a b l e 3

Occurrence order of grinding wheel natural oscillations modes*

No.	1	2	3	4	5	6	7
f, Hz	544.59	544.62	1187.6	1429.7	1429.71	1451.8	1451.81
Mode							
	Repeated modes			Repeated modes		Repeated modes	
No.	8	9	10	11	12	13	14
f, Hz	1983.3	1983.5	2555.5	2555.51	3440.4	3440.8	3503.5
Mode							
	Repeated modes		Repeated modes		Repeated modes		
No.	15	16	17	18	19	20	
f, Hz	3508.8	3508.81	3850.0	3850.1	4503.5	4503.51	
Mode							
	Repeated modes		Repeated modes		Repeated modes		

* – GW 1 600×50×305 25A F60 L 7 V 50 2 class GOST P 52781-2007

Thus, a pair of the lowest modes are bending modes with two nodal diameters, f_1 and f_2 (n = 2, s = 0), followed by the bending mode f_3 with one nodal circle (n = 0, s = 1), called the "*umbrella*" mode in the literature [21]. This result agrees with the analytical calculations of vibration modes of grinding wheels by *B. A. Glagovsky* and *I. B. Moskovenko* [22]. In the study of vibrations of discs with a central axial hole, the letters n and s denote the number of nodal diameters and nodal circles, respectively. The grinding wheels considered in this study belong to this category.

The bending modes manifested in pairs f_4 and f_5 (n = 3, s = 0), f_{10} and f_{11} (n = 4, s = 0), and f_{17} and f_{18} (n = 5, s= 0) are similar and differ only in the number of nodal diameters. The pairs f_8 and f_9 (n = 1,

$s = 1$) and f_{12} and f_{13} ($n = 2$, $s = 1$) differ by the presence of a nodal circle and a different number of nodal diameters. The pairs f_6 and f_7 ($n = 2$, $s= 0$), f_{15} and f_{16} ($n = 3$, $s = 0$), f_{19} and f_{20} ($n = 1$, $s = 1$), and mode f_{14} ($n = 0$, $s = 1$) belong to the class of radial modes. These are characterized by tension-compression stresses, in which oscillations of microvolumes occur in the plane of the grinding wheel.

The peculiarity of the pairwise manifestation of modes with nodal diameters ($n \neq 0$) is emphasized. These modes are called multiple modes since they are vibration modes with close (or coinciding) natural frequencies, the same mode set but different orientations of nodal lines. Multiple modes appear in pairs and are characterized by the relative displacement of nodal diameters by some angle. Such modes occur in systems with a high degree of symmetry (e.g., circular discs, spherical shells, square plates). Their existence has been confirmed by both experimental studies and analytical calculations [23–26].

The smallest number of nodal lines, whether nodal diameters or nodal circles, are characteristic of the lowest modes, i.e., modes formed at the lowest frequencies characteristic of the "grinding wheel" system. As the number of nodal lines manifested in the vibrational motion of a particular mode increases, the frequency at which this mode occurs also increases. It is well known that the lowest modes are of primary importance in the overall dynamics of the vibrational process of an elastic solid. To describe the contribution of each mode, coefficients of modal participation and modal mass have been introduced. These coefficients will be discussed in more detail in "*Modal Participation Coefficients*".

Modal participation coefficients

The participation coefficient indicates the relative contribution of each mode to the displacement or rotation of the system when excited in a specific direction and manner. Since no rotational modes or angular vibrations of the grinding wheel were identified in the computer simulations, the participation coefficients for rotational directions are not considered in this study.

Participation coefficients are calculated when it is necessary to determine the parameters of an external load that could potentially cause undesirable resonance in the system [27]. Such calculations make it possible to assess the significance of each mode participating in the vibration process. These modes are characterized by high vibration energies and sensitivity to specific types of loads. After identifying a significant mode in strength calculations, either the system's operating modes should be changed or the design modernized to avoid undesirable consequences.

Fig. 4 shows the graph of participation coefficients of grinding wheel No. 3 – *GW 1 600×50×305 25A F60 L 7 V 50 2* class *GOST R 52781-2007* – plotted along three coordinate axes. It demonstrates that the most significant eigenmodes of vibration of the grinding wheel are modes f_1 and f_2, which are most pronounced in the *X* and *Y* directions. Regarding the *Z* axis, the largest contribution in this direction is made by the "*umbrella*" mode f_3.

This mode will be used for acoustic monitoring of the grinding process. When applying boundary conditions, the displacement of the grinding wheel model is restricted – it is rigidly fixed along the seat diameter on the machine spindle. Additionally, a prestressing condition distributed over the volume of the grinding wheel is imposed, resulting from the centrifugal forces during rotation at a speed of 1,590 RPM.
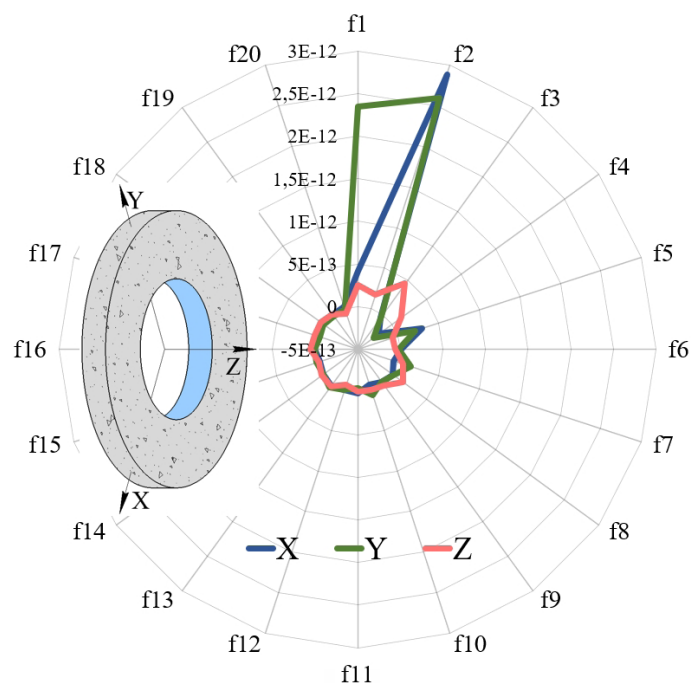
Fig. 4. Participation factors of the natural vibration modes of the grinding wheel along the coordinate axes

The order of eigenmodes' manifestation changes significantly as a result of calculating them under these specified boundary conditions. The bending mode with the highest values of modal participation coefficients and modal masses becomes the lowest and most significant mode, featuring a nodal circle coinciding with the end region — the "*umbrella*" mode. The participation of this mode in the overall dynamics of the grinding wheel vibrations is much greater (more than 30 times) than that of the others and, accordingly, it generates the most powerful acoustic wave.

Comparison of experimental and calculated spectral compositions of grinding wheels

In figs. 5, *a–k*, the black lines show the spectral compositions obtained experimentally using the method described in section "*Experimental study of natural vibrations of grinding wheels*". These graphs illustrate the distribution of the natural frequencies of grinding wheels with the studied characteristics.

During computer modeling and the modal analysis process, the values of *Poisson's* ratio (**ν**) and *Young's* modulus (**E**) were adjusted to align the calculated frequency values (shown in the graphs as red vertical lines) with the experimental frequencies. The parametric optimization problem was solved using the fitting method. A perfect fit can only be achieved when the real geometric dimensions of the grinding wheels exactly match their modeled counterparts.

The frequencies coincide at a satisfactory level. The deviation of the calculated frequencies from the experimental values does not exceed 5 %. Consequently, the values of the integral elastic parameters, **ν** and **E**, were obtained for each grinding wheel considered:

1. *25A **F36** L* – **ν** = 0.25; **E** = 51.25 GPa;
2. *25A **F46** L* – **ν** = 0.215; **E** = 46 GPa;
3. *25A **F60** L* – **ν** = 0.18; **E** = 41.5 GPa;
4. *25A **F80** L* – **ν** = 0.17; **E** = 40 GPa;
5. *25A **F120** L* – **ν** = 0.16; **E** = 45.5 GPa;
6. *25A F60 **N*** – **ν** = 0.22; **E** = 48 GPa;
7. *25A F60 **P*** – **ν** = 0.225; **E** = 54 GPa;
8. *25A F60 **S*** – **ν** = 0.2; **E** = 67.5 GPa;
9. *14A F60 L* – **ν** = 0.25; **E** = 41.2 GPa;
10. *64C F60 L* – **ν** = 0.26; **E** = 43 GPa;
11. *92A F60 L* – **ν** = 0.27; **E** = 53 GPa.

Thus, although labor-intensive, this approach to determining **ν** and **E** is recognized as effective. The agreement between the calculated and experimental frequencies allows us to conclude that the simulated values of *Poisson's* ratio and *Young's* modulus of the grinding wheels correspond to those of their prototypes. Therefore, the main objective of this work has been achieved.

Currently, work is underway to develop a mathematical model of the sound pressure generated during grinding and a methodology for predicting the grinding wheel service life based on acoustic indices. This model requires taking into account the actual elasticity parameters of grinding wheels and establishing a relationship between these parameters and the wheels' characteristics.

The values of **ν** and **E** obtained during this study were used as parameters to develop a sound pressure model of the grinding process. Preliminary results show the model's qualitative agreement with, and adequacy to, the experimental acoustic data obtained during the grinding process study.

Dependence of integral elastic parameters on grinding wheel characteristics

The study of grinding wheels No. 1, No. 2, No. 3, No. 4, and No. 5 determined the influence of abrasive grain size on the elastic parameters, **ν** and **E**. *Poisson's* ratio decreases as the abrasive grain size decreases. *Young's* modulus decreases until the grain size reaches 0.2 mm; thereafter, the trend reverses and begins to increase. However, there is insufficient data to conclude whether the increase in *Young's* modulus will continue as the grain size is further reduced.

Fig. 6 shows graphs reflecting this dependence in terms of granularity versus *Poisson's* ratio and granularity versus *Young's* modulus. Next, regression equations and curves were obtained using *MS Excel*. The regression curves constructed from the experimental data are expressed by second-degree polynomial
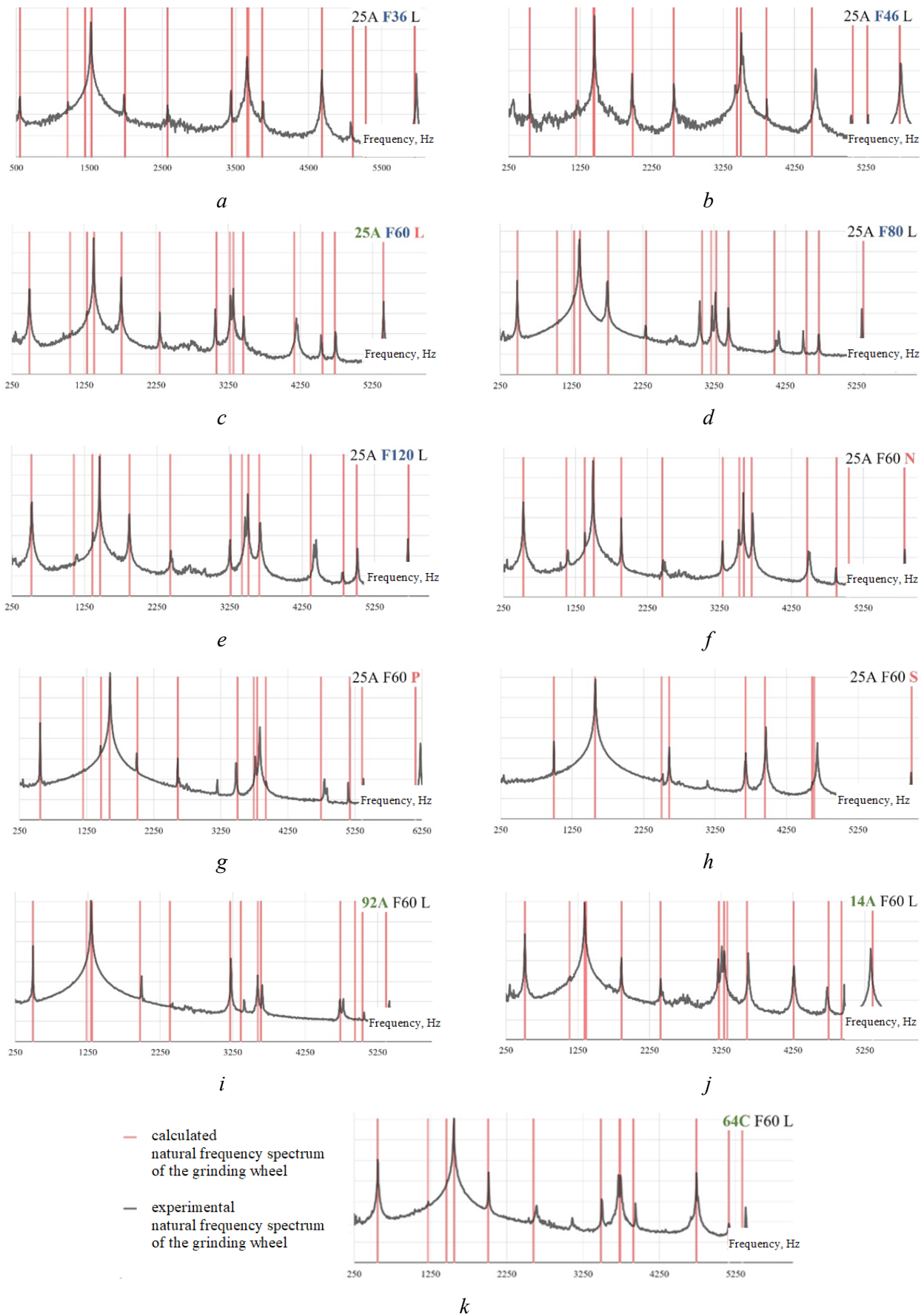
Fig. 5. Comparison of empirical and calculated spectral compositions of natural vibrations of grinding wheel:
*a – 25A **F36** L; b – 25A **F46** L; c – **25A F60 L**; d – 25A **F80** L; e – 25A **F120** L; f – 25A F60 **N**; g – 25A F60 **P**; h – 25A F60 **S**;*
*I – **14A** F60 L; j – **92A** F60 L; k – **64C** F60*
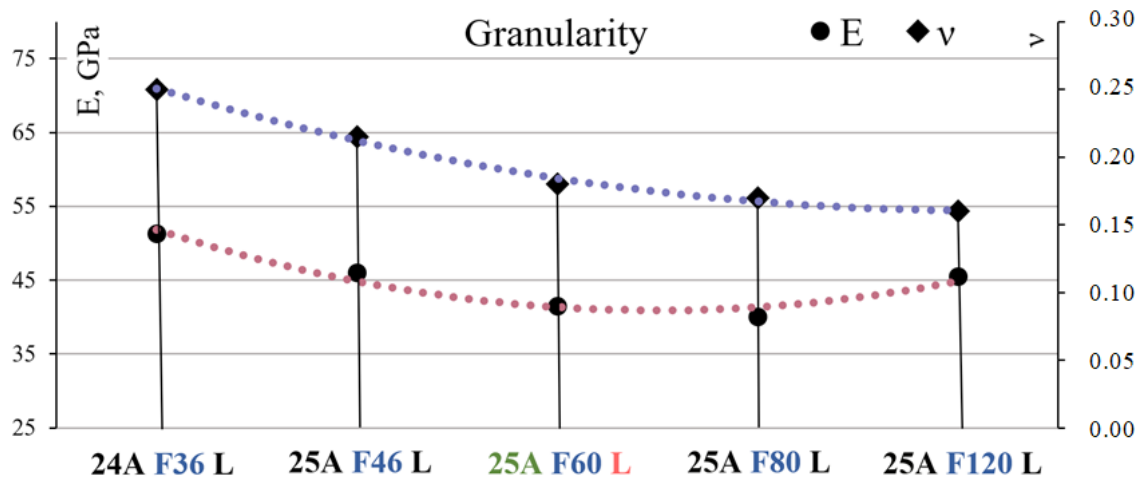
Fig. 6. Influence of grinding wheel grit on the value of *Poisson's* ratio and *Young's* modulus

dependencies with approximation reliability levels of $R^2 = 0.949$ for the *Young's* modulus dependency curve and $R^2 = 0.993$ for the *Poisson's* ratio dependency curve. This indicates a strong correlation between the values of **v**, *E* and the grain size factor.

$$v = 0.0054 \cdot x^2 - 0.054 \cdot x + 0.3 ; \qquad E = 1.75 \cdot x^2 - 12.25 \cdot x + 62.35 .$$

It should be noted that the obtained regression relations are not claimed to be universal and can only be applied under the conditions in which they were derived. For instance, the values of **v** and *E* can be determined for a grinding wheel with the following characteristics: an abrasive of white electrocorundum with a hardness grade of *L* and an average structure number of **6** on a ceramic bond. For a grinding wheel with a grit size of *F100* (grit size ranging from 0.15 to 0.11 mm), the values of *Poisson's* ratio and *Young's* modulus are 0.164 and 42.66 GPa, respectively.

Similarly, the effect of hardness on the elastic performance of grinding wheels has been established. An increase in grinding wheel hardness results in higher values of *Young's* modulus. *Young's* modulus characterizes the stiffness of the system and its ability to resist elastic deformation. This is reflected in the study of natural vibrations of a solid body. Grinding wheels with higher *E* values exhibit a shift of natural frequencies toward the high-frequency range (see Fig. 5).

The change in hardness of grinding wheels with the same structure is due to the redistribution of the proportions of the main components: grain, bond, and pores. An increase in hardness is promoted by a decrease in pore volume and an increase in bond volume. Therefore, it can be concluded that there is a positive correlation between hardness and stiffness, or between the characteristics of plastic and elastic deformation of the grinding wheel, as expressed by *Young's* modulus.

Poisson's ratio increases with hardness in the interval from *L* to *P*. After reaching a maximum value of 0.23, it begins to decrease. See fig. 7 for the graphs.

The obtained regression dependencies have approximation confidence levels close to unity ($R^2 = 0.9913$ for the *Young's* modulus curve and $R^2 = 0.999$ for the *Poisson's* ratio curve). Therefore, there is a strong correlation between the values of **v**, *E*, and the hardness factor.

$$v = -0.0162 \cdot x^2 + 0.0877 \cdot x + 0.109 ; \qquad E = 1.75 \cdot x^2 - 0.35 \cdot x + 40.5 .$$

These empirical regression models can be used to determine the values of **v** and *E* for white electrocorundum grinding wheels with an *F60* grain size and medium structure on a ceramic bond for several hardness grades: *K*, *M*, *O*, *R*, and *T*:
– *25A F60 K* has values **v** = 0.148; *E* = 40.76 GPa;
– *25A F60 M* has values **v** = 0.200; *E* = 43.91 GPa;
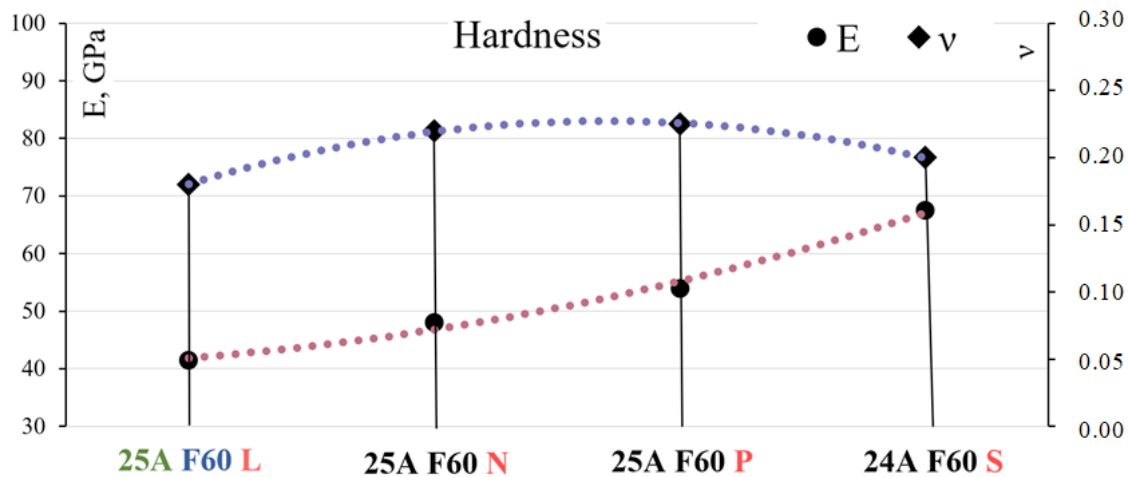
Fig. 7. Influence of grinding wheel hardness on the value of *Poisson's* ratio and *Young's* modulus

– *25A F60 **O*** has values **ν** = 0.227; ***E*** = 50.56 GPa;
– *25A F60 **R*** has values **ν** = 0.217; ***E*** = 60.713 GPa;
– *25A F60 **T*** has values **ν** = 0.175; ***E*** = 74.36 GPa.

Values of *Poisson's* ratio and *Young's* modulus were also obtained for grinding wheels made of normal electrocorundum, white electrocorundum, chromotitanium electrocorundum, and green silicon carbide (see fig. 8). Since the abrasive material of the grinding wheel cannot be quantified, regression analysis and the development of empirical relationships are not applicable in this case, unlike in the study of the effect of grain size and hardness on the elastic parameters of the tool. The values of **ν** and ***E*** in fig. 8 do not permit further applications or insights beyond what is obtained directly.
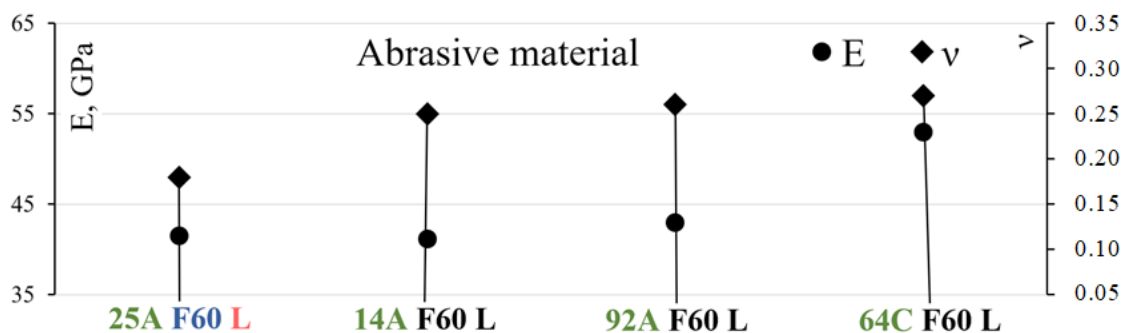
Fig. 8. Influence of abrasive material on the value *Poisson's* ratio and *Young's* modulus

Conclusion

1. The order of appearance of the eigenmodes of grinding wheel vibrations remains unchanged over a wide range of **ν** and ***E*** values. The lowest eigenmodes used for acoustic monitoring of grinding wheels are a pair of bending modes f_1, f_2 ($n = 2$, $s = 0$) and the bending mode f_3 ($n = 0$, $s = 1$).

2. In the absence of boundary conditions, modes f_1 and f_2 ($n = 2$, $s = 0$) contribute most significantly to the dynamics of grinding wheel vibrations along the *X* and *Y* coordinate axes. In the *Z* direction, the largest contribution is made by eigenmode f_3 ($n = 0$, $s = 1$); however, this contribution is much smaller than that of f_1 and f_2.

3. The values of *Poisson's* ratio and *Young's* modulus for the studied grinding wheels were determined by correlating the experimental and calculated spectral compositions of the natural frequency distributions. The values vary within the following ranges: $0.16 < \textbf{ν} < 0.27$ and 40 GPa $< \textbf{\textit{E}} < 67.5$ GPa. Grinding wheels with significantly different characteristics (e.g., *25A F80 L* and *25A F60 S*) may have slightly different

Poisson's ratio values ($\nu = 0.17$ and $\nu = 0.2$, respectively). This underscores the importance of accurately determining the integral elastic parameters of the tool to correctly model the sound pressure generated during the grinding process. Even a slight error in determining *Poisson's* ratio can lead to discrepancies between the modeled wheel's characteristics and its actual behavior.

4. Empirical regression dependencies of the integral elastic parameters of grinding wheels on abrasive grain size and hardness have been obtained with a high degree of reliability and accuracy.

References

1. Ardashev D.V., Zhukov A.S. Issledovanie spektral'nogo sostava svobodnykh akusticheskikh kolebanii shlifoval'nykh krugov na keramicheskoi svyazke [Research of spectral composition of natural acoustic vibrations of ceramic-bonded grinding wheels]. *Metalloobrabotka = Metalworking*, 2023, no. 1 (133), pp. 3–20. DOI: 10.25960/mo.2023.1.3. (In Russian).

2. Ardashev D.V., Zhukov A.S. Investigation of the relationship between the cutting ability of the tool and the acoustic signal parameters during profile grinding. *Obrabotka metallov (tekhnologiya, oborudovanie, instrumenty) = Metal Working and Material Science*, 2022, vol. 24, no. 4, pp. 64–83. DOI: 10.17212/1994-6309-2022-24.4-64-83. (In Russian).

3. Li C., Song Z., Huang X., Zhao H., Jiang X., Mao X. Analysis of dynamic characteristics for machine tools based on dynamic stiffness sensitivity. *Processes*, 2021, vol. 9 (12), art. 2260, pp. 1–16. DOI: 10.3390/pr9122260.

4. Xiao H., Hu X., Luo S., Li W. Developing and testing the proto type structure for micro tool fabrication. *Machines*, 2022, vol. 10 (10), art. 938, pp. 1–21. DOI: 10.3390/machines10100938.

5. Lin C.-Y., Luh Y.-P., Lin W.-Z., Lin B.-C., Hung J.-P. Modeling the static and dynamic behaviors of a large heavy-duty lathe machine under rated loads. *Computation*, 2022, vol. 10 (12), art. 207, pp. 1–18. DOI: 10.3390/computation10120207.

6. Chan T.-C., Chang C.-C., Ullah A., Lin H.-H. Study on kinematic structure performance and machining characteristics of 3-axis machining center. *Applied Sciences*, 2023, vol. 13 (8), art. 4742, pp. 1–29. DOI: 10.3390/app13084742.

7. Behera R., Chan T.-C., Yang J.-S. Innovative structural optimization and dynamic performance enhancement of high-precision five-axis machine tools. *Journal of Manufacturing and Materials Processing*, 2024, vol. 8 (4), art. 181, pp. 1–25. DOI: 10.3390/jmmp8040181.

8. Vázquez C.R., Guajardo-Cuéllar A. Prediction of vertical vibrations of a CNC router type geometry. *Applied Sciences*, 2024, vol. 14 (2), art. 621, pp. 1–23. DOI: 10.3390/app14020621.

9. Chi Y., Dai W., Lu Z., Wang M., Zhao Y. Real-time estimation for cutting tool wear based on modal analysis of monitored signals. *Applied Sciences*, 2018, vol. 8 (5), art. 708, pp. 1–13. DOI: 10.3390/app8050708.

10. Nie W., Zheng M., Xu S., Liu Y., Yu H. Stability analysis and structure optimization of unequal-pitch end mills. *Materials*, 2021, vol. 14 (22), art. 7003, pp. 1–13. DOI: 10.3390/ma14227003.

11. Wang J., Qian J., Huang K., Shang Z., Yu J. Chatter and surface waviness analysis in Oerlikon face hobbing of spiral bevel gears. *Aerospace*, 2024, vol. 11 (7), art. 535, pp. 1–25. DOI: 10.3390/aerospace11070535.

12. Mladjenovic C., Monkova K., Zivkovic A., Knezev M., Marinkovic D., Ilic V. Experimental identification of milling process damping and its application in stability lobe diagrams. *Machines*, 2025, vol. 13 (2), art. 96, pp. 1–24. DOI: 10.3390/machines13020096.

13. Nowakowski L., Blasiak S., Skrzyniarz M., Rolek J. Experimental-analytical method for determining the dynamic coefficients of turning tools. *Materials*, 2025, vol. 18 (3), art. 563, pp. 1–15. DOI: 10.3390/ma18030563.

14. Ovchinnikov A.I. Materialy dlya abrazivnogo instrumenta. Obzor [Materials for an abrasive tool. Review]. *Nauka i obrazovanie = Science and Education*, 2013, no. 7, pp. 41–68, DOI: 10.7463/0713.0577449. (In Russian).

15. Abyzov A.M. Oksid alyuminiya i alyumooksidnaya keramika (Obzor). Ch. 1. Svoistva Al_2O_3 i promyshlennoe proizvodstvo dispersnogo Al_2O [Aluminum oxide and alumina ceramics (Review). Part 1. Properties of Al_2O_3 and industrial production of dispersed Al_2O_3]. *Novye ogneupory = New Refractories*, 2019, no. 1, pp. 16–23. DOI: 10.17073/1683-4518-2019-1-16-23.

16. Zhang H., Jiao F., Niu Y., Li C., Zhang Z., Tong J. Design and experimental study of longitudinal-torsional composite ultrasonic internal grinding horn. *Micromachines*, 2023, vol. 14 (11), art. 2056, pp. 1–17. DOI: 10.3390/mi14112056.

17. Li F., Chen Y., Zhu D. Revealing the sound transmission loss capacities of sandwich metamaterials with re-entrant negative Poisson's ratio configuration. *Materials*, 2023, vol. 16 (17), art. 5928, pp. 2–21. DOI: 10.3390/ma16175928.

18. Zhang Y., Tu H., Wang Y., Xu G., Gao D. A normal mode model based on the spectral element method for simulating horizontally layered acoustic waveguides. *Journal of Marine Science and Engineering*, 2024, vol. 12 (9), art. 1499, pp. 1–16. DOI: 10.3390/jmse12091499.

19. Wang Y., Zhao D., Jia Y., Wang S., Du Y., Li H., Zhang B. Acoustic sensors for monitoring and localizing partial discharge signals in oil-immersed transformers under array configuration. *Sensors*, 2024, vol. 24 (14), art. 4704, pp. 1–24. DOI: 10.3390/s24144704.

20. Dai Y., Li S., Feng M., Chen B., Qiao J. Fundamental study of phased array ultrasonic cavitation abrasive flow polishing titanium alloy tubes. *Materials*, 2024, vol. 17 (21), art. 5185, pp. 1–19. DOI: 10.3390/ma17215185.

21. Yuganov V.S. *Ispol'zovanie nizkochastotnykh akusticheskikh kolebanii dlya tekushchego kontrolya protsessa shlifovaniya*. Diss. kand. tekhn. nauk [Use of low-frequency acoustic oscillations for current control of the grinding process. PhD eng. sci. diss.]. Ul'yanovsk, 1999. 198 p.

22. Glagovskii B.A., Moskovenko I.B. *Nizkochastotnye akusticheskie metody kontrolya v mashinostroenii* [Low-frequency acoustic control methods in mechanical engineering]. Leningrad, Mashinostroenie Publ., 1977. 203 p.

23. Smirnov V.A., Nanasov M.P. [Calculation of frequencies and forms of vibrations of a round plate]. *Perspektivy razvitiya stroitel'nykh konstruktsii* [Prospects of building structures development]. Materials of scientific-practical conference. Leningrad, LDNTP Publ., 1987, pp. 68–72. (In Russian).

24. Ivanov V.P. *Kolebaniya rabochikh koles turbomashin* [Vibrations of turbomachine impellers]. Moscow, Mashinostroenie Publ., 1983. 224 p.

25. Makaeva R.Kh., Karimov A.Kh., Tsareva A.M. Issledovanie rezonansnykh kolebanii diskov s primeneniem golograficheskoi interferometrii [Research of resonance vibrations of discs with application of holographic interferometry]. *Vestnik dvigatelestroeniya = Herald of Aeroenginebuilding*, 2012, no. 2, pp. 161–165.

26. Tsareva A.M. *Eksperimental'no-raschetnyi metod opredeleniya rezonansnykh chastot i form kolebanii detalei tipa diskov s primeneniem golograficheskoi interferometrii*. Avtoref. diss. kand. tekhn. nauk [Experimental-calculation method of determination of resonance frequencies and vibration forms of disc-type parts using holographic interferometry. Author's abstract of PhD eng. sci. diss.]. Kazan', 2007. 20 p.

27. Vázquez M., López V., Campos R., Cadenas E., Marin P. Structural and modal analysis of a small wind turbine blade considering composite material and the IEC 61400-2 standard. *Energies*, 2025, vol. 18 (3), art. 566, pp. 1–26. DOI: 10.3390/en18030566.

Conflicts of Interest

The authors declare no conflict of interest.

Obrabotka metallov –
Metal Working and Material Science

Journal homepage: http://journals.nstu.ru/obrabotka_metallov

Numerical and experimental investigation of heat transfer augmentation in roughened pipes

Siddhanath Nishandar [1, a], *Ashok Pise* [1, b], *Pramodkumar Bagade* [2, c, *]

[1] Department of Mechanical Engineering, Government College of Engineering, Karad, Shivaji University, Kolhapur, Maharashtra 445414, India

[2] Department of Mechanical Engineering, TSSM's Bhivarabai Sawant College of Engineering and Research (BSCOER), Narhe, Pune, Maharashtra 445414, India

[a] https://orcid.org/0000-0001-6190-3412, ✉ siddhant.nishandar04@gmail.com; [b] https://orcid.org/0009-0003-0276-8996, ✉ ashokpise@gmail.com; [c] https://orcid.org/0000-0002-4069-1542, ✉ pramodbagade@gmail.com

ARTICLE INFO

ABSTRACT

Introduction. In many technical applications, such as thermal energy systems, chemical processing, power production, and *HVAC*, efficient heat transfer (*HT*) is essential. Research on improving *HT* performance in circular pipes is still crucial, especially when it comes to changes that cause thermal boundary layers to be disrupted and turbulence to grow. **Purpose of the work:** The purpose of this work is to thoroughly examine how convective heat transfer can be improved in circular pipes with purposefully roughened surfaces. It focuses on how surface roughness, flow pulsations, *Reynolds* number (*Re*), and heat flow rate (*Q*) affect thermal performance. **Methods of investigation.** A combination of experimental and numerical methods is employed to assess the thermo-fluid dynamics inside the pipe. Lab-scale experiments and computational fluid dynamics (*CFD*) simulations are used to investigate temperature distribution, velocity and pressure fields, turbulent kinetic energy (*TKE*), vorticity, eddy viscosity, local heat transfer coefficient (*h*), and *Nusselt* number (*Nu*). Additionally, sinusoidal pulsations are introduced at the inlet and the outlet, with regular oscillations in frequency (*f*) and amplitude (*A*), over a turbulent flow range ($6,753 \leq Re \leq 31,000$). **Results and discussion.** The results show that surface roughness enhances *HT* by significantly increasing turbulence and disrupting the thermal boundary layer. *TKE* becomes a significant factor when there is a strong correlation between higher *HT* coefficients and rising turbulence intensity. *HT* performance is further improved by introducing flow pulsations; downstream pulsation increases *Nu* by 20–22% and upstream pulsing by 16–19%. The outcomes demonstrate how effectively controlled flow pulsations and surface roughness combine to optimize heat transfer. This collaborative approach holds great potential for compact and highly efficient thermal system designs in industrial environments.

Introduction

To improve heat exchanger performance while lowering size and operating costs, several tactics have been investigated. These tactics are typically divided into two categories: passive and active. Passive methods – such as the use of finned or spirally roughened tubes – decrease the thickness of the thermal boundary layer and improve heat transfer (*HT*) by creating turbulence close to the tube wall. In recent years, these methods have drawn more attention. Active approaches, on the other hand, make use of external energy sources and include strategies like fluid pulsation, jet impingement, mechanical vibration, and the use of electrostatic fields to boost HT efficiency.

* Corresponding author
Bagade Pramodkumar M., Ph.D. (Aerospace Engineering), Professor
Department of Mechanical Engineering,
TSSM's Bhivarabai Sawant College of Engineering and Research (BSCOER),
Narhe, Pune,
445414, Maharashtra, India
Tel.: +91 9075279575, **e-mail:** pramodbagade@gmail.co

Concentrated temperature gradients can disrupt the boundary layer in both laminar and turbulent regimes, lowering thermal resistance and raising the local heat transfer coefficient, particularly in the presence of forced convection. Pulsating flow, in particular, is essential for modifying shear forces, boundary layer characteristics, and overall thermal resistance to improve HT. Consequently, there is currently significant interest in studying how pulsating flow affects convective heat transfer.

Natural pulsating flows are found in many engineering systems, including:

– eddy turbulence - chaotic disturbances inherent in turbulent flow, leading to fluctuations in velocity and pressure.

– turbomachinery - periodic variations in pressure and velocity at the compressor and turbine blades, caused by rotor rotation and flow interaction with the blades.

– transient flows - changes caused by fluctuations in the system's operational parameters.

Practical applications of pulsating flows also include:

– reciprocating internal combustion engines - intake and exhaust systems characterized by periodic flow variations due to the engine's operating cycles.

– gas turbine engines - flow oscillations caused by surge conditions.

– positive displacement pumps: the operating principle of these pumps is based on generating pulsating flow.

– human respiration - airflow that spontaneously pulsates as part of human breathing.

Although pulsating flows are sometimes perceived as undesirable disturbances, they can also enhance processes such as fuel-air mixing in combustion systems. The findings presented in the literature vary: some research indicates that heat transfer (*HT*) has improved, while others indicate that it has not improved at all or has even decreased. Important factors affecting heat transfer include surface geometry, pulsation location, *Reynolds* number (***Re***), *Prandtl* number (***Pr***), pulsation frequency (***f***), and amplitude (***A***).

Description of the problem

The heat transfer (*HT*) mechanisms in pulsating flow over roughened surfaces have not yet been fully clarified by previous studies, which are often limited to narrow parameter ranges. More research is required to determine how the placement of the pulsation source, surface roughness patterns, *Reynolds* number (***Re***), and pulsation frequency affect turbulent flow and heat transfer characteristics.

Objectives

The present study is conducted with the following objectives:

1. Investigate the effects of various factors affecting pulsating flow experimentally and numerically.
2. Establish empirical correlations based on the observed flow dynamics.
3. Analyze the effects of pulsation orientation on heat transfer.
4. Examine the differences between the performance of pulsating flow and steady-state flow.

The scope and importance of the study

Convective heat transfer is crucial for many engineering systems. Even though oscillatory flow has shown promise in enhancing heat transfer (HT), there is currently a scarcity of research on its application in thermal systems, specifically within pipe walls. Understanding the thermo-hydrodynamics of pulsating flow is crucial because higher HT leads to higher efficiency. This work fills that gap by focusing on circular pipes under sinusoidal pulsation. Future research will examine other pipe geometries and pulsation types that were not covered in this study.

Pulsating flow heat transfer (*HT*) is essential to many industrial sectors, including thermoelectric and nuclear power [5, 6], food processing [7], pharmaceuticals [8], smart buildings [9], *HVAC* [10], transportation [11], agriculture [12], petrochemicals [13], material handling [14], bulk manufacturing [15], and many more. Increased HT efficiency has led to improvements in heat exchanger design, such as the use of innovative channel forms and compact tubing. Without sacrificing functionality, these developments raise volumetric power density and use less material. *Rowin et al.* investigated *HT* prediction

on uneven surfaces [16]. *Qu et al.* [17] demonstrated that internal capillary tube roughness significantly improves startup and operational stability in micro-pulsating heat pipes (*PHPs*). Surface tension, fluid viscosity, and wall roughness all affect flow resistance, which limits stable pulse operation in fixed-diameter *PHPs* [18].

Singh et al. [19] investigated ordered roughness and pulsed flow in microchannels using 2*D* simulations. Due to enhanced vortex activity, pulsation raised the *Nusselt* number (*Nu*) by up to 32.76% regardless of roughness. They also found that the optimal pulsation frequency varies with hydraulic diameter and that rough walls result in larger pressure decreases, even with heat transfer (*HT*) improvements. *Wu* and *Cheng* [20] discovered *Nu* fluctuations in shape-variable trapezoidal silicon microchannels. In water-filled minichannels, *Lin et al.* [21] discovered that roughness heights between 18 and 96 μm improved HT. *Lu et al.* [22] confirmed that roughness raised flow resistance and *Nu* in laminar microchannel flows. *Croce et al.* [23] showed that roughness shape has a greater effect on pressure drop than *Nu*. Despite extensive research on pulsating flow dynamics, heat transfer (HT) mechanisms remain incompletely understood [24–32]. Analytical and numerical investigations in laminar flow [33–37] demonstrate localized *HT* effects, with pulsation-induced *Nu* fluctuations being dominant near the pipe entrance and decreasing downstream.

Despite extensive research on pulsating flow dynamics, the underlying heat transfer (*HT*) mechanisms remain incompletely understood [24–32]. Analytical and numerical investigations in laminar flow regimes [33–37] demonstrate localized HT effects, wherein pulsation-induced *Nu* fluctuations are most pronounced near the pipe entrance and diminish in the downstream direction.

Methodology

Fig. 1 shows the experimental setup. A copper pipe, 400 mm in length and 28 mm in diameter, serves as the test section. Flexible joints hold it in place at both ends. Four *K*-type thermocouples are embedded in axial grooves on the outer surface of the pipe and connected to a multichannel recorder via a multipoint switch to record temperature measurements. A 400 mm long nickel-chromium heater (resistivity = = 15.5 Ω/m) provides uniform heat input. Airflow is provided by a 1.5 HP centrifugal blower (800 CFM), selected for its ability to maintain turbulent flow conditions. An electrically operated solenoid valve introduces flow pulsations. Operational boundaries are influenced by static pressure, temperature rise, and *Reynolds* number (*Re*).

A flow control valve (¾" brass valve, 12V DC, 1.5 A/18 W, orifice size 25 mm, normally closed, stainless steel components), as shown in Fig. 2, is used to regulate airflow with a sub-second response time. The valve allows for adjustment of the pulsation mechanism to provide the required amplitude and frequency of pulsation.
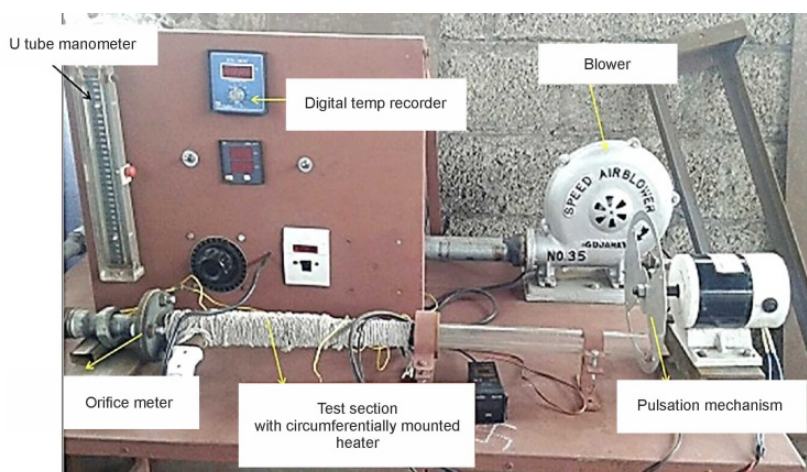
Fig. 1. Experimental set up

Fig. 2. Flow control valve

Numerical Simulation Approach

ANSYS Fluent was used for the simulations. The governing equations were the *3D Navier-Stokes* equations (Eqs. 1–6), which incorporate eddy viscosity (μ_t), strain rate (E_{ij}), and velocity components (u_i). Energy transport was governed by Eq. (7). The friction factor and theoretical *Nusselt* number (*Nu*) were determined using Eq. (8) and the *Dittus-Boelter* correlation (Eq. 9) [38–41].

$$\frac{\partial p}{\partial t} + \frac{\partial(\rho u)}{\partial x} + \frac{\partial(\rho v)}{\partial y} + \frac{\partial(\rho w)}{\partial z} = 0 \tag{1}$$

$$u\frac{\partial u}{\partial x} + v\frac{\partial u}{\partial y} + w\frac{\partial u}{\partial z} = -\frac{1}{\rho}\frac{\partial p}{\partial x} + \mu\left(\frac{\partial^2 u}{\partial x^2} + \frac{\partial^2 u}{\partial y^2} + \frac{\partial^2 u}{\partial z^2}\right) \tag{2}$$

$$u\frac{\partial v}{\partial x} + v\frac{\partial v}{\partial y} + w\frac{\partial v}{\partial z} = -\frac{1}{\rho}\frac{\partial p}{\partial y} + \mu\left(\frac{\partial^2 v}{\partial x^2} + \frac{\partial^2 v}{\partial y^2} + \frac{\partial^2 v}{\partial z^2}\right) \tag{3}$$

$$u\frac{\partial w}{\partial x} + v\frac{\partial w}{\partial y} + w\frac{\partial w}{\partial z} = -\frac{1}{\rho}\frac{\partial p}{\partial z} + \mu\left(\frac{\partial^2 w}{\partial x^2} + \frac{\partial^2 w}{\partial y^2} + \frac{\partial^2 w}{\partial z^2}\right) \tag{4}$$

$$\frac{\partial p(\rho k)}{\partial t} + \frac{\partial(\rho k u_i)}{\partial x_i} = \frac{\partial}{\partial x_j}\left[\frac{\mu_t}{\sigma_k}\frac{\partial k}{\partial x_j}\right] + 2\mu_t E_{ij}E_{ij} - \rho\varepsilon \tag{5}$$

$$\frac{\partial p(\rho k\varepsilon)}{\partial t} + \frac{\partial(\rho\varepsilon u_i)}{\partial x_i} = \frac{\partial}{\partial x_j}\left[\frac{\mu_t}{\sigma_s}\frac{\partial\varepsilon}{\partial x_j}\right] + C_{1s}\frac{\varepsilon}{k}2\mu_t E_{ij}E_{ij} - C_{2s}\rho\frac{\varepsilon^2}{k} \tag{6}$$

$$\frac{\partial}{\partial x}\left(k\frac{\partial T}{\partial x}\right) + \frac{\partial}{\partial y}\left(k\frac{\partial T}{\partial y}\right) + \frac{\partial}{\partial z}\left(k\frac{\partial T}{\partial z}\right) + q_v = \rho C_p\frac{\partial T}{\partial t} \tag{7}$$

$$f = \frac{\Delta P}{\dfrac{(L/D)\rho V^2}{2}}; \qquad V = \frac{\dot{m}}{\rho\pi D^2/4} \tag{8}$$

$$Nu = 0.023Re^{0.8}Pr^{0.4} \tag{9}$$

Mesh Generation

Mesh quality significantly impacts accuracy. A near-orthogonal grid with $y^+ = 0.5$ (spacing $y = 1.3628\times10^{-5}$) ensures accurate wall resolution [42]. The structured mesh consisted of 1,283,136 nodes. Fig. 3 shows a cross-sectional view of the mesh. Velocity inlet conditions included a constant uniform profile for validation and a sinusoidal pulsing profile for dynamic cases, as defined by $V = U_0[1 + A\sin(2\pi ft)]$, where A denotes amplitude, f frequency, t time, and U_0 mean velocity. A heat flux was applied at the wall, and a pressure outlet condition was established at the pipe exit.

Fig. 3. Meshing at the cross section

Boundary Conditions

The following boundary conditions were applied:

1. A pulsating velocity profile was imposed at the inlet using a user-defined function for sinusoidal velocity input.

2. A constant heat flux boundary condition was applied to the pipe wall.

3. A pressure outlet boundary condition was applied at the pipe exit.

The **k-ε** turbulence model was used to resolve turbulence effects.

Validation

The present study was validated against the results of *Elshafie et al.* [43], who investigated pulsating turbulent flow ($10{,}000 \leq$ **Re** $\leq 40{,}000$; 6.6–68 Hz) in heated pipes. Numerical accuracy was confirmed by Fig. 4, which demonstrates excellent agreement in the average *Nusselt* number (**Nu**) between the present simulations and those of *Elshafie et al.*

Fig. 5 depicts the transient variations in the surface heat transfer coefficient (**h**). The fluctuations stabilize after **t** = 2.5 s; therefore, **t** = 6 s was deemed sufficient for steady-state calculations. In all cases, **h** increases with **Re**.
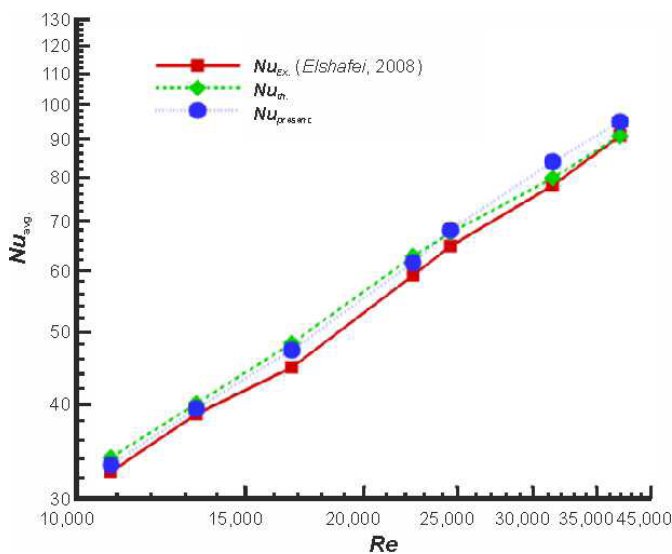
Fig. 4. Comparison of the average *Nusselt* number with the theoretical and experimental results of *Elshafie* [43]
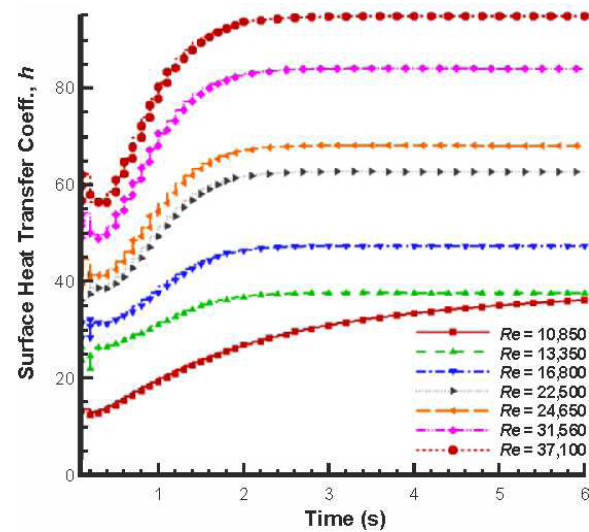
Fig. 5. Surface *HT* coefficient (**h**) obtained for different **Re**

Effects of Surface Roughness

Surface roughness enhances heat transfer (*HT*) by disrupting the thermal boundary layer [44], although it also increases pressure drop [45, 46]. Due to the complexity of the phenomena, extensive experimental research is required [47]. *MacDonald et al.* [48] demonstrated the impact of roughness on drag using direct numerical simulation (*DNS*) across sinusoidal surfaces ($k^+ = 10$, $\lambda = 0.05$–0.54). *Meyer et al.* [49] reported that roughness increases *HT* in laminar flow but has a negligible influence in turbulent regimes. *Abdelfattah et al.* [56] investigated 48-element impinging jets with hemispherical, droplet, and cylindrical roughness elements; cylinders enhanced *HT*, while droplets reduced drag.

Wall roughness affects momentum and energy transport [57]. Investigations of roughened pipes indicate that the log-law behavior is altered by a roughness function f_r, based on the roughness height **Ks+**. Equation (10) is used to account for roughness in the velocity profile, where **k** = 0.4187 (*von Karman* constant). *ANSYS Fluent* classifies hydrodynamically smooth, transitional, and completely rough regimes based on the *Cebeci-Bradshaw* method, using **ΔB** and **Ks+**.

$$\frac{u_p u^*}{\tau_w / \rho} = \frac{1}{k} \ln\left(E \frac{\rho u^* y_p}{\mu} \right) - \Delta B \tag{10}$$

Results and Discussion

Elshafie et al. [43] experimentally studied pulsating turbulent airflow in a heated pipe under constant heat flux, a configuration relevant to modern industrial heat transfer applications. They examined pulsation frequencies ranging from 6.6 to 68 Hz and *Reynolds* numbers (**Re**) from 10,000 to 40,000. Their findings demonstrated that the *Nusselt* number (**Nu**) was significantly influenced by both Re and frequency (**f**), particularly in the entrance region, where changes were more pronounced than in the fully developed zone. The downstream position of the oscillator near the pipe exit affected the distribution of local heat transfer (*HT*).

In this study, analogous investigations were conducted for **Re** = 13,350 to 37,100. Centerline velocity and total pressure increased with increasing **Re**, while the wall surface temperature decreased. These results are summarized in Table 1, which demonstrates that turbulent kinetic energy (*TKE*) and vorticity consistently increase with **Re**. Fig. 6 shows velocity profiles for **Re** = 37,100 under upstream pulsation, downstream pulsation, and no pulsation (*A* = 0.2, *f* = 6.7). The pulsing cases exhibit only slight variations in vorticity and lower velocities compared to the baseline (no pulsation) case. These patterns indicate that while pressure, velocity, *TKE*, and ω increase with increasing **Re**, surface temperature decreases. Consequently, **h** and **Nu** increase with **Re**, supporting the validity of the numerical method and exhibiting good agreement with theoretical and experimental findings from *Elshafie et al.* [43].

Table 1

Flow properties for various *Re* values

Re	V_{mean} (m/s)	V_{max} (m/s)	T_{max} (K)	Press. (Pa)	*TKE*	ω (s^{-1})
10,850	7.1313	10.3	329	115	1.15	1.000
13,350	8.7745	12.5	325	160	1.6	1.250
16,800	11.0420	15.6	322	255	2.7	1.600
22,500	14.7885	20.8	320	465	5	2.100
24,650	16.2016	22.6	318	552	6	2.300
31,560	20.7433	28.8	316	925	10	2.800
37,100	24.3846	33	314.2	1.300	15	3.200

a   *b*
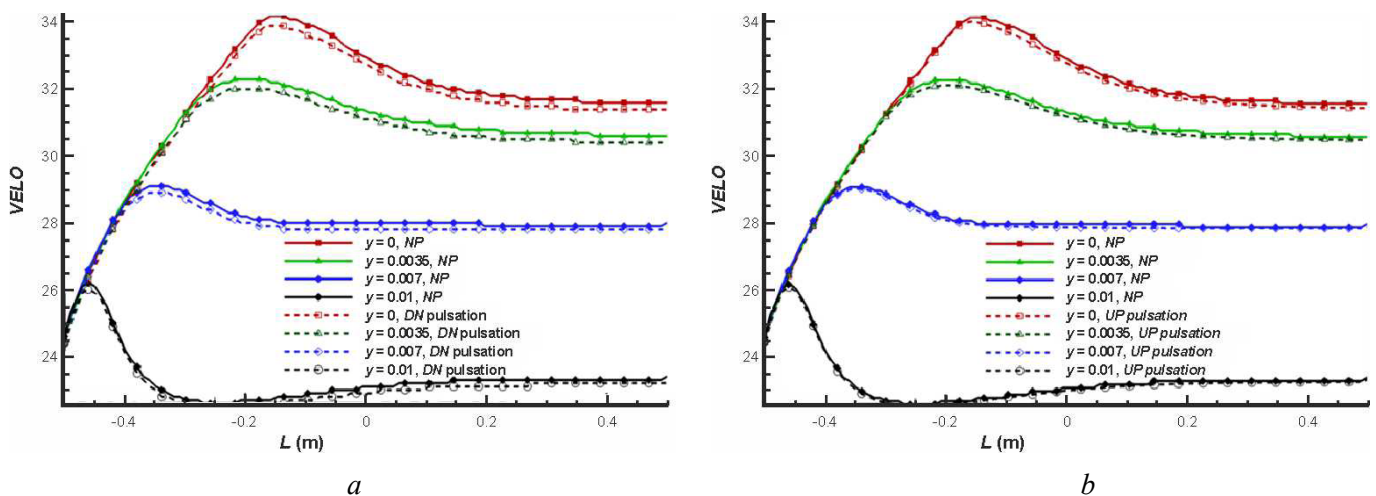
Fig. 6. Comparison of velocity (*V*) profiles along the pipe length for **Re** = 37,100, under steady-state (without pulsations) and pulsating flow conditions (*A* = 0.2, *f* = 6.7):

a – DN pulsation = downstream pulsation; *b* – UP pulsation = upstream pulsation

Effect of location of pulsation

This section reports the effects of pulsation location. Two cases were considered:
– pulsation located downstream of the flow.
– pulsation located upstream of the flow.

Pulsation located at the downstream of the flow

Fig. 7 illustrates the increase in the mean heat transfer (*HT*) coefficient with increasing **Re** and heat input (**Q**). The enhancement ranges from 20% to 27% at **f** = 3.33 Hz and **Q** = 100 W, and from 30% to 36% at **f** = 1 Hz. Tables 2 and 3 present values of h and **Nu** for various **Re** and **Q** without pulsation. As **Re** and **Q** increase, **Nu** increases steadily, indicating improved *HT* performance.

Fig. 7. Heat transfer as a function of **Re** at varying heat input, with pulsation frequencies of **f** = 1 Hz and **f** = 3.33 Hz at downstream pulsation
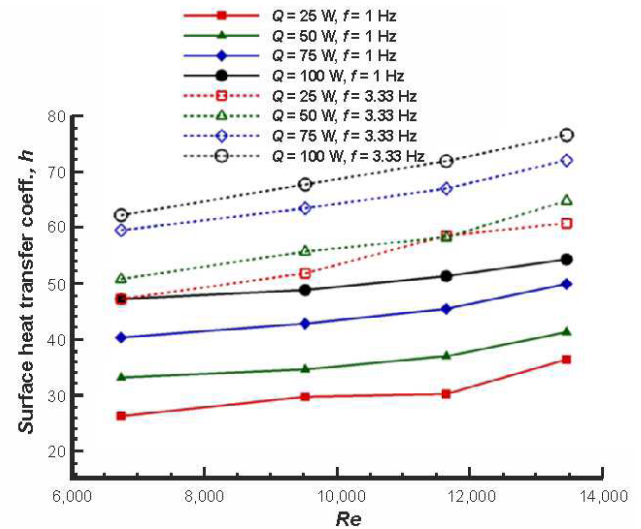
Table 2

Surface HT coefficient (*h*) at different *Re* and heat input without pulsation

Experimental heat transfer coefficient, *h*				
Re	*Q* = 25 W	*Q* = 50 W	*Q* = 75 W	*Q* = 100 W
6,753	22.1	33.04	40.25	47.13
9,504	27.92	34.48	42.77	48.74
11,618	32.11	36.88	45.4	51.26
13,414	35.53	41.19	49.89	54.29

Table 3

Variations in *Nu* with *Re* at different heat input without any pulsation

Nusselt number, *Nu*				
Re	*Q* = 25 W	*Q* = 50 W	*Q* = 75 W	*Q* = 100 W
6,753	23.43	31	37	44
9,504	29.59	32	40	45
11,618	34.04	34	42	48
13,414	37.66	38	46	50

Nu demonstrably improves with increasing heat input. The findings indicate that as *Re* and heat input increase, the mean heat transfer coefficient (h_{mean}) also increases. At f = 1 Hz, a 17–23% increase in the heat transfer (*HT*) coefficient is observed at *Q* = 100 W.

Pulsation located at the upstream of the flow

Similarly, upstream pulsation enhances heat transfer (*HT*) as *Re* and *Q* increase. At *Q* = 100 W and f = 1 Hz, the *HT* enhancement ranges from 22% to 26%, while at f = 3.33 Hz, it ranges from 29% to 33%. The generally higher *Nu* values observed under downstream pulsation, as shown in Tables 4 and 5, suggest its superior *HT* effect.

Table 4

Nu at different heat inputs with pulsation frequency, f = 1Hz and 3.33Hz when pulsating mechanism is mounted downstream

Reynolds **number**	Nusselt number, Nu							
	f = 1.0 Hz				*f = 3.33 Hz*			
Re	**25 W**	**50 W**	**75 W**	**100 W**	**25 W**	**50 W**	**75 W**	**100 W**
6,753	31	34	40	46	44	47	55	58
9,504	33	35	43	49	48	52	62	67
11,618	36	38	47	51	54	54	62	67
13,414	42	45	51	55	56	60	67	71

Table 5

HT Coefficient vs. Reynolds Number at Various Heat Inputs for Pulsation Frequencies f=1Hz and 3.33 Hz when pulsating mechanism is mounted upstream

Reynolds **number**	*Nusselt number, Nu*							
	f = 1.0 Hz				*f = 1.0 Hz*			
Re	**25 W**	**50 W**	**75 W**	**100 W**	**25 W**	**50 W**	**75 W**	**100 W**
6,753	26	32	38	44	37	42	48	54
9,504	29	34	40	47	41	43	53	56
11,618	29	35	43	49	44	48	56	60
13,414	34	39	48	52	52	53	61	63

Effects of pulsation frequency

Table 6 shows that increasing the pulsation frequency (*f*) from 1 Hz to 3.33 Hz significantly increases the experimental heat transfer coefficient ($h_{expt.}$) and the experimental Nusselt number ($Nu_{expt.}$). For instance, at *Re* = 6753 during downstream pulsation, $h_{expt.}$ rises from 32.91 to 47.15, and $Nu_{expt.}$ rises from 30.96 to 44.36. Similarly, at *Re* = 13,414 and f = 3.33 Hz, $h_{expt.}$ and $Nu_{expt.}$ reach 60.75 and 57.15, respectively.

Figs. 8, *a–d* illustrate the relationship between the *Reynolds* number (*Re*), heat input (*Q* = 25 W and 100 W), pulsation frequency (1 Hz, 3.33 Hz), pulsation location (upstream, downstream), the surface heat transfer coefficient (*h*), and the *Nusselt* number (*Nu*). Higher *Re* improves heat transfer at both heat inputs. In all cases, the 3.33 Hz pulsation produces the highest *h* and *Nu* values, particularly with downstream pulsation. Downstream pulsation consistently outperforms upstream pulsation. Both frequency and *Re* enhance thermal performance, with more pronounced effects at higher heat inputs (100 W). These trends indicate that pulsation settings are crucial for optimizing heat transfer.

Experimental HT Coefficient and *Nu* for Different *Re*s and Frequencies
for *Q* = 25 *W*. *DS*= downstream; *US*=upstream

Reynolds number	$h_{expt.}$				$Nu_{expt.}$			
	f = 1.0 Hz		*f = 3.33 Hz*		*f = 1.0 Hz*		*f = 3.33 Hz*	
Re	DS	US	DS	US	DS	US	DS	US
6753	32.91	28.21	47.15	39.99	30.96	26.54	44.36	37.62
9504	35.9	30.97	51.79	43.88	33.77	29.13	48.72	41.28
11618	38.53	31.59	58.5	47.15	36.25	29.72	55.03	44.36
13414	45.13	36.31	60.75	56.41	42.46	34.16	57.15	53.07
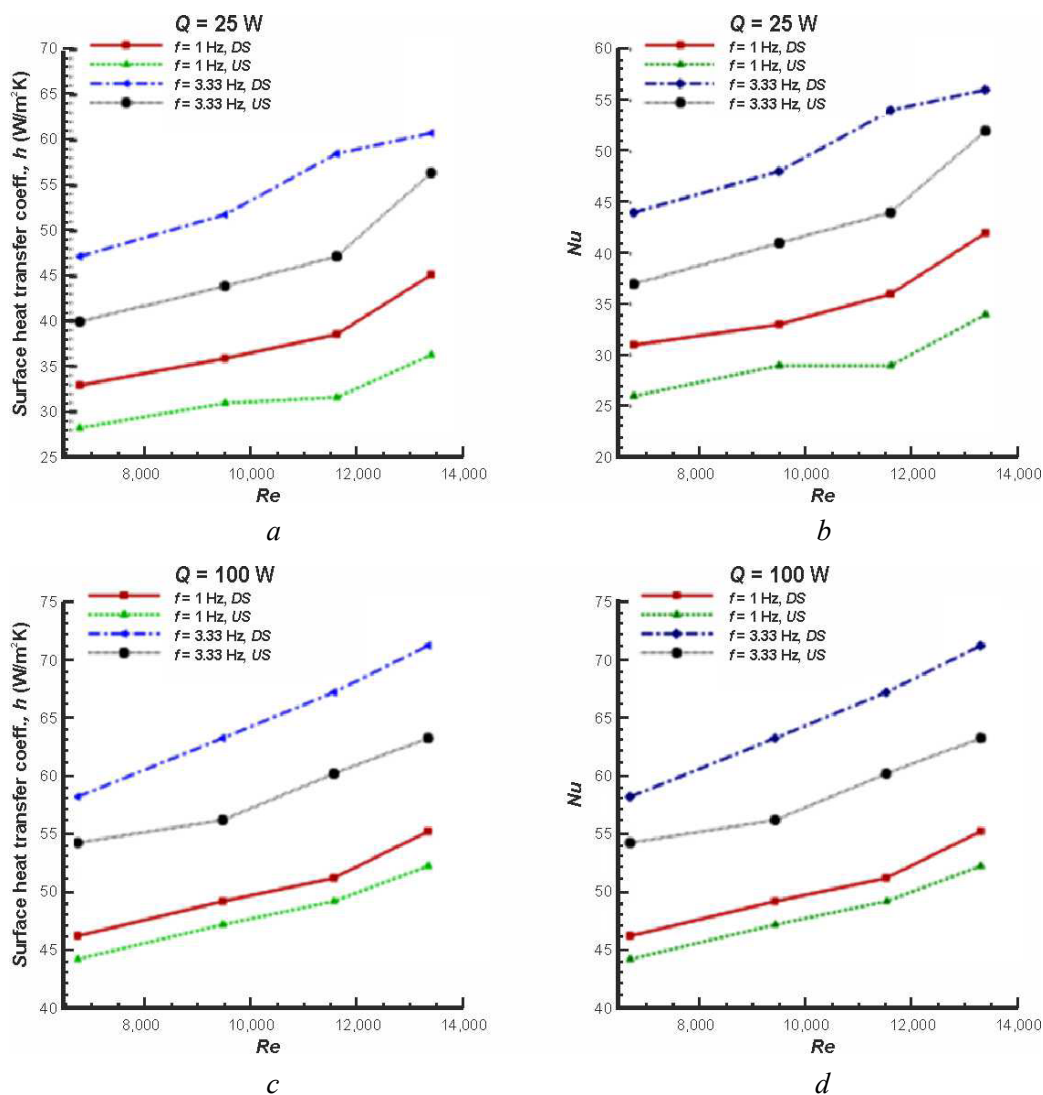
Fig. 8. Changes in *Nu* and *h* values as a function of *Re* for various pulsation
frequencies at heat inputs of *Q* = 25 W and *Q* = 100 W

Numerical Results

Although the heat transfer (*HT*) coefficients and *Nusselt* number (*Nu*) values are derived from experiments, simulations provide a better understanding of the influencing flow mechanics. Fig. 9 displays vorticity contours under upstream pulsation for *Re* = 6753, *Q* = 954 W/m², *A* = 0.1, and *f* = 1 Hz. Shear-
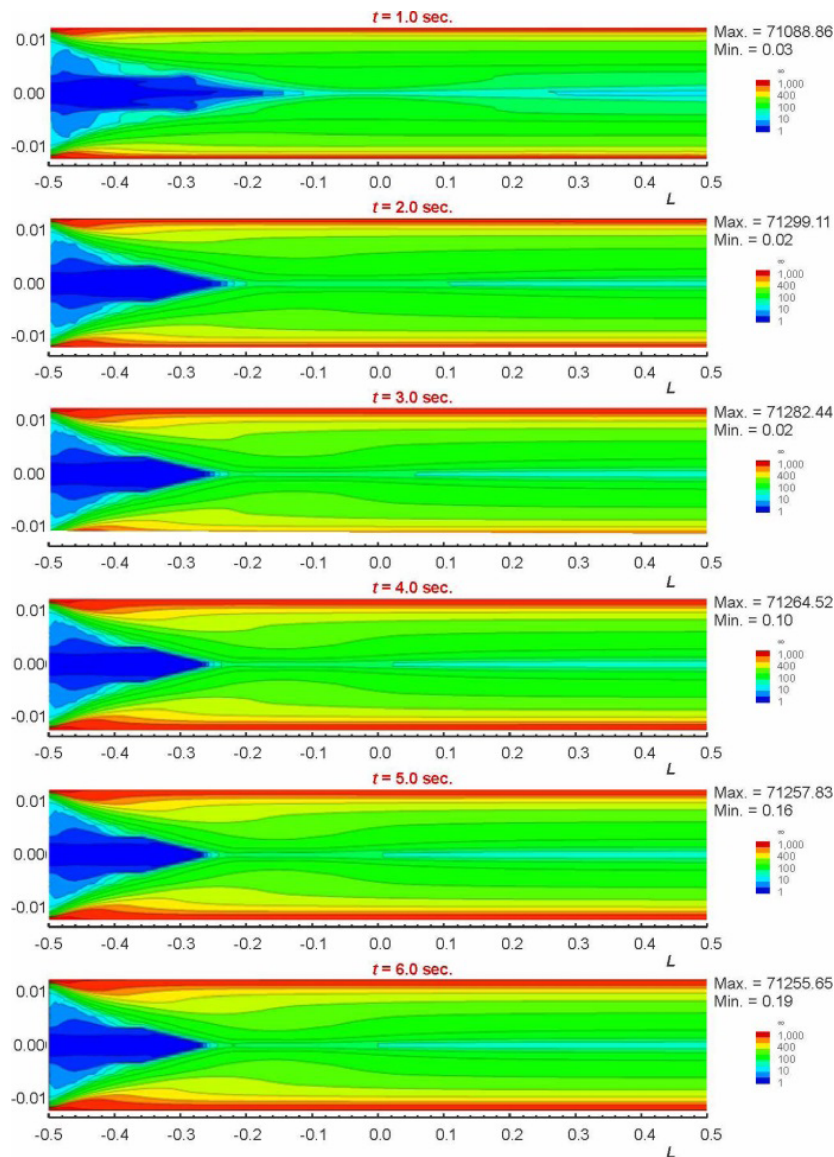
Fig. 9. Velocity contour plots for Re = 6,753, heat input Q = 954 W/m², pulsation amplitude A = 0.1, pulsation frequency f = 1 Hz at downstream pulsation

induced turbulence is evidenced by vorticity peaks near the walls. Flow disturbances are evident near the core, and their impact diminishes beyond L = −0.25 m.

Fig. 10 compares the velocity contours under upstream and downstream pulsation. In the upstream case, a longer high-velocity region extends toward the pipe exit, indicating a more widespread pressure drop and increased turbulence. Conversely, downstream pulsation localizes the high-velocity region, which may lead to concentrated pressure zones and non-uniform *HT*.

Fig. 11 displays the pressure contours at t = 6 s. The peak pressure is higher downstream (63.21) compared to upstream due to the downstream pulsation, suggesting localized acceleration effects. Fig. 12 displays the turbulent kinetic energy (*TKE*) contours for upstream pulsation from t = 1 s to 6 s. *TKE* increases from 0.55 to 0.92 over time, indicating growing turbulence that enhances *HT*. The persistent and significant symmetry of the distribution promotes uniform *HT*.

Although turbulent kinetic energy (*TKE*) development initiates and concentrates more rapidly near the boundaries, *TKE* increases overall, which aligns with the observed higher local heat transfer (*HT*). The symmetry and rapid increase in turbulence observed with downstream pulsation confirm its effectiveness in enhancing convective *HT*.
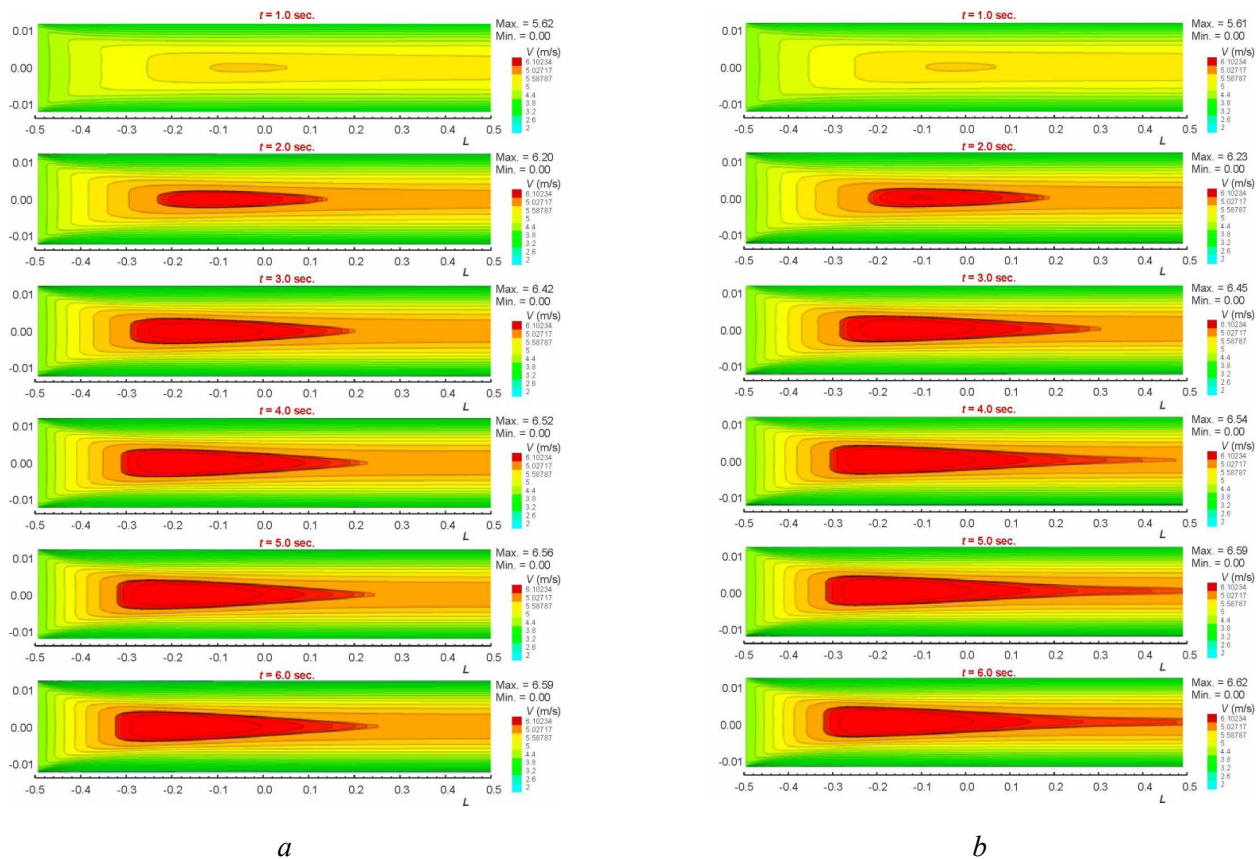
Fig. 10. Comparison of velocity contours for **Re** = 6,753, heat input **Q** = 954 W/m², pulsation amplitude **A** = 0.1, pulsation frequency **f** = 1 Hz at downstream pulsation (left) and upstream pulsation (right)
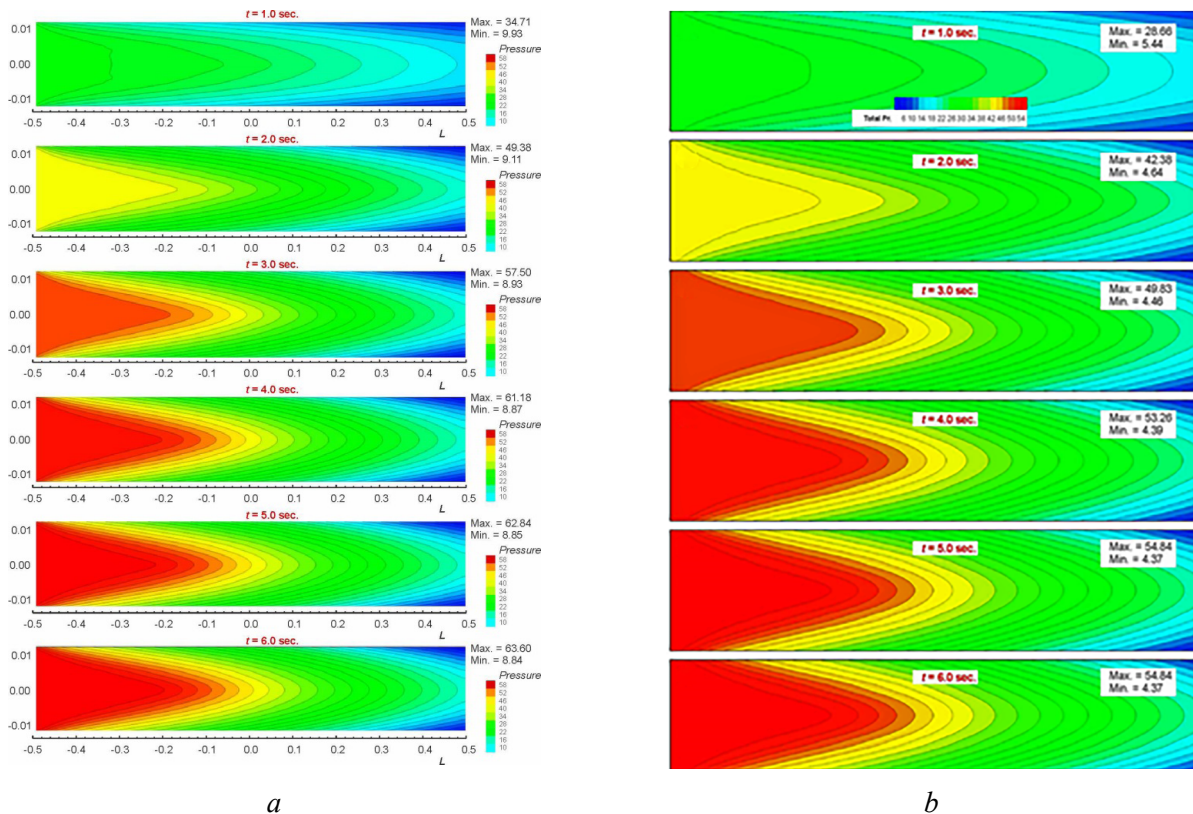
Fig. 11. Pressure contour plots in mid **y**-plane for **Re** = 6,753, heat input **Q** = 954 W/m², pulsation amplitude **A** = 0.1, pulsation frequency **f** = 1 Hz at downstream pulsation (left) and upstream pulsation (right)
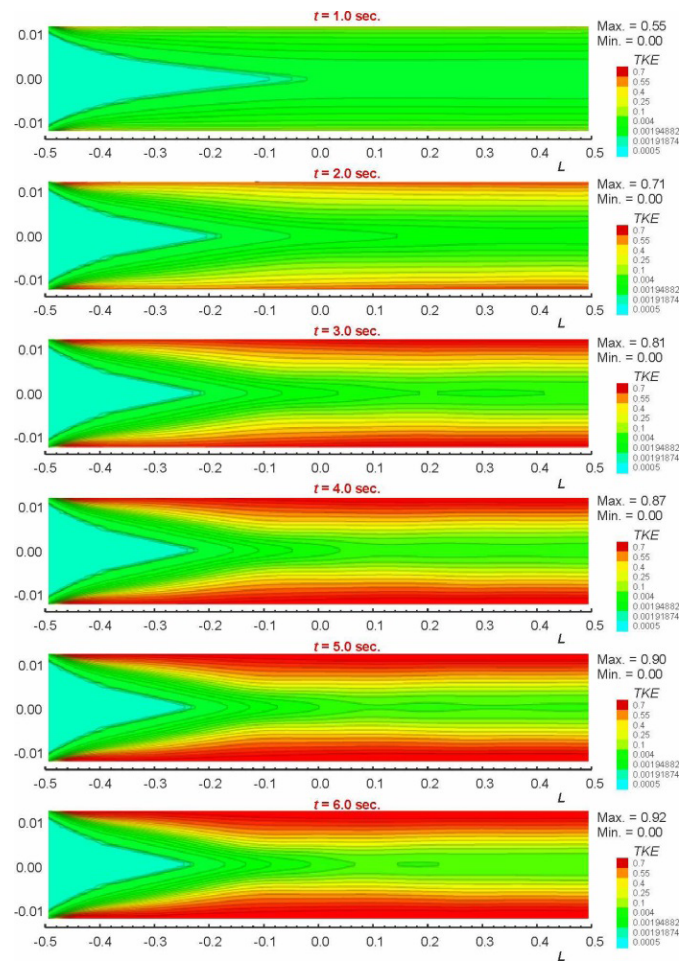
Fig. 12. Turbulent kinetic energy (*TKE*) contour
plots in the mid *y*-plane for *Re* = 6,753, heat input
Q = 954 W/m², pulsation amplitude *A* = 0.1, pulsation
frequency *f* = 1 Hz at upstream pulsation

These results demonstrate that pulsation, particularly when applied downstream, significantly enhances HT through increased turbulence, vorticity, and velocity variations. The primary mechanisms contributing to improved heat transport in pulsating flows are enhanced eddy formation and the generation of shear layers.

Conclusion

The enhancement of heat transfer (*HT*) in a circular pipe with surface roughness under turbulent flow conditions was investigated using a combined experimental and computational approach. The study focused on the effects of surface roughness, pulsation frequency (*f*), *Reynolds* number (*Re*), heat input (*Q*), and amplitude (*A*) on *HT* characteristics. Key parameters evaluated included velocity, pressure, and temperature distributions, turbulent kinetic energy (*TKE*), vorticity, eddy viscosity, the surface *HT* coefficient (*h*), and the *Nusselt* number (*Nu*). The following key conclusions can be drawn from the results:

1. TKE as a driver of HT enhancement:

a) *TKE* is critical for the production and sustenance of turbulence, which dominates the pulsating heat transfer mechanism.

b) Increased *TKE* strengthens fluid-wall interactions, enhancing convective *HT*, particularly with downstream pulsation as observed in this study.

c) These results align with those of previous studies [2, 3, 4], even those that did not consider roughness effects [60].

2. Impact of pulsating flow:

a) Pulsation, whether applied upstream or downstream, significantly affects turbulence parameters, with the downstream configuration exhibiting a more pronounced effect.

b) For $6753 \leq Re \leq 31000$, downstream pulsation enhanced *HT* by 20%–22%, while upstream pulsation improved *HT* by 16%–19%.

c) Pulse intensity, governed by *f* and *A*, influences the extent of turbulence penetration. No single *f* and *A* combination consistently optimizes *HT* enhancement. Future work will focus on optimization studies to determine optimal parameter combinations.

3. Future directions:

a) Future studies should investigate other fluids with varying viscosities and *Prandtl* numbers, such as water and oil.

b) Analyses should be extended to non-circular pipe geometries, such as finned or rectangular channels.

c) *HT* for non-*Newtonian* fluids under pulsating flow should be analyzed for applications in the food and pharmaceutical industries.

d) Future work should combine advanced *CFD* with experimental validation to achieve reliable predictive modeling and optimization.

In conclusion, this study demonstrates that the synergistic combination of surface roughness and pulsating flow effectively enhances *HT* performance, providing a promising approach for improving industrial heat exchanger applications.

References

1. Ye Q., Zhang Y., Wei J. A comprehensive review of pulsating flow on heat transfer enhancement. *Applied Thermal Engineering*, 2021, vol. 196, p. 117275. DOI: 10.1016/j.applthermaleng.2021.117275.

2. Yang B., Gao T., Gong J., Li J. Numerical investigation on flow and heat transfer of pulsating flow in various ribbed channels. *Applied Thermal Engineering*, 2018, vol. 145, pp. 576–589. DOI: 10.1016/j.applthermaleng.2018.09.041.

3. Duan D., Cheng Y., Ge M., Bi W., Ge P., Yang X. Experimental and numerical study on heat transfer enhancement by flow-induced vibration in pulsating flow. *Applied Thermal Engineering*, 2022, vol. 207, p. 118171. DOI: 10.1016/j.applthermaleng.2022.118171.

4. Shang F., Fan S., Yang Q., Liu J. An experimental investigation on heat transfer performance of pulsating heat pipe. *Journal of Mechanical Science and Technology*, 2020, vol. 34, pp. 425–433. DOI: 10.1007/s12206-019-1241-x.

5. Ganapathy V. *Steam generators and waste heat boilers: For process and plant engineers*. Boca Raton, CRC Press, 2014. 539 p. ISBN 9781138077683.

6. Zohuri B. *Application of compact heat exchangers for combined cycle driven efficiency in next generation nuclear power plants: A novel approach*. Cham, Springer Nature Link, 2015. 366 p. eISBN 978-3-319-23537-0. DOI: 10.1007/978-3-319-23537-0.

7. Bassols J., Kuckelkorn B., Langreck J., Schneider R., Veelken H. Trigeneration in the food industry. *Applied Thermal Engineering*, 2002, vol. 22 (6), pp. 595–602. DOI: 10.1016/S1359-4311(01)00111-9.

8. Šalić A., Tušek A., Zelić B. Application of microreactors in medicine and biomedicine. *Journal of Applied Biomedicine*, 2012, vol. 10 (3), pp. 137–153. DOI: 10.2478/v10136-012-0011-1.

9. Sharma A., Tyagi V.V., Chen C.R., Buddhi D. Review on thermal energy storage with phase change materials and applications. *Renewable and Sustainable Energy Reviews*, 2009, vol. 13 (2), pp. 318–345. DOI: 10.1016/j.rser.2007.10.005.

10. Ameen A. *Refrigeration and air conditioning*. PHI Learning Pvt. Ltd., 2006. 512 p. ISBN 8120326717. ISBN 978-8120326712.

11. Oliet C., Oliva A., Castro J., Pérez-Segarra C.D. Parametric studies on automotive radiators. *Applied Thermal Engineering*, 2007, vol. 27 (11), pp. 2033–2043. DOI: 10.1016/j.applthermaleng.2006.12.006.

12. Heldman D., Moraru C.E., eds. *Encyclopedia of agricultural, food, and biological engineering*. 2nd ed. Boca Raton, CRC Press, 2010. DOI: 10.1201/9780429257599.

13. Coker A.K. Introduction. Coker A.K. *Petroleum refining design and application handbook*. John Wiley & Sons, 2018, ch. 1, pp. 1–6. ISBN 978-1-119-25710-3. DOI: 10.1002/9781119257110.ch1.

14. Coker A.K. Thermodynamic properties of petroleum and petroleum fractions. Coker A.K. *Petroleum refining design and application handbook*. John Wiley & Sons, 2018, ch. 4, pp. 63–110. DOI: 10.1002/9781119257110.ch4.

15. Beddoes J., Bibby M. *Principles of metal manufacturing processes*. Butterworth-Heinemann, 1999. DOI: 10.1016/B978-0-340-73162-8.X5000-0.

16. Abu Rowin W., Xia Y., Wang S., Hutchins N. Accurately predicting turbulent heat transfer over rough walls: a review of measurement equipment and methods. *Experiments in Fluids*, 2024, vol. 65, p. 86. DOI: 10.1007/s00348-024-03812-1.

17. Qu W., Ma H.B. Theoretical analysis of startup of a pulsating heat pipe. *International Journal of Heat and Mass Transfer*, 2007, vol. 50 (11–12), pp. 2309–2316. DOI: 10.1016/j.ijheatmasstransfer.2006.10.043.

18. Chen X., Lin Y., Shao S., Wu W. Study on heat transfer characteristics of ethane pulsating heat pipe in middle-low temperature region. *Applied Thermal Engineering*, 2019, vol. 152, pp. 697–705. DOI: 10.1016/j.applthermaleng.2019.02.125.

19. Singh S., Singh S.K., Mali H.S., Dayal R. Numerical investigation of heat transfer in structured rough microchannels subjected to pulsed flow. *Applied Thermal Engineering*, 2021, vol. 197, p. 117361. DOI: 10.1016/j.applthermaleng.2021.117361.

20. Wu H.-W., Lay R.-F., Lau C.-T., Wu W.-J. Turbulent flow field and heat transfer in a heated circular channel under a reciprocating motion. *Heat and Mass Transfer*, 2004, vol. 40 (10), pp. 769–778. DOI: 10.1007/s00231-003-0464-6.

21. Lin T.-Y., Kandlikar S.G. An experimental investigation of structured roughness effect on heat transfer during single-phase liquid flow at microscale. *Journal of Heat Transfer*, 2012, vol. 134, p. 101701. DOI: 10.1115/1.4006844.

22. Lu H., Xu M., Gong L., Duan X., Chai J.C. Effects of surface roughness in microchannel with passive heat transfer enhancement structures. *International Journal of Heat and Mass Transfer*, 2020, vol. 148, p. 119070. DOI: 10.1016/j.ijheatmasstransfer.2019.119070.

23. Croce G., D'agaro P., Nonino C. Three-dimensional roughness effect on microchannel heat transfer and pressure drop. *International Journal of Heat and Mass Transfer*, 2007, vol. 50 (25), pp. 5249–5259. DOI: 10.1016/j.ijheatmasstransfer.2007.06.021.

24. Gerrard J.H. An experimental investigation of pulsating turbulent water flow in a tube. *Journal of Fluid Mechanics*, 1971, vol. 46 (1), pp. 43–64. DOI: 10.1017/S0022112071000399.

25. Clamen M., Minton P. An experimental investigation of flow in an oscillating pipe. *Journal of Fluid Mechanics*, 1977, vol. 81 (3), pp. 421–431. DOI: 10.1017/S0022112077002146.

26. Shemer L., Wygnanski I., Kit E. Pulsating flow in a pipe. *Journal of Fluid Mechanics*, 1985, vol. 153, pp. 313–337. DOI: 10.1017/S0022112085001276.

27. Eckmann D.M., Grotberg J.B. Experiments on transition to turbulence in oscillatory pipe flow. *Journal of Fluid Mechanics*, 1991, vol. 222, pp. 329–350. DOI: 10.1017/S002211209100112X.

28. Ohmi M., Usui T., Tanaka O., Toyoma M. Pressure and velocity distributions in pulsating turbulent pipe flow. Part 2. Experimental investigations. *Bulletin of JSME*, 1976, vol. 19 (134), pp. 951–957. DOI: 10.1299/jsme1958.19.951.

29. Iguchi M., Park G., Koh Y. The structure of turbulence in pulsatile pipe flows. *KSME Journal*, 1993, vol. 7, pp. 185–193. DOI: 10.1007/BF02970963.

30. Genin L.G., Koval A.P., Manchkha S.P., Sviridov V.G. Hydrodynamics and heat transfer with pulsating fluid flow in tubes. *Thermal Engineering*, 1992, vol. 39 (5), pp. 251–255.

31. Einav S., Sokolov M. An experimental study of pulsatile pipe flow in the transition range. *Journal of Biomechanical Engineering*, 1993, vol. 115 (4A), pp. 404–411. DOI: 10.1115/1.2895504.

32. Carvalho Jr J.A. Behavior of solid particles in pulsating flows. *Journal of Sound and Vibration*, 1995, vol. 185 (4), pp. 581–593. DOI: 10.1006/jsvi.1995.0402.

33. Lu P.-C. Discussion: "Heat Transfer for Pulsating Laminar Duct Flow" (Siegel, R., and Perlmutter, M., 1962, ASME J. Heat Transfer, 84, pp. 111–122). *Journal of Heat Transfer*, 1962, vol. 84, pp. 111–122. DOI: 10.1115/1.3684308.

34. Faghri M., Javdani K., Faghri A. Heat transfer with laminar pulsating flow in a pipe. *Letters in Heat and Mass Transfer*, 1979, vol. 6 (4), pp. 259–270. DOI: 10.1016/0094-4548(79)90013-4.

35. Krishnan K.N., Sastri V.M.K. Heat transfer in laminar pulsating flows of fluids with temperature dependent viscosities. *Wärme- und Stoffübertragung*, 1989, vol. 24 (1), pp. 27–42. DOI: 10.1007/BF01599503.

36. Cho H., Hyun J. Numerical solutions of pulsating flow and heat transfer characteristics in a pipe. *International Journal of Heat and Fluid Flow*, 1990, vol. 11 (4), pp. 321–330. DOI: 10.1016/0142-727X(90)90056-H.

37. Kim S.Y., Kang B.H., Hyun J.M. Heat transfer from pulsating flow in a channel filled with porous media. *International Journal of Heat and Mass Transfer*, 1994, vol. 37 (14), pp. 2025–2033. DOI: 10.1016/0017-9310(94)90304-2.

38. Gül H. Experimental investigation of heat transfer in oscillating circular pipes: High frequencies and amplitudes. *Scientific Research and Essays*, 2013, vol. 8 (13), pp. 524–531. DOI: 10.5897/SRE12.721.

39. Dittus F., Boelter L. Heat transfer in automobile radiators of the tubular type. *International Communications in Heat and Mass Transfer*, 1985, vol. 12 (1), pp. 3–22. DOI: 10.1016/0735-1933(85)90003-X.

40. Winterton R.H.S. Technical notes: Where did the dittus and boelter equation come from? *International Journal of Heat and Mass Transfer*, 1998, vol. 41 (4–5), pp. 809–810. DOI: 10.1016/S0017-9310(97)00177-4.

41. McAdams W.H. *Heat transmission*. 3rd ed. New York, McGraw-Hill, 1954. ISBN 0070447993. ISBN 9780070447998.

42. Bagade P.M., Bhumkar Y.G., Sengupta T.K. An improved orthogonal grid generation method for solving flows past highly cambered aerofoils with and without roughness elements. *Computers and Fluids*, 2014, vol. 103, pp. 275–289. DOI: 10.1016/j.compfluid.2014.07.031.

43. Elshafei E.A.M., Safwat Mohamed M., Mansour H., Sakr M. Experimental study of heat transfer in pulsating turbulent flow in a pipe. *International Journal of Heat and Fluid Flow*, 2008, vol. 29 (4), pp. 1029–1038. DOI: 10.1016/j.ijheatfluidflow.2008.03.018.

44. Cebeci T., Bradshaw P. *Physical and computational aspects of convective heat transfer*. New York, Springer, 2012. DOI: 10.1007/978-1-4612-3918-5.

45. Kays W., Crawford M., Weigand B. *Convective heat and mass transfer*. McGraw-Hill, 2005. ISBN 0072468769. ISBN 978-0072468762.

46. Chung D., Hutchins N., Schultz M.P., Flack K.A. Predicting the drag of rough surfaces. *Annual Review of Fluid Mechanics*, 2021, vol. 53, pp. 439–471. DOI: 10.1146/annurev-fluid-062520-115127.

47. Alfarawi S., Abdel-Moneim S.A., Bodalal A. Experimental investigations of heat transfer enhancement from rectangular duct roughened by hybrid ribs. *International Journal of Thermal Sciences*, 2017, vol. 118, pp. 123–138. DOI: 10.1016/j.ijthermalsci.2017.04.017.

48. MacDonald M., Chan L., Chung D., Hutchins N., Ooi A. Turbulent flow over transitionally rough surfaces with varying roughness densities. *Journal of Fluid Mechanics*, 2016, vol. 804, pp. 130–161. DOI: 10.1017/jfm.2016.459.

49. Everts M., Ayres S.R., Mulock Houwer F.A., Vanderwagen C.P., Kotze N.M., Meyer J.P. The influence of surface roughness on heat transfer in the transitional flow regime. *Proceedings of the 15th International Heat Transfer Conference*. Begellhouse, 2014. DOI: 10.1615/IHTC15.cnv.008338.

50. Meyer J., Olivier J. Transitional flow inside enhanced tubes for fully developed and developing flow with different types of inlet disturbances: Part I – Adiabatic pressure drops. *International Journal of Heat and Mass Transfer*, 2011, vol. 54 (7), pp. 1587–1597. DOI: 10.1016/j.ijheatmasstransfer.2010.11.027.

51. Meyer J., Olivier J. Transitional flow inside enhanced tubes for fully developed and developing flow with different types of inlet disturbances: Part II – Heat transfer. *International Journal of Heat and Mass Transfer*, 2011, vol. 54 (7), pp. 1598–1607. DOI: 10.1016/j.ijheatmasstransfer.2010.11.026.

52. García A., Solano J.P., Vicente P.G., Viedma A. The influence of artificial roughness shape on heat transfer enhancement: Corrugated tubes, dimpled tubes and wire coils. *Applied Thermal Engineering*, 2012, vol. 35, pp. 196–201. DOI: 10.1016/j.applthermaleng.2011.10.030.

53. Mousa M.H., Miljkovic N., Nawaz K. Review of heat transfer enhancement techniques for single phase flows. *Renewable and Sustainable Energy Reviews*, 2021, vol. 137, p. 110566. DOI: 10.1016/j.rser.2020.110566.

54. Everts M., Meyer J.P. Heat transfer of developing and fully developed flow in smooth horizontal tubes in the transitional flow regime. *International Journal of Heat and Mass Transfer*, 2018, vol. 117, pp. 1331–1351. DOI: 10.1016/j.ijheatmasstransfer.2017.10.071.

55. Kobayashi S., Inokuma K., Murata A., Iwamoto K. Effects of flow pulsation and surface geometry on heat transfer performance in a channel with teardrop-shaped dimples measured by transient technique. *ASME Journal of Heat and Mass Transfer*, 2024, vol. 146, p. 072001. DOI: 10.1115/1.4065117.

56. Abdelfattah M., Aziz M.A., Maghrabie H.M. Numerical analysis of heat transfer and fluid flow structures of jet impingement on a flat plate with different shapes of roughness elements. *Numerical Heat Transfer, Part A: Applications*, 2024, pp. 1–26. DOI: 10.1080/10407782.2024.2379032.

57. *Ansys Fluent Theory Guide*. ANSYS, Inc., 2021.

58. Nikuradse J. *Laws of flow in rough pipes*. *NACA Technical Memorandums*, NACA-TM-1292. NACA, 1950. 62 p.

59. Cebeci T., Bradshaw P. *Momentum transfer in boundary layers*. Washington, Hemisphere Pub. Corp., 1977. 407 p. ISBN 0070103003. ISBN 9780070103009.

60. Nishandar S.V., Pise A.T., Bagade P.M., Gaikwad M.U., Singh A. Computational modelling and analysis of heat transfer enhancement in straight circular pipe with pulsating flow. *International Journal on Interactive Design and Manufacturing (IJIDeM)*, 2024, vol. 19 (3), pp. 1951–1969. DOI: 10.1007/s12008-024-01907-x.

61. Dwivedi R., Somatkar A., Chinchanikar S. Modeling and optimization of roller burnishing of Al6061-T6 process for minimum surface roughness, better microhardness and roundness. *Obrabotka metallov (tekhnologiya, oborudovanie, instrumenty) = Metal Working and Material Science*, 2024, vol. 26, no. 3, pp. 52–65. DOI: 10.17212/1994-6309-2024-26.3-52-65.

Conflicts of Interest

The authors declare no conflict of interest.

Obrabotka metallov -
Metal Working and Material Science

Journal homepage: http://journals.nstu.ru/obrabotka_metallov

The effect of the grinding method on the grain shape coefficient of black silicon carbide

Vladimir Nosenko [1, a, *], Daniel Rivas Peres [2, b], Aleksey Aleksandrov [1, c], Aleksandr Sarazov [1, d]

[1] Volzhsky Polytechnic Institute (branch) of Volgograd State Technical University, 43a Engelsa str., Volzhskiy, 404120, Russian Federation
[2] JSC "Volzhsky Abrasive Plant", 169 F.G. Loginov Str., Volzhsky, 404119, Russian Federation

[a] https://orcid.org/0000-0002-5074-1099, ✉ vladim.nosenko2014@yandex.ru; [b] https://orcid.org/0009-0000-7733-236X, ✉ rivas-peres_de@vabz.ru;
[c] https://orcid.org/0000-0003-1986-9139, ✉ alexalexal2011@yandex.ru; [d] https://orcid.org/0009-0007-3052-5691, ✉ sarazov_av@mail.ru

ARTICLE INFO

ABSTRACT

Introduction. JSC Volzhsky Abrasive Plant is the sole producer of silicon carbide in Russia and the largest producer in Europe. The company employs various methods, equipment, and technologies for grinding abrasive materials, which influence the geometric parameters of the grains. The most prominent and widely used methods for grinding silicon carbide in current production are roller-press grinding and rotary grinding. **The purpose of this work** is to study the effect of the roller-press and rotary methods of grinding black silicon carbide, which are used at the JSC Volzhsky Abrasive Plant, on the shape factor, length, and width of the grains in the sample fractions. **Research methods.** The initial material obtained in accordance with the current technological process was selected after crushing in a rod mill. One sample was crushed using the roller-press method, and the other was crushed using the rotary method. The crushed silicon carbide was sieved into fractions using a *Ro-Tap* sieve analyzer. The geometric parameters and grain shape were determined in five fractions, and 800 grains were measured in each fraction. The horizontal projection of the grain profile was obtained using an *Altami SM0870-T* optical stereoscopic microscope. Special software was used to process the projections and determine the geometric parameters. **Results and discussion.** It has been established that the shape factor and grain length follow the maximum value law, while the width follows the normal distribution law. The strength of the correlation between geometric parameters ranges from weak to strong, and the direction of the relationships varies from positive to negative. Graphical dependencies are presented, demonstrating the correlation and regression relationships between the geometric parameters of the grains in the fractions. Rotary grinding results in an average increase of 5% in the number of isometric grains compared to roller-press grinding, while the number of needle-like grains decreases by a factor of 3. The research findings are intended for optimizing the formulation and manufacturing technology of abrasive and refractory products.

Introduction

The grain shape of grinding powders has a significant effect on the properties of abrasive tools and the quality of the machined surface of parts [1–3], and is a determining indicator in the manufacture of refractory products [4, 5]. Isometric grains contribute to reducing wear, increasing the durability of abrasive tools, and improving machining performance [6–9].

The grains attain the desired size and shape through a technological process involving multi-stage crushing and grinding of the abrasive material. These operations are performed using various equipment

* Corresponding author
Nosenko Vladimir A., D.Sc. (Engineering), Professor, Head of department
Volzhsky Polytechnic Institute
(branch) of Volgograd State Technical University,
43a Engelsa str.,
404120, Volzhskiy, Russian Federation
Tel.: +7 904 403-31-74, **e-mail:** vladim.nosenko2014@yandex.ru

and crushing methods, such as jaw, ball, cone, rod, roller (roller press), and rotary crushers [10–16]. If sorting the crushed grains by shape is required, they undergo additional treatment [17–21].

The most common quantitative criterion for the shape of abrasive grains is the shape factor, defined as the ratio of the length *l* of the grain projection on a horizontal plane to the width *b*. Length is defined as the largest distance between perimeter points (the maximum *Feret* diameter). Width is calculated as the sum of the maximum distances from the length line to the left and right sides of the perimeter, divided by the length line (*ISO 9276-6-2008*, *GOST R 70336-2022*). In effect, the grain projection is inscribed in a rectangle where the longest side corresponds to the length of the grain, and the shortest side corresponds to the width.

The crushing and grinding methods of abrasive materials significantly affect the shape and properties of the resulting particles. For example, studies have shown that when crushing corundum using roller, cone, and ball crushers, a ball crusher yields the greatest isometricity [11, 12].

The influence of grinding methods on the geometric parameters and shape of grains within the current technological process for producing abrasive materials at JSC Volzhsky Abrasive Plant, a leading enterprise in the industry, is of particular interest. The relevance of this research is further supported by the fact that JSC Volzhsky Abrasive Plant is "the only producer of silicon carbide in Russia and the largest in Europe" [22].

Silicon carbide is used to manufacture grinding powders and micro-powders, a wide range of abrasive tools, refractories, and specialized products. These diverse applications, encompassing abrasive machining of various parts and the production of a wide range of items, preclude the establishment of uniform requirements for geometric parameters and grain shape. Consequently, it is essential to consider the specific characteristics of the machined surface and the properties of the target product.

For example, in cutting operations where the objective is to increase productivity, cutting wheels made of grinding powders with a shape factor $kf = l/b = 2.2$ are employed, where *l* and *b* represent the length and width of the grain, respectively. Conversely, if minimizing abrasive tool consumption is the primary concern, isometric grains with a shape factor of $l/b = 1.3$ are preferred [23].

To grind silicon carbide, the plant employs various methods, equipment, and processing parameters that influence the geometric characteristics and properties of the grains. Roller press grinding and rotary grinding are among the most common methods implemented at JSC Volzhsky Abrasive Plant.

Grain sizes exhibit significant variation. For instance, *GOST R 52381-2005* specifies a range of grain and fraction sizes spanning from 4,750 μm, to 45 μm. Furthermore, based on grain composition, grinding powders are categorized into 30 grain sizes, each containing 5 distinct fractions.

The ***purpose of the paper*** is to investigate the effect of roller press grinding and rotary grinding of black silicon carbide, as implemented at JSC Volzhsky Abrasive Plant, on the grain shape factor of fraction samples.

Tasks:

– to determine the distribution patterns of black silicon carbide grain shape factors, along with the geometric parameters influencing them (grain length and width);

– to analyze correlation and regression relationships between grain shape factors and geometric parameters;

– to identify trends in geometric parameters of grains within fraction samples produced by roller press grinding and rotary grinding.

Research Methodology

The input materials for roller press and rotary grinding were produced under identical conditions following the current technological process. Black silicon carbide feedstock was sequentially processed using a cone crusher and a rod mill.

Following drying, a portion of the abrasive material was ground using a roller press, while the remaining portion was subjected to rotary grinding.

The *PVI 800/150* roller press used at JSC Volzhsky Abrasive Plant is characterized by: adjustable hydraulic pressure applied to only one roll, which avoids over-grinding; and material crushing within an

adjustable layer between the rolls. The grinding parameters were: rotational speed – 50 Hz, pressure – 28 kg/cm^3, roll gap – 2 mm.

The *VSI Barmac 5100SE* vertical shaft impact (*VSI*) crusher operates on a stone-on-stone principle, with a rotor speed of 3,000 rpm and a throughput of 4 tons per hour. The crushing chamber's lining pockets are filled with compacted silicon carbide, which significantly reduces metal-on-metal abrasion and promotes the formation of more isometric grains. During typical operation, grinding generates a substantial amount of fine silicon carbide particles (dust). Therefore, a dust extraction system is integrated into the crushing chamber to ensure compliance with the abrasive grain quality requirements of *GOST R 52381*.

Input material fractions were obtained by sieving powders using a *Ro-Tap* machine. Five fractions were selected for analysis, with the nominal cell sizes of the upper and lower control sieves presented in Table 1. The average nominal cell size (*Wmi*) of the upper (*Wui*) and lower (*Wli*) sieves was used as the primary parameter characterizing the grain size of each fraction, calculated as: *Wmi* = (*Wui* + *Wli*)/2. In accordance with *GOST R 52381*, the ratio *Wui/Wli* should fall within the range of 1.18–1.21.

Table 1

Grinding powder fractions *(GOST R 52381)*

Fraction designation	Nominal size of sieve cells		
	Upper sieve *Wu*, μm	Lower sieve *Wl*, μm	Average value *Wmi* = (*Wu*+*Wl*)/2, μm
1	2,360	2,000	2,180
2	1,700	1,400	1,550
3	1,000	850	925
4	600	500	550
5	300	250	275

Grain profile images were captured using an *Altami CM0870–T* optical stereoscopic microscope. Image processing and geometric parameter calculations were performed using dedicated software [24]. A total of 800 grains were measured within each fraction. The following geometric parameters were determined and analyzed: grain length (*l*), grain width (*b*), and shape factor (*l/b* ratio).

Research Results and Discussion

Based on the empirical grain size distribution patterns (Figs. 1–3), four distribution models were evaluated to determine the theoretical distribution: normal, lognormal, gamma, and the law of maximum value. The normal distribution is typically used to model distributions exhibiting symmetrical right and left branches on graphs [25].

a

b
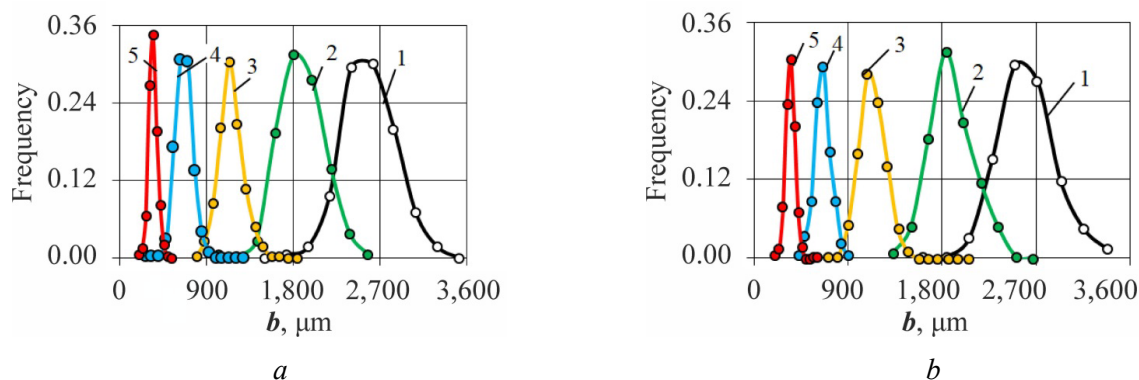
Fig. 1. Experimental distributions of grain width *b* for fractions after roller-press (*a*) and rotary (*b*) grinding methods
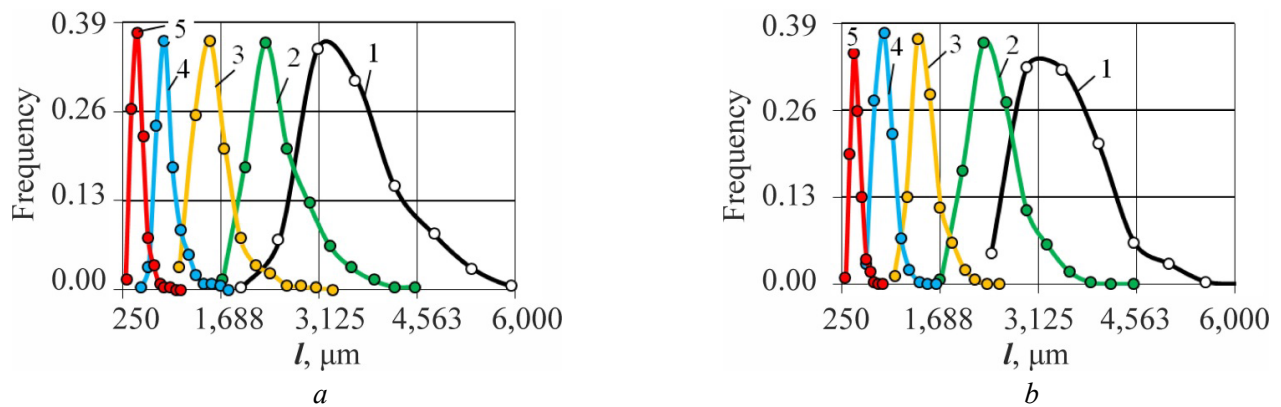
Fig. 2. Experimental distribution of grain length *l* for fractions after roller-press (*a*) and rotary (*b*) milling methods
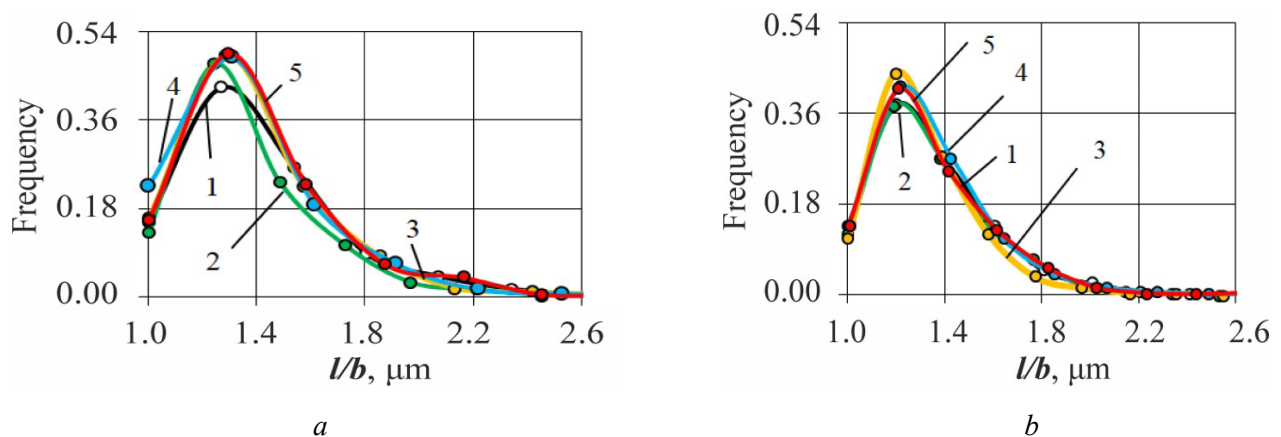
Fig. 3. Experimental distribution of the aspect ratio *l/b* for fractions after roller-press (*a*) and rotary (*b*) milling methods

In Table 2, the observed and critical values of the *Pearson's* chi-squared test statistic satisfying the condition $\chi^2_{obs} < \chi^2_{crit}$ are highlighted in bold. This indicates that the sample data conforms to the distribution model under consideration. The grain length distribution in nine out of ten fractions aligns with the gamma distribution (90 %) and the law of maximum value (90%). The lognormal distribution provides a better fit for the grain length distributions resulting from rotary grinding (in four out of five fractions). The grain length of the roller-ground material does not conform to the lognormal distribution.

Grain width in all considered fractions follows a normal distribution (Table 3). The observed values of the *Pearson's* chi-squared test statistic in these fractions are less than the critical values. The grain shape factor in nine out of ten fractions adheres to both the gamma distribution and the law of maximum value (90 %). Based on these findings, the following distribution models were adopted: grain width follows a normal distribution, while grain length and shape factor adhere to the law of maximum value.

The *Pearson* correlation coefficient is a widely used statistical measure that quantifies the strength of the linear relationship between two variables. Its application requires that both variables are normally distributed and derived from the same sample. Given that the grain width follows a normal distribution, while grain length and shape factor adhere to the law of maximum value, any selected pair of geometric grain parameters will not satisfy the condition of the normal distribution law. Therefore, *Spearman's* rank criterion was used to estimate the strength of the relationship between the parameters [25]. This involved converting the natural values of the geometric parameters into ranks. Specifically, the numerical values of the geometric parameters were ranked in ascending order, and each value was assigned an ordinal number (rank) accordingly.

Fig. 4 presents a graphical representation of the correlations between the geometric parameters of grains obtained through roller press and rotary grinding. The *x*-axis displays the arithmetic mean of the nominal

Table 2

The reliability of the correspondence of the observed grain length distribution to the theoretical one according to *Pearson's* chi-squared test χ²

Grinding method	Fraction	Lognormal		Gamma distribution		Length maximum value	
		χ^2_{obs}	χ^2_{crit}	χ^2_{obs}	χ^2_{crit}	χ^2_{obs}	χ^2_{crit}
Roller-press	1	53.5	11.1	**5.8**	**11.1**	**16.7**	**16.9**
	2	37.4	11.1	**5.5**	**9.5**	**1.7**	**11.1**
	3	36.9	11.1	**11.1**	**18.3**	**8.9**	**12.6**
	4	54.7	11.1	**8.0**	**18.3**	**9.3**	**11.1**
	5	18.2	9.5	**8.5**	**11.1**	**3.8**	**12.6**
Rotary	1	**7.9**	**9.5**	**3.5**	**9.5**	14.4	11.1
	2	**7.4**	**9.5**	11.1	9.5	**9.3**	**11.1**
	3	15.1	9.5	**6.4**	**18.3**	**8.6**	**11.1**
	4	**6.2**	**9.5**	**8.2**	**9.5**	11.8	14.1
	5	**6.6**	**9.5**	**8.2**	**18.3**	**9.1**	**11.1**
Reliability, %		40		90		90	

Table 3

Reliability of the correspondence of the observed distributions of grain width and shape factor according to *Pearson's* test

Method	Fraction	Width		Shape coefficient			
		Normal		Log-normal		Maximum value	
		χ^2_{obs}	χ^2_{crit}	χ^2_{obs}	χ^2_{crit}	χ^2_{obs}	χ^2_{crit}
Roller-press	1	**5.8**	**5.8**	34.0	7.8	**6.0**	**11.1**
	2	**5.5**	**5.5**	68.9	11.1	**7.6**	**7.8**
	3	**11.1**	**11.1**	40.1	7.8	**3.1**	**7.8**
	4	**8.0**	**8.0**	54.6	11.1	**9.4**	**11.1**
	5	**8.5**	**8.5**	66.9	14.1	**8.3**	**11.1**
Rotor	1	**3.5**	**3.5**	30.2	12.6	**4.6**	**12.6**
	2	**11.1**	**11.1**	52.4	12.6	**11.3**	**12.6**
	3	**6.4**	**6.4**	30.4	9.5	**5.4**	**12.6**
	4	**8.2**	**8.2**	29.9	9.5	**4.3**	**9.5**
	5	**8.2**	**8.2**	62.5	12.6	**3.3**	**9.5**
Reliability. %		100		0		100	

Fig. 4. Spearman's rank correlation coefficient ρ between geometric parameters of grains in different fractions:
● – roller-press grinding; ○ – rotary grinding
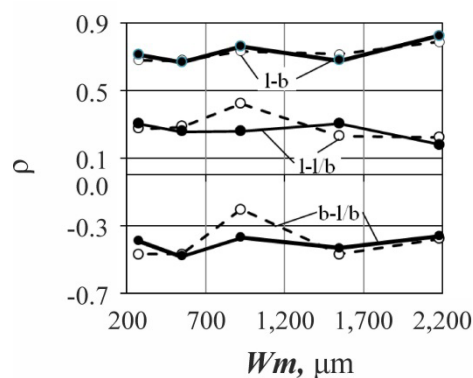
cell sizes of the upper and lower sieves (*Wm*) for each fraction (refer to Table 1). The strength of the correlation coefficients was evaluated using the *Chaddock* scale.

The *Spearman's* rank correlation coefficient (ρ) between grain length (*l*) and grain width (*b*) does not exceed 0.3. The average ρ value for the *l-b* relationship is 0.21 for roller-press grinding and 0.25 for rotary grinding. The correlation strength between the grain shape factor (*l/b*) and grain length (*l*) is significantly higher, with an average ρ value exceeding 0.7. The strength of the relationship between the shape factor (*l/b*) and grain width for the selected fractions ranges from −0.35 to −0.50, indicating an inverse relationship where the shape factor decreases as grain width increases.

Based on the absolute values of the correlation coefficients, the strength of the relationship between grain length (*l*) and width (*b*) falls into the "weak" category, while the relationship between grain width (*b*) and shape factor (*l/b*) is categorized as "moderate". The correlation coefficients between grain length (*l*) and shape factor (*l/b*) are at the lower end of the "strong" relationship category, ranging from 0.69 to 0.84 with an average of 0.76. In accordance with the established scale for ρ, this indicates a strong correlation. The grinding method does not appear to have a significant effect on the correlation strength.

We explored the feasibility of modeling the relationships between geometric parameters using a standard set of functional dependencies within *Microsoft Excel*. Table 4 presents the constant values and coefficients of determination (R^2) for the approximations of the relationships between the geometric grain parameters, based on the following dependencies:

$$l = a_1 b; \tag{1}$$

$$l/b = a_2 b + c_1; \tag{2}$$

$$l/b = a_3 l; \tag{3}$$

$$l/b = a_4 l + c_2. \tag{4}$$

Table 4

Constant coefficients and confidence coefficients for approximating the relationship between geometric parameters of grains

Roller-press grinding										
Fraction	$l = a_1 b$		$l/b = a_2 b + c$			$l/b = a_3 l$		$l/b = a_4 l + c_2$		
	a_1	R^2	a_2	c	R^2	a_3	R^2	a_4	c_2	R^2
1	1.39	0.10	−0.00044	2.54	0.16	0.00054	0.65	0.00037	0.065	0.72
2	1.34	0.10	−0.00046	2.25	0.17	0.00053	0.55	0.00044	0.247	0.57
3	1.37	0.10	−0.00079	2.30	0.13	0.00087	0.69	0.00078	0.141	0.70
4	1.35	0.20	−0.0017	2.49	0.22	0.0015	0.55	0.00135	0.145	0.56
5	1.37	0.15	−0.0029	2.41	0.19	0.0029	0.55	0.00255	0.176	0.54
$R^2 m$	–	0.13	–	–	0.17	–	0.58	–	–	0.63
Rotary grinding										
Fraction	$l = a_1 b$		$l/b = a_2 b + c$			$l/b = a_3 l$		$l/b = a_4 l + c_2$		
	a_1	R^2	a_2	c	R^2	a_3	R^2	a_4	c_2	R^2
1	1.33	0.15	−0.00037	2.31	0.17	0.00038	0.64	0.00035	0.138	0.64
2	1.32	0.21	−0.00051	2.30	0.21	0.00053	0.56	0.00046	0.188	0.57
3	1.29	0.13	−0.00075	2.16	0.20	0.00089	0.47	0.00070	0.277	0.51
4	1.32	0.25	−0.0015	2.32	0.24	0.0015	0.49	0.00129	0.219	0.51
5	1.31	0.21	−0.0029	2.31	0.24	0.0029	0.45	0.00238	0.243	0.48
$R^2 m$	–	0.19	–	–	0.21	–	0.52			0.54

For grains produced by roller-press and rotary grinding, the accuracy of the approximation using the linear dependence $l = a_1 b$ (1) does not exceed 0.25, indicating a weak correlation. Similarly, modeling the dependence of the shape factor (**l/b**) on grain width (**b**) using equation (2) yielded low approximation accuracy. A significant improvement in R^2 was achieved using a direct proportional relationship (3), with average approximation reliability coefficients of 0.58 and 0.52 for grains produced by roller-press and rotary grinding, respectively. Replacing the proportional relationship with a linear one (4) resulted in only a marginal increase in approximation reliability.

As an illustration, fig. 5 depicts the regression relationships between the geometric parameters of fraction 3 grains produced by roller-press grinding (figs. 5, *a*; 5, *b*) and rotary grinding (figs. 5, *c*; 5, *d*). The data points in figs. 5, *a* and 5, *b* were approximated using a direct proportional relationship ($l = a_1 b$), while those in figs. 5, *b* and 5, *c* were approximated using a linear relationship ($l/b = a_2 b + c$).

It is worth noting that following roller-press grinding, the relative proportion of grains with a length exceeding, for example, 4,650 µm (fig. 5, *a*), is significantly higher than that after rotary grinding (fig. 5, *c*), which affects the shape factor. The number of grains with a shape factor **l/b** > 2 is 3.5 times greater after roller-press grinding than after rotary grinding (figs. 5, *b* and 5, *d*). Similar trends are observed in other fractions.

Fig. 6 illustrates the dependence of the shape factor on grain length for each of the five fractions. Within the range of **l/b** values from 2 to 4, the distribution density of needle-shaped grains obtained by roller-press grinding (fig. 6, *a*) is substantially higher than that of those produced by rotary grinding (fig. 6, *b*). In the larger fractions (1–3) obtained by roller-press grinding (fig. 6, *a*), grains with a shape factor exceeding 3 are absent. Grains with a shape factor exceeding 3 are absent in all fractions produced by rotary grinding (fig. 6, *b*).
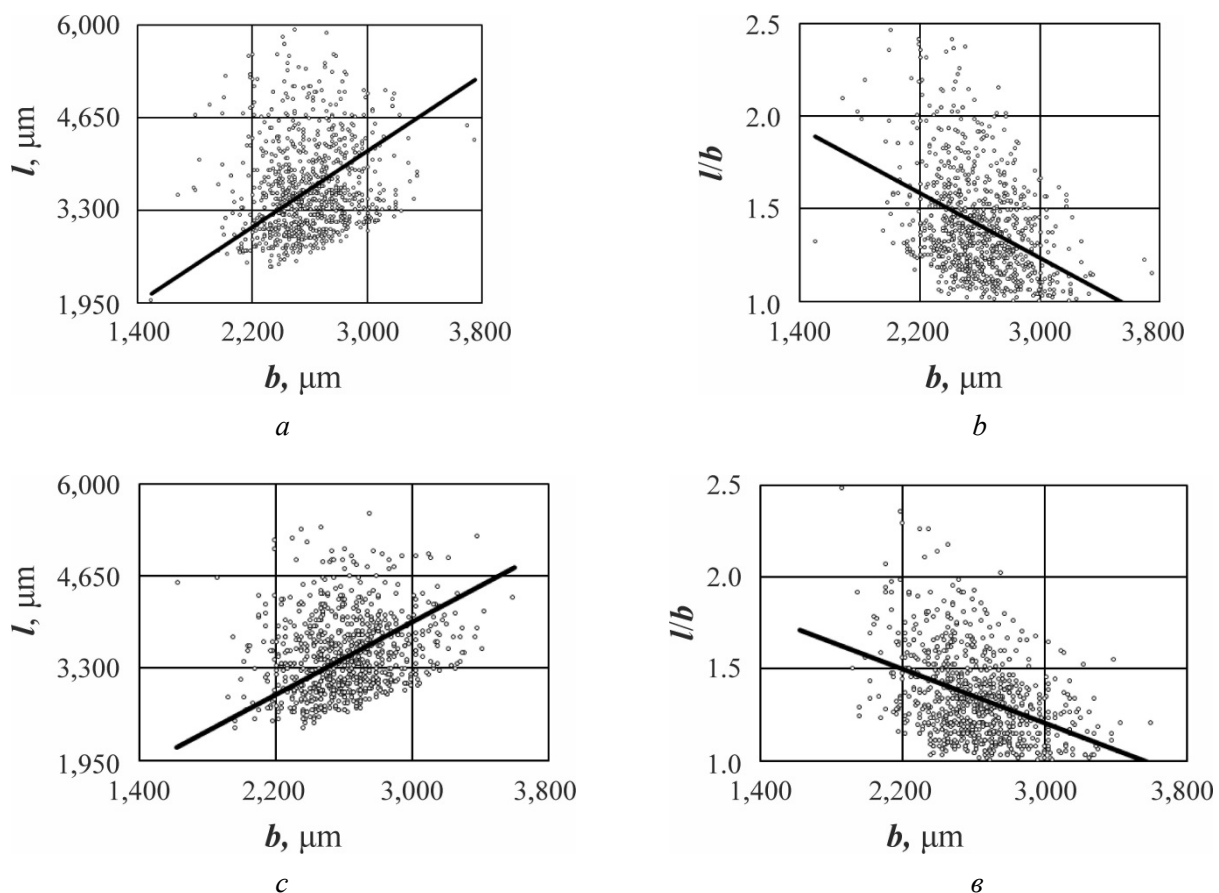
Fig. 5. Regression relationships between geometric parameters of grains in fraction **2**:

a, b – roller-press grinding; *c, d* – rotary grinding
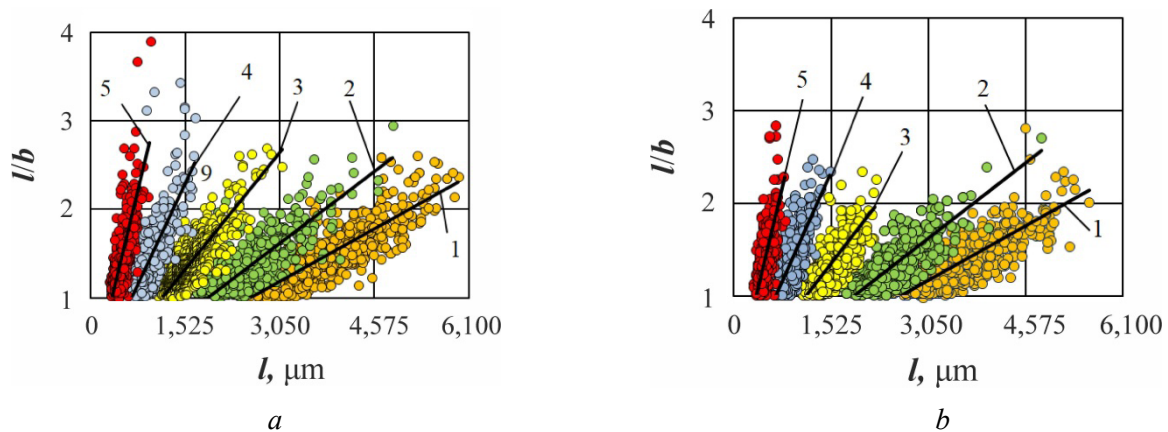
Fig. 6. Dependence of the aspect ratio *l/b* on grain width *b* for five fractions after roller-press (*a*) and rotary (*b*) grinding

A quantitative evaluation of the content of needle-shaped and isometric grains obtained by roller-press and rotary grinding is presented in fig. 7. Following roller-press grinding, the content of needle-shaped grains (*l/b* > 2) in the five fractions ranges from 2.8 % to 5.2 %, while following rotary grinding, it ranges from 0.9 % to 1.9 %. On average, the number of needle-shaped grains in the five-fraction samples is reduced threefold after rotary grinding compared to roller-press grinding.
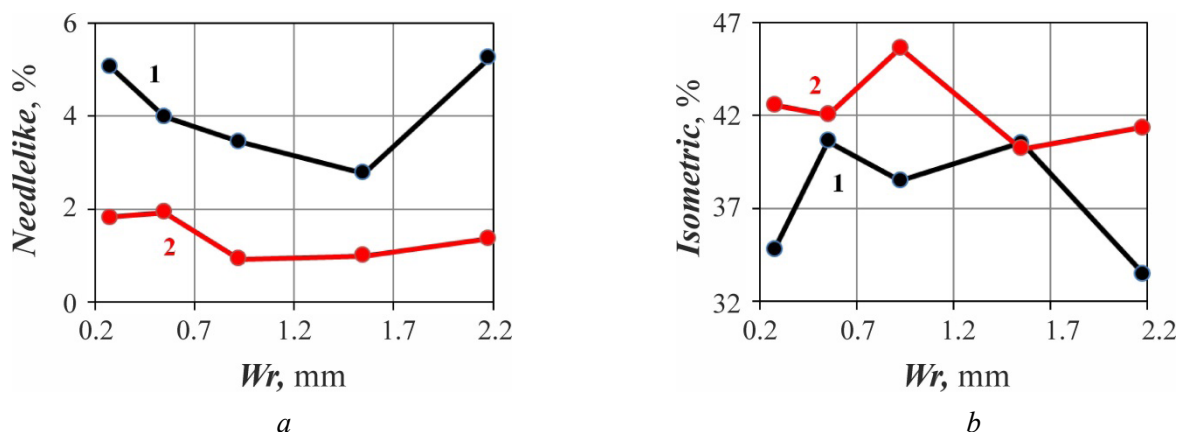
Fig. 7. Content of needlelike (*a*) and isometric (*b*) grains after roller-press (1) and rotary (2) grinding, depending on the average cell size of the upper and lower sieves of the *Wm* fraction

The proportion of isometric grains (*l/b* ≤ 1.3) after both roller-press and rotary grinding ranges from 33 % to 46 % (fig. 7). Rotary grinding yields the highest proportion of isometric grains, ranging from 40 % to 46 %. Following roller-press grinding, the proportion of isometric grains ranges from 33 % to 41 %. The average proportion of isometric grains is approximately 42 % after rotary grinding and 37 % after roller-press grinding, representing a 5 % decrease.

Conclusions

1. The grain shape factor distributions after roller-press and rotary grinding adhere to the law of maximum value. The geometric parameters used to calculate the shape factor follow these distribution models: grain length – the law of maximum value, grain width – the normal distribution.

2. Given that, of the three geometric parameters analyzed, only grain width follows the normal distribution, it is impossible to meet a prerequisite for using the *Pearson* correlation coefficient: the analyzed datasets of geometric parameters must conform to a normal distribution. Consequently, *Spearman's* rank criterion was employed to assess the relationship strength.

3. The following *Spearman's* rank criterion (**ρ**) were obtained: between grain length (***l***) and width (***b***), **ρ** does not exceed 0.3, indicating a weak, direct correlation; between grain width (***b***) and shape factor (***l/b***), **ρ** ranges from −0.35 to −0.50, indicating a moderate, inverse correlation; and between grain length (***l***) and shape factor (***l/b***), **ρ** exceeds 0.7, indicating a strong, direct correlation.

4. Using graphical examples of the relationships between geometric parameters in fraction 2, it is demonstrated that the number of grains with a length approaching the upper size limit (***l*** ≥ 4,650 μm) is significantly higher after roller-press grinding compared to rotary grinding.

5. Rotary grinding increases the proportion of isometric grains by an average of 5 % compared to roller-press grinding and by 8 % in the largest fraction. Roller-press grinding is characterized by a higher content of needle-shaped grains. The average content of needle-shaped grains across the five fractions is approximately 4 %. Rotary grinding reduces the number of needle-shaped grains threefold. The content of needle-shaped grains increases from larger fractions to smaller fractions and from rotary grinding to roller-press grinding.

References

1. Bogutsky V.B., Shron L.B. Izmenenie kharakteristik rabochei poverkhnosti shlifoval'nogo kruga za period ego stoikosti [Change in the characteristics of the grinding wheel face during its redress life]. *Vestnik YuUrGU. Seriya: Mashinostroenie = Bulletin of the South Ural State University. Series: Mechanical Engineering*, 2019, vol. 19, no. 2, pp. 66–74. DOI: 10.14529/engin190206.

2. Bratan S.M., Kharchenko A.O., Chasovitina A.S. Analiz i modelirovanie zakonomernostei izmeneniya razmerov profilei abrazivnykh zeren i ploshchadok iznosa v protsesse shlifovaniya [Analysis and modeling of patterns of changes in the size of profiles of abrasive grains and platforms wear in the grinding process]. *Vestnik sovremennykh tekhnologii = Journal of Modern Technologies*, 2020, no. 1, pp 43–48.

3. Chen J., Cui C., Huang G., Huang H., Xu X. Characterization of grain geometrical features for monolayer brazed grinding wheels based on grain cross-sections. *The International Journal of Advanced Manufacturing Technology*, 2019, vol. 105, pp. 1425–1436. DOI: 10.1007/s00170-019-04354-1.

4. Schnabel' M., Buhr A., Schmidtmeier D., Chatterdjee S., Dutton J. Sovremennye predstavleniya o plavlenykh i spechennykh ogneupornykh zapolnitelyakh [The modern concepts of the fused and sintered refractory aggregates]. *Novye ogneupory = New Refractories*, 2016, no. 3, pp. 107–114. DOI: 10.17073/1683-4518-2016-3-107-114.

5. Odarchenko I.B., Prusenko I.N. Rol' ogneupornogo napolnitelya v protsessakh strukturoobrazovaniya sterzhnevykh smesei [The role of refractory filler in the processes of structural formation of core mixtures]. *Lit'e i metallurgiya = Foundry Production and Metallurgy*, 2017, no. 4, pp. 89–93.

6. Yoshihara N., Takahashi H., Mizuno M. Effect of the abrasive grain distribution on ground surface roughness. *International Journal of Automation Technology*, 2022, vol. 16 (1), pp. 38–42. DOI: 10.20965/ijat.2022.p0038.

7. Sazonov S.E., Emchenko E.A., Strelyanaya Yu.O. Issledovanie povysheniya effektivnosti protsessa shlifo-vaniya krugami iz klassifitsirovannogo po forme abrazivnogo zerna [Study of increasing efficiency of the circular grinding process from classified by the form of abrasive grain]. *Aktual'nye problemy v mashinostroenii = Actual Problems in Machine Building*, 2020, vol. 7, no. 3–4, pp. 59–63.

8. Shatko D.B., Lyukshin V.S. Issledovanie rezhushchei sposobnosti edinichnykh abrazivnykh zeren v zavisimosti ot ikh formy i prostranstvennoi orientatsii [Investigation of cutting capacity of single abrasive grains depending on their shape and spatial orientation]. *Vestnik Kuzbasskogo gosudarstvennogo tekhnicheskogo universi-teta = Bulletin of the Kuzbass State Technical University*, 2023, no. 5, pp. 23–30. DOI: 10.26730/1999-4125-2023-5-23-30.

9. Korotkov A., Korotkov V. Grinding tools made of grains with controlled shape and orientation. *MATEC Web of Conferences*, 2018, vol. 224, p. 01071. DOI: 10.1051/matecconf/201822401071.

10. Garshin A.P., Fedotova S.M. *Abrazivnye materialy i instrumenty. Tekhnologiya proizvodstva* [Abrasive materials and tools. Manufacturing technology]. St. Petersburg, Polytechnic University Publ., 2008. 1009 p. ISBN 978-5-7422-1853-1.

11. Tamás L., Rácz Á. Comparison of particle size and shape distribution of corundum produced by industrial ball mill and material bed compression. *Multidiszciplináris tudományok*, 2021, vol. 11, pp. 59–67. DOI: 10.35925/j.multi.2021.5.6.

12. Li Z., Zhai H., Tan M. Particle shape characterization of brown corundum powders by SEM and image analysis. *IET Conference Publications*, 2006, pp. 1310–1313. DOI: 10.1049/cp:20060969.

13. Wang Y., Mei J., Zou Y., Zhang D., Cao X. Machine learning reveals the influences of grain morphology on grain crushing strength. *Acta Geotechnica*, 2021, vol. 16, pp. 3617–3630. DOI: 10.1007/s11440-021-01270-1.

14. Tang P., Dai B., Zhou Z., Ma W. Crushing mechanism analysis of sintered ore and study of particle size distribution pattern after crushing. *Ironmaking & Steelmaking: Processes, Products and Applications*, 2024, vol. 51, pp. 527–545. DOI: 10.1177/03019233241248987.

15. Ajaka O., Akinbinu V. Design, fabrication and performance analysis of a planetary roll mill for fine grinding. *ARPN Journal of Engineering and Applied Sciences*, 2011, vol. 6, pp. 75–90.

16. Cao J., Liu L., Han Y., Feng A. Comminution behavior and mineral liberation characteristics of low-grade hematite ore in high pressure grinding roll. *Physicochemical Problems of Mineral Processing*, 2019, vol. 55, pp. 575–585. DOI: 10.5277/ppmp18169.

17. Lyukshin V.S., Shatko D.B. Sovershenstvovanie protsessa sortirovki abrazivov po forme [Improving the process of sorting abrasives by shape]. *Vestnik Kuzbasskogo gosudarstvennogo tekhnicheskogo universiteta = Bulletin of the Kuzbass State Technical University*, 2022, no. 4 (152), pp. 13–22. DOI: 10.26730/1999-4125-2022-4-13-22.

18. Shatko D.B., Lyukshin V.S., Strelnikov P.A. Separation of abrasive materials according to the form. *Materials Science Forum*, 2018, vol. 927, pp. 35–42. DOI: 10.4028/www.scientific.net/MSF.927.35.

19. Vaisberg L.A., Ustinov I.D. Fenomenologiya vibratsionnoi klassifikatsii i usredneniya po krupnosti granulyarnykh materialov [Phenomenology for vibration-induced size segregation and mixing of granular materials]. *Nauchno-tekhnicheskie vedomosti SPbPU. Estestvennye i inzhenernye nauki = St. Petersburg Polytechnic University Journal of Engineering Science and Technology*, 2019, vol. 25, no. 1, pp. 181–189. DOI: 10.18721/JEST.25118.

20. Baidakova N.V. O printsipakh upravleniya tekhnologicheskoi chast'yu klassifikatora tipa VDK na operatsiyakh spetsrasseva abrazivnykh materialov [Principles of the engineering management of the classifier of TAC type on operations of the special sieving of abrasive materials]. *Tyazheloe mashinostroenie = Heavy Mechanical Engineering*, 2023, no. 4, pp. 29–32.

21. Korotkov A.N., Kostenkov S.A., Lyukshin V.S., Prokaev N.V. *Ustroistvo dlya separatsii shlifoval'nykh zeren po forme* [Device for separation of abrasive grains by shape]. Patent RF, no. 2236303, 2004.

22. OAO «Volzhskii abrazivnyi zavod» [OJSC "Volzhsky Abrasive Works"]. Website. Available at: https://vabz.ru/ (accessed 21.08.2025).

23. Korotkov A.N., Dubov G.M. Povyshenie effektivnosti otreznogo shlifovaniya [Increase in cutoff grinding efficiency]. *Obrabotka metallov (tekhnologiya, oborudovanie, instrumenty) = Metal Working and Material Science*, 2008, no. 4 (41), pp. 4–6.

24. Nosenko V.A., Rybanov A.A., Makushkin I.A., Shegai A.A., Bukshtanovich K.A. *Programma dlya avtomatizirovannogo opredeleniya geometricheskikh parametrov shlifoval'nogo zerna po fotografii «Zerno NM VPI»* [Program for automated determination of geometric parameters of abrasive grain by photograph 'Zerno NM VPI'"]. The Certificate on official registration of the computer program, no. 2011610144, 2011.

25. Gmurman V.E. *Teoriya veroyatnostei i matematicheskaya statistika* [Probability theory and mathematical statistics]. 12th ed. Moscow, Yurait Publ., 2012. 478 p. ISBN 978-5-9916-1589-1.

Conflicts of Interest

The authors declare no conflict of interest.

Obrabotka metallov –
Metal Working and Material Science

Journal homepage: http://journals.nstu.ru/obrabotka_metallov

Investigation of the process of surface decarburization of steel 20 after cementation and heat treatment

Yulia Karlina [1, a, *], Vladimir Konyukhov [2, 3, b], Tatiana Oparina [2, c]

[1] National Research Moscow State University of Civil Engineering, 26 Yaroslavskoe Shosse, Moscow, 129337, Russian Federation
[2] Irkutsk National Research Technical University, 83 Lermontova str., Irkutsk, 664074, Russian Federation
[3] Cherepovets State University, 5 Lunacharsky pr., Cherepovets, 162600, Russian Federation

[a] https://orcid.org/0000-0001-6519-561X, jul.karlina@gmail.com; [b] https://orcid.org/0000-0001-9137-9404, konyukhov_vyu@mail.ru;
[c] https://orcid.org/0000-0002-9062-6554, martusina2@yandex.ru

ARTICLE INFO

ABSTRACT

Introduction. In industry, the method of carburizing with a solid carburizer is used to saturate the surface layer with carbon. In practice, it is necessary to prevent or reduce surface decarburization of steel as much as possible, either by using a protective atmosphere or by heating under conditions in which the oxidation process of the metal surface layer occurs faster than the decarburization process. During decarburization, a ferrite structure is formed in the surface layer, which, under contact loads, reduces the resistance to crack initiation and increases the probability of fatigue failure of the product as a whole. **The purpose of this work** is to evaluate the effect of heating temperature during carburizing and subsequent hardening, as well as equalizing period, on the depth of the decarburized layer during chemical-thermal treatment of low-carbon steel. **Research methods.** The chemical composition of the steel as delivered was determined. The analyses were performed using an optical emission spectrometer, model *LAVFA18B Spectrolab*. For the study, unalloyed hypoeutectoid Steel 20 was selected, with an initial ferrite-pearlite microstructure. The samples had a rectangular shape with average dimensions of 50 mm × 10 mm × 10 mm. Carbon saturation was carried out on one side (from the side of the poured carburizer, while the reverse surface of the samples was protected by a layer of clay). The samples were placed in a metal container, filled with carburizer in a 25–30 mm layer, closed with a lid, and sealed. Carbon saturation was carried out at 900 °C for 4–8 hours. After that, the box with samples was taken out of the furnace and cooled in air. Quenching was carried out in a furnace in air (humidity was not measured) at furnace heating temperatures of T = 780 °C, 850 °C, and 950 °C with a equalizing period of 4.6 h in a laboratory electric resistance furnace with a chamber volume of V = 22 dm³. Metallographic examination and microhardness measurements were performed. **Results and discussion.** During the experiments, it was noted that the heating temperature for carburizing and quenching plays an important role in decarburization. At a temperature of 700 °C, the decarburization phenomenon was not observed, indicating that the decarburization reaction did not occur below this temperature. When the temperature exceeds 750 °C, the samples exhibit obvious decarburization, and the ferrite structure is columnar, oriented perpendicular to the decarburized surface. A partial decarburized layer appears in the samples at 850 °C, and the thickness of the full decarburized layer decreases. Above 900 °C, the sample mainly shows a partial decarburized layer because, at this temperature, the steel structure is fully austenitic. Above 1,000 °C, the layer thickness increases rapidly, showing exponential growth. The experiments also demonstrated the effect of heating and equalizing periods on the depth of the decarburized layer. The presented results will be useful in chemical-thermal treatment of products requiring high surface hardness.

Introduction

Steels are currently among the most widely used materials in various industrial applications because they are easily accessible, machinable, and weldable [1]. The surfaces of machine parts, tools, and fasteners are exposed to external forces and must possess enhanced strength and wear resistance. Typically, improved mechanical properties of the steel surface can be achieved by modifying the microstructure and chemical composition. This is usually accomplished by using high-carbon and alloy steels as well as various thermal or thermochemical treatments [1, 2].

* Corresponding author
Karlina Yulia I., Ph.D. (Engineering), Research Associate
National Research Moscow State Construction University,
Yaroslavskoe shosse, 26,
129337, Moscow, Russian Federation
Tel.: +7 914 879-85-05, **e-mail:** jul.karlina@gmail.com

The effectiveness of heat treatment applied to carbon steels (C% < 0.25) remains limited because such treatment does not sufficiently improve surface properties (hardness, wear and impact resistance, fatigue, etc.) to meet the stringent surface requirements of contacting parts [1–10].

Among chemical-thermal treatment methods, carburization (using solid, gas, or liquid saturating media) is one of the most effective processing techniques. It aims to enrich the surface with carbon in the atomic state (from 0.7 to 0.9 wt.%) by diffusion into the austenite phase (at temperatures from 870 to 980 °C depending on the process), followed by quenching and tempering to enhance the mechanical properties of the surface according to the decreasing carbon gradient at a very limited depth, without affecting the core [1–5]. Taking this into account, it becomes possible to reduce the cost of the final product by using carbon steels (C% < 0.25) instead of expensive high-carbon alloy steels. On the other hand, the presence of carbon limits grain refinement on the steel surface, which suppresses the mobility of plastic deformation during solid-to-solid interaction [5–8].

Recently, various researchers have actively developed metal surface layers with gradient solid phases, using different technological methods of surface alloying with carbon, nitrogen, boron, etc. [6, 7].

In [7–13], studies were conducted on the influence of alloying elements such as *Si*, *Ni*, *Cr*, and *Mo* on the carburization characteristics of steels. A significant influence of these alloying elements on the carburization behavior of *AISI 1018*, *4820*, *5120*, and *8620* steels was demonstrated. The authors consider decarburization as the reverse process of carburization and conclude that alloying elements also significantly affect the decarburization of steel. Experimental results showed that *Si* promotes decarburization of ferrite, whereas *Cr* inhibits it in high-carbon steels.

In [15], the influence of certain alloying elements on the decarburization of *TRIP* steel (transformation-induced plasticity) was studied. Experimental results revealed that increasing the content of *Si* and *P* accelerates decarburization. Decarburization is a process wherein carbon atoms diffuse outward from the material and react with furnace gas. Therefore, the effect of alloying elements on steel decarburization primarily affects the diffusion of carbon atoms.

Many authors [1–8] investigated the thermodynamics and activity coefficients of carbon in *FCC* (face-centered cubic) *Fe–Mn–C*, *Fe–Si–C*, *Fe–Ni–C*, and other ternary alloys. Experimental results showed that *Mn* decreases the activity coefficient of carbon in austenite, which in turn reduces the diffusion coefficient of carbon. Conversely, the effect of *Si* on the diffusion coefficient of *C* in austenite is opposite to that of *Mn*. Although experimental methods can reveal the effect of alloying elements on carbon atom diffusion, elucidating the underlying atomic-level mechanisms remains a challenging practical task.

In the practice of many enterprises, an easily implemented, simple, and inexpensive method of carburizing machine parts and mechanisms made of low-carbon steels is the use of a solid carburizer. In industry [1, 2], a two-stage process is traditionally applied: the first stage involves saturating parts with carbon using a solid carburizer followed by air cooling, and the second stage involves hardening and tempering. To reduce carburization period, the heating and equalizing temperature is set in the range of 900–1150 °C [10, 11]. A mandatory requirement for parts subjected to such processing is the allowance of 1–3 mm for subsequent machining in order to remove the decarburized layer. The addition of a large amount of carbon and other alloying elements to these steels leads to serious segregation of composition and surface decarburization of the products.

It has been reported that composition segregation and decarburization have a negative effect on impact toughness, fatigue life, wear resistance, and other properties critical to the performance of medium carbon steels [4–7]. Decarburization reduces surface hardness and fatigue strength of steel, thereby shortening its service life [1, 2, 8–13].

Decarburization of the steel surface results in insufficient hardness in the surface region due to the reduction of carbon content, which greatly reduces fatigue life. Obviously, when steel is heated to high temperatures without a protective atmosphere, the surface layer reacts with oxygen, carbon dioxide, or steam in the furnace atmosphere, causing oxidation and decarburization simultaneously [1, 2]. Decarburization is a classic surface degradation phenomenon in the heat treatment of steels [14].

To prevent decarburization, considerable efforts have been made to develop anti-decarburization coatings [6–10]. Decarburization of steel is influenced by many factors, including heating temperature and heating period [1, 2], atmosphere [12, 13], alloying elements [2, 7, 9], scale layer characteristics [1], electric field [2], etc. Among these, heating temperature and heating period have been proposed as the two most important control variables according to practical experience [1, 2, 15, 16–22].

The purpose of this work is to evaluate the effects of heating temperature during carburizing and quenching, as well as equalizing period, on the depth of the decarburized layer formed during quenching.

Materials and methods

The chemical composition of the steel in the delivered condition was determined using an optical emission spectrometer, model *LAVFA18B Spectrolab*. For this study, non-alloyed hypoeutectoid Steel 20, compliant with *GOST 1050-2013*, with an initial ferrite-pearlite microstructure, was selected. Rectangular samples measuring approximately 50 mm × 10 mm × 10 mm were cut from a rolled sheet of Steel 20. Mechanical cleaning and grinding of the samples were performed; the surfaces were free of oxide traces.

The carburizer used as the cementing mixture consisted of charcoal grains sized 3.6–10 mm, coated with a barium carbonate film according to *GOST 2407–83*. Carbon saturation was carried out on one side (the side in contact with the poured carburizer), while the reverse surface of the samples was protected by a layer of clay. The samples were placed in a metal container and covered with a 25–30 mm layer of carburizer. The container was sealed with a lid. The operating temperature for carbon saturation of the sample surfaces was set at 900 °C, with a saturation period of 4–8 hours [1, 2]. After saturation, the container with samples was removed from the furnace and cooled in air.

Samples were cleaned of scale using a grinding machine. The influence of surface oxides on decarburization kinetics was eliminated by grinding the samples before quenching, as surface oxides increase the apparent decarburization [1, 2]. Quenching was performed in a furnace in air (humidity was not measured) at furnace temperatures of 780 °C, 850 °C, and 950 °C, with equalizing periods of 4 and 6 hours, using a laboratory electric resistance furnace with a chamber volume of $V = 22$ dm³.

Each sample was placed at the same position in the preheated furnace on a refractory brick in the chamber's center. This ensured identical conditions and the fastest possible heating of each sample to the quenching temperature.

Heating temperatures were monitored using a certified contact thermocouple, which was in contact with the side surface of the sample during heating (introduced into the furnace through a small hole in the furnace door). Heating period was counted from the moment the control thermometer inside the furnace reached the target temperature. Temperature fluctuations during heating were within the range of $T_a - 1 \text{ °C} \leq T \leq T_a + 3 \text{ °C}$, where T_a is the ambient temperature. After equalizing, quenching was carried out in water. The depth of decarburization [1, 2, 14] was investigated using optical microscopy by two methods: the traditional method using an optical microscope equipped with a grid, and computer-assisted measurement based on the image displayed on the screen. Metallographic samples were prepared by wet grinding with *SiC* paper up to 4,000 grit, polishing with ¼ μm diamond paste, and etching with 3% HNO_3 in ethanol.

Decarburization varies on different surfaces (top and side surfaces exposed to atmosphere, and the bottom surface in contact with the refractory brick, including edges and corners) due to differences in oxidation states. Typically, decarburization is more pronounced on surfaces with lower oxidation capacity; therefore, the bottom surfaces usually exhibit stronger decarburization [13, 15].

This study focused exclusively on flat surfaces exposed to the atmosphere. Decarburization was measured on three sections perpendicular to the long side of the sample on the top and both side surfaces.

Results of the research

Carbon content analysis

The surface layer of the low-alloy steel initially had a relatively low carbon content of approximately **α** = (0.21 ± 0.06) wt. %. before carburization, which corresponded to the initial carbon amount of low alloy steels, as shown in Table.

Effect of carburization period on carbon content in Steel 20

	Chemical elements, %						
	C	*Si*	*Mn*	*S*	*P*	*Ni*	*Cr*
GOST 1050-2013	0.17–0.24	0.17–0.37	0.35–0.65	up to 0.035	up to 0.030	up to 0.30	up to 0.25
Fact	0.21	0.27	0.36	up to 0.035	up to 0.030	up to 0.30	up to 0.25
Cementation period: 4 hours	0.53	0.27	0.36	up to 0.035	up to 0.030	up to 0.30	up to 0.25
Cementation period: 6 hours	0.68	0.27	0.36	up to 0.035	up to 0.030	up to 0.30	up to 0.25

However, after carburization of varying duration, the carbon content in the surface layer gradually increased. Specifically, after 4 hours of carburization, the carbon content reached **α** = (0.53 ± 0.016) wt. %, after 6 hours, it reached **α** = (0.68 ± 0.012) wt. %. Experiments with longer saturation duration were also carried out.

The results of the experiments are shown in Fig. 1–3. It was found that increasing the saturation period of the samples with carbon to 8 hours increases the carbon content in the surface layer of steel. Moreover, with saturation of 8 hours or more, the samples completely have a pearlite structure with a carbon content of 0.8 %. Based on these experiments, it was subsequently decided to reduce the saturation time to 2 hours in order to minimize the experiments.

Microstructural analysis

After carburizing, a significant increase in the surface layer thickness by more than 41 % was observed as the equalizing period increased (Figs. 1 and 2). The thickness increased from approximately 1,100 μm to more than 1,500 μm, as shown in Fig. 3.

As the equalizing period in the furnace increases, a decarburized layer appears during heating for hardening. This can be seen from the results of microhardness measurements in Fig. 4 and the metallographic analysis of the surface in Fig. 5. The effect of heating temperature on hardening is shown in Fig. 6.

In our experiments, it was found that temperature played an important role in decarburization. At 700 °C, no decarburization phenomenon was observed, indicating that the decarburization reaction did not occur in the samples below 700 °C. When the temperature exceeds 750 °C, the sample exhibits obvious

a	b	c	d
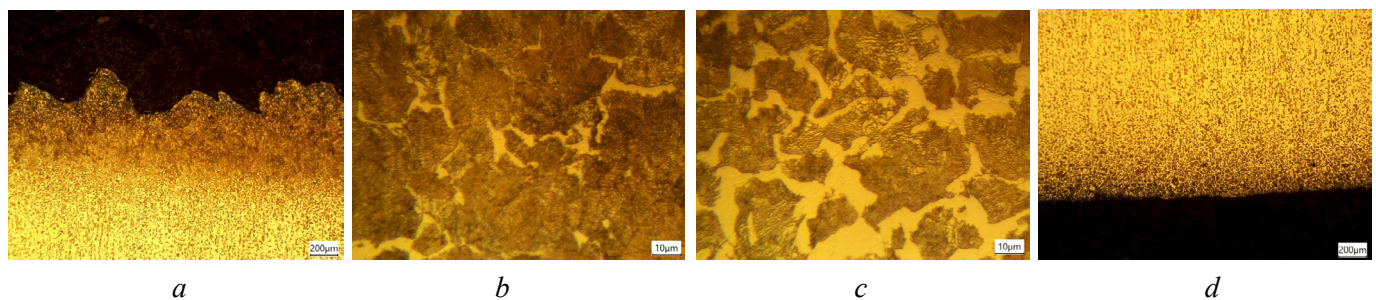
Fig. 1. The microstructure of the cemented layer of Steel 20 after equalizing for 4 hours at 900 °C:

a – surface layer; *b* – at a depth of 100 μm; *c* – transition layer to the base metal; *d* – reverse side of the sample
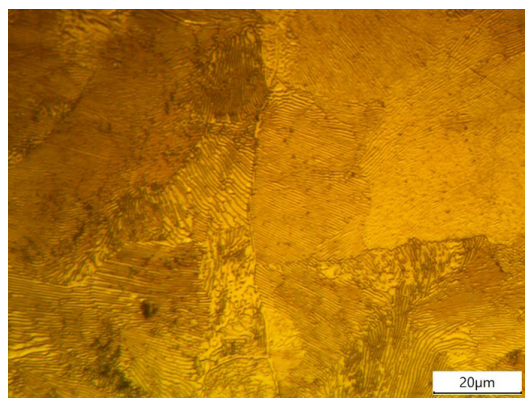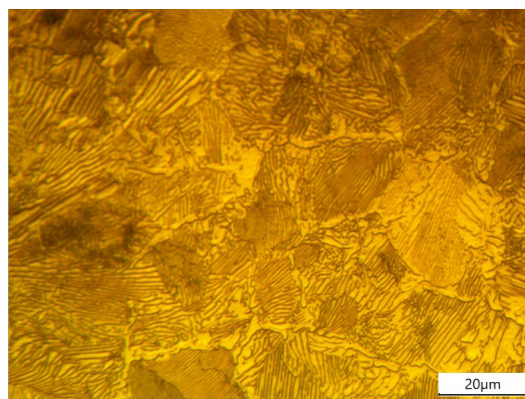
a   *b*

Fig. 2. Pearlite structure in the carburized layer of Steel 20 after equalizing for 6 hours at 900 °C:
a – pearlite structure in the surface layer; *b* – in the middle of the sample

Fig. 3. Comparative evaluation of carbon content, microhardness, and depth of the cemented layer as a function of saturation period
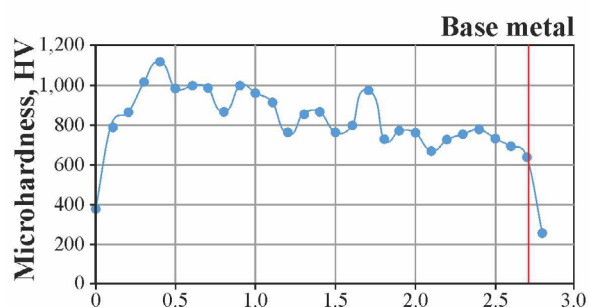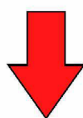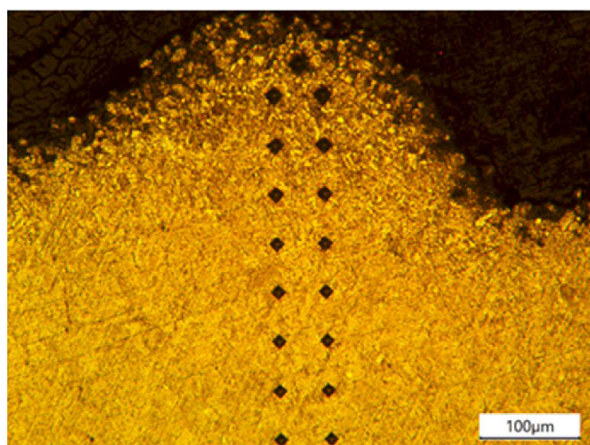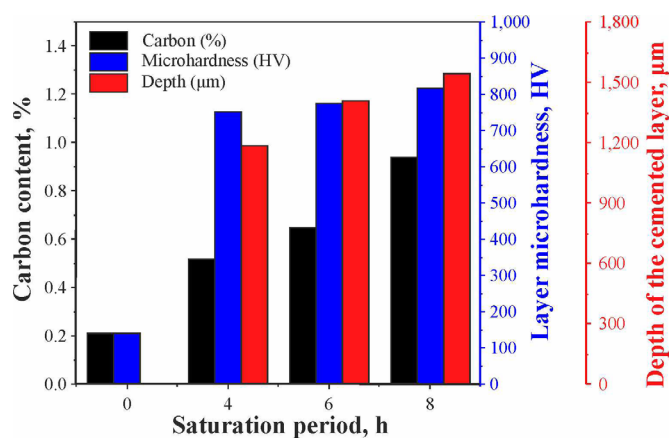
Fig. 4. Photo of point of indentation and graph of microhardness distribution across the depth of the surface cemented layer

a   *b*   *c*
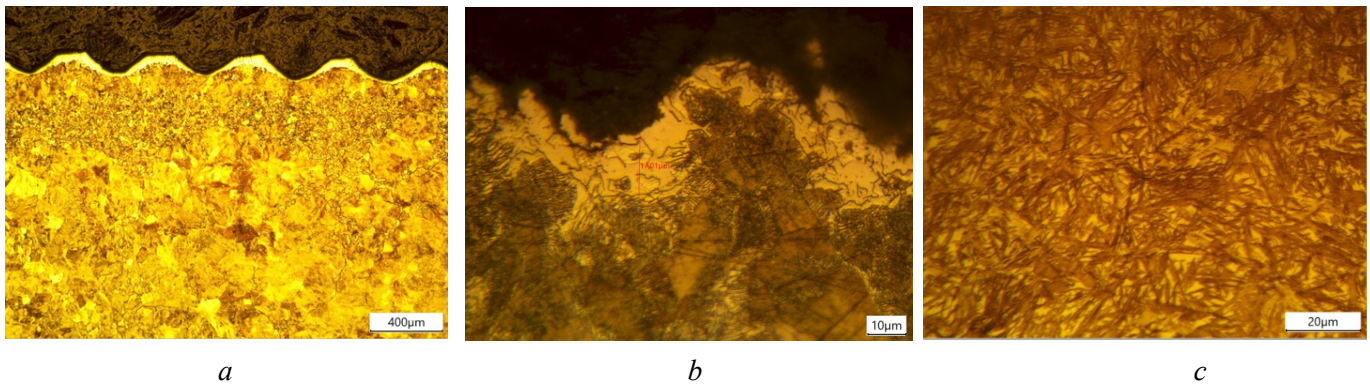
Fig. 5. Photo of the surface layer after heating for hardening at 950 °C and equalizing for 6 hours:
a and *b* – decarburized layer at different magnifications; *c* – quenched martensite in the surface layer
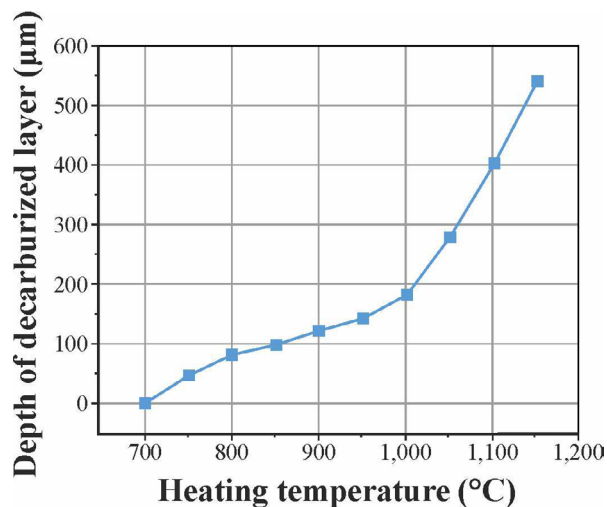
Fig. 6. Depth of decarburization as a function of heating temperature (equalizing for 50 min)

decarburization, and the ferrite structure becomes columnar, perpendicular to the decarburization surface. A partly decarburized layer appears in the sample at 850 °C, and the thickness of the fully decarburized layer decrease. The decarburized layer is composed of both complete and partial decarburization zones. Above 900 °C, the sample mainly shows a partly decarburized layer, because at this temperature the steel structure is completely austenitic, as ferrite and pearlite (a mixture of cementite and ferrite) are transformed into austenite. Carbon from austenite passes into the furnace atmosphere and interacts with furnace oxygen. As a result, the steel becomes depleted in carbon content. The average depth of the fully decarburized layer of each sample is shown in Fig. 7. As shown in Fig. 6, at a heating temperature below 1,000 °C, the thickness of the total decarburized layer increases slowly. However, above 1,000 °C, the thickness increases rapidly, showing exponential growth. The experiments showed the effect of heating and equalizing periods on the depth of the decarburized layer (Fig. 7).

The depth of the decarburized layer was measured using an optical microscope, and the average decarburization depth of the samples is shown in Fig. 6. As can be seen in Fig. 6, the depth of the decarburized layer of the samples increased exponentially with the heating temperature, and parabolically with the equalizing period in the furnace at different temperatures (Fig. 7), with the growth rate gradually slowing down.

To protect the surface of the cemented layer, it is necessary to apply a coating that will protect the surface from contact with the furnace atmosphere during heating for hardening (Fig. 8). It is known that the effective depth of the cemented layer is related to the hardness in depth after hardening, which ranges from 555 to 600 HV (Fig. 8).
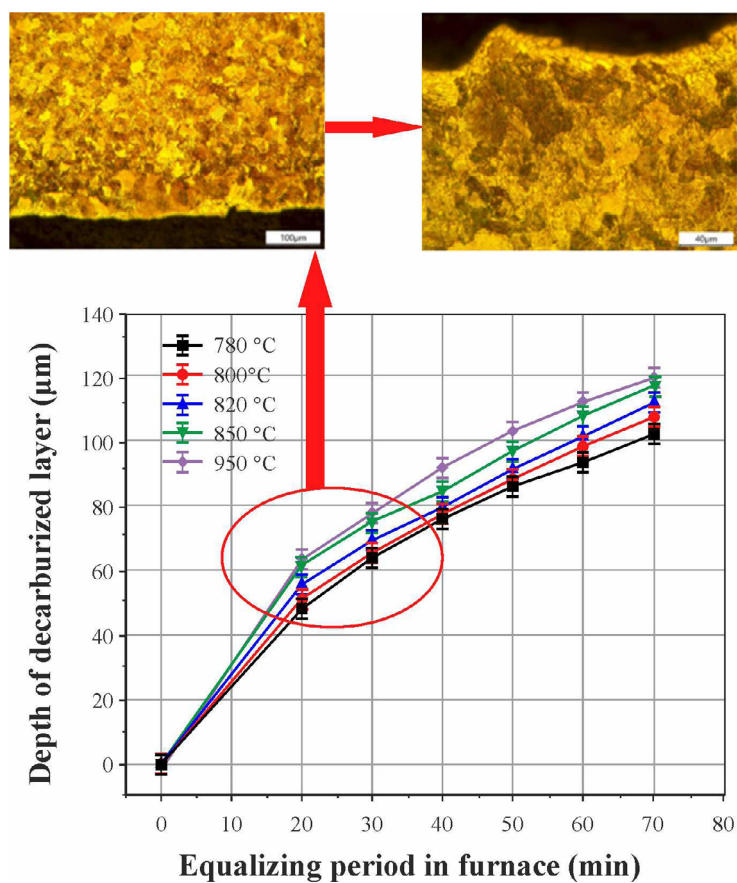
Fig. 7. The effect of heating temperature and equalizing period on the overall depth of decarburization
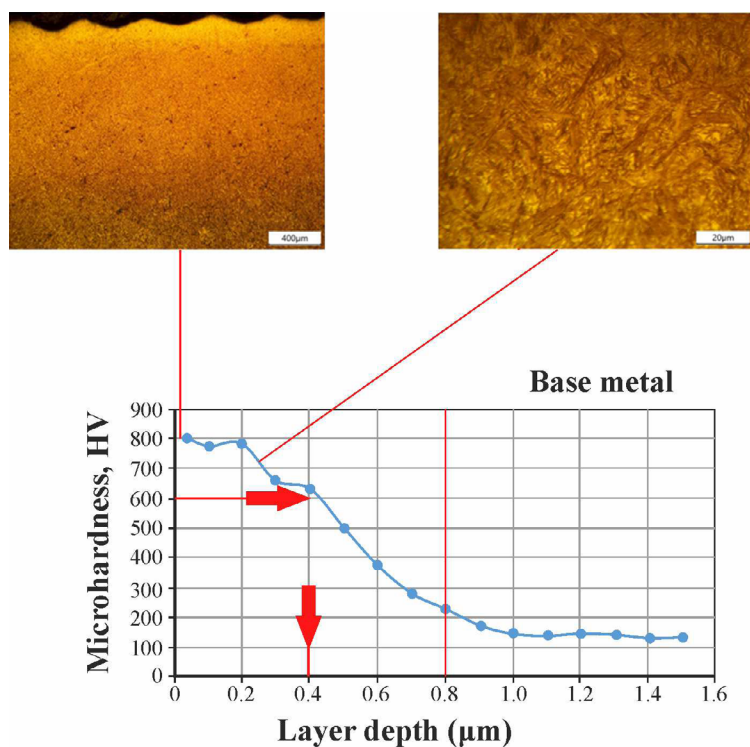
Fig. 8. Microstructure of the surface layer after cementation quenching with surface protection from oxygen

Discussion of the results

From the analysis of the literature, it is evident [1–12, 17–21] that the theoretical discussion of the depth of decarburization during heating remains a debatable issue.

The works [1, 2] provide information that in 1946 *Pennington* conducted a comprehensive study of the decarburization of carbon steel in the temperature range of 691–927 °C in an atmosphere containing 20 % $H_2O – H_2$, in which oxidation of steel could not occur. In this study, it was found that a ferrite "band" formed on the steel surface at 732–893 °C, but not at 691 °C and 927 °C, while the maximum ferrite thickness was observed at 790–815 °C. *Pennington* explained the decrease in ferrite thickness above 905 °C by a decrease in the solubility of carbon in ferrite to zero at 905 °C. One of the limitations of *Pennington's* analysis was the assumption that the carbon concentration in the formed ferrite was constant throughout the ferrite layer and, therefore, that carbon diffusion within the ferrite did not contribute to its growth. Simultaneous oxidation and decarburization were studied by *Birks* and colleagues in 1970. Based on these studies, it was stated that "the mechanism by which decarburization of steels occurs has been well studied, particularly in the case of plain carbon and low alloy steels" [1, 2]. However, the scope of the studies by *Birks* et al. was limited. First, the studies focused on decarburization occurring only in the austenite. Second, although it was recognized that in an oxidizing atmosphere decarburization occurs through a reaction between the scale and dissolved carbon in the steel, *Birks* and colleagues continued to assume that the carbon concentration at the scale-steel interface was zero because of its low value.

It is known that decarburization and surface oxidation occur simultaneously on the steel surface when heated in an oxidizing environment. In essence, decarburization is a reaction between carbon in the matrix and oxygen, while oxidation is a reaction between iron and oxygen. Therefore, decarburization is closely related to oxidation, and the relationship between them is competitive. The formation of an oxide layer on the steel surface consumes part of the decarburized surface layer and, thus, reduces the final observed decarburization thickness. Therefore, to obtain more accurate results, it is necessary to take into account the oxidation process. The absolute thickness of the total decarburized layer can be considered as the sum of the thicknesses of the observed total decarburization and the oxide scale. In practice, the thickness of the oxide scale cannot be measured accurately, since the oxide layer tends to flake off from the sample surface during the cooling period and subsequent manipulations.

When examining the *Fe–O* phase diagram [1, 2], we assumed that the oxide layer on the surface of iron and unalloyed steel consists of only one oxide, *FeO*, which is formed during heating in air at temperatures ($T > 570$ °C). In reality, according to [1, 2], the high partial pressure of oxygen and different iron chemical valence create an oxide layer consisting of three different oxides at these temperatures. The sequence from the oxide with the least amount of oxygen, closest to the metal, to the oxide with the highest amount of oxygen, closest to the atmosphere, has been recorded as: FeO / Fe_3O_4 / Fe_2O_3 — wustite / magnetite / hematite [1, 2]. The layer thickness is generally constant at ($T > 700$ °C), and its composition is approximately 95 % FeO, 4 % Fe_3O_4, and 1 % Fe_2O_3 [1, 2].

At temperatures ($T = 570–800$ °C), however, results can be found [16–22] that deviate both in terms of composition and thickness of the individual layers, demonstrating the complexity of the oxidation of iron and unalloyed steel in this temperature range [14]. The formation of a three-layer oxide layer can be explained simply using direct oxidation chemical reactions. The mechanism of formation of a three-layer oxide layer at the FeO/Fe_3O_4 and Fe_3O_4/Fe_2O_3 phase boundaries remains a subject of discussion due to its complexity, which is a consequence of specific transport processes through individual oxide layers [2, 15, 16].

When discussing carbon oxidation, it is necessary to take into account the microstructure of the steel at the heating temperature and the temperature range of stability for CO_2 and CO. Carbon in unalloyed hypoeutectoid steel at temperatures $T > A_{C1}$ is present only in solid solution dissolved in *Fe-α* (ferrite) and *Fe-γ* (austenite). Ferrite is stable at $T < A_{C3}$, and austenite is stable at $T > A_{C1}$. Carbon reacts with oxygen to form CO and CO_2 during heating of steel in air. The reactions of direct oxidation of carbon by oxygen ($C + O_2 \rightarrow CO_2$ and $2C + O_2 \rightarrow 2CO$) intersect at approximately T ≈ 700 °C [1, 2]. The lines of both reactions show that at $T > 700$ °C, CO is more stable, or that CO is preferentially formed at T > A_{C1} [1, 2].

This means that, relative to the *Boudouard* equilibrium ($C + CO_2 \leftrightarrow 2CO$), the reaction proceeds from left to right at T > 700 °C) [1, 2, 12, 17], indicating a tendency towards decarburization at $\textbf{\textit{T}} > A_{C1}$. Since an increase in temperature favors the preferential oxidation of carbon to form *CO*, the equilibrium concentration of *CO* in the resulting gas mixture also increases [1, 2].

According to [20–22], it is important to know that gas mixtures ($CO + CO_2$) cause decarburization of steel if their composition lies below or to the right of the equilibrium line for this steel, while they cause carburization if their composition lies above or to the left of this line.

During heating for quenching in air, decarburization of steel is initiated by the general oxidation of the steel surface due to the high partial pressure of oxygen. The oxidation and decarburization reactions occur simultaneously; therefore, various effects on both processes are intertwined, some directly proportional and some inversely proportional. As mentioned earlier, decarburization is visible only if the oxidation of the steel surface is slower than its decarburization, i.e., when the oxidation of carbon and the rate of carbon diffusion are greater than the oxidation rate. Visible decarburization depends on the oxidation potential of the atmosphere in the quenching furnace, which also determines the degree of surface oxidation. This is the reason for the large differences in visible decarburization that occur when heating in air or, for example, in a mixture of $N_2 + 2\% O_2$ [8].

Visible decarburization is always greater when heated in low-oxygen atmospheres [8, 10]. It is also influenced by the adherence of the oxide layer to the steel surface (poor adherence of the oxide layer increases decarburization due to a decrease in the oxidation rate) and its permeability to gases (an impermeable oxide layer reduces decarburization), the carbon content of the steel, and the cooling rate after heating, while different alloying elements affect the kinetics of oxidation and decarburization. At low cooling rates, decarburization also occurs during cooling, especially in the two-phase ($\alpha + \gamma$) region where the surface ferrite layer thickens due to slower oxidation. In hypoeutectoid unalloyed steels, the overall visible decarburization decreases with higher cooling rates. This is a consequence of the decrease and convergence of the temperatures A_{r3} and A_{r1} and the resulting decrease in ferrite content due to the increased pearlite content [1, 2]. At some point for each steel characteristic, the critical cooling rate is reached, A_{r3} and A_{r1} temperatures become equal. At this point, there is no longer any hypoeutectoid ferrite in the microstructure. If the cooling rate is thus high enough for the partially decarburized layer, then hypoeutectoid ferrite will no longer form in this layer either, and only pearlite will exist there.

At even higher cooling rates, bainite or martensite is formed in the partially decarburized layer. Because of this, the partially decarburized layer is not fully visible at higher cooling rates and may disappear completely at a sufficiently high cooling rate, leaving only the fully decarburized surface layer visible. The metallographically determined decarburization depth is always smaller than the actual depth [1, 2]. In metallographic analysis, it is also necessary to take into account the limited ability of the human eye to detect small differences in the content of ferrite and pearlite or globular cementite in ferrite (spheroidized state), which further reduces the estimated thickness of the decarburized layer and increases the observation error. More accurate values for the decarburization depth are determined by microhardness measurements, but these are still not as accurate as the actual depths measured by chemical analysis [19, 22].

Thus, our experiments show a significant increase in carbon content by more than three times with longer equalizing periods during the carburizing process (Fig. 3).

The observed increase in carbon content can be explained by carbon diffusion, which is influenced by both the absorption rate and the carburizing duration. This diffusion process facilitates the reaction with iron in the low alloy gear steel, resulting in the formation of a new carbon-based phase. A similar trend of increasing carbon content in the surface layer of *Fe-C-Mn* steels with longer carburizing periods has been observed [14–20]. The increase in thickness indicates successful diffusion of carbon into the surface layer during carburizing. As carbon diffuses into the steel, it combines with iron to form a new carbon-based phase, resulting in an increase in the layer thickness. This increased thickness is desirable, as it implies improved mechanical properties after quenching.

Conclusion

1. Oxidation, maximum visible surface decarburization, and the completely decarburized ferrite layer increase with increasing heating period during quenching in a furnace with an air atmosphere, following the parabolic growth law. It is shown that with increasing heating temperature for quenching, the depth of the decarburized layer increases exponentially. The decarburization temperature plays a more important role in the decarburization rate compared to other influencing factors, since decarburization is a thermally activated process and exhibits high temperature sensitivity.

2. It was found that heating to a quenching temperature of T = 850–870 °C for t = 1 hour, under oxidizing furnace conditions, leads to decarburization of the surface layer to a depth of 5–10 μm.

3. It was found that heating to a quenching temperature of T = 1,100 °C in the oxidizing atmosphere of the furnace, with holding times ranging from 0.5 hours to 2 hours at an ambient temperature of T_a, results in the formation of a ferrite layer with a thickness of 50-100 μm.

References

1. Lakhtin Yu.M. *Metallovedenie i termicheskaya obrabotka metallov* [Metallology and heat treatment of metals]. Moscow, Metallurgiya Publ., 1983. 359 p.

2. Lakhtin Yu.M., Arzamasov B.N. *Khimiko-termicheskaya obrabotka metallov* [Chemical and thermal treatment of metals]. Moscow, Metallurgiya Publ., 1985. 256 p.

3. Choi S., Zwaag S.V.D. Prediction of decarburized ferrite depth of hypoeutectoid steel with simultaneous oxidation. *ISIJ International*, 2012, vol. 52 (4), pp. 549–558. DOI: 10.2355/isijinternational.52.549.

4. Zhang C.L., Xie L.Y., Liu G.L., Chen L., Liu Y.Z., Li J. Surface decarburization behavior and its adverse effects of air-cooled forging steel C70S6 for fracture splitting connecting rod. *Metals and Materials International*, 2016, vol. 22 (5), pp. 836–841. DOI: 10.1007/s12540-016-5657-x.

5. Carroll R.I., Beynon J.H. Decarburisation and rolling contact fatigue of a rail steel. *Wear*, 2006, vol. 260 (4–5), pp. 523–537. DOI: 10.1016/j.wear.2005.03.005.

6. Ren C.X., Wang D.Q.Q., Wang Q., Guo Y.S., Zhang Z.J., Shao C.W., Yang H.J., Zhang Z.F. Enhanced bending fatigue resistance of a 50CrMnMoVNb spring steel with decarburized layer by surface spinning strengthening. *International Journal of Fatigue*, 2019, vol. 124, pp. 277–287. DOI: 10.1016/j.ijfatigue.2019.03.014.

7. Zhao X.J., Guo J., Wang H.Y., Wen Z.F., Liu Q.Y., Zhao G.T., Wang W.J. Effects of decarburization on the wear resistance and damage mechanisms of rail steels subject to contact fatigue. *Wear*, 2016, vol. 364–365, pp. 130–143. DOI: 10.1016/j.wear.2016.07.013.

8. Li S., Feng H., Wang S., Gao J., Zhao H., Wu H., Xu S., Feng Q., Li H., Liu X., Wu G. Phase transformation behaviors of medium carbon steels produced by twin roll casting and compact strip production processes. *Materials*, 2023, vol. 16 (5), p. 1980. DOI: 10.3390/ma16051980.

9. Xiao Z., Huang Y., Liu H., Wang S. Hot tensile and fracture behavior of 35CrMo steel at elevated temperature and strain rate. *Metals*, 2016, vol. 6 (9), p. 210. DOI: 10.3390/met6090210.

10. Wang X., Lianqi W., Zhou X., Zhang X., Shufeng Y., Chen Y. Protective bauxite-based coatings and their anti-decarburization performance in spring steel at high temperatures. *Journal of Materials Engineering and Performance*, 2013, vol. 22, pp. 753–758. DOI: 10.1007/s11665-012-0309-x.

11. Chen Y.R., Zhang F., Liu Y. Decarburization of 60Si2MnA in 20 Pct H_2O-N_2 at 700 °C to 900 °C. *Metallurgical and Materials Transactions A*, 2020, vol. 51, pp. 1808–1821.

12. Chen Y.R., Zhang F. New development in decarburization research and its application to spring steels. *High Temperature Corrosion of Mater*, 2023, vol. 100, pp. 109–143. DOI: 10.1007/s11085-023-10181-3.

13. Gildersleeve M.J. Relationship between decarburisation and fatigue strength of through hardened and carburising steels. *Materials Science and Technology*, 1991, vol. 7 (4), pp. 307–310.

14. GOST R 54566–2011. *Standartnye metody ispytanii dlya otsenki glubiny obezuglerozhennogo sloya* [State Standard R 54566–2011. Steel. Standard test methods for estimating the depth of decarburized layer]. Moscow, Standartinform Publ., 2014. 15 p.

15. Zorc M., Nagode A., Burja J., Kosec B., Zorc B. Surface decarburization of the hypo-eutectoid carbon steel C45 during annealing in steady air at temperatures T > A_{C1}. *Metals*, 2018, vol. 8, p. 425. DOI: 10.3390/met8060425.

16. Stepankin I.N., Pozdnyakov E.P. K voprosu izgotovleniya melkorazmernogo shtampovogo instrumenta iz ekonomno legirovannykh stalei s diffuzionnym uprochneniem poverkhnostnogo sloya [To the issue of manufacturing of small-size stamping tools from economically alloyed steels with diffusion hardening of the surface layer].

Kuznechno-shtampovochnoe proizvodstvo. Obrabotka materialov davleniem = Forging and Stamping Production. Material Working by Pressure, 2015, no. 9, pp. 25–32.

17. Çalik A. Effect of cooling rate on hardness and microstructure of AISI 1020, AISI 1040 and AISI 1060 Steels. *International Journal of Physical Sciences*, 2009, vol. 4 (9), pp. 514–518.

18. Ramesh B., Vempati S.R., Manjunath C., Elsheikh A.H. Examination of minimum quantity lubrication performance in the hard turning of AISI/SAE 1060 high-carbon steel. *Journal of Materials Engineering and Performance*, 2024, vol. 34 (13), pp. 136861–13696. DOI: 10.1007/s11665-024-10070-z.

19. Dewangan S., Mainwal N., Khandelwal M., Jadhav P.S. Performance analysis of heat treated AISI 1020 steel samples on the basis of various destructive mechanical testing and microstructural behavior. *Australian Journal of Mechanical Engineering*, 2022, vol. 20 (1), pp. 74–87. DOI: 10.1080/14484846.2019.1664212.

20. Chen R.Y., Yeun W.Y.D. Review of the high-temperature oxidation of iron and carbon steels in air or oxygen. *Oxidation of Metals*, 2003, vol. 59 (5), pp. 433–468.

21. Voort G.F.V. Understanding and measuring decarburization. *AM&P Technical Articles*, 2015, vol. 173 (2), pp. 22–27.

22. Konstantinova M.V., Balanovskiy A.E., Gozbenko V.E., Kargapoltsev S.K., Karlina A.I., Shtayger M.G., Guseva E.A., Kuznetsov B.O. Application of plasma surface quenching to reduce rail side wear. *IOP Conference Series: Materials Science and Engineering*, 2019, vol. 560 (1), p. 012146. DOI: 10.1088/1757-899X/560/1/012146.

23. Yelemessov K., Baskanbayeva D., Martyushev N.V., Skeeba V.Y., Gozbenko V.E., Karlina A.I. Change in the properties of rail steels during operation and reutilization of rails. *Metals*, 2023, vol. 13, p. 1043. DOI: 10.3390/met13061043.

24. Shtayger M.G., Balanovskiy A.E., Kargapoltsev S.K., Gozbenko V.E., Karlina A.I., Karlina Yu.I., Govorkov A.S., Kuznetsov B.O. Investigation of macro and micro structures of compounds of high-strength rails implemented by contact butt welding using burning-off. *IOP Conference Series: Materials Science and Engineering*, 2019, vol. 560 (1), p. 012190. DOI: 10.1088/1757-899X/560/1/012190.

25. Balanovskiy A.E., Shtayger M.G., Karlina A.I., Kargapoltsev S.K., Gozbenko V.E., Karlina Yu.I., Govorkov A.S., Kuznetsov B.O. Surface hardening of structural steel by cathode spot of welding arc. *IOP Conference Series: Materials Science and Engineering*, 2019, vol. 560 (1), p. 012138. DOI: 10.1088/1757-899X/560/1/012138.

26. Skeeba V.Yu., Ivancivsky V.V., Kutyshkin A.V., Parts K.A. Hybrid processing: the impact of mechanical and surface thermal treatment integration onto the machine parts quality. *IOP Conference Series: Materials Science and Engineering*, 2016, vol. 126 (1), p. 012016. DOI: 10.1088/1757-899x/126/1/012016.

27. Efremenkov E.A., Martyushev N.V., Skeeba V.Yu., Grechneva M.V., Olisov A.V., Ens A.D. Research on the possibility of lowering the manufacturing accuracy of cycloid transmission wheels with intermediate rolling elements and a free cage. *Applied Sciences*, 2022, vol. 12 (1), p. 5. DOI: 10.3390/app12010005.

28. Martyushev N.V., Skeeba V.Yu. The method of quantitative automatic metallographic analysis. *Journal of Physics: Conference Series*, 2017, vol. 803 (1), p. 012094. DOI: 10.1088/1742-6596/803/1/012094.

29. Skeeba V.Yu., Ivancivsky V.V. Reliability of quality forecast for hybrid metal-working machinery. *IOP Conference Series: Earth and Environmental Science*, 2018, vol. 194 (2), p. 022037. DOI: 10.1088/1755-1315/194/2/022037.

30. Zverev E.A., Skeeba V.Y., Skeeba P.Y., Khlebova I.V. Defining efficient modes range for plasma spraying coatings. *IOP Conference Series: Earth and Environmental Science*, 2017, vol. 87 (8), p. 082061. DOI: 10.1088/1755-1315/87/8/082061.

31. Skeeba V.Yu. Hybrid process equipment: improving the efficiency of the integrated metalworking machines initial designing. *Obrabotka metallov (tekhnologiya, oborudovanie, instrumenty) = Metal Working and Material Science*, 2019, vol. 21, no. 2, pp. 62–83. DOI: 10.17212/1994-6309-2019-21.2-62-83. (In Russian).

32. Borisov M.A., Lobanov D.V., Yanyushkin A.S., Skeeba V.Yu. Investigation of the process of automatic control of current polarity reversal in the conditions of hybrid technology of electrochemical processing of corrosion-resistant steels. *Obrabotka metallov (tekhnologiya, oborudovanie, instrumenty) = Metal Working and Material Science*, 2020, vol. 22, no. 1, pp. 6–15. DOI: 10.17212/1994-6309- 2020-22.1-6-15. (In Russian).

33. Mamadaliev R.A., Bakhmatov P.V., Martyushev N.V., Skeeba V.Y., Karlina A.I. Influence of welding regimes on structure and properties of steel 12KH18N10T weld metal in different spatial positions. *Metallurgist*, 2022, vol. 65 (11–12), pp. 1255–1264. DOI: 10.1007/s11015-022-01271-9.

34. Balanovsky A.E., Shtayger M.G., Kondrat'ev V.V., Van Huy V., Karlina A.I. Plasma-arc surface modification of metals in a liquid medium. *IOP Conference Series: Materials Science and Engineering*, 2018, vol. 411 (1), p. 012013. DOI: 10.1088/1757-899X/411/1/012013.

35. Karlina A.I., Karlina Y.I., Gladkikh V.A. Studying the microstructure, phase composition, and wear resistance of alloyed layers after laser surface melting of low-carbon steel 20. *Metallurgist*, 2024, vol. 68 (5), pp. 757–766. DOI: 10.1007/s11015-024-01782-7.

36. Karlina A.I., Karlina Y.I., Kondratiev V.V., Kononenko R.V., Breki A.D. Study of wear of an alloyed layer with chromium carbide particles after plasma melting. *Crystals*, 2023, vol. 13 (12), p. 1696. DOI: 10.3390/cryst13121696.

Conflicts of Interest

The authors declare no conflict of interest.

Obrabotka metallov -
Metal Working and Material Science

Journal homepage: http://journals.nstu.ru/obrabotka_metallov

Effect of heat treatment on the structure and properties of high-entropy alloy AlCoCrFeNiNb$_{0.25}$

Zhanna Kovalevskaya [a, *], *Yuanxun Liu* [b]

National Research Tomsk Polytechnic University, 30 Lenin Avenue, Tomsk, 634050, Russian Federation

[a] https://orcid.org/0000-0003-3040-8851, ✉ kovalevskaya@tpu.ru; [b] https://orcid.org/0009-0002-8501-2643, ✉ yuansyun1@tpu.ru

ABSTRACT

Introduction. Currently, one of the most studied high-entropy alloys (*HEAs*) is the *CoCrFeNi* system with the addition of a fifth component. An example of such an alloy is *AlCoCrFeNi* alloyed with additional elements. *Nb* alloying promotes the formation of a solid solution and a secondary *Laves* phase in the alloy, and leads to the formation of eutectics between these phases. The optimal combination of mechanical properties achieved in the hypoeutectic alloy *AlCoCrFeNiNb$_{0.25}$* was the basis for the choice of this alloy for further studies under heat treatment conditions. *Purpose of the work.* To investigate the effect of heat treatment, including heating to temperatures of 900°C, 1,000°C and 1,100°C with subsequent cooling in air, on the structure and properties of *AlCoCrFeNiNb$_{0.25}$*. **The methods of investigation** were optical metallography, X-ray diffraction analysis, microhardness measurement, and compression tests. **Results and Discussion.** *AlCoCrFeNiNb$_{0.25}$* alloy retains the solid solution structure based on the *BCC* phase not only in the cast state, but also after heat treatment. Irrespective of heat treatment parameters, the alloy retains the hypoeutectic structure consisting of solid solution dendrites and eutectic with the *Laves* phase in the interdendritic space. Heat treatment leads to changes in the phase composition of the alloy and refinement of structural components. When heated to 900°C, along with the existing solid solution and *Laves* phase, σ-phase is released in the structure, which increases the microhardness of the alloy, but does not provide improvement of strength properties due to its low plasticity. The strength properties of the alloy are significantly improved by heat treatment with heating up to 1,000°C and 1,100°C. Heating up to 1,100°C is accompanied by an increase in residual strain. The main reasons for this effect may be transformations occurring both in the solid solution of the *BCC* phase (dissolution of the *B$_2$* phase, rearrangement of the substructure, increase in the lattice parameter) and in the eutectic (increase in the proportion of the *Laves* phase, refinement of eutectic cells).

Introduction

For over two decades, the global community of materials scientists has been developing and investigating a novel class of metal alloys, known as high-entropy alloys (*HEAs*) [1–4]. Unlike conventional metal alloys with a single principal component, *HEAs* are composed of multiple principal components in equiatomic or near-equiatomic concentrations [3]. Due to the high mixing entropy, *HEAs* typically exhibit disordered solid solutions. This phase configuration endows them with enhanced strengthening capabilities and favorable ductility characteristics, making *HEAs* promising candidates for structural materials [4–6]. One of the most extensively studied systems is the *CoCrFeNi* alloy, which is often modified by the addition of a fifth element, such as *Cu*, *Mo*, *Mn*, or *Al* [7–11]. For instance, the thoroughly studied *AlCoCrFeNi* alloy demonstrates excellent synergy of its constituents, as well as the ability to control its phase composition and structure by heat treatment. Consequently, the resulting alloy achieves an advantageous combination of strength and ductility properties [12–19].

In the search for optimal *HEA* compositions for the manufacture of machine components, contemporary researchers are advancing in two primary directions: either reducing/increasing the content of one of the

* Corresponding author
Kovalevskaya Zhanna G., D.Sc. (Engineering), Professor
National Research Tomsk Polytechnic University,
30 Lenin ave.,
634050, Tomsk, Russian Federation
Tel.: +7 3822 706-351, **e-mail:** kovalevskaya@tpu.ru

components of the existing *HEAs* [6, 19–21] or introducing additional elements as alloying agents, such as *Ti*, *Zr*, *Si*, *V*, *C*, *Nb*, and others [22–27].

Several studies have demonstrated the effect of *Nb* doping on the structure and properties of *AlCoCrFeNi* and related *HEA* systems [28–31]. It is well established that *Nb* and the *HEA* components exhibit negative mixing enthalpies. Furthermore, *Nb* possesses the largest atomic size in the system. These characteristics of *Nb* contribute to the formation, on one hand, of a stable solid solution with enhanced interatomic bonds, and on the other hand, of secondary phases that are essential for alloy strengthening. For instance, the work [28] showed that *Nb* doping of the *AlCoCrFeNi HEA* resulted in the formation of a eutectic structure that included the ordered *Laves* phase *(CoCr)Nb*. This leads to alterations in the microstructure and properties of the alloy, where the compressive yield strength and hardness increase, while ductility decreases. An optimal combination of mechanical properties is achieved in the hypoeutectic *AlCoCrFeNiNb$_{0.25}$* alloy, which was chosen for this investigation.

Various heat treatment methods, including annealing and quenching, are employed to strengthen *HEAs* [20, 32–37]. In certain instances, heat treatment can enhance both strength and ductility of *HEAs* [5]. This unique effect, which is not typical for conventional alloys, necessitates thorough investigation and analysis.

The ***purpose of this paper*** is to investigate the effect of heat treatment on the structure and properties of the *AlCoCrFeNiNb$_{0.25}$* high-entropy alloy (*HEA*). The heat treatment process involves heating to 900 °C, 1,000 °C, and 1,100 °C followed by air cooling.

Methods

The *AlCoCrFeNiNb$_{0.25}$* alloy with a near-equiatomic composition was produced by the arc melting method in a water-cooled copper crucible under an argon atmosphere. The alloy, whose chemical composition is detailed in Table 1, was made of components with more than 99.5 wt. % purity. To ensure the homogeneity of the chemical composition, the ingot was remelted at least five times. The dimensions of the resulting ingot were 70×35×12 mm. Prior to heat treatment, ingots were cut into fragments measuring 35×12×6 mm. After heat treatment, the central portions of the fragments were further cut into parallelepipeds measuring 10×4×4 mm. The cut samples were polished and used for compression testing. The remaining portions of the fragments were utilized for X-ray diffraction analysis, microstructural evaluation, and microhardness measurements.

T a b l e 1

Chemical composition of *AlCoCrFeNiNb$_{0.25}$* (at.% and wt.%)

Element	Al	Co	Cr	Ni	Fe	Nb
at.%	19.1	19.1	19.1	19.1	19.1	4.5
wt.%	9.8	21.5	18.9	21.4	20.4	8.0

Samples of the *AlCoCrFeNiNb$_{0.25}$* alloy were heat-treated as follows: heating to 900 °C, 1,000 °C, and 1,100 °C, holding for 1 h, and air cooling. For simplicity, the heat-treated samples were designated as *T900*, *T1000*, and *T1100,* respectively while the as-cast sample was designated *T30*

Thin sections were prepared from the samples, and their microstructure was analyzed using an *Axio Observer A1m* optical microscope and a *Quanta 200* scanning electron microscope (*SEM*) equipped with an *EDAX* energy-dispersive X-ray spectroscopy (*EDS*) unit. The phase composition was determined using an *XRD-6000* diffractometer with *Cu-Kα* radiation. The scanning angles ranged from 20° to 80° with a step of 0.02°. Microhardness measurements were performed with a *PMT-3* hardness tester with a load of 100 g. Compression tests were performed using a universal testing machine (*MTS SANS CMT5105*) at a compression rate of $5×10^{-3}$ mm/s. At least three samples per treatment condition were measured.

Results and Discussion

Fig. 1, *a* shows X-ray diffraction (*XRD*) patterns of the *AlCoCrFeNiNb*$_{0.25}$ alloy in the as-cast state and after heat treatment. In the as-cast state, the alloy consists of a primary *BCC* phase, which represents a disordered solid solution of all components present in the system. The disorder of the solid solution in the primary phase is attributed to the redistribution of components with various atomic radii in the *BCC* lattice and their segregation into two phases with different parameters. The solid solution disorder manifests in the *XRD* pattern as splitting of the main *BCC* peak into two distinct peaks (Fig. 1, *b*). Furthermore, the *XRD* pattern exhibits peaks corresponding to the crystal lattice of the *Nb*-rich *Laves* phase, which can be identified as *(CoCr)Nb* with a hexagonal structure, as well as the [001] reflection peak of the *B2* phase representing *AlNi* with a *BCC* lattice [29, 32].
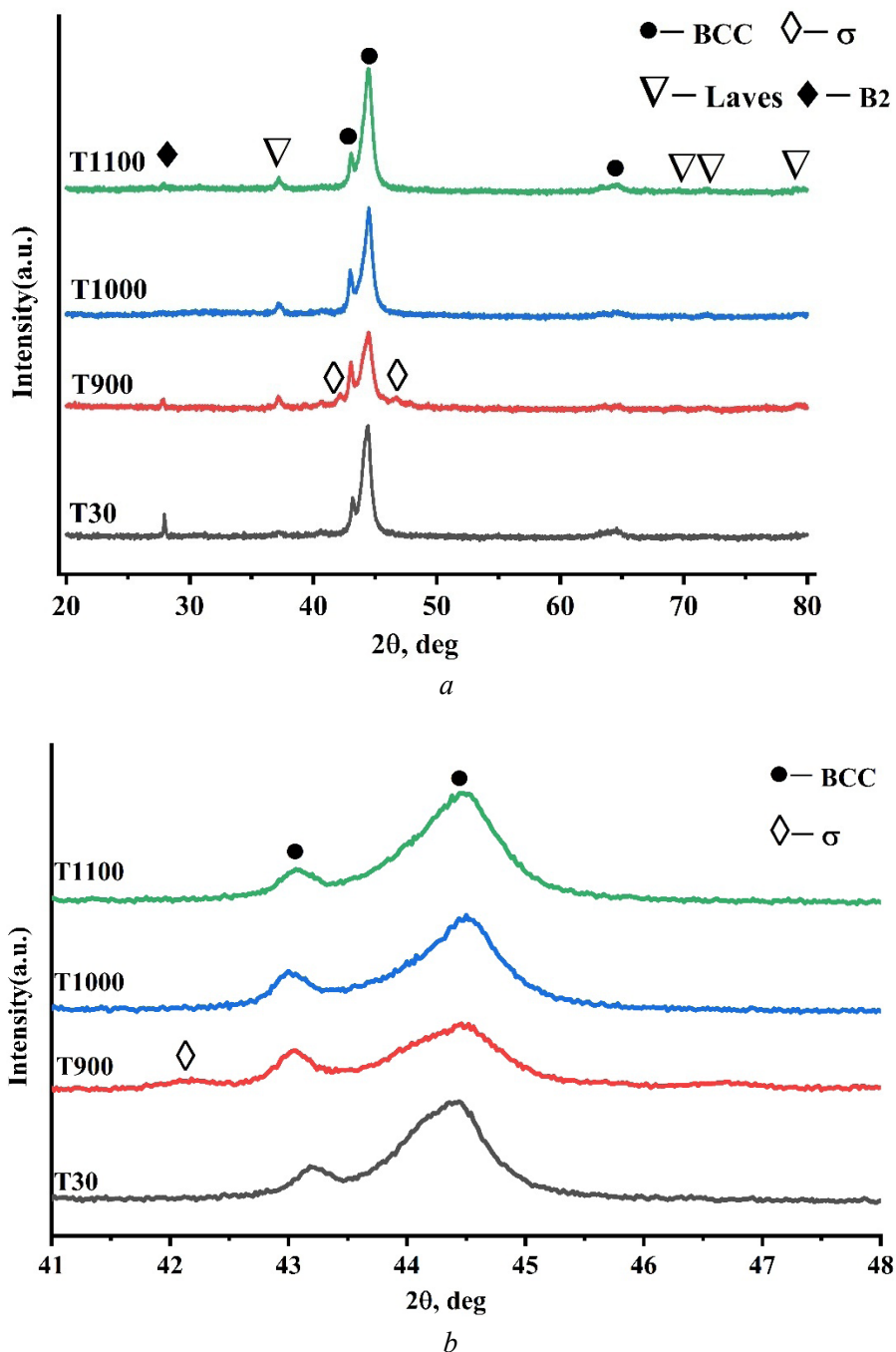

Fig. 1. XRD patterns of *AlCoCrFeNiNb*$_{0.25}$ alloy in the as-cast state and after heat treatment (*a*) with enlarged image in the 2θ range of 41–48° (*b*)

The existence of the *Laves* phase is characteristic of *AlFeNiCoCrNb* alloys where the *Nb* concentration corresponds to a molar ratio of 0.25 or higher. In this case, *Nb* not only dissolves in the primary *BCC* phase but also promotes the formation of the secondary – *Laves* – phase, which forms a eutectic mixture with the *BCC* phase [29].

According to the findings of [32], during cooling of the *AlFeNiCoCr* alloy, the primary crystallized *BCC* phase may incoherently separate into a mixture of an unordered *BCC* phase enriched in *Cr-Fe* and an ordered *B2* phase enriched in *Al-Ni*, which is evidenced by the presence of a peak corresponding to the *B2* phase in the *XRD* pattern.

Subsequent heat treatment of the alloy leads to the following changes in the *XRD* patterns. As the heating temperature increases, the intensity of the *B2*-phase peak decreases, while the intensity of the peak corresponding to the *Laves* phase slightly increases. In addition, changes occur in the lattice of the primary *BCC* phase. Fig. 1, *b* presents an enlarged view of the (110) peak of the *BCC* phase. It is evident that, with an increase in the heating temperature, the peak shifts towards smaller angles, indicating an increase in the lattice parameter of the *BCC* solid solution, which suggests changes in the composition of the solid solution.

After heat treatment at 900 °C, peaks of a new phase emerge, which is identified as the tetragonal σ phase composed of *Cr* and *Fe*. The σ phase is absent at higher heating temperatures. The phenomenon of the σ-phase precipitation and dissolution in the *BCC* phase within a similar temperature range was also observed previously [29].

The *XRD* analysis of the *AlCoCrFeNiNb$_{0.25}$* alloy throughout the entire heating temperature range shows that the primary phase remains an unordered *BCC* solid solution. However, upon heating of the *AlFeNiCoCr* alloy without *Nb*, part of the material transforms into an *FCC* solid solution [29]. Thus, the addition of *Nb* helps stabilize the *BCC* phase and maintain a predominantly single-phase structure in the high-entropy alloy.

Fig. 2 depicts the microstructure of the *AlCoCrFeNiNb$_{0.25}$* alloy both in the as-cast state and after heat treatment. The alloy consistently exhibits a dendritic morphology with hypoeutectic characteristics. The microstructure comprises primary dendritic and interdendritic eutectic regions. Dendritic regions consist of a *BCC* phase, while the eutectic structure is a mixture of the *BCC* and *Laves* phases. In the as-cast state, dendritic segregation results in compositional heterogeneity: dendritic cores (*BCC* phase) are enriched in *Ni* and *Al*, whereas the dendritic periphery and eutectic regions are enriched in *Cr* and *Fe*. *Nb* partially dissolves in the *BCC* phase, but most of it enters the composition of the *Laves* phase [29]. Results of the elemental analysis in different zones of the as-cast alloy are detailed in Table 2. The same pattern of formation of the dendritic structure in the alloy was reported in [15, 29].

The dendritic structure that exhibits a dark contrast after etching is surrounded by lighter layers of the *Laves* phase, which represents a secondary phase. The secondary *Laves* phase forms along the solid solution boundaries during dendritic growth and is attributed to the reduced solubility of niobium in the solid solution of the principal components during cooling. The enrichment of the peripheral regions of dendrites with niobium and chromium creates conditions for the formation of the secondary *Laves* phase based on these components.

Fig. 2, *b* shows a defective eutectic structure. Grains of the *Laves* phase are divided into fragments with random crystallographic orientations. Since the eutectic, which includes the *Laves* phase, forms in the interdendritic space, it is structurally impossible to distinguish between the secondary *Laves* phase and the *Laves* phase present in the eutectic.

Heat treatment at 900–1,100 °C does not alter the dendritic structure of the alloy (Fig. 2). The dendrite width along the secondary axes ranges from 11 to 15 μm. Increasing the heating temperature from 900 °C to 1,100 °C leads to changes in the structure of the eutectic, this can be observed in high-magnification metallographic images (Figs. 2, *f*, *h*). At the heating temperature of 900 °C, no noticeable changes in the eutectic structure occur. However, at 1,000 °C, *Laves* phase fragments begin to align, which is typical of the eutectic, and the formed lines alternate with the solid solution. At 1,100 °C, eutectic grains are well defined in the interdendritic space (Fig. 2, *h*).The *XRD* analysis confirms the eutectic transformation: the peak intensity of the *Laves* phase increases with temperature. This may arise from either the coalescence of
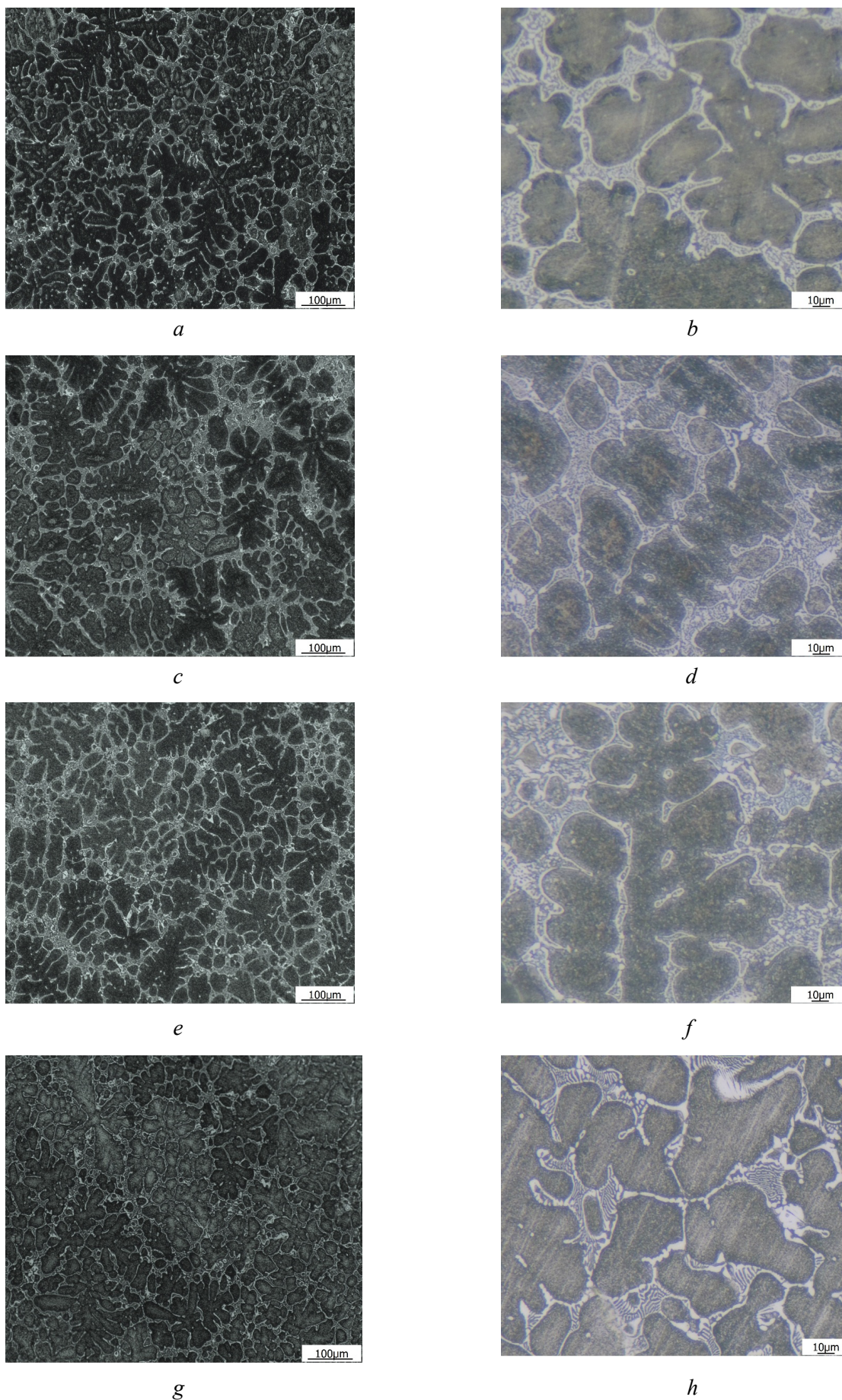
Fig. 2. Microstructure of *AlCoCrFeNiNb$_{0.25}$* alloy in the as-cast state and after heat treatment:
T30 (a, b); T900 (c, d); T1000 (e, f); T1100 (g, h)

T a b l e 2

Chemical compositions (at.%) in the *AlCoCrFeNi* alloy in the as-cast state

T30	Al	Cr	Fe	Co	Ni	Nb
Dendrite core	17.76	16.46	18.61	20.30	24.56	2.40
Dendrite periphery	14.85	21.61	20.75	20.14	21.06	1.59
Solid solution in eutectics	12.09	23.86	22.05	19.78	19.28	2.96
Laves phase	3.80	18.36	21.43	23.66	11.56	21.17

secondary-phase grains or from its increased fraction in interdendritic zones via solid solution precipitation (Fig. 1, *a*).

The *XRD* analysis confirms that an ordered σ phase forms in the alloy at 900°C. In [32], it was reported that the **σ** phase precipitated from the disordered solid solution where it was enriched in *Cr* and *Fe* in the form of dispersed particles. Our *SEM* studies reveal that **σ**-phase particles are distributed throughout the dendrite volume (Fig. 3, *b*). After heat treatment at 1,000 °C, **σ**-phase particles are still observed, but in smaller amounts (Fig. 3, *c*). At 1,100 °C, they completely disappear (Fig. 3, *d*).

The *SEM* analysis reveals that heat treatment significantly alters the structure of the solid solution within dendrites (Fig. 3). During alloy solidification, the cooling process leads to the spinodal decomposition of the disordered solid solution into a *Fe*- and *Cr*-enriched disordered solid solution and an ordered *B2* phase enriched in *Ni* and *Al* [32]. This decomposition results in the formation of the so-called basket weave
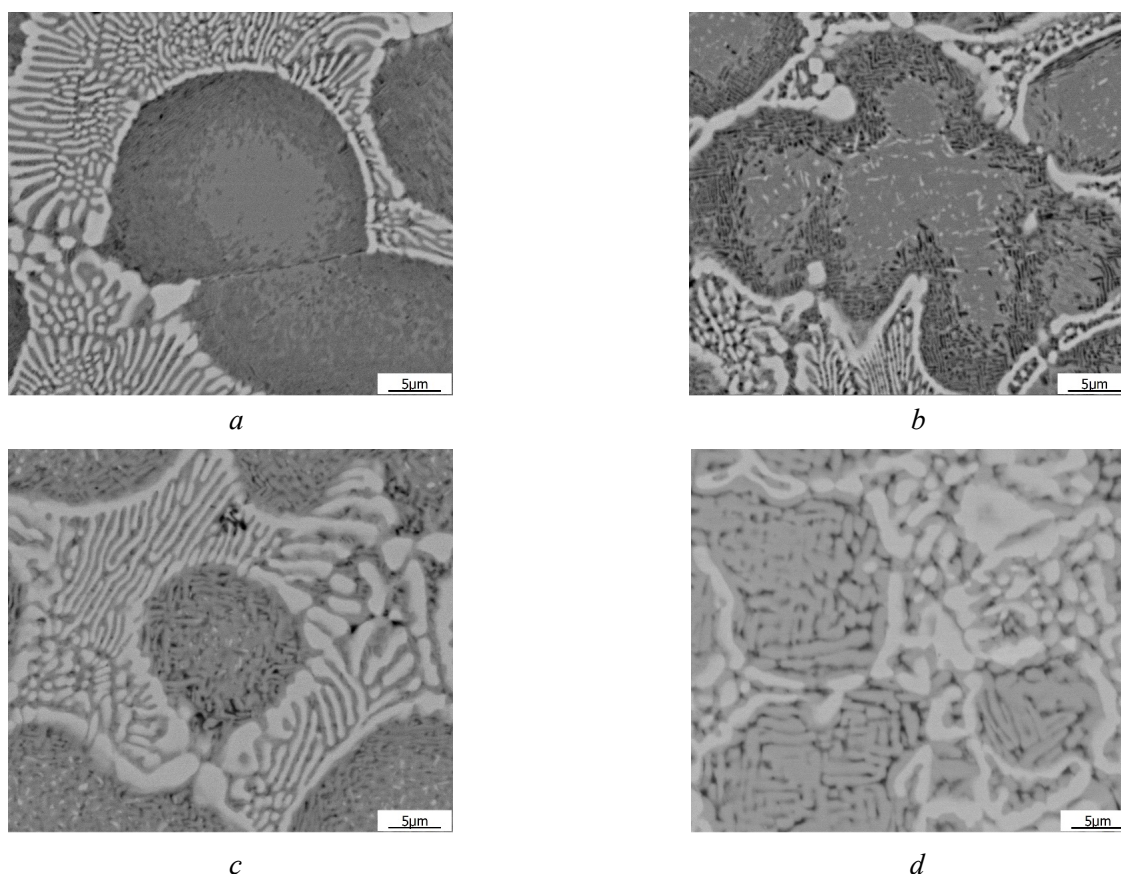

a

b

c

d

Fig. 3. Microstructure of *AlFeNiCoCrNb$_{0.25}$* alloy in the as-cast state and after heat treatment, obtained using *SEM*: *T30* (*a*); *T900* (*b*); *T1000* (*c*); *T1100* (*d*)

structure, which was described in detail in [15, 32, 37]. In the investigated as-cast alloy, a characteristic basket weave or banded structure forms in the peripheral regions of dendrites, which is attributed to the spinodal decomposition of the solid solution. No banded structure is observed in the center of dendrites (Fig. 3, *a*).

When the alloy is heated to 900 °C and subsequently cooled, structural heterogeneity in dendrites and the basket weave structure become more pronounced (Fig. 3, *b*). Furthermore, as mentioned above, σ-phase particles precipitate from the solid solution. According to X-ray structural analysis, after heat treatment, the proportion of the ordered *B2* phase decreases, suggesting that the observed contrast within the basket weave structure is due not to the spinodal decomposition of the solid solution into two phases but rather to the heterogeneous segregation of atomic components within the disordered solid solution, as described in [15]. At 1,000 °C, the basket weave structure increases in size and occupies the entire volume of dendrites (Fig. 3, *c*). Further heating to 1,100 °C causes coarsening (Fig. 3, *d*).

The average microhardness and the microhardness of the structural components of the alloy are presented in Table 3. In all heat treatment conditions, the interdendritic regions demonstrate significantly higher microhardness compared to the dendritic cores.

Table 3

Microhardness of *AlCoCrFeNiNb$_{0.25}$* alloy in the as-cast state and after heat treatment

Measurement area	*T30* HV	*T900* HV	*T1000* HV	*T1100* HV
Dendrites	614 ± 44	582 ± 37	489 ± 53	520 ± 35
Eutectic	640 ± 47	902 ± 66	620 ± 45	636 ± 46
Average value	625 ± 28	730 ± 47	545 ± 52	572 ± 56

The maximum microhardness in dendrites of the as-cast alloy is attributed to the unique structure of the solid solution of the alloy components, which forms during crystallization and cooling. The spinodal decomposition of the disordered solid solution coupled with the precipitation of the ordered *B2* phase strengthens the alloy. However, heating of the alloy during heat treatment leads to a partial loss of the order characteristic of the *B2* phase, resulting in a decrease in the microhardness of dendrites. Nevertheless, the precipitation of σ-phase particles upon heating to 900 °C allows the microhardness to remain at a high level. When the heating temperature increases to 1,000 °C, the strengthening effect of the σ-phase particles disappears. During heat treatment at 1,100 °C, coalescence of the basket weave structure occurs, leading to the formation of more distinct phase boundaries, possibly due to the increased heterogeneous segregation of atomic components within the solid solution. This, in turn, slightly increases the microhardness in the dendritic zones of the alloy.

In the interdendritic space of the as-cast alloy, the microhardness of the eutectic is only slightly higher than that of the solid solution in dendrites. This means that strengthening due to spinodal decomposition is comparable in magnitude to that due to the *Laves* phase (a solid intermetallic compound) in the eutectic. During heating at 900 °C, as mentioned above, σ-phase particles precipitate from the solid solution and concentrate in the *Cr*-rich interdendritic space. This significantly increases the microhardness of the eutectic due to strengthening of the solid solution with σ-phase particles in its composition. Dispersed σ-phase particles precipitate in the solid solution of all structural components, significantly enhancing the microhardness in dendrites. Heating to 1,000 °C and 1,100 °C leads to the dissolution of σ-phase particles in the primary phase [11], which contributes to a decrease in the microhardness in the interdendritic space to the values of the initial structure. This is due to the removal of the effect of strengthening due to σ-phase particles.

When evaluating the integral microhardness of all structural components of the alloy, the overall trend in the variation of microhardness with heating temperature is retained (Table 3).
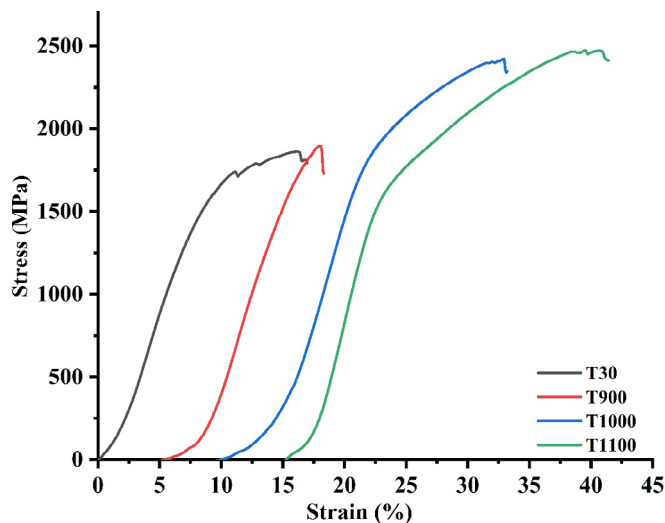
Fig. 4. Compressive stress-strain curves of the *AlFeNiCoCrNb$_{0.25}$* alloy in the as-cast state and after heat treatment

Fig. 4 illustrates compressive stress-strain responses of the as-cast and heat-treated alloys. The offset yield strength, compressive strength, and residual strain are presented in Table 4. The as-cast alloy exhibits good strength and plasticity characteristics. Structural transformations in the alloy during heating to 900 °C have little effect on the strength properties of the material but significantly reduce its plasticity. This reduction is attributed to the precipitation of the brittle σ phase in the structure. The authors of [32] also pointed out the effect of decreased plasticity within a similar temperature range of heat treatment.

During heat treatment at 1,000 °C and 1,100 °C, a significant increase is observed in the strength characteristics of the alloy. At 1,100 °C, the residual strain also increases. Based on the results of *XRD* analysis and optical microscopy, it can be suggested that the main reason for this effect is transformations occurring both in the solid solution of the *BCC* phase (*B2*-phase dissolution, substructure rearrangement, and an increase in the lattice parameter) and in the eutectic (increase in the proportion of the *Laves* phase and refinement of eutectic cells). The simultaneous increase in plasticity is likely due to the relief of internal stresses, a reduction in the number of crystalline defects, and coalescence of structural components in dendrites and the eutectic. However, a more precise analysis of this unique effect on the properties of the *AlCoCrFeNiNb$_{0.25}$* alloy requires further research.

T a b l e 4

Offset yield strength, compressive strength and residual strain of *AlCoCrFeNiNb$_{0.25}$* alloy in the as-cast state and after heat treatment

	$\sigma_{0.2}$ (MPa)	σ_u (MPa)	ε (%)
T30	1356	1962	7.7
T900	1605	1894	2.8
T1000	1502	2438	9.8
T1100	1369	2494	16.4

Conclusions

Doping of the *AlCoCrFeNi* high entropy alloy with niobium in a molar ratio of 0.25 led to the stabilization of the solid solution based on the body-centered cubic (*BCC*) phase both in the as-cast state and after heat treatment involving heating to 900 °C, 1,000 °C, and 1,100 °C followed by air cooling. The resulting structure of the alloy, regardless of the heat treatment modes, consisted of dendrites of the solid solution and a eutectic with the *Laves* phase in the interdendritic space.

Heat treatment altered the phase composition of the alloy and improved its structural components. Upon heating to 900 °C, alongside the already formed solid solution and *Laves* phase, the σ phase precipitated in the structure, which increased the microhardness of the alloy. However, this did not improve the strength properties due to the low plastic characteristics of the σ phase.

The strength characteristics of the alloy significantly increased during heat treatment at 1,000 °C and 1,100 °C. At 1,100 °C, the residual strain also rose. The main reasons for this effect may include

transformations both in the solid solution of the *BCC* phase (such as the *B2*-phase dissolution, substructure rearrangement, and an increase in the lattice parameter) and in the eutectic (an increase in the proportion of the *Laves* phase and refinement of eutectic cells).

References

1. Yeh J.W., Chen S.K., Lin S.J., Gan J.Y., Chin T.S., Shun T.T., Tsau C.H., Chang S.Y. Nanostructured high-entropy alloys with multiple principal elements: novel alloy design concepts and outcomes. *Advanced Engineering Materials*, 2004, vol. 6, pp. 299–303. DOI: 10.1002/adem.200300567.

2. Cantor B., Chang I.T.H., Knight P., Vincent A.J.B. Microstructural development in equiatomic multicomponent alloys. *Materials Science and Engineering: A*, 2004, vol. 375–377, pp. 213–218. DOI: 10.1016/j.msea.2003.10.257.

3. Gromov V.E., Shlyarova Yu.A., Konovalov S.V., Vorob'ev S.V., Peregudov O.A. Application of high-entropy alloys. *Izvestiya vuzov. Chernaya metallurgiya = Izvestiya. Ferrous Metallurgy*, 2021, vol. 64 (10), pp. 747–754. DOI: 10.17073/0368-0797-2021-10-747-754. (In Russian).

4. Bataeva Z.B., Ruktuev A.A., Ivanov I.V., Yurgin A.B., Bataev I.A. Review of alloys developed using the entropy approach. *Obrabotka metallov (tekhnologiya, oborudovanie, instrumenty) = Metal Working and Material Science*, 2021, vol. 23, no. 2, pp. 116–146. DOI: 10.17212/1994-6309-2021-23.2-116-146. (In Russian).

5. Li W., Xie D., Li D., Zhang Y., Gao Y., Liaw P.K. Mechanical behavior of high-entropy alloys. *Progress in Materials Science*, 2021, vol. 118, p. 100777. DOI: 10.1016/j.pmatsci.2021.100777.

6. Shang Y., Brechtl J., Pistidda C., Liaw P.K. Mechanical behavior of high-entropy alloys: A review. *High-Entropy Materials: Theory, Experiments, and Applications*. Springer, 2021, pp. 435–522. DOI: 10.1007/978-3-030-77641-1_10.

7. Sheng H.F., Gong M., Peng L.M. Microstructural characterization and mechanical properties of an $Al_{0.5}$CoCrFeCuNi high-entropy alloy in as-cast and heat-treated/quenched conditions. *Materials Science and Engineering: A*, 2013, vol. 567, pp. 14–20. DOI: 10.1016/j.msea.2013.01.006.

8. Sui Q., Wang Z., Wang J., Xu S., Liu B., Yuan Q., Zhao F., Gong L., Liu J. Additive manufacturing of CoCrFeNiMo eutectic high entropy alloy: Microstructure and mechanical properties. *Journal of Alloys and Compounds*, 2022, vol. 913, p. 165239. DOI: 10.1016/j.jallcom.2022.165239.

9. Ruktuev A.A., Lazurenko D.V., Ogneva T.S., Kuzmin R.I., Golkovski M.G., Bataev I.A. Structure and oxidation behavior of CoCrFeNiX (where X is Al, Cu, or Mn) coatings obtained by electron beam cladding in air atmosphere. *Surface and Coatings Technology*, 2022, vol. 448, p. 128921. DOI: 10.1016/j.surfcoat.2022.128921.

10. Laplanche G., Kostka A., Horst O.M., Eggeler G., George E.P. Microstructure evolution and critical stress for twinning in the CrMnFeCoNi high-entropy alloy. *Acta Materialia*, 2016, vol. 118, pp. 152–163. DOI: 10.1016/j.actamat.2016.07.038.

11. Wang W.R., Wang W.L., Wang S.C., Tsai Y.C., Lai C.H., Yeh J.W. Effects of Al addition on the microstructure and mechanical property of AlxCoCrFeNi high-entropy alloys. *Intermetallics*, 2012, vol. 26, pp. 44–51. DOI: 10.1016/j.intermet.2012.03.005.

12. Arun S., Radhika N., Saleh B. Effect of additional alloying elements on microstructure and properties of AlCoCrFeNi high entropy alloy system: A comprehensive review. *Metals and Materials International*, 2025, vol. 31 (2), pp. 285–324. DOI: 10.1007/s12540-024-01752-3.

13. Zhang S., Wu C.L., Zhang C.H., Guan M., Tan J.Z. Laser surface alloying of FeCoCrAlNi high-entropy alloy on 304 stainless steel to enhance corrosion and cavitation erosion resistance. *Optics & Laser Technology*, 2016, vol. 84, pp. 23–31. DOI: 10.1016/j.optlastec.2016.04.011.

14. Manzoni A., Daoud H., Völkl R., Glatzel U., Wanderka N. Phase separation in equiatomic AlCoCrFeNi high-entropy alloy. *Ultramicroscopy*, 2013, vol. 132, pp. 212–215. DOI: 10.1016/j.ultramic.2012.12.015.

15. Wang Y.P., Li B.S., Ren M.X., Yang C., Fu H.Z. Microstructure and compressive properties of AlCrFeCoNi high entropy alloy. *Materials Science and Engineering: A*, 2008, vol. 491 (1–2), pp. 154–158. DOI: 10.1016/j.msea.2008.01.064.

16. Kunce I., Polanski M., Karczewski K., Plocinski T., Kurzydlowski K.J. Microstructural characterisation of high-entropy alloy AlCoCrFeNi fabricated by laser engineered net shaping. *Journal of Alloys and Compounds*, 2015, vol. 648, pp. 751–758. DOI: 10.1016/j.jallcom.2015.05.144.

17. Zhang C., Zhang F., Diao H., Gao M.C., Tang Z., Poplawsky J.D., Liaw P.K. Understanding phase stability of Al-Co-Cr-Fe-Ni high entropy alloys. *Materials & Design*, 2016, vol. 109, pp. 425–433. DOI: 10.1016/j.matdes.2016.07.073.

18. Osintsev K.A., Gromov V.E., Konovalov S.V., Panchenko I.A., Vashchuk E.S. Structural-phase state of high-entropy Al-Co-Cr-Fe-Ni alloy obtained by wire-arc additive technology. *Polzunovskiy vestnik*, 2016, no. 1, pp. 141–146. DOI: 10.25712/ASTU.2072-8921.2021.01.020. (In Russian).

19. Zemanate A.M., Júnior A.M.J., Andreani G.F. de Lima, Roche V., Cardoso K.R. Corrosion behavior of AlCoCrFeNix high entropy alloys. *Electrochimica Acta*, 2023, vol. 441, p. 141844. DOI: 10.1016/j.electacta.2023.141844.

20. Niu S., Kou H., Guo T., Zhang Y., Wang J., Li J. Strengthening of nanoprecipitations in an annealed Al$_{0.5}$CoCrFeNi high entropy alloy. *Materials Science and Engineering: A*, 2016, vol. 671, pp. 82–86. DOI: 10.1016/j.msea.2016.06.040.

21. Ivanov I.V., Emurlaev K.I., Kuper K.E., Safarova D.E., Bataev I.A. Structural transformations during annealing of cold-worked high-entropy alloy Al$_{0.3}$CoCrFeNi. *Izvestiya vuzov. Chernaya metallurgiya = Izvestiya. Ferrous Metallurgy*, 2022, vol. 65 (8), pp. 539–547. DOI: 10.17073/0368-0797-2022-8-539-547. (In Russian).

22. Zhou J.L., Cheng Y.H., Wan Y.X., Chen H., Wang Y.F., Yang J.Y. Strengthening by Ti, Nb, and Zr doping on microstructure, mechanical, tribological, and corrosion properties of CoCrFeNi high-entropy alloys. *Journal of Alloys and Compounds*, 2024, vol. 984, p. 173819. DOI: 10.1016/j.jallcom.2024.173819.

23. Shi H., Fetzer R., Jianu A., Weisenburger A., Heinzel A., Lang F., Müller G. Influence of alloying elements (Cu, Ti, Nb) on the microstructure and corrosion behaviour of AlCrFeNi-based high entropy alloys exposed to oxygen-containing molten Pb. *Corrosion Science*, 2021, vol. 190, p. 109659. DOI: 10.1016/j.corsci.2021.109659.

24. Pan B., Xu X., Yang J., Zhan H., Feng L., Long Q., Zhou H. Effect of Nb, Ti, and V on wear resistance and electrochemical corrosion resistance of AlCoCrNiMx (M=Nb, Ti, V) high-entropy alloys. *Materials Today Communications*, 2024, vol. 39, p. 109314. DOI: 10.1016/j.mtcomm.2024.109314.

25. Astafurova E.G., Melnikov E.V., Reunova K.A., Moskvina V.A., Astafurov S.V., Panchenko M.Yu., Mikhno A.S., Tumbusova I. Temperature dependence of mechanical properties and plastic flow behavior of cast multicomponent alloys Fe$_{20}$Cr$_{20}$Mn$_{20}$Ni$_{20}$Co$_{20-x}$C$_x$ (x = 0, 1, 3, 5). *Fizicheskaya mezomekhanika = Physical Mesomechanics*, 2021, vol. 24, no. 4, pp. 52–63. DOI: 10.24412/1683-805X-2021-4-52-63. (In Russian).

26. Astafurova E.G., Reunova K.A., Melnikov E.V., Panchenko M.Yu., Astafurov S.V., Maier G.G., Moskvina V.A. On the difference in carbon-and nitrogen-alloying of equiatomic FeMnCrNiCo high-entropy alloy. *Materials Letters*, 2020, vol. 276, p. 128183. DOI: 10.1016/j.matlet.2020.128183.

27. Shubert A.V., Konovalov S.V., Panchenko I.A. A review of research on high-entropy alloys, its properties, methods of creation and application. *Obrabotka metallov (tekhnologiya, oborudovanie, instrumenty) = Metal Working and Material Science*, 2024, vol. 26, no. 4, pp. 153–179. DOI: 10.17212/1994-6309-2024-26.4-153-179.

28. Dalan F.C., Sobrinho A.S.D.S., Nishihora R.K., Santos S.F., Martins G.V., Cardoso K.R. Effect of Nb and Ti additions on microstructure, hardness and wear properties of AlCoCrFeNi high-entropy alloy. *Journal of Alloys and Compounds*, 2025, vol. 1010, p. 177117. DOI: 10.1016/j.jallcom.2024.177117.

29. Ma S.G., Zhang Y. Effect of Nb addition on the microstructure and properties of AlCoCrFeNi high-entropy alloy. *Materials Science and Engineering: A*, 2012, vol. 532, pp. 480–486. DOI: 10.1016/j.msea.2011.10.110.

30. Gromov V.E., Konovalov S.V., Efimov M.O., Panchenko I.A., Shlyarov V.V. Ways to improve the properties of high-entropy alloys Cantor CoCrFeNiMn and CoCrFeNiAl. *Izvestiya vuzov. Chernaya Metallurgiya = Izvestiya. Ferrous Metallurgy*, 2024, vol. 67 (3), pp. 283–292. DOI: 10.17073/0368-0797-2024-3-283-292. (In Russian).

31. Zhang M., Zhang L., Liaw P.K., Li G., Liu R. Effect of Nb content on thermal stability, mechanical and corrosion behaviors of hypoeutectic CoCrFeNiNbx high-entropy alloys. *Journal of Materials Research*, 2018, vol. 33 (19), pp. 3276–3286. DOI: 10.1557/jmr.2018.103.

32. Munitz A., Salhov S., Hayun S., Frage N. Heat treatment impacts the micro-structure and mechanical properties of AlCoCrFeNi high entropy alloy. *Journal of Alloys and Compounds*, 2016, vol. 683, pp. 221–230. DOI: 10.1016/j.jallcom.2016.05.034.

33. Güler S., Alkan E.D., Alkan M. Vacuum arc melted and heat treated AlCoCrFeNiTiX based high-entropy alloys: Thermodynamic and microstructural investigations. *Journal of Alloys and Compounds*, 2022, vol. 903, p. 163901. DOI: 10.1016/j.jallcom.2022.163901.

34. Huang S., Wu H., Xu Y., Zhu H. Effects of heat treatment on the precipitation behaviors and mechanical properties of Nb-doped CrMnFeCoNi0.8 high-entropy alloy. *Materials Science and Engineering: A*, 2023, vol. 885, p. 145611. DOI: 10.1016/j.msea.2023.145611.

35. Fang Y., Ma P., Wei S., Zhang Z., Yang D., Yang H., Konda G.P., Wan S., Jia Y. Selective laser melting of AlCoCrFeMnNi high entropy alloy: Effect of heat treatment. *Journal of Materials Research and Technology*, 2023, vol. 26, pp. 7845–7856. DOI: 10.1016/j.jmrt.2023.09.121.

36. Chen L., Bobzin K., Zhou Z., Zhao L., Öte M., Königstein T., Tan Z., He D. Effect of heat treatment on the phase composition, microstructure and mechanical properties of $Al_{0.6}CrFeCoNi$ and $Al_{0.6}CrFeCoNiSi_{0.3}$ high-entropy alloys. *Metals*, 2018, vol. 8 (11), p. 974. DOI: 10.3390/met8110974.

37. Shang G., Liu Z.Z., Fan J., Lu X.G. Effect of heat treatment on the microstructure and nanoindentation behavior of AlCoCrFeNi high entropy alloy. *Intermetallics*, 2024, vol. 169, p. 108302. DOI: 10.1016/j.intermet.2024.108302.

Conflicts of Interest

The authors declare no conflict of interest.

Obrabotka metallov –
Metal Working and Material Science

Corrosion properties of coatings produced from self-fluxing powders by the detonation spraying method

Vyacheslav Sirota [a, *], **Dmitrii Prokhorenkov** [b], **Anton Churikov** [c], **Daniil Podgorny** [d], **Natalia Alfimova** [e], **Andrey Konnov** [f]

Belgorod State Technological University named after V.G. Shukhov, 46 Kostyukova st., Belgorod, 308012, Russian Federation

[a] https://orcid.org/0000-0003-4634-7109, zmas36@mail.ru; [b] https://orcid.org/0000-0002-6455-8172, bstu-cvt-sem@yandex.ru;
[c] https://orcid.org/0000-0002-1829-2676, churikov.toni@mail.ru; [d] https://orcid.org/0000-0001-7435-5005, dan_podgor@mail.ru;
[e] https://orcid.org/0000-0003-3013-0829, alfimovan@mail.ru; [f] https://orcid.org/0009-0009-3245-0747, andrekonnov555@yandex.ru

ARTICLE INFO

ABSTRACT

Introduction. This paper presents the results of a comprehensive study of the corrosion properties of innovative coatings based on self-fluxing *NiCrBSi* alloys (*PR-NKh17SR4*) modified with 10 wt.% boron carbide (B_4C) nanoparticles, produced by detonation spraying. The relevance of the study stems from the critical need to develop new high-performance materials for protecting essential equipment operating under extreme conditions, including marine environments, chemically aggressive solutions, and elevated temperatures. Particular attention is paid to a detailed analysis of the influence of B_4C on corrosion mechanisms, the formation of protective passivating layers, and the relationship between microstructure and functional properties of the coatings. **Objective.** A comprehensive evaluation of the effect of 10 wt.% B_4C addition on the corrosion resistance, microstructure, and mechanical properties of coatings in comparison with the base alloy *NiCrBSi* alloy (*PR-NKh17SR4*) and the commercially available counterpart *NiCr/WC* alloy (*VSNGN-85*), widely used in industry. **Methods.** The coatings were applied to *0.40% C-Mn* steel substrates using a multi-chamber cumulative detonation spraying unit (*MKDU*). Modern analytical methods were employed for thorough characterization: scanning electron microscopy (*SEM, Mira 3*) with energy-dispersive spectroscopy, X-ray diffraction (*XRD, ARL X'TRA* diffractometer) with quantitative phase composition assessment using the *Rietveld* method. Corrosion tests were conducted in a 3.5% *NaCl* solution simulating marine environments, using potentiostatic measurements and electrochemical impedance spectroscopy on a *SmartStat PS-10-4* potentiostat-galvanostat. The depth of corrosion penetration was evaluated using confocal laser microscopy (*Lext OLS5000*) with a resolution of 10 nm. **Results and discussion.** It was established that the addition of 10 wt.% B_4C leads to the formation of a unique multilayered coating structure with an amorphous phase content of up to 12.3% and promotes the formation of passivating chromium (Cr_2O_3) and boron (B_2O_3) oxides. Electrochemical measurements revealed an exceptionally low corrosion rate of 0.0014 mm/year, which is an order of magnitude lower than that of the base alloy (0.021 mm/year) and 30 times lower than that of the commercial counterpart *NiCr/WC* alloy (*VSNGN-85*) (0.041 mm/year). The modified coating exhibits remarkably high polarization resistance (215±25 kΩ·cm²) and minimal porosity (0.6±0.1%). The microhardness reached 680±40 HV, significantly exceeding that of the base alloy (520±30 HV), which is attributed to the formation of dispersed *NiB₂* particles. *XRD* and *EDS* analyses confirmed the catalytic effect of B_4C, facilitating a more complete transition of silicon into nickel silicide (*NiSi*). The developed coatings possess a unique combination of high corrosion resistance, wear resistance, and adhesive strength. The obtained results recommend this technology for creating protective coatings for critical components in the oil and gas industry, shipbuilding, and energy sectors. Future research prospects include optimizing powder compositions and spraying parameters for various operational conditions, including elevated temperatures and combined loads.

* Corresponding author
Sirota Vyacheslav V., Ph.D. (Physics and Mathematics)
Belgorod State Technological University named after V.G. Shukhov,
46 Kostyukova st.,
308012, Belgorod, Russian Federation
Tel.: +7 904 539-14-08, **e-mail:** zmas36@mail.ru

Introduction

Modern wear-resistant coatings made of self-fluxing nickel-based alloys are widely used in industry [1]. However, when operating in aggressive environments, such as seawater or chemically active solutions, these coatings are subjected not only to mechanical stress but also to corrosive degradation. In this case, the corrosion rate can significantly affect their wear resistance and durability, leading to premature failure of components and substantial economic losses [2–4].

The relevance of this work lies in the need for a comprehensive study of the corrosion behavior of wear-resistant coatings, since their traditional evaluation is mainly limited to mechanical characteristics, such as hardness and abrasion resistance [5–8]. However, even high-strength coatings, for example, those based on tungsten or boron carbides, can lose their operational properties due to corrosion processes developing at particle boundaries or pores [9–12]. It is particularly important to investigate corrosion kinetics, as it determines not only the service life of the coating but also its interaction with the substrate, ultimately affecting the overall performance of the system [13–15].

In this study, the detonation spraying method was used to apply the coatings, which offers several significant advantages over alternative technologies. The key advantages of the detonation spraying method include: high particle velocity (up to 2,500 m/s), ensuring better coating adhesion to the substrate and reducing porosity [16], lower heating of the sprayed material, minimizing the risk of undesirable phase transformations and oxidation [17], and the ability to precisely control process parameters, including the gas mixture composition and explosion energy, allowing for optimization of the coating structure and properties [18].

The practical significance of this work lies in the potential application of the obtained results in the development of new wear- and corrosion-resistant coatings for equipment in the oil and gas industry, shipbuilding, and energy sectors operating under extreme conditions. The scientific novelty of the study consists in establishing quantitative relationships between the boron carbide content, detonation spraying parameters, and the corrosion resistance of nickel-chromium-boron-silicon coatings, which has not been previously addressed in the literature to such an extent.

The objective of this work was to evaluate the corrosion rate of wear-resistant coatings based on the self-fluxing alloy PR-NKh17SR4 and its modified counterpart with the addition of boron carbide.

The specific aims of this study were to:

– mechanically blend the self-fluxing powder *NiCrBSi* alloy (*PR-NKh17SR4*) with 10 % boron carbide (B_4C) and assess the uniformity of particle distribution;

– compare the granulometric composition and bulk density of the initial powders and the resulting mixture;

– study the microstructure of the coatings using scanning electron microscopy (*SEM*) and X-ray diffraction (*XRD*) analysis;

– perform electrochemical tests (potentiostatic measurements, impedance spectroscopy) in a 3.5 % *NaCl* solution,

– compare the corrosion behavior of *NiCrBSi* alloy (*PR-NKh17SR4*), *NiCrBSi* (*PR-NKh17SR4*)+10 wt. % B_4C coatings, and a commercial counterpart *NiCr/WC* alloy (*VSNGN-85*).

Methods

For the research, plates made of structural steel grade *0.4 C-Mn (40G)* (40×40×5 mm) were used as substrates. The chemical composition of the steel complies with the requirements of *GOST 1050-2013*. Spectral analysis performed on an optical emission spectrometer "*ISKROLINE 100*" (Russia) confirmed that the steel met the declared grade. The content of the main alloying elements was as follows: 0.40 % carbon, 0.25 % silicon, and 0.78 % manganese, with the total content of sulfur and phosphorus not exceeding 0.03 % each.

Substrate surface preparation involved thorough sandblasting with quartz sand (grain size 1.0±0.2 mm) at a compressed air pressure of 0.6 MPa.

For coating deposition, a multi-chamber cumulative detonation spraying setup (*MKDU*, BSTU named after V.G. Shukhov, Russia) was employed. A distinctive feature of this setup is its dual-chamber system with a focusing lens, enabling particle velocities of up to 2,500 m/s. The system is equipped with a precision gas mixture supply unit and an automated process parameter control system. The gas mixture composition (propane-butane/oxygen/air) was set at a ratio of 13/57/30 vol. %. The process parameters were optimized based on the authors' previous research [19–20].

Three types of powders were used as feedstock materials. The base material was the self-fluxing powder *NiCrBSi* alloy (*PR-NKh17SR4*) produced by *POLEMA JSC* (Russia). To prepare a composite mixture based on this self-fluxing powder, boron carbide grade *F1200* manufactured by *Promkhim LLC* (Russia) was used. The addition of 10 wt. % boron carbide was performed by mechanical mixing in a *Pulverisette 6* planetary mono-mill (*Fritsch*, Germany) at a rotation speed of 200 rpm for 120 minutes. The uniform distribution of boron carbide particles in the *NiCrBSi* alloy (*PR-NKh17SR4*) powder was visually confirmed by backscattered electron imaging (Fig. 1, *d*).

As a reference material, commercial powder *NiCr/WC* alloy (*VSNGN-85*) produced by *Technicord LLC* (Russia) was employed. This material was selected as a typical representative of wear-resistant coatings widely used in industry. The elemental composition of the initial powders was analyzed using energy-dispersive spectroscopy, particle morphology was determined by electron microscopy imaging, and apparent density was measured using a graduated cylinder. The characterization results of the initial powders are presented in Table 1.

Fig. 1 shows the morphology of the initial powders and prepared mixture.

The samples were prepared for microstructure and corrosion properties investigation using a precision cutting machine *IsoMet 5000* (*Buehler*, Germany) and a grinding-polishing machine *MetaServ 250* (*Buehler*, Germany). The final polishing was performed with a 3 μm *Carat* diamond polishing disc (*Labortek*, Russia). Porosity evaluation was conducted on coating cross-sections using the *SIAMS 800* hardware-software complex analyzer. The thickness of the deposited coatings was controlled with an ultrasonic thickness

T a b l e 1

Characteristics of the initial powders

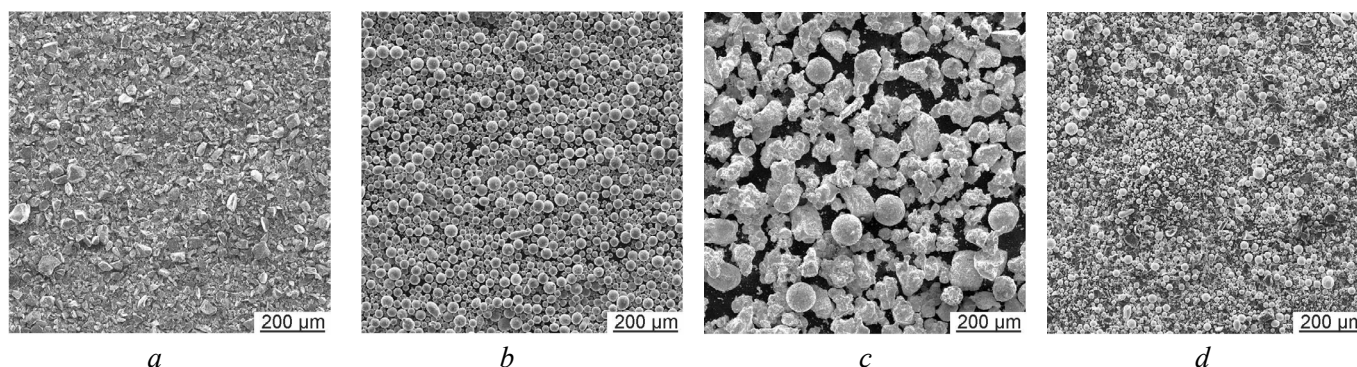| Material	Chemical composition, wt.%							Particle morphology	Apparent density, g/cm^3
	C	Cr	Si	B	Fe	W	Ni		
NiCrBSi alloy (*PR-NKh17SR4*)	1.0	17.1	4.1	3.6	4.8	–	bal.	Spherical	4.1±0.2
NiCrBSi (*PR-NKh17SR4*)+ 10 wt. % B_4C	3.1	15.0	3.5	11.1	4.3	–	bal.	Mixed spherical/angular	3.9±0.2
NiCr/WC alloy (*VSNGN-85*)	5.3	2.5	0.6	0.55	0.4	79.8	bal.	Agglomerated	7.0±0.2

a   *b*   *c*   *d*

Fig. 1. Micrographs of the initial powders and mixture. (*a*), (*b*), (*c*) *SE* images of B_4C, *NiCrBSi* (*PR-NKh17SR4*), and *NiCr/WC* (*VSNGN-85*) powders, respectively. (*d*) *BSE* image of the *NiCrBSi* (*PR-NKh17SR4*)+10 wt. % B_4C mixture
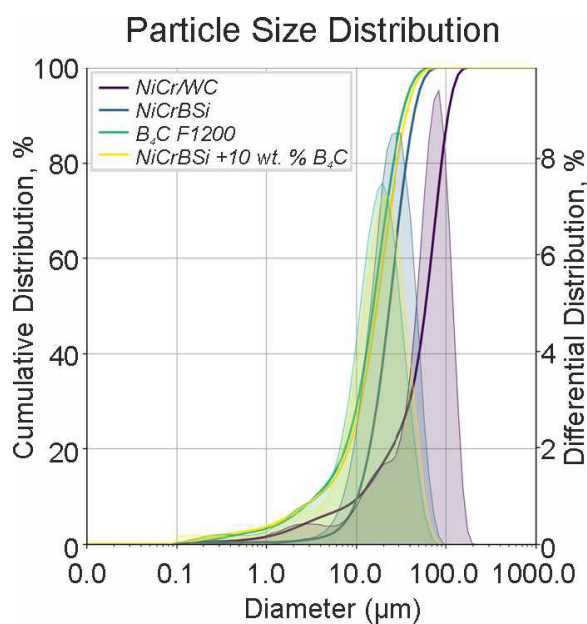
Particle Size Distribution

Fig. 2. Particle size distribution of the initial powders and mixture

gauge *45MG* (*Olympus*, Japan). The particle size distribution of the initial powders and mixture was determined using an *Analysette 22 NanoTec Plus* powder granulometry analyzer (*Fritsch*, Germany), as shown in Fig. 2.

The investigation of the obtained coatings was performed using a comprehensive set of modern analytical methods to thoroughly evaluate their structural and functional properties. Microstructural studies were conducted using a *Mira 3* scanning electron microscope (*Tescan*, Czech Republic) equipped with an *X-Max 50* energy-dispersive spectroscopy system and *AZtec* software (*Oxford* Instruments, UK). Secondary electron (*SE*) and backscattered electron (*BSE*) imaging, along with elemental composition analysis, were performed at an accelerating voltage of 15 kV and a working distance of 15 mm. The *EDS* data were processed using specialized *AZtec* software.

Porosity evaluation was carried out by analyzing *SEM* images of coating cross-sections with a 1,000 **µ**m field of view using *ImageJ* software.

The phase composition of the coatings was examined by X-ray diffraction analysis using an *ARL X'TRA* diffractometer with *Cu-Kα* radiation (λ = 1.5418 Å). Measurements were performed in **θ-2θ** scanning mode within the angular range of 10–90° with a step size of 0.02° and an exposure time of 1 s per point. Phase identification was conducted using the *PDF-2* database from the International Centre for Diffraction Data (*ICDD*).

Corrosion testing was performed using a three-electrode electrochemical cell with a *SmartStat PS-10-4* potentiostat-galvanostat. A 3.5 % sodium chloride solution (pH = 6.8±0.2), prepared from analytically pure ("chemically pure") grade reagent and distilled water, served as the working electrolyte. The reference electrode was a silver/silver chloride (*Ag*/*AgCl*) electrode, and the counter electrode was made of graphite.

The electrochemical testing protocol consisted of several sequential stages. Initially, the open circuit potential (*OCP*) was monitored for 60 minutes until it reached a steady-state condition (±10 mV/10 min). This was followed by electrochemical impedance spectroscopy (*EIS*) measurements across a frequency range of 50 kHz to 10 mHz with an *AC* signal amplitude of 10 mV. The obtained *Nyquist* spectra were fitted using equivalent electrical circuits with the "*impedance.py*" script [21]. Subsequently, potentiodynamic polarization curves were recorded at a scan rate of 1 mV/s, covering a potential range from −300 mV versus *OCP* to +1.2 V versus *Ag*/*AgCl*, or until reaching a current density of 10 mA/cm^2. Special attention was paid to analyzing the *Tafel* regions of both anodic and cathodic branches to determine kinetic parameters of the corrosion process. For each sample, a minimum of three replicate tests were conducted, followed by statistical analysis of the results.

Post-corrosion characterization included surface examination using scanning electron microscopy. The depth of corrosion penetration was evaluated using a confocal laser microscope with a vertical resolution of 10 nm.

Mechanical tests involved *Vickers* microhardness measurement criteria on a *NEXUS 4504-IMP* hardness tester (*INNOVATEST*, Netherlands) at 1 kg and a holding time of 15 s. For each sample, at least 10 measurements were made with subsequent exclusion of gross errors using the *Student* criterion.

Results and Discussion

A comprehensive study of the coating microstructure revealed significant differences between the studied compositions. The coating based on the self-fluxing powder *NiCrBSi* (*PR-NKh17SR4*) demonstrated

a characteristic layered structure with clearly defined boundaries between individual sprayed particles (Fig. 3, *a*). The average size of the structural elements was 10–30 **μ**m, which corresponds to the granulometry of the original powder. The porosity determined by quantitative image analysis did not exceed 0.7±0.1 %, with most of the pores located at the interparticle boundaries.
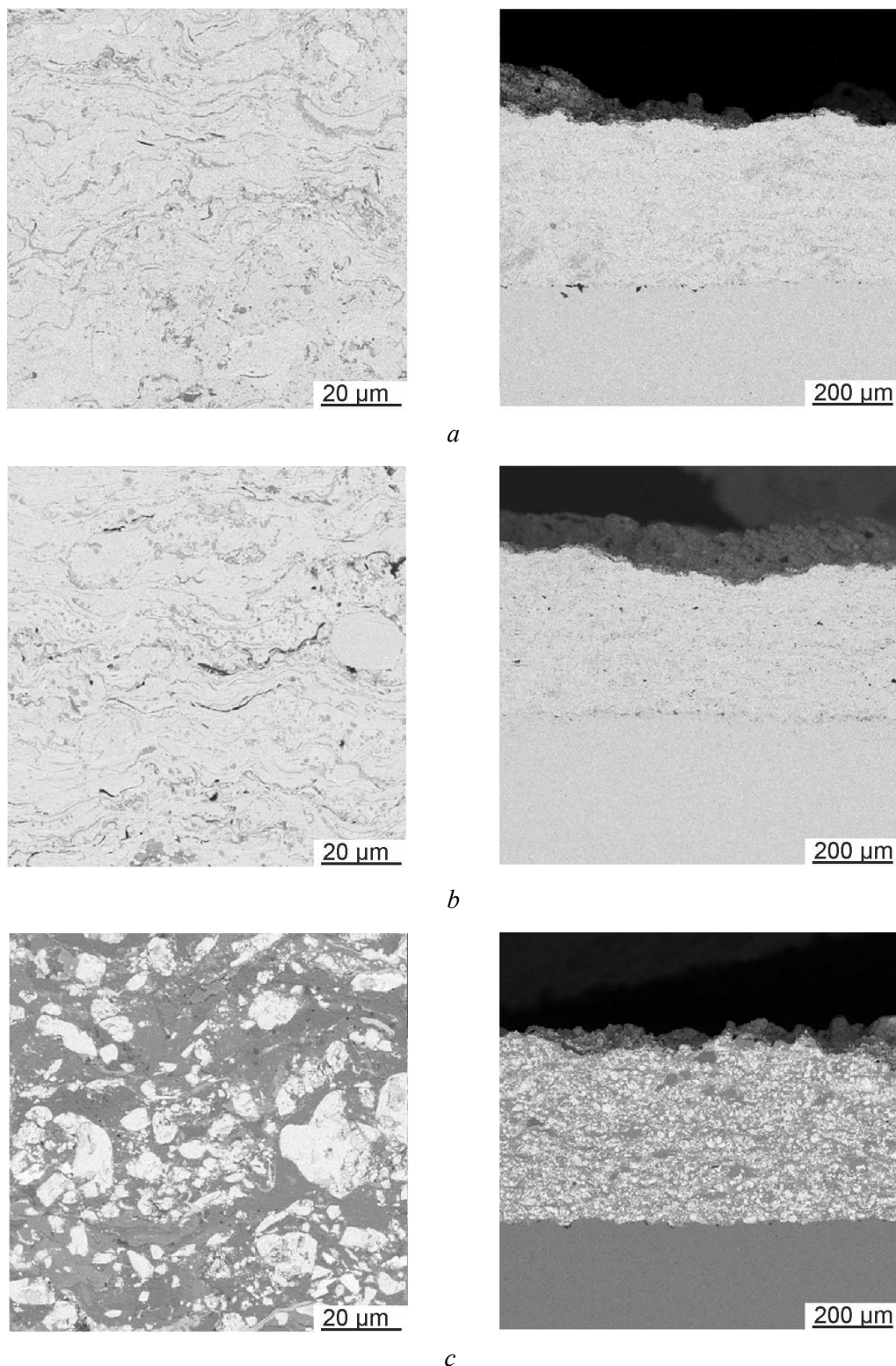

Fig. 3. SEM images of the cross-sectional microstructure of the coatings:
a – NiCrBSi (PR-NKh17SR4); b – NiCrBSi (PR-NKh17SR4)+10 wt.% *B₄C; c – NiCr/WC*
(VSNGN-85)

The introduction of 10 % boron carbide resulted in a significant change in the microstructure (Fig. 3, *b*). While maintaining the average size of the structural elements and porosity at the same level (Table 2), a qualitative change in the boundaries between individual sprayed particles was observed.

Table 2

Structural characteristics of the studied coatings

Parameter	NiCrBSi (PR-NKh17SR4)	NiCrBSi (PR-NKh17SR4)+10 % B_4C	NiCr/WC (VSNGN-85)
Average thickness, μm	410±15	390±40	430±30
Porosity, %	0.7±0.1	0.6±0.1	0.9±0.3
Hardness HV_1	520±30	680±40	1,250±120

EDS analysis showed saturation of grain boundaries with boron and the total boron content close to the added one (see Fig. 4). At the same time, the content of boron carbide particles was significantly lower than in the initial mixture. This indirectly indicates partial decomposition of boron carbide and active interaction of boron with other components of the coating in the process. X-ray phase analysis also showed the presence of an amorphous peak and broadening of the base of the nickel peak, which confirms the formation of solid solutions in greater quantities compared to the *NiCrBSi* (*PR-NKh17SR4*) coating (see Fig. 5). For data processing and quantitative phase analysis, the *Rietveld* method implemented in the *Match3* software was used, which allows for taking into account the overlap of peaks and the influence of microstructural factors.

The *NiCr/WC* (*VSNGN-85*) coating has a characteristic "island" structure with clearly defined tungsten carbide particles in a nickel matrix (see Fig. 3, *c*). X-ray phase analysis also showed sharp peaks of tungsten carbide against the background of diffuse peaks corresponding to nickel-based solid solutions. The results of electrochemical studies showed a significant effect of the coating composition on their corrosion behavior in a 3.5 % *NaCl* solution. Potentiometric measurements revealed significant differences in the corrosion potential values (Fig. 7, *a*). The most noble potential (−250±30 mV) was recorded for the *NiCrBSi* (*PR-NKh17SR4*)+10 % B_4C coating, which indicates its increased thermodynamic stability.

Analysis of the polarization curves (Fig. 6) revealed that the boron carbide-modified coating exhibited the lowest corrosion current density (0.8±0.02 μA/cm^2), which was an order of magnitude lower than that of the base composition (6.5±0.2 μA/cm^2). Electrochemical impedance spectroscopy confirmed the formation of a dense protective film on the modified coating surface, as evidenced by the high polarization resistance values (215±25 kOhm·cm² and low constant phase element parameters (45±5 μF·cm^{-2}·s^{-1}).
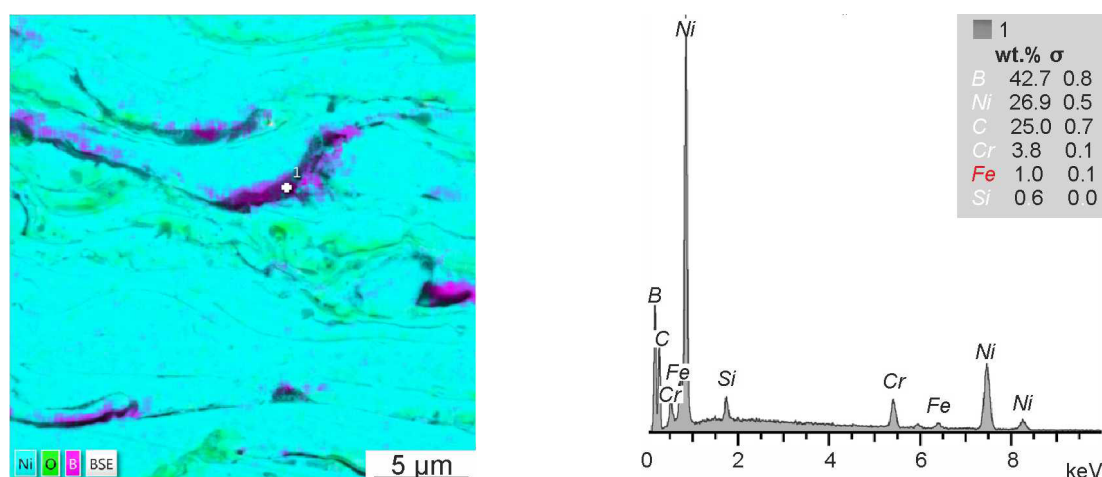
Fig. 4. *EDS* mapping of the cross-section of *NiCrBSi* (*PR-NKh17SR4*)+10 wt.% B_4C

X-ray diffraction patterns of samples
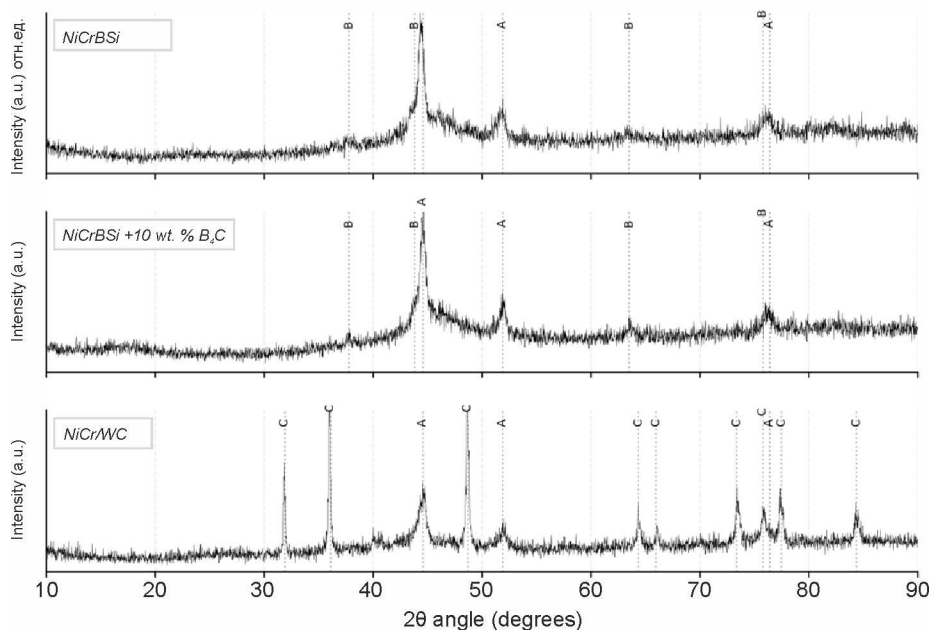
Fig. 5. XRD patterns of the studied coatings:
A – Fm-3m (***a*** = 0.350 ± 0.003 nm) Solid solutions of interstitial and substitutional types based on nickel; ***B*** – Fm-3m (***a*** = 0.414 ± 0.003 nm) Intermetallic compounds; ***C*** – P-6m2 (***a*** = 0.291 nm, ***c*** = 0.284 nm) – Tungsten carbide (*WC*)
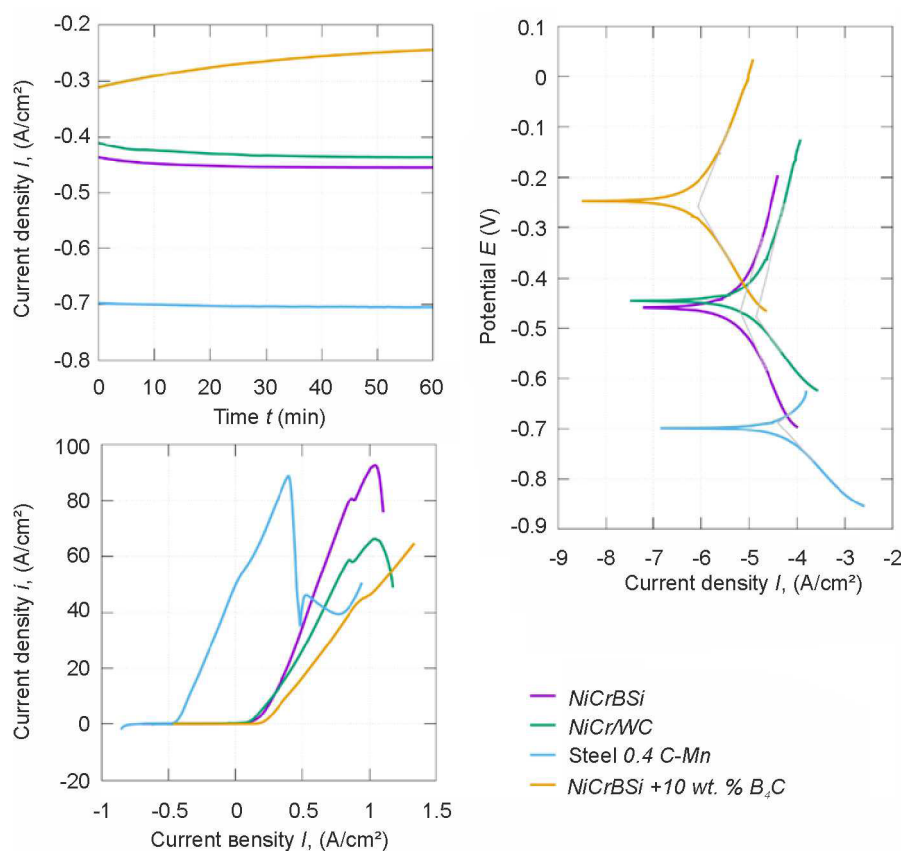
Fig. 6. Kinetics of the open circuit potential (*OCP*) establishment (left top); linear polarization curves (bottom left); and *Tafel* plots (right) in an aqueous solution containing 3.5% *NaCl*. Potential data are given relative to a silver/silver chloride (Ag/AgCl) electrode

The *Tafel* slopes for both anodic and cathodic reactions were determined from polarization curves plotted in semi-logarithmic coordinates (see Fig. 6), enabling calculation of corrosion current densities and potentials (Table 3). The results demonstrated that the boron carbide-modified coating exhibited the lowest corrosion current density (0.8 μA/cm^2), which was one order of magnitude lower than both the base *NiCrBSi* (*PR-NKh17SR4*) composition (6.5 μA/cm^2) and the *NiCr/WC* (*VSNGN-85*) coating (13.9 μA/cm^2).

Table 3

Corrosion behavior parameters in 3.5 % *NaCl*

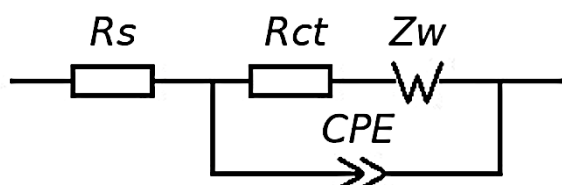| Parameter	Steel *0.4 C-Mn*	*NiCrBSi* (*PR-NKh-17SR4*)	*NiCrBSi* (*PR-NKh-17SR4*)+10 % B_4C	*NiCr/WC* (*VSNGN-85*)
E_{corr} (vs. *SCE*) (mV)	−690±15	-470±10	−260±10	−480±12
i_{corr} (μA/cm²)	40.2±1.5	6.5±0.2	0.8±0.02	13.9±0.4
R_{ct} (kΩ·cm²)	0.4±0.1	6.6±0.8	66.4±5.2	3.1±1.0
$QCPE$ (μF·cm^{-2}·s^{-1})	0.3	600	240	1100
n	1	0.63	0.66	0.6

Fig. 7. *Randles-Ershler* equivalent circuit

Electrochemical impedance spectroscopy studies in 3.5 % *NaCl* aqueous solution revealed that the impedance data for all investigated coatings fitted well with the *Randles-Ershler* equivalent circuit model (Fig. 7). In this circuit, the constant phase element (*CPE*) describes the double layer capacitance, R_{ct} represents the charge transfer resistance, and *ZW* corresponds to *Warburg* impedance associated with diffusion processes. The typical *Nyquist* plot featured a semicircular segment that rapidly transitioned into a sloping straight line (diffusion impedance) in the high-frequency region. However, the *NiCr/WC* (*VSNGN-85*) coating exhibited several inflection points, attributed to the presence of large heterogeneous phases (tungsten carbide and binder).

The electrochemical impedance spectroscopy data of the coatings and the substrate with superimposed approximation lines using the *Randles-Erschler* equivalent circuit are presented in Fig. 8 as *Nyquist* plots. The approximation parameters (see Table 3) confirmed the formation of a dense protective film on the surface of the *NiCrBSi* (*PR-NKh17SR4*)+10 wt.% B_4C coating, as evidenced by high values of polarization resistance and low values of the phase element constant. The low degree index of the studied coatings (0.6–0.7) indicates the heterogeneity and porosity of the coatings, which is consistent with the microstructure (see Fig. 3). At the same time, for the *NiCrBSi* (*PR-NKh17SR4*)+10 wt.% B_4C coating, this parameter is higher for the others, that is, it indicates higher homogeneity and lower porosity.

After corrosion tests, the surface of the coatings was examined using electron microscopy methods (see Fig. 9).

On the *NiCrBSi* (*PR-NKh17SR4*)+10 wt.% B_4C coating, shallow, predominantly surface corrosion was observed, while on the reference *NiCr/WC* (*VSNGN-85*) coating, numerous deep corrosion lesions of the metal bond were noted along the boundaries of tungsten carbide particles.

Conclusion

1. The conducted study allowed us to comprehensively evaluate the corrosion properties of self-fluxing powder coatings obtained by detonation spraying. The results showed that the introduction of 10 % boron
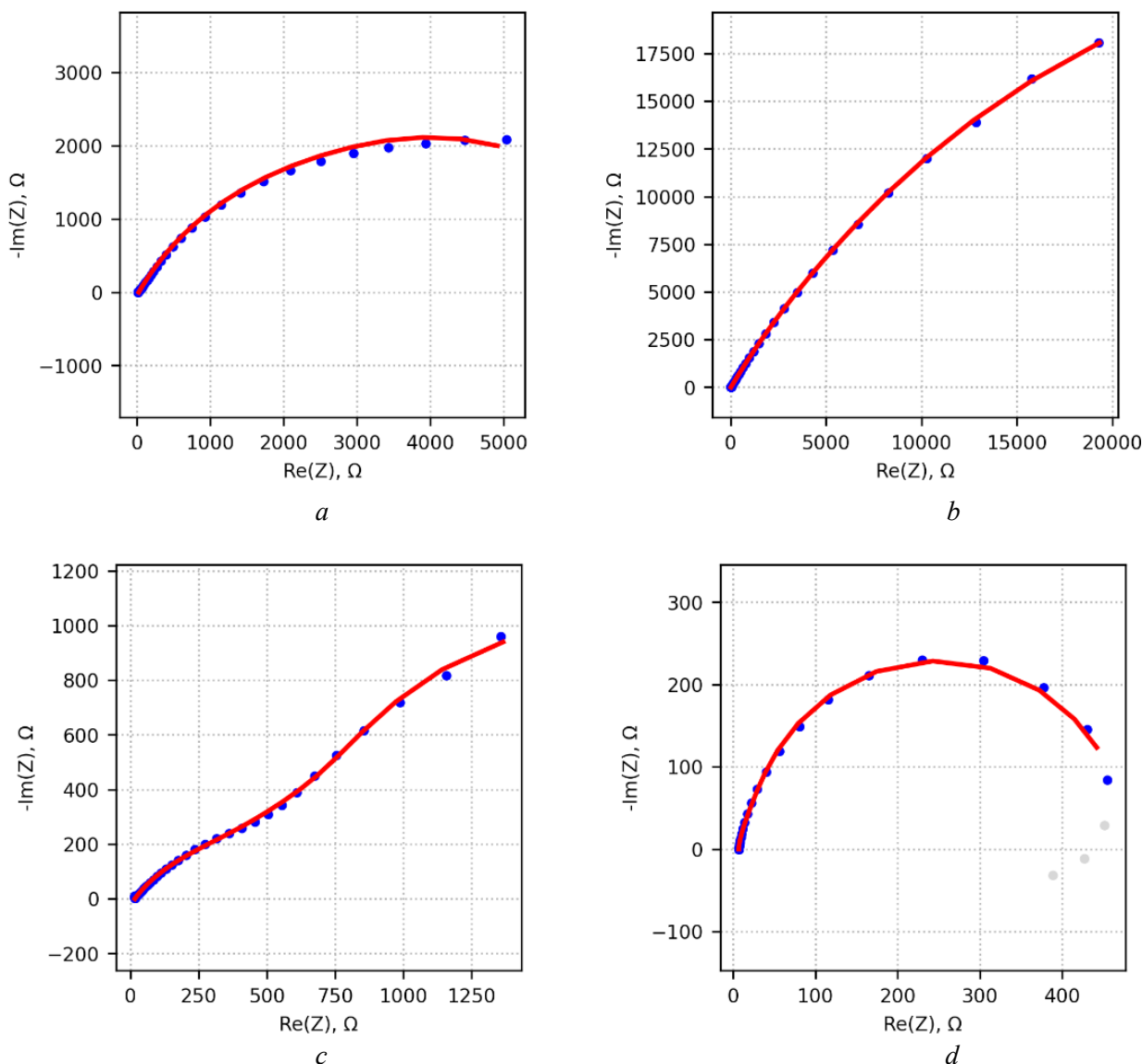
Fig. 8. Nyquist plots of coatings in an aqueous solution containing 3.5% *NaCl* near the stationary potential in the frequency range from 50 kHz to 10 MHz:

a – NiCrBSi PR-NKh17SR4); b – NiCrBSi (PR-NKh17SR4)+10 wt.% B₄C; c – NiCr/WC (VSNGN-85);
d – 0.4% C-Mn

carbide into the self-fluxing alloy *NiCrBSi* (*PR-NKh17SR4*) significantly improves the corrosion resistance of the coating.

2. The modified coating demonstrates the most noble corrosion potential (−260±10 mV) and the minimum corrosion current (0.8±0.02 μA/cm^2), which indicates its high thermodynamic and kinetic stability in an aggressive environment. These indicators significantly exceed the characteristics of both the base alloy *NiCrBSi* (*PR-NKh17SR4*) and the commercial coating *NiCr/WC* (*VSNGN-85*).

3. Microstructural analysis revealed that boron carbide promotes the formation of a dense multilayer protective system, including an external passivation layer based on chromium and boron oxides, a main matrix with dispersed *NiB$_2$* particles, and an increase in the volume of the *NiSi* phase. Such a structure not only reduces the porosity of the coating, but also provides effective protection against the development of general and crevice corrosion.

4. Impedance spectroscopy confirmed the formation of a dense protective film, as evidenced by high values of polarization resistance (215±25 kOhm cm^2) and low values of the phase element constant.
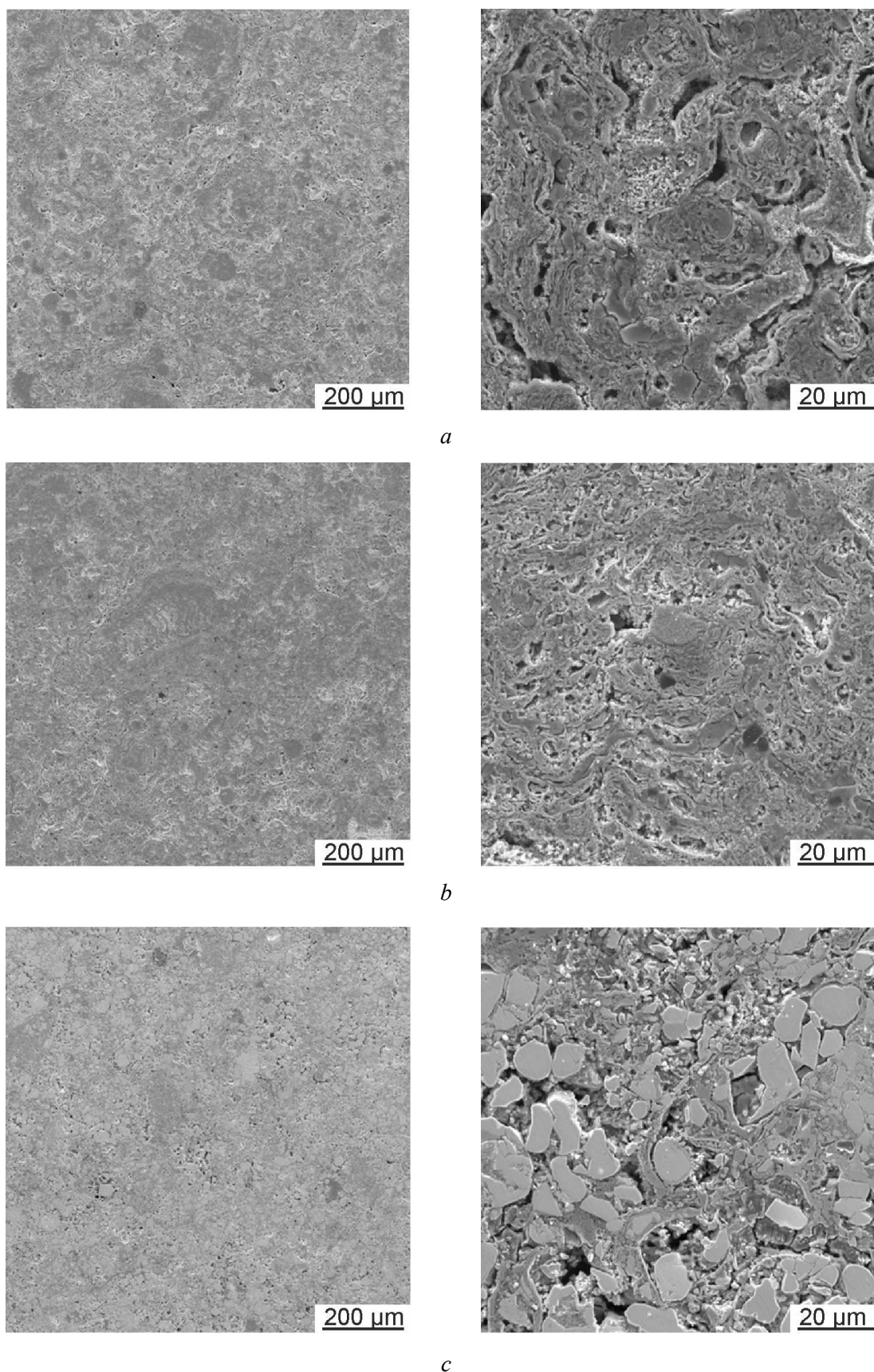
Fig. 9. SEM images of the surface microstructure after corrosion tests:
a – NiCrBSi (*PR-NKh17SR4*); *b – NiCrBSi* (*PR-NKh17SR4*)+10 wt.% *B$_4$C*
and *c – NiCr/WC* (*VSNGN-85*)

References

1. Simunovic K., Saric T., Simunovic G. Different approaches to the investigation and testing of the Ni-based self-fluxing alloy coatings – A review. Part 1: General facts, wear and corrosion investigations. *Tribology Transactions*, 2014, vol. 57 (6), pp. 955–979.

2. Koch G.H., Brongers M.P.H., Thompson N.G., Virmani Y.P., Payer J.H. Cost of corrosion in the United States. *Handbook of environmental degradation of materials*. William Andrew Publishing, 2005, pp. 3–24. DOI: 10.1016/B978-081551500-5.50003-3.

3. Thompson N.G., Yunovich M., Dunmire D. Cost of corrosion and corrosion maintenance strategies. *Corrosion Reviews*, 2007, vol. 25 (3–4), pp. 247–262. DOI: 10.1515/CORRREV.2007.25.3-4.247.

4. Baorong H.O.U., Dongzhu L.U. Corrosion cost and preventive strategies in China. *Bulletin of Chinese Academy of Sciences*, 2018, vol. 33 (6), pp. 601–609. DOI: 10.16418/j.issn.1000-3045.2018.06.008. (In Chinese).

5. Mariani F.E., Rêgo G.C., Neto A.L., Totten G.E., Casteletti L.C. Wear behavior of a borided nickel-based self-fluxing thermal spray coating. *Materials Performance and Characterization*, 2016, vol. 5 (4). DOI: 10.1520/MPC20150064.

6. Vidaković I., Šimunović K., Heffer G., Špada V. Microstructural analysis of flame-sprayed and PTA-deposited nickel-based self-fluxing alloy coatings. *Welding in the World*, 2024, vol. 68 (11), pp. 2819–2836. DOI: 10.1007/s40194-024-01814-5.

7. Kretinin V.I., Teppoev A.V., Sokolova V.A., Polyanskaya O.A., Alekseeva S.V. Justification of strengthening of working bodies of forestry machines with self-fluxing alloys during gas-flame spraying. *IOP Conference Series: Earth and Environmental Science*, 2021, vol. 876 (1), p. 012045. DOI: 10.1088/1755-1315/876/1/012045.

8. Dong X.Y., Luo X.T., Zhang S.L., Li C.J. A novel strategy for depositing dense self-fluxing alloy coatings with sufficiently bonded splats by one-step atmospheric plasma spraying. *Journal of Thermal Spray Technology*, 2020, vol. 29, pp. 173–184. DOI: 10.1007/s11666-019-00943-4.

9. Liu C.W., Qin E.W., Chen G.X., Wei S.C., Zou Y., Ye L., Wu S.H. Effect of flame remelting on the microstructure, wear and corrosion resistance of HVOF sprayed NiCrBSi coatings. *Advanced Materials Research*, 2024, vol. 1179, pp. 157–168. DOI: 10.4028/p-v2xcOL.

10. Shuecamlue S., Taman A., Khamnantha P., Banjongprasert C. Influences of flame remelting and WC-Co addition on microstructure, mechanical properties and corrosion behavior of NiCrBSi coatings manufactured via HVOF process. *Surfaces and Interfaces*, 2024, vol. 48, p. 104135. DOI: 10.1016/j.surfin.2024.104135.

11. Shabanlo M., Amini Najafabadi R., Meysami A. Evaluation and comparison the effect of heat treatment on mechanical properties of NiCrBSi thermally sprayed coatings. *Anti-Corrosion Methods and Materials*, 2018, vol. 65 (1), pp. 34–37. DOI: 10.1108/ACMM-02-2017-1756.

12. Xuan H.N., Chen L., Li N., Wang H., Zhao C., Bobrov M., Lu S., Zhang L. Temperature profile, microstructural evolution, and wear resistance of plasma-sprayed NiCrBSi coatings under different powers in a vertical remelting way. *Materials Chemistry and Physics*, 2022, vol. 292, p. 126773. DOI: 10.1016/j.matchemphys.2022.126773.

13. Fayomi O.S.I., Akande I.G., Odigie S. Economic impact of corrosion in oil sectors and prevention: an overview. *Journal of Physics: Conference Series*, 2019, vol. 1378 (2), p. 022037. DOI: 10.1088/1742-6596/1378/2/022037.

14. Kania H. Corrosion and anticorrosion of alloys/metals: the important global issue. *Coatings*, 2023, vol. 13 (2), p. 216. DOI: 10.3390/coatings13020216.

15. Shekari E., Khan F., Ahmed S. Economic risk analysis of pitting corrosion in process facilities. *International Journal of Pressure Vessels and Piping*, 2017, vol. 157, pp. 51–62. DOI: 10.1016/j.ijpvp.2017.08.005.

16. Zlobin S.B., Ulianitsky V.Yu., Shtertser A.A., Smurov I. High-velocity collision of hot particles with solid substrate, under detonation spraying: detonation splats. *Thermal Spray: Expanding Thermal Spray Performance to New Markets and Applications*. ASM, 2009, pp. 714–717. DOI: 10.31399/asm.cp.itsc2009p0714.

17. Tucker R.C. Jr. Structure property relationships in deposits produced by plasma spray and detonation gun techniques. *Journal of Vacuum Science and Technology*, 1974, vol. 11 (4), pp. 725–734. DOI: 10.1116/1.1312743.

18. Sundararajan G., Sen D., Sivakumar G. The tribological behaviour of detonation sprayed coatings: the importance of coating process parameters. *Wear*, 2005, vol. 258 (1–4), pp. 377–391. DOI: 10.1016/j.wear.2004.03.022.

19. Sirota V.V., Zaitsev S.V., Prokhorenkov D.S., Limarenko M.V., Skiba A.A., Churikov A.S., Dan'shin A.L. Detonation application of a hard composite coating to cutters for centrifugal beet shredders. *Russian Engineering Research*, 2023, vol. 43 (9), pp. 1142–1145. DOI: 10.3103/s1068798x23090216.

20. Sirota V.V., Zaitsev S.V., Limarenko M.V., Churikov A.S., Podgornyi D.S. The effect of the introduction of B4C on the adhesive and cohesive properties of self-fluxing coatings. *Construction Materials and Products*, 2024, vol. 7 (6). DOI: 10.58224/2618-7183-2024-7-6-5.

21. Murbach M.D., Gerwe B., Dawson-Elli N., Tsui L. impedance.py: A Python package for electrochemical impedance analysis. *Journal of Open Source Software*, 2020, vol. 5 (52), p. 2349. DOI: 10.21105/joss.02349.

Conflicts of Interest

The authors declare no conflict of interest.

Obrabotka metallov -
Metal Working and Material Science

Journal homepage: http://journals.nstu.ru/obrabotka_metallov

The influence of structural state on the mechanical and tribological properties of Cu-Al-Si-Mn bronze

Andrey Filippov [a, *], Nikolay Shamarin [b], Sergei Tarasov [c], Natalya Semenchyuk [d]

Institute of Strength Physics and Materials Sciences SB RAS, 2/4 per. Academicheskii, Tomsk, 634055, Russian Federation

[a] https://orcid.org/0000-0003-0487-8382, ✉ avf@ispms.ru; [b] https://orcid.org/0000-0002-4649-6465, ✉ shnn@ispms.ru;
[c] https://orcid.org/0000-0003-0702-7639, ✉ tsy@ispms.ru; [d] https://orcid.org/0000-0001-6547-7676, ✉ natali.t.v@ispms.ru

ABSTRACT

Introduction. Electron beam additive manufacturing (*EBAM*) is a promising method for producing new alloys with unique properties. At the same time, existing problems with obtaining a high-quality structure require a search for a technical solution that ensures grain refinement and the formation of a more homogeneous microstructure. For strain-hardened copper alloys, severe plastic deformation (*SPD*) methods are effective ways to control their structural state and mechanical properties. Currently, the effect of severe plastic deformation on the structure, mechanical, and tribological properties of *Cu-Al-Si-Mn* bronze, which is promising for industrial application, has not been studied. **The aim of this work** is to study the relationship between the structural state formed as a result of severe plastic deformation and the mechanical and tribological properties of *Cu-Al-Si-Mn* bronze samples. The paper studies samples of *Cu-Al-Si-Mn* bronze, made from bronze (*3% Si-1% Mn*) wires and commercially pure aluminum using multiwire electron beam additive manufacturing. For targeted changes in structure and properties, the resulting additively manufactured blanks were subjected to severe plastic deformation. Multi-axial forging and rolling were used as *SPD* methods, aimed at significant grain refinement and increased strength characteristics. The work uses such **research methods** as transmission electron microscopy (*TEM*) for a detailed analysis of the submicron structure after *SPD*, X-ray diffraction (*XRD*) to identify the phase composition of the alloy, tensile tests to determine key mechanical properties such as tensile strength, yield strength, and percentage of elongation, microhardness measurements to assess the hardening of samples using *Vickers* loads, confocal laser scanning microscopy (*CLSM*) for three-dimensional analysis of the surface topography and studying the morphology of worn surfaces, and dry sliding friction tests to assess the wear resistance of the material and the friction coefficient in the absence of lubrication under specified loads and sliding speeds. **Results and discussion.** Based on the data of transmission electron microscopy, it was found that the use of multi-axial forging and rolling led to significant changes in the structure of the material, as well as its phase composition. Based on the X-ray diffraction analysis, it was revealed that severe plastic deformation contributed to the deformation-induced dissolution of the **γ**- and **β**-phases. The results of tensile tests showed that the highest strength is achieved after intense plastic deformation by rolling, after multi-axial forging. *SPD* by multi-axial forging and subsequent rolling led to an increase in the microhardness of bronze. The results of tribological tests showed that *SPD* contributes to a decrease in the friction coefficient (*FC*) compared to the material in the printed state. Heat treatment of samples after *SPD* led to an increase in *FC* and an increase in fluctuations in its value. *SPD* by multi-axial forging and subsequent rolling contributes to a significant increase in the wear resistance of samples under dry sliding friction conditions. Low-temperature annealing after *SPD* leads to a decrease in the wear resistance of deformed samples. Thus, the use of *SPD* makes it possible to increase the strength and wear resistance of bronze samples of the *Cu-Al-Si-Mn* system.

Introduction

Bronzes are metal alloys that have a range of qualities making them essential for numerous uses, especially in corrosive environments and under sliding friction. The structural and phase states of bronzes dictate their mechanical, tribological, and corrosion properties, which are chosen based on the alloy's intended use and can be modified through suitable alloying. The key alloying elements for bronzes are aluminum, iron, nickel, tin, zinc, lead, manganese, and silicon, which are part of the composition of well-known bronze grades from the *Cu-Al*, *Cu-Mn*, *Cu-Zn*, *Cu-Pb*, *Cu-Si*, *Cu-Al-Fe*, *Cu-Ni-Al*, and *Cu-Al-Fe-Ni*

systems. The desired level of properties is attained not just by adjusting the alloying components but also through further thermal treatment and mechanical processing, which influences the material's physical and mechanical properties [1]. Even though a significant amount of work has already been accomplished in this field, ongoing exploratory research continues to be directed toward the creation of innovative structural and functional materials to meet contemporary industrial demands [1].

Although significant progress has been made in this field, ongoing exploratory research continues to focus on creating new structural and functional materials for contemporary industrial requirements.

The present phase of progress in material technologies is linked to the enhancement of additive techniques for creating items from robust materials that have excellent processability, adequate corrosion resistance, and wear resistance. To achieve an additive material with an adequate level of strength and functional characteristics, it is essential to identify a logical combination of printing parameters and filament formulation. The most crucial factor is the selection of the alloying element composition that will yield the required structure and phase constitution. Following this, the thermal treatment and mechanical processing modes for the printed material are established to achieve the intended functional characteristics.

Aluminum bronzes are noted for their excellent strength and formability under pressure. Incorporating silicon enhances ductility and improves resistance to corrosion and cyclic impact loads, all while preserving high strength. These properties can be further enhanced by adding manganese to the *Cu-Al-Si* system, which promotes increased strength, hardness, and corrosion resistance. Silicon and manganese enhance the stability of the ductile *FCC* α-phase formed from alloying elements in copper and inhibit the development of the brittle β-Cu_3Al phase. Nonetheless, high concentrations of these elements can also result in the formation of silicide particles and other reinforcement phases within the *Mn-Al* system. This is crucial for enhancing the mechanical characteristics of bronze through mechanical processes (forging, rolling, etc.). In industrial alloys of the *Cu-Al* system, with approximately 8–12 wt. % *Al*, the phases that exist in equilibrium at room temperature include the solid solution phase α-*Cu(Al)* and the intermetallic compounds β-Cu_3Al and $γ_2$-Cu_9Al_4. The latter is the product of the decomposition of high-temperature β-Cu_3Al into $γ_2$-Cu_9Al_4 and α-*Cu*. The development of $γ_2$-Cu_9Al_4 causes a reduction in the plasticity and corrosion resistance of bronze; thus, attempts are being made to remove it. One method to accomplish this could involve encouraging the diffusionless change from β to β′. The presence of β′-Cu_3Al greatly influences the mechanical characteristics by enhancing microhardness and strength [5, 6, 7].

In the *Cu-Si* system, the predominant phase is the solid solution α-*Cu(Si)*. A multiphase composition, comprising copper silicides, develops when the silicon content exceeds 5 wt.% [8]. The creation of copper silicides with higher silicon levels leads to enhanced strength and hardness in copper alloys [9].

The scenario is more intricate with the *Cu-Al-Si* system. The majority of the research on this system centers on analyzing the phase composition in areas with ele-vated aluminum levels [10–12], along with high silicon concentrations [13]. It has been previously noted that in such bronze, structures with *FCC*, *BCC*, and *HCP* crystal lattices, along with silicide particles, may develop [14]. The composition of phases is directly influenced by the amounts of aluminum and silicon, along with the temperature and the rate of solidification. This study suggests that a rise in aluminum content aids in creating a more multiphase structure. According to the modeling results [15], at temperatures of 500 °C and 700 °C in the *Cu-Al-Si* ternary system with approximately 10 at.% *Al* and about 3 at.% *Si*, the alloy appears to be multiphase. Nonetheless, this paper does not provide findings from structural studies that validate this information.

Aluminum bronzes typically exhibit a structure with large columnar grains or dendrites after casting. Similarly, in the three-dimensional printing process using electron beam additive manufacturing, bronzes based on copper-aluminum (*Cu-Al*), copper-silicon-manganese (*Cu-Si-Mn*), and copper-aluminum-manganese (*Cu-Al-Mn*) systems also develop a columnar grain structure in the samples [16–18]. These grains are undesirable, hindering the material's strength and ductility. Therefore, a critical challenge for current researchers is to devise methods for controlling the microstructure of bronze alloys – through techniques like thermomechanical processing or alloying — to ensure improvements in their strength, wear resistance, and fatigue life.

Bronzes containing aluminum, silicon, and manganese are considered strain-hardening alloys. Applying severe plastic deformation (*SPD*) methods is a practical approach to intentionally modify their structural-phase state and, thereby, their mechanical properties. These methods encompass: forging, rolling, equal-channel angular pressing, high-pressure torsion, and surface plastic deformation [19, 20].

Currently, the impact of *SPD* on the structural, mechanical, and tribological characteristics of the *Cu-Al-Si-Mn* bronze system, a material with considerable potential for industrial use, remains unexplored. This is particularly the case for materials fabricated via additive manufacturing techniques.

In light of the foregoing review, the inherent promise of the material, and the identified deficiencies in existing studies, the ***objective of this research*** was established: to explore the correlations between the diverse structural states and the properties of the *Cu-Al-Si-Mn* copper alloy.

To realize this objective, the following experimental ***tasks*** were undertaken:

– to characterize the structure and phase composition of samples in the as-printed condition and following the application of intense plastic deformation techniques;

– to evaluate mechanical properties, specifically tensile strength and microhardness, for samples exhibiting various structural states;

– to analyze the tribological behavior of the samples;

– to examine the morphology of the wear track surfaces.

Methods

To investigate the influence of structural states on the properties of *Cu-Al-Si-Mn* bronze, samples in the form of prismatic blocks (20×20×40 mm³) were fabricated using electron beam additive manufacturing. Printing was performed by simultaneously feeding two wires: *Cu-3 Si-1 Mn* (*BrKMts 3-1*) and commercially pure aluminum, in a ratio of 90 % bronze to 10 % aluminum [21]. The chemical composition of the samples was 93.8 wt.% *Cu*, 2.5 wt.% *Al*, 2.8 wt.% *Si*, 0.9 wt.% *Mn*. The printed blocks were subjected to severe plastic deformation (*SPD*) by means of multi-directional forging and rolling. In addition, the samples were also subjected to low-temperature heat treatment after *SPD*. The designations of the investigated samples and the processing parameters are listed in Table.

Designation of samples and methods for forming their structure

Sample designation	Method of forming a structural state
1	Electron beam additive manufacturing
2	Multi-axial forging along three geometric axes until 40% plastic deformation is achieved in each direction
3	Rolling after multi-axial forging until 50% plastic deformation is achieved
4	Low-temperature annealing (30 min. at 400°C) after multi-axial forging with rapid cooling in water
5	Low-temperature annealing (30 min. at 400°C) after rolling with rapid cooling in water

Flat tension test specimens were cut from the obtained samples using an electrical discharge machine for mechanical testing on a *Testsystem UTS-110M* testing machine. The tensile speed was 1 mm/min. Samples in the form of plates were additionally cut for conducting X-ray diffraction analysis on a *Shimadzu XRD-7000* diffractometer. Microhardness measurements were performed using a *Tochline-TBM* microhardness tester with a load of 100 N. The fine structure of the samples was investigated by transmission electron microscopy on a *JEOL JEM-2100* microscope.

Tribological tests were conducted at a fixed sliding speed of 0.1 m/s and a normal load of 20 N under dry sliding friction conditions using a pin-on-disk scheme. Disks were cut from bronzes with different structural states. Counterbodies were made of ball-bearing steel (*1 C-1.5 Cr*). *Tescan MIRA 3 LMU* and *Olympus OLS-4100* microscopes were used to investigate the surface condition of the samples after friction

using scanning electron microscopy and laser scanning microscopy, respectively. Energy-dispersive X-ray spectroscopy (*EDS*) was performed to identify the features of the sample condition after friction.

Results and Discussion

Based on previously obtained results [21] from metallographic studies, it was established that the structure of the printed bronze consists of α-*Cu(Al)* solid solution grains with a size of approximately 75 μm, interspersed with layers of a secondary phase. Upon examination of the fine structure using transmission electron microscopy, it was revealed that the printed bronze (<u>Sample 1</u>) exhibits laths representing α/β eutectoid lamellae, in which the decomposition β→γ_2+ α has occurred (Fig. 1, *a*). The high dislocation density and two overlapping systems of deformation twins (Fig. 1, *b*) are a result of multi-directional forging (<u>Sample 2</u>). Rolling (<u>Sample 3</u>) creates a high dislocation density and deformation twins within the material (Fig. 1, *c*). Primary systems of deformation twins can be disrupted due to the high degree of deformation and replaced by secondary ones, which are significantly smaller than those formed during the multi-directional forging stage. In <u>Sample 4</u> (Fig. 1, *d*), one system of deformation twins predominates, remaining intact even after annealing, indicating their sufficiently high stability with respect to heating. In <u>Sample 5</u> (Fig. 1, *e*), stacking faults, recrystallized submicron grains, and annealing microtwins were formed in the material. These structural changes indicate that the high degree of deformation promoted recrystallization of grains even during annealing below the recrystallization temperature.

X-ray diffraction analysis revealed the influence of the *SPD* method and subsequent heat treatment on the phase composition of the printed bronze. The X-ray diffraction patterns clearly show intense reflections of the α-*Cu(Al)* phase, with the (111) peak being the highest, indirectly indicating the absence of a growth texture (Fig. 2, *a*). Upon detailed examination, reflections of γ_2-*Cu$_9$Al$_4$* were also identified, which are only found in samples of the as-printed bronze (<u>Sample 1</u>, Figs. 2, *c*, *d*) and samples after multi-directional
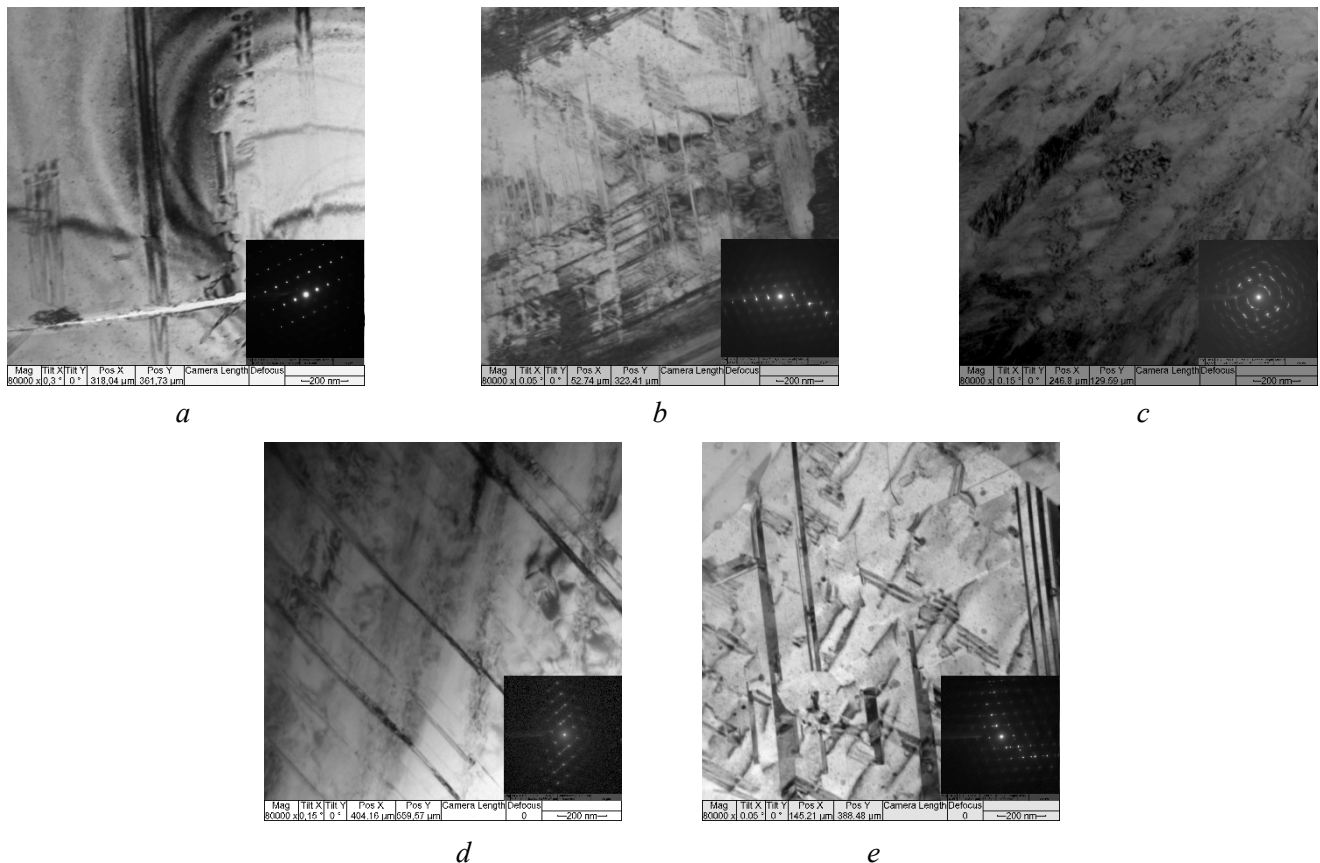

a

b

c

d

e

Fig. 1. TEM images of the typical microstructure of *Cu-Al-Si-Mn* bronze samples. Sample 1 (*a*), sample 2 (*b*), sample 3 (*c*), sample 4 (*d*) and sample 5 (*e*)
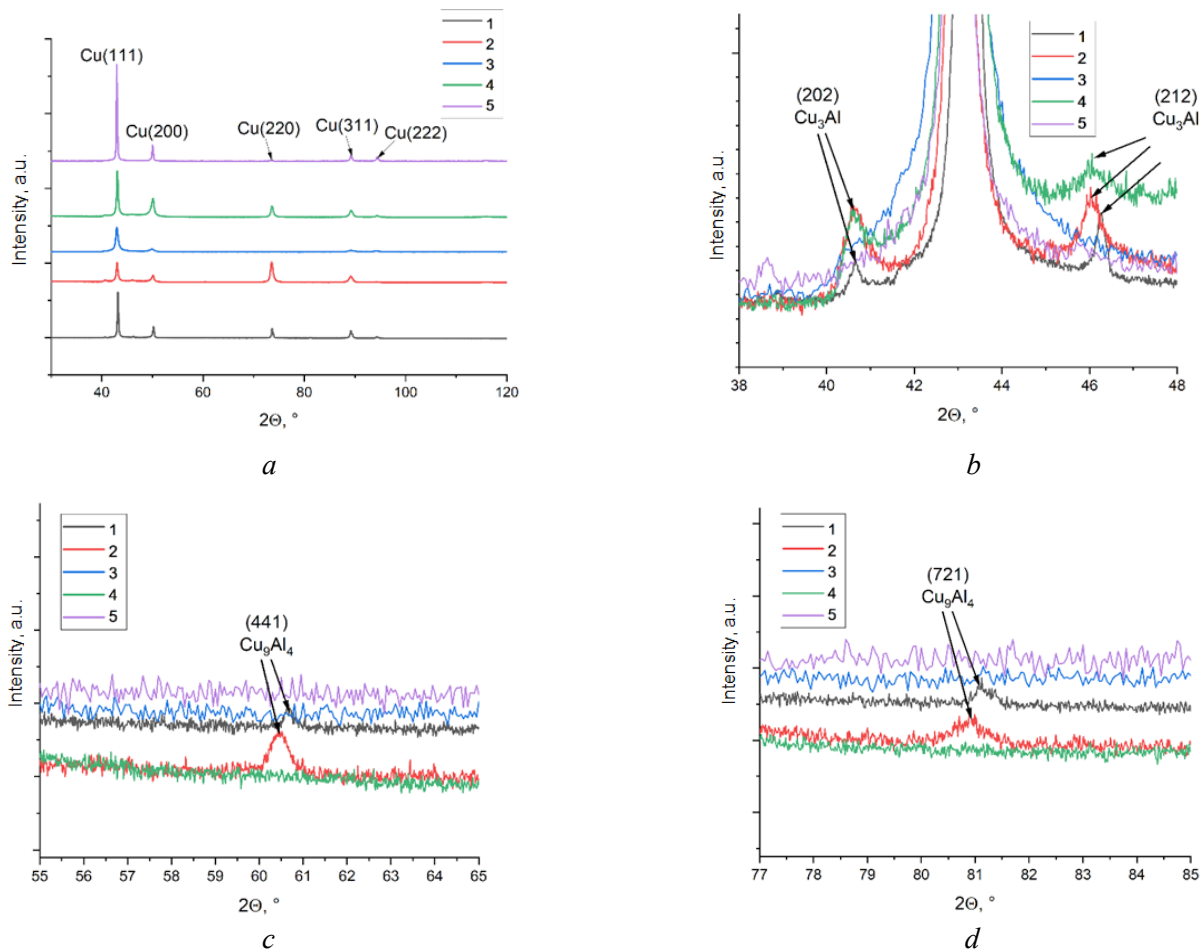
Fig. 2. X-ray diffraction (*XRD*) patterns of *Cu-Al-Si-Mn* bronze samples

forging (<u>Sample 2</u>, Figs. 2, *c*, *d*). The intensity of the reflections from this phase increased after multi-directional forging, presumably due to the formation of γ_2-Cu_9Al_4 during plastic deformation within the *Cu-Al* system. It is known that γ_2-Cu_9Al_4 is formed during mechanical alloying and friction stir processing and decomposes into its components when heated above 180 °C [22]. Therefore, either intermediate annealing before rolling or complete annealing at 400 °C can completely eliminate this phase.

In addition, reflections of the β-Cu_3Al phase are observed, which are found in samples of the as-printed bronze (<u>Sample 1</u>, Figs. 2, *c*, *d*), samples after multi-directional forging (<u>Sample 2</u>, Figs. 2, *c*, *d*), and heat-treated samples after multi-directional forging (<u>Sample 4</u>, Figs. 2, *c*, *d*).

One of the key factors affecting the phase composition of samples after *SPD* is the mechanism of deformation-induced dissolution of intermetallic phases [23]. As a result of *SPD*, particles of secondary phases dissolve, are fragmented, and refined under the influence of high stresses and a dislocation density close to the theoretical limit [24]. The possibility of precipitation of finely dispersed intermetallic particles is also not excluded, which is also a consequence of *SPD* and leads to additional strengthening of the alloy.

The modification of the material's structure through severe plastic deformation (*SPD*), followed by subsequent heat treatment, resulted in changes to the mechanical properties of the bronze, in comparison to the as-printed condition. The conducted investigations clearly demonstrate that the sequential application of *SPD* methods — namely, multi-directional forging and rolling — causes a substantial increase in the tensile strength of the bronze compared to the initial state obtained by the electron beam additive manufacturing method (Fig. 3, *a*).

In particular, the use of multi-directional forging provided a significant strength increase of 179 MPa, while the rolling process led to an even more pronounced enhancement of mechanical properties, increasing the tensile strength by 515 MPa.

Following heat treatment via annealing, conducted at a temperature of 400 °C, a further strengthening effect was demonstrated for both types of deformed samples. Notably, for samples that had undergone multi-directional forging, annealing contributed to a further increase in tensile strength by 30 MPa. Regarding the samples after rolling, annealing at the same temperature resulted in a more substantial additional increase in strength, amounting to 43 MPa.

The performed analysis also revealed that *SPD* induces a significant increase in the yield strength of the bronze, relative to the characteristics of the samples formed after additive manufacturing. Multi-directional forging led to a substantial increase in yield strength (by 359 MPa), whereas the application of rolling produced an even more significant increase – 725 MPa

Subsequent heat treatment via annealing, also demonstrated a positive influence on this parameter for all types of samples considered after *SPD*. In particular, for samples pre-processed by multi-directional forging, annealing contributed to a further increase in yield strength by 16 MPa. In the case of samples subjected to rolling, a similar annealing process resulted in a greater additional increase in yield strength, which amounted to 26 MPa.

The application of multi-directional forging and rolling led to a reduction in the relative elongation of the bronze samples by 2.6 and 4.5 times, respectively, compared to the as-printed sample (Fig. 3, *b*). Annealing at 400 °C resulted in a minor increase in relative elongation of 1.1 % for the sample after multi-directional forging and 1.8 % for the sample after rolling.
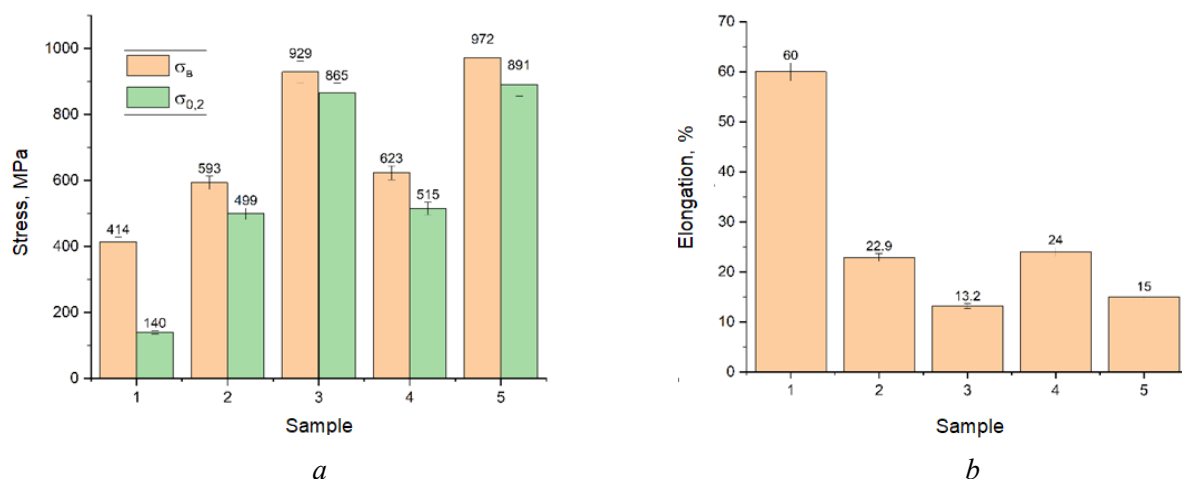

Fig. 3. Mechanical properties of *Cu-Al-Si-Mn* bronze samples

Based on the experimental data, it was established that *SPD* significantly affects the strength and ductility of the printed *Cu-Al-Si-Mn* bronze samples. An increase in strength and a decrease in ductility are expected for an alloy with an *FCC* lattice, due to strain hardening mechanisms and structural refinement. Annealing has a minimal impact on the strength of the post-SPD samples, while their ductility improves by approximately 5–13.6 % compared to the deformed state. This is due to the influence on the structure and phase composition of the samples. On the one hand, annealing led to partial recrystallization of the structure and a reduction in the number of crystal lattice defects. On the other hand, the sizes of the structural elements remained at the submicron level. As a result, an increase in ductility and the retention of the material's strength were achieved. The small increase in strength after annealing is associated with the cooperative contribution from grain boundary and dislocation strengthening mechanisms in the *FCC* alloy and has been previously noted for alloys with an ultrafine-grained structure [25–29]. In addition, the contribution to solid solution strengthening comes from the deformation-induced dissolution of secondary phase particles [30], as well as the possible precipitation of dispersed phases from the solution as a result of aging.

Severe plastic deformation (*SPD*) through multi-directional forging followed by rolling increased the microhardness of the bronze by 46% and 80%, respectively, compared to the as-printed samples (Fig. 4). Annealing the multi-directionally forged sample at 400°C increased the microhardness from 2.05 GPa to

2.37 GPa. Based on the microstructural data and phase composition, the increased hardness is likely due to the dissolution of the primary β-phase and the precipitation of secondary coherent phases within the grain volume. Annealing the rolled sample at 400°C decreased the microhardness from 2.52 GPa to 2.25 GPa. As annealing did not alter the phase composition of the rolled sample, the change in microhardness is attributed solely to structural modifications within the material.

During the tribological tests, the change in the coefficient of friction (*CoF*) over time was recorded (Fig. 5, *a*), from which the average value was calculated (Fig. 5, *b*). When the printed bronze sample (<u>Sample 1</u>) was subjected to friction, the *CoF* remained relatively constant throughout the test at 0.245, with the amplitude of fluctuations not exceeding 0.02. In addition to

Fig. 4. Microhardness of *Cu-Al-Si-Mn* bronze samples

changing the mechanical properties, multi-directional forging also affected the tribological properties of the investigated bronze. At the start of the test, the *CoF* for <u>Sample 2</u> was 0.2, but then decreased to 0.14 within the first 300 seconds. Then the *CoF* gradually increased to 0.172, and its short-term fluctuations did not exceed 0.05. After rolling (<u>Sample 3</u>), the *CoF* changed insignificantly; its average value was 0.189, and short-term fluctuations were 0.03. Heat treatment of the sample after multi-directional forging led to an increase in the average *CoF* to 0.18, and short-term fluctuations to 0.05 (Fig. 5, *a*, <u>Sample 4</u>). During friction, the *CoF* monotonically increased from the beginning to the end of the test. Heat treatment of the sample after rolling led to an increase in the average *CoF* to 0.226, and short-term fluctuations to 0.05 (Fig. 5, *a*, <u>Sample 5</u>). The change in *CoF* during friction was not monotonic. At the initial stage, the *CoF* increased, but then decreased approximately in the second half of the test.

Fluctuations in the coefficient of friction reflect dynamic alterations during the sliding friction process. The greater their amplitude, the more unstable the friction process becomes, which may reflect a change in the conditions of contact interaction between the steel ball and the bronze. Based on the obtained results, it can be noted that *SPD* contributes to a reduction in the *CoF* compared to the as-printed material. Heat treatment of the samples after *SPD* led to an increase in the *CoF* and an increase in the amplitude of its fluctuations.

Based on the analysis of optical image data, characteristic regions reflecting the condition of the wear track surface on the bronze samples were identified (Fig. 6). After friction of the as-printed bronze, fine microgrooves formed on the track, oriented along the direction of the friction force, along with dark areas
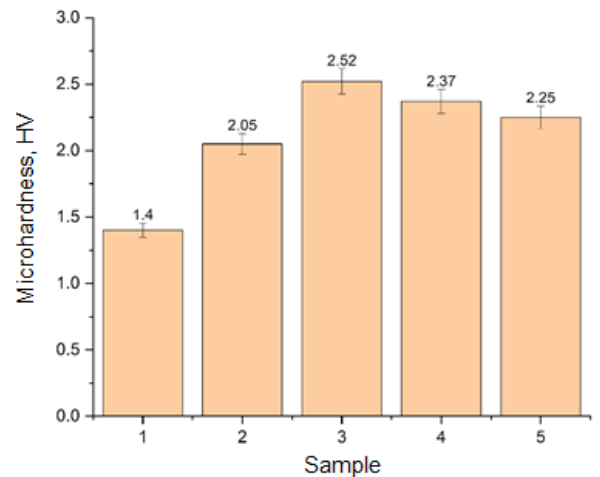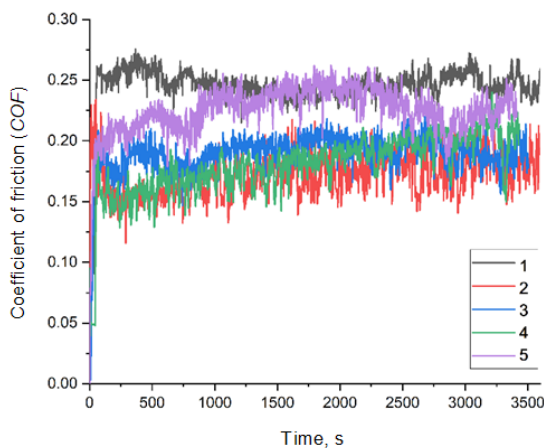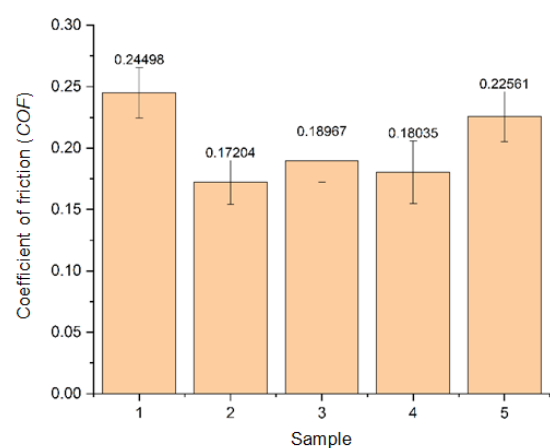

a	*b*

Fig. 5. Coefficients of friction as a function of time during sliding tests (*a*) and their average values (*b*)

containing oxidized material (Fig. 6, *a*). Signs of plastically displaced material are visible at the edges of the track, indicating substantial plastic deformation of the material. Following friction of the bronze sample with the structure produced by multi-directional forging (Fig. 6, *b*), fragments of detached wear particles are observed on the surface, in addition to microgrooves and extended regions of oxidized material. Rolling significantly influenced the post-friction condition of the material (Fig. 6, *c*). The resulting image reveals that the wear track consists of microgrooves without noticeable oxidation or wear debris. After annealing the multi-directionally forged sample (Fig. 6, *d*), the microgrooves are preserved and become more pronounced; the traces of oxidation approximately coincide with those observed on the deformed Sample 2. Concurrently, individual wear particles are absent. Annealing the rolled sample (Fig. 6, *e*) had a minimal effect on the morphology of the wear track surface; only a slight increase in its width was observed, suggesting an increase in the wear volume.
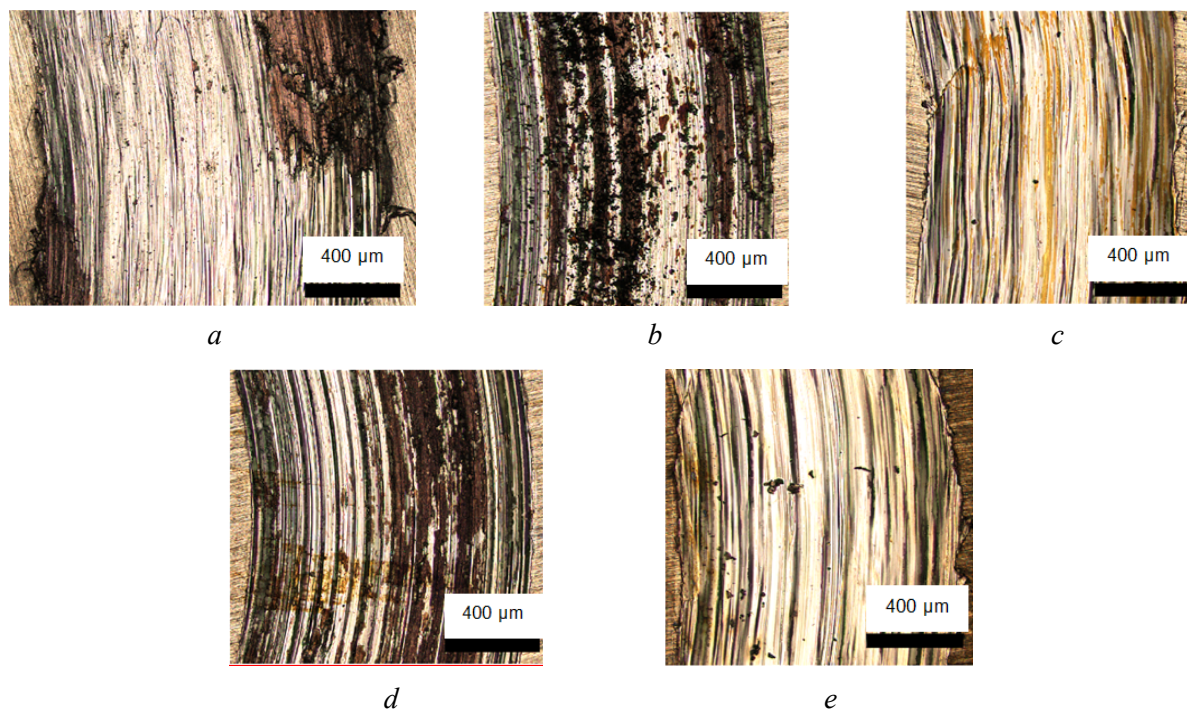

a   *b*   *c*

d   *e*

Fig. 6. Optical images of the wear track surfaces of *Cu-Al-Si-Mn* bronze samples. Sample 1 (*a*), sample 2 (*b*), sample 3 (*c*), sample 4 (*d*) and sample 5 (*e*)

Annealing promotes increased material plasticity; therefore, the amount of wear particles on the heat-treated samples after *SPD* by multi-directional forging decreased. This is attributed to a reduced likelihood of fracture of the ductile bronze material due to deformation induced by the steel counterbody.

Following the tribological tests, the surface condition of the steel balls was also investigated (Fig. 7). Signs of adhesive material transfer were observed on the surfaces of all the balls, a characteristic feature of bronze-steel friction pairs [31]. Bronze particles detaching during sliding friction adhered to the surface of the steel counterbody due to adhesive bonds. This process results in the formation of a protective layer, acting as a third body between the sample and the counterbody. The state of this layer is dependent on the wear characteristics of the softer material – the bronze. Previous results indicated that the wear of as-printed bronze results in the formation of microgrooves on its surface accompanied by minor oxidation. Correspondingly, grooves and minor areas with oxidized material are also observed on the surface of the ball (Fig. 7, *a*). Increased oxidation during friction of bronze Sample 2 and Sample 4 (following multi-directional forging and subsequent annealing) is reflected in the formation of an adherent layer on the counterbody's surface. Instead of microgrooves, the formation of a mechanical mixture of non-uniform thickness, composed of bronze and oxidized material, is observed (Fig. 7, *b*, *d*).
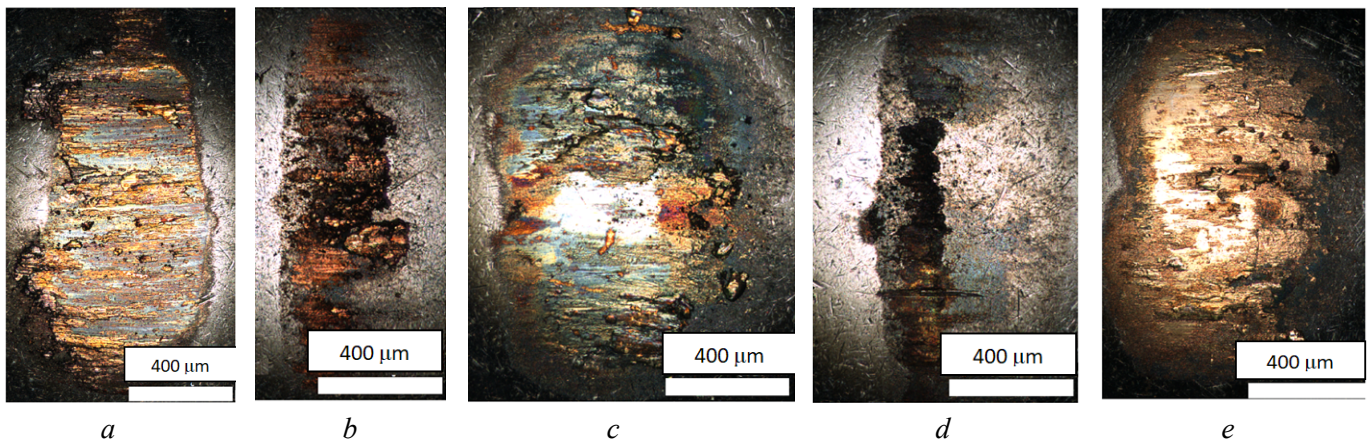
Fig. 7. Optical images of the steel ball surfaces after sliding against *Cu-Al-Si-Mn* bronze samples. Sample 1 (*a*),
sample 2 (*b*), sample 3 (*c*), sample 4 (*d*) and sample 5 (*e*)

Following friction of Sample 3 and Sample 5 (Fig. 7 *c*, *d*), a noticeable layer of bronze, transferred from the wear track, forms on the surface of the balls. Its formation is attributed to a reduction in the oxidation of the copper alloy surface during sliding friction in the examined structural states, which also leads to less pronounced mechanical removal of material from the ball surfaces.

To provide a more detailed assessment of the wear track surface condition, energy-dispersive X-ray spectroscopy (*EDS*) analysis was performed (Figs. 8, 9). As a result of friction, dark layers of material formed, unevenly covering the worn surface of the *Cu-Al-Si-Mn* alloy samples. *EDS* analysis revealed that these layers contained an increased concentration of oxygen (Fig. 9). Therefore, these layers consist of a mechanical mixture of bronze and wear particles, which underwent oxidation due to thermomechanical
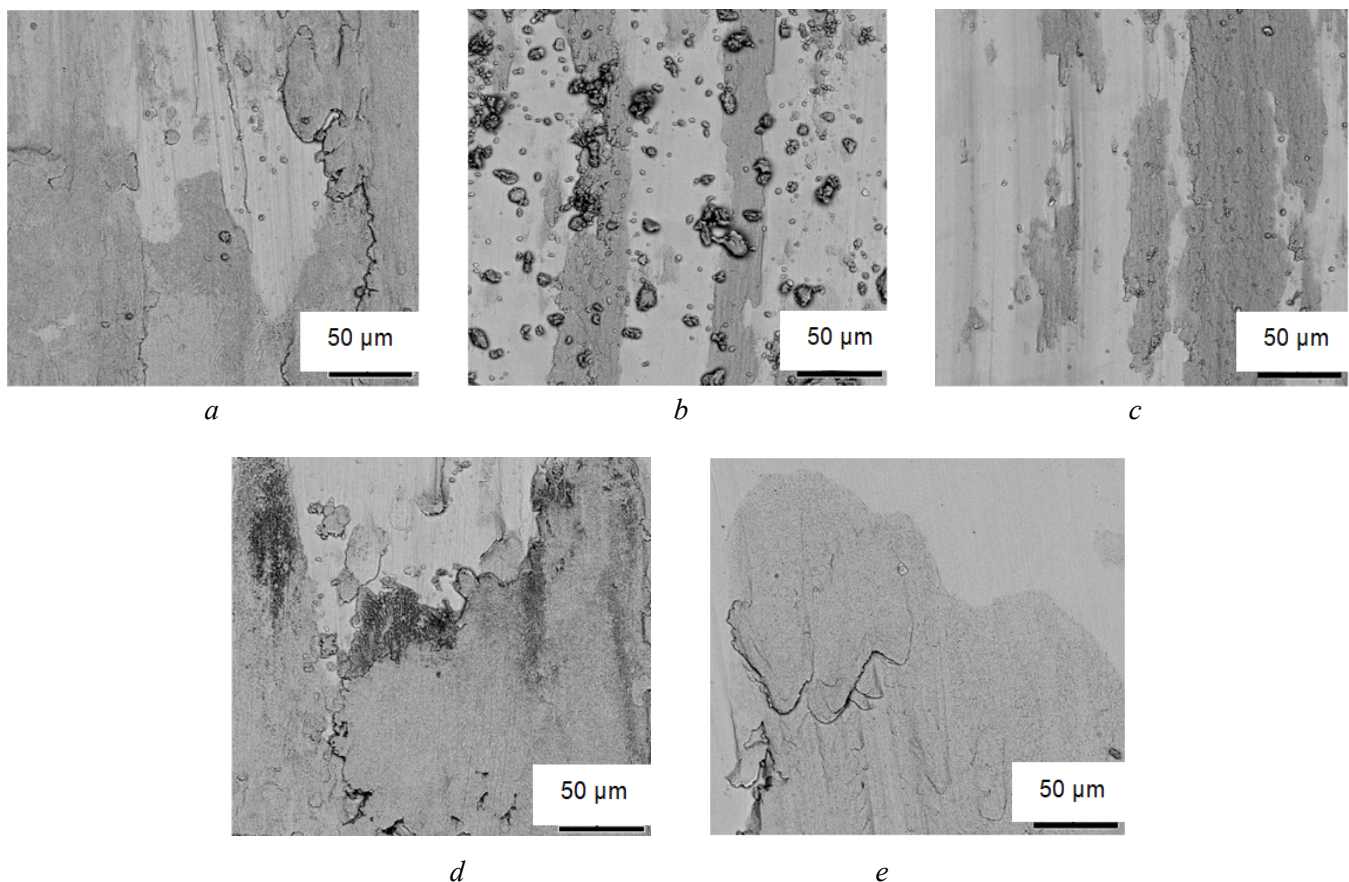

Fig. 8. *SEM* images of the wear track surfaces of *Cu-Al-Si-Mn* bronze. Sample 1 (*a*), sample 2 (*b*), sample 3 (*c*),
sample 4 (*d*) and sample 5 (*e*)
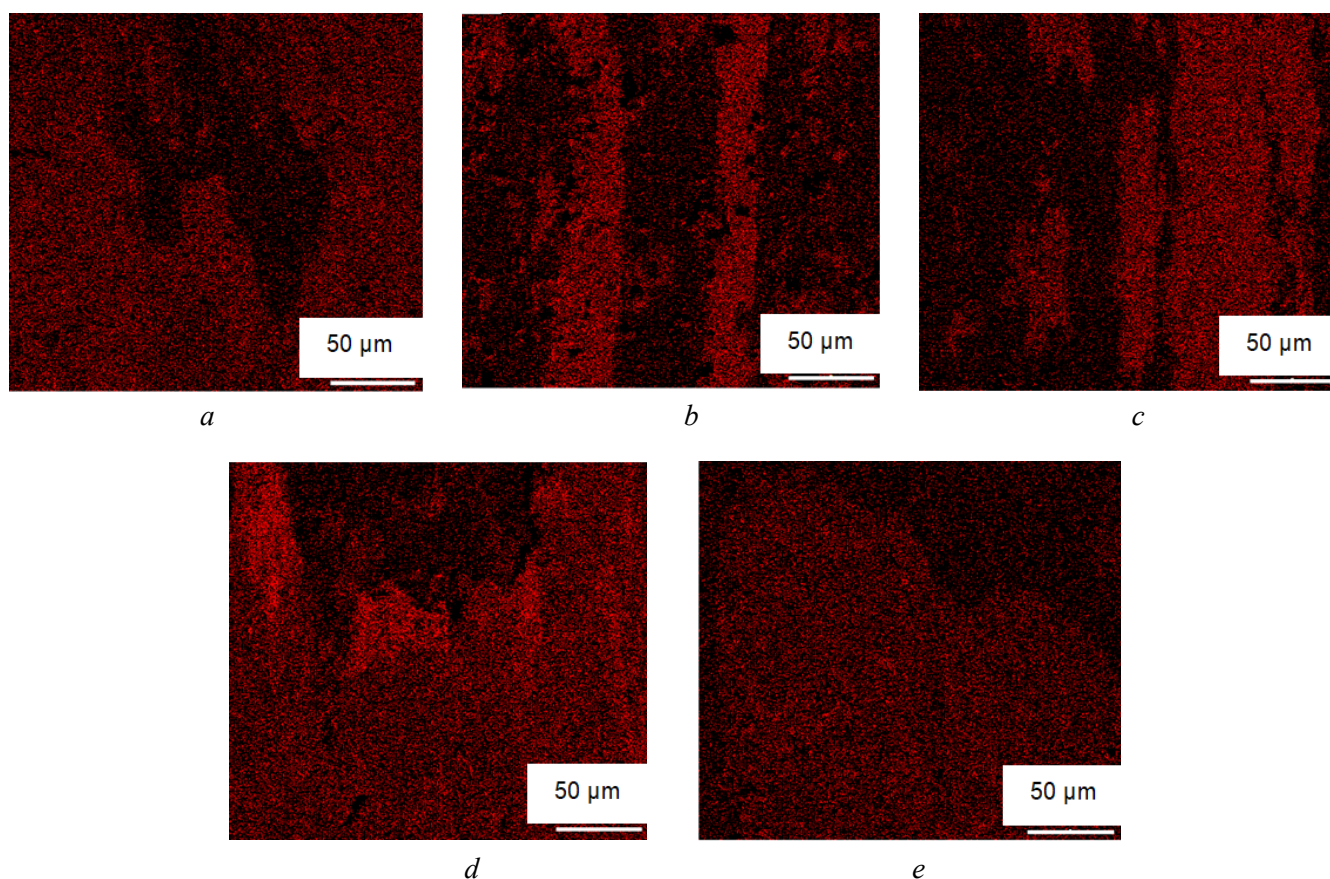
Fig. 9. Elemental mapping of oxygen on the wear track surfaces of *Cu-Al-Si-Mn* bronze. Sample 1 (*a*), sample 2 (*b*), sample 3 (*c*), sample 4 (*d*) and sample 5 (*e*)

action during sliding friction. During friction, these layers were disrupted by repeated mechanical action from the counterbody.

Three-dimensional surface scanning provided detailed data on the morphology of the wear track cross-sections, as shown in Fig. 10. The profile shape of each track closely mirrored the spherical configuration of the steel balls used, without any noticeable deviations. Furthermore, the track profiles clearly visualized characteristic surface microroughness formed during frictional interaction and subsequent wear of the material.

Quantification of wear, achieved through accurate determination of the cross-sectional area of the obtained profiles, revealed a significant disparity in the wear resistance of the samples. Specifically, printed

Fig. 10. Cross-sectional profiles (*a*) and areas (*b*) of the wear tracks of *Cu-Al-Si-Mn* bronze

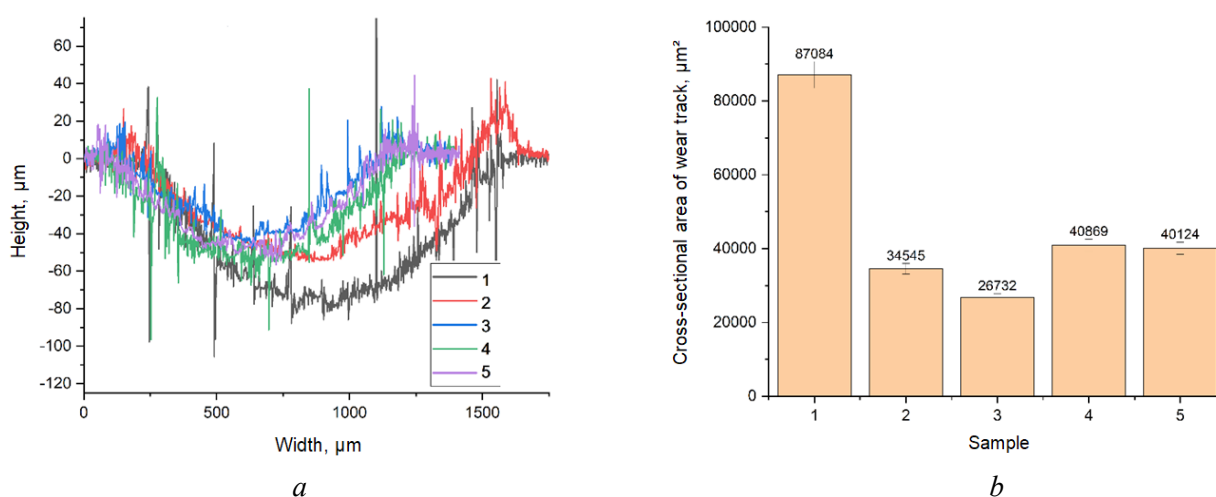sample 1 (Fig. 10) exhibited the lowest wear resistance, supported by the highest wear area value of 87,084 μm², significantly exceeding the respective values of the other examined samples. The wear on the sample after multi-side forging (Fig. 10, sample 2) was notably lower, measuring 34,545 μm². The sample's wear after rolling (Fig. 10, sample 3) was the lowest at 26,732 μm². Following heat treatment after multi-side forging, the wear of the specimen (Fig. 10, sample 4) increased to 40,869 μm². Following heat treatment after rolling, the wear of the sample (Fig. 10, sample 5) increased to 40,124 μm². These experimental data confirm that incremental plastic deformation (*IPD*) results in reduced bronze wear compared to the printed condition. Heat treatment, in turn, increased the wear of samples relative to their deformed state.

Conclusion

This study investigated the effect of severe plastic deformation (*SPD*) on the structural state, mechanical properties, and tribological performance of a *Cu-Al-Si-Mn* copper alloy fabricated by electron beam additive manufacturing. The experimental results established a correlation between the microstructure, tensile mechanical properties, and tribological behavior of the bronze alloy under unlubricated sliding friction.

1. *SPD* via multi-side forging and rolling resulted in a high density of dislocations and deformation twins within the material.

2. Annealing at 400 °C following multi-side forging led to partial recrystallization of the material; however, a system of deformation twins remained, demonstrating considerable structural stability. Low-temperature annealing at 400 °C after rolling resulted in the development of stacking faults, recrystallized submicron grains, and annealing micro-twins within the material.

3. X-ray diffraction analysis indicated that rolling and annealing induced deformation dissolution of secondary phases (β- and γ-phases), resulting in the *Cu-Al-Si-Mn* alloy becoming a single-phase consisting of the α-phase of face-centered cubic (*FCC*) copper.

4. Multi-side forging and rolling enhanced the tensile strength of the bronze alloy by factors of 1.43 and 2.24, respectively, while reducing its relative elongation by factors of 2.6 and 4.5 compared to the as-printed condition.

5. Annealing had a minimal impact on the strength of the post-*SPD* samples, whereas their ductility increased by approximately 5–13.6% relative to the deformed condition.

6. *SPD* via multi-side forging followed by rolling increased the microhardness of the bronze by 46% and 80%, respectively, compared to the as-printed samples. Annealing the sample at 400 °C after multi-side forging led to a 15.6% increase in microhardness. Annealing the sample at 400 °C after rolling resulted in a 12% decrease in microhardness.

7. Multi-side forging and rolling reduced wear by factors of 2.5 and 3.3, respectively, compared to the alloy in its as-printed state. Annealing increased the wear of the alloy by a factor of 1.5.

8. Based on these findings, a processing route involving a combination of multi-side forging, followed by rolling and low-temperature annealing, is proposed to enhance the mechanical and tribological properties of the *Cu-Al-Si-Mn* copper alloy. These experimental results provide valuable insights for developing practical strategies aimed at significantly improving the strength properties and wear resistance of bronzes in the *Cu-Al-Si-Mn* system, fabricated using electron beam additive manufacturing.

References

1. Osintsev O.E., Fedorov V.N. *Med' i mednye splavy: otechestvennye i zarubezhnye marki* [Copper and copper alloys. domestic and foreign brands]. 2nd ed., rev. Moscow, Innovatsionnoe mashinostroenie Publ., 2016. 360 p. ISBN 978-5-9907638-3-8.

2. Kolubaev E.A., Rubtsov V.E., Chumaevsky A.V., Astafurova E.G. Micro-, Meso- and macrostructural design of bulk metallic and polymetallic mate-rials by wire-feed electron-beam additive manufacturing. *Physical Mesomechanics*, 2022, vol. 25 (6), pp. 479–491. DOI: 10.1134/S1029959922060017.

3. Qu S., An X.H., Yang H.J., Huang C.X., Yang G., Zang Q.S., Wang Z.G., Wu S.D., Zhang Z.F. Microstructural evolution and mechanical properties of Cu-Al alloys subjected to equal channel angular pressing. *Acta Materialia*, 2009, vol. 57 (5), pp. 1586–1601. DOI: 10.1016/j.actamat.2008.12.002.

4. Massalski T.B. The Al-Cu (Aluminum-Copper) system. *Bulletin of Alloy Phase Diagrams*, 1980, vol. 1, pp. 27–33. DOI: 10.1007/BF02883281.

5. Kroupa A., Zobač O., Richter K.W. The thermodynamic reassessment of the binary Al-Cu system. *Journal of Materials Science*, 2021, vol. 56, pp. 3430–3443. DOI: 10.1007/s10853-020-05423-7.

6. Zobac O., Kroupa A., Zemanova A., Richter K.W. Experimental description of the Al-Cu binary phase diagram. *Metallurgical and Materials Transactions A*, 2019, vol. 50, pp. 3805–3815. DOI: 10.1007/s11661-019-05286-x.

7. Alés A. Study of different structures derives of β−Cu3Al by means of ab-initio calculations and quasi-harmonic approximation. *Computational Condensed Matter*, 2022, vol. 31, p. e00652. DOI: 10.1016/j.cocom.2022.e00652.

8. Hallstedt B., Gröbner J., Hampl M., Schmid-Fetzer R. Calorimetric measurements and assessment of the binary Cu-Si and ternary Al-Cu-Si phase diagrams. *Calphad*, 2016, vol. 53, pp. 25–38. DOI: 10.1016/j.calphad.2016.03.002.

9. Sufryd K., Ponweiser N., Riani P., Richter K.W., Cacciamani G. Exper-imental investigation of the Cu-Si phase diagram at x(Cu)>0.72. *Intermetallics*, 2011, vol. 19 (10), pp. 1479–1488. DOI: 10.1016/j.intermet.2011.05.017.

10. Phillips H.W.L. The constitution of aluminum-copper-silicon alloys. *Journal of the Institute of Metals*, 1953, vol. 82, pp. 9–15.

11. Raghavan V. Al-Cu-Si (Aluminum-Copper-Silicon). *Journal of Phase Equilibria and Diffusion*, 2007, vol. 28, pp. 180–182. DOI: 10.1007/s11669-007-9024-y.

12. He C.-Y., Du Y., Chen H.-L., Xu H. Experimental investigation and thermodynamic modeling of the Al-Cu-Si system. *Calphad*, 2009, vol. 33, pp. 200–210. DOI: 10.1016/j.calphad.2008.07.015.

13. Riani P., Sufryd K., Cacciamani G. About the Al-Cu-Si isothermal sec-tion at 500 °C and the stability of the ε-Cu15Si4 phase. *Intermetallics*, 2009, vol. 17, pp. 154–164. DOI: 10.1016/j.intermet.2008.10.011.

14. Miettinen J. Thermodynamic description of the Cu-Al-Si system in the copper-rich corner. *Calphad*, 2007, vol. 31, pp. 449–456. DOI: 10.1016/j.calphad.2007.05.001.

15. Ponweiser N., Richter K.W. New investigation of phase equilibria in the system Al-Cu-Si. Journal of *Alloys and Compounds*, 2012, vol. 512, pp. 252-263. DOI: 10.1016/j.jallcom.2011.09.076

16. Filippov A., Shamarin N., Moskvichev E., Savchenko N., Kolubaev E., Khoroshko E., Tarasov S. Heat input effect on microstructure and mechanical properties of Electron Beam Additive Manufactured (EBAM) Cu-7.5wt.%Al Bronze. *Materials*, 2021, vol. 14 (22), p. 6948. DOI: 10.3390/ma14226948.

17. Filippov A., Shamarin N., Moskvichev E., Savchenko N., Kolubaev E., Khoroshko E., Tarasov S. The effect of heat input, annealing, and deformation treatment on structure and mechanical properties of Electron Beam Additive Manufactured (EBAM) silicon bronze. *Materials*, 2022, vol. 15, p. 3209. DOI: 10.3390/ma15093209.

18. Zykova A., Panfilov A., Chumaevskii A., Vorontsov A., Gurianov D., Savchenko N., Kolubaev E., Tarasov S. Decomposition of β′-martensite in an-nealing the additively manufactured aluminum bronze. *Materials Letters*, 2023, vol. 338, p. 134064. DOI: 10.1016/j.matlet.2023.134064.

19. Shangina D.V., Gubicza J., Dodony E., Bochvar N.R., Straumal P.B., Tabachkova N.Yu., Dobatkin S.V. Improvement of strength and conductivity in Cu-alloys with the application of high pressure torsion and subsequent heat-treatments. *Journal of Materials Science*, 2014, vol. 49, pp. 6674–6681. DOI: 10.1007/s10853-014-8339-4.

20. Valiev R.Z., Islamgaliev R.K., Alexandrov I.V. Bulk nanostructured materials from severe plastic deformation. *Progress in Materials Science*, 2000, vol. 45, pp. 103–189. DOI: 10.1016/S0079-6425(99)00007-9.

21. *Filippov A.V., Khoroshko E.S., Shamarin N.N., Kolubaev E.A., Tarasov S.Yu.* Study of the properties of silicon bronze-based alloys printed using electron beam additive manufacturing technology. *Obrabotka metallov (tekhnologiya, oborudovanie, instrumenty) = Metal Working and Material Science*, 2023, vol. 25, no. 1, pp. 110–130. DOI: 10.17212/1994-6309-2023-25.1-110-130. (In Russian).

22. Besson R., Avettand-Fenoel M.-N., Thuinet L., Kwon J., Addad A., Roussel P., Legris A. Mechanisms of formation of Al4Cu9 during mechanical alloying: An experimental study. *Acta Materialia*, 2015, vol. 87, pp. 216–224. DOI: 10.1016/j.actamat.2014.12.050.

23. Faizova S.N., Aksenov D.A., Faizov I.A., Nazarov K.S. Unusual kinetics of strain-induced diffusional phase transformations in Cu-Cr-Zr alloy. *Letters on Materials*, 2021, vol. 11 (2), pp. 218–222. DOI: 10.22226/2410-3535-2021-2-218-222.

24. Tolmachev T.P., Pilyugin V.P., Patselov A.M., Gapontseva T.M., Plotnikov A.V., Churbaev R.V., Inozemtsev A.V. Features of the strain-induced dissolution and structure of fracture surfaces in Cu-Co alloys. *Diagnostics, Resource and Mechanics of Materials and Structures*, 2019, iss. 6, pp. 48–57. DOI: 10.17804/2410-9908.2019.6.048-057. (In Russian).

25. Ma S., Li X., Yang X., Fu L., Liu L., Xia M., Shan A. Effect of annealing temperature on microstructure and properties of a heavy warm rolled nickel aluminum bronze alloy. *Metallurgical and Materials Transactions A*, 2023, vol. 54, pp. 293–311. DOI: 10.1007/s11661-022-06873-1.

26. Naydenkin E.V., Grabovetskaya G.P. Deformation behavior and plastic strain localization of nanostructured materials produced by severe plastic deformation. *Materials Science Forum*, 2009, vol. 633–634, pp. 107–119. DOI: 10.4028/www.scientific.net/MSF.633-634.107.

27. Panin V.E., Egorushkin V.E., Panin A.V. Fizicheskaya mezomekhanika deformiruemogo tverdogo tela kak mnogourovnevoi sistemy. 1. Fizicheskie osnovy mnogourovnevogo podkhoda [Physical Mesomechanics of Deformable Solids as a Multilevel System. I. Physical Fundamentals of the Multilevel Approach]. *Fizicheskaya mezomekhanika = Physical Mesomechanics*, 2006, vol. 9, no. 3, pp. 9–22. (In Russian).

28. Grabovetskaya G.P., Mishin I.P., Kolobov Yu.R. Vliyanie dispersnogo uprochneniya na zakonomernosti i mekhanizmy polzuchesti medi s submikrometrovym razmerom zeren [The effect of precipitating hardening on regularities and mechanisms of submicron-grain copper creep]. *Izvestiya vysshikh uchebnykh zavedenii. Poroshkovaya metallurgiya i funktsional'nye pokrytiya = Powder Metallurgy and Functional Coatings*, 2009, no. 2, pp. 38–43. (In Russian).

29. Kozlov E.V., Zhdanov A.N., Koneva N.A. Bar'ernoe tormozhenie dislokatsii. Problema Kholla-Petcha [Barrier hindrance of dislocations. The Hall-Petch problem]. *Fizicheskaya mezomekhanika = Physical Mesome-chanics*, 2006, vol. 9, no. 3, pp. 81–92. (In Russian).

30. Faizov I.A., Mulyukov R.R., Aksenov D.A., Faizova S.N., Zemlyakova N.V., Cardoso K., Zeng Y. Rastvorenie chastits vtorykh faz v nizkolegirovannom mednom splave sistemy Cu-Cr-Zr pri obrabotke metodom ravnokanal'nogo uglovogo pressovaniya [Dissolution of second-phase particles in a low-alloyed copper alloy of the Cu-Cr-Zr system processed by equal-channel angular pressing]. *Pis'ma o materialakh = Letters on Materials*, 2018, vol. 8, no. 1, pp. 110–114. DOI: 10.22226/2410-3535-2018-1-110-114. (In Russian).

31. Ilie F. Tribological behaviour of the steel/bronze friction pair (journal bearing type) functioning with selective mass transfer. *International Journal of Heat and Mass Transfer*, 2018, vol. 124, pp. 655–662. DOI: 10.1016/j.ijheatmasstransfer.2018.03.107.

Conflicts of Interest

The authors declare no conflict of interest.

Obrabotka metallov –
Metal Working and Material Science

Journal homepage: http://journals.nstu.ru/obrabotka_metallov

Fabrication, characterization and performance evaluation of zinc oxide doped nanographite material as a humidity sensor

Farrukh Waheed [1, a], Amtul Qayoom [2, b], Muhammad Faizan Shirazi [3, c, *]

[1] Department of Computer Science, Usman Institute of Technology University, ST-13, Abul Hasan Isphahani Road, Block 7, Gulshan-e-Iqbal, Karachi, 75300, Pakistan

[2] Department of Chemistry, NED University of Engineering and Technology, University Road, Karachi, 75270, Pakistan

[3] Department of Electronic Engineering, NED University of Engineering and Technology, University Road, Karachi, 75270, Pakistan

[a] https://orcid.org/0009-0004-6527-0965, ✉ fwbaig@uitu.edu.pk; [b] https://orcid.org/0000-0003-0149-2177, ✉ amtulq@neduet.edu.pk;
[c] https://orcid.org/0000-0002-4488-8860, ✉ faizanshirazi@neduet.edu.pk

ARTICLE INFO

ABSTRACT

Introduction. The growing demand for real-time environmental monitoring technologies has led to increased interest in high-performance humidity sensors with rapid response, high sensitivity, and long-term stability. Zinc oxide (*ZnO*) is a widely used semiconducting oxide material for such applications due to its chemical stability and sensitivity to humidity variations. However, its performance can be further enhanced through material engineering. This study investigates the doping of *ZnO* nanoparticles with nanographite material (*NGM*) to improve humidity-sensing characteristics. The **purpose of the work** is to develop ZnO–NGM nanocomposite-based capacitive humidity sensors with improved response/recovery time and sensitivity by modifying the electronic and surface properties of *ZnO* through *NGM* doping. **Research methods.** ZnO–NGM nanocomposites with varying *NGM* content (1 wt.%, 2 wt.%, 4 wt.%, 5 wt.%, and 10 wt.%) were synthesized via a chemical precipitation route. The optical behavior of pure *ZnO* was analyzed using *UV–Vis* spectroscopy, which revealed a sharp absorption edge at 367 nm, indicating a bandgap near 3.3 eV. Structural and morphological properties were examined using X-ray diffraction (*XRD*) and scanning electron microscopy (*SEM*), confirming *NGM* integration and enhanced surface porosity. The composite sensing films were deposited onto *FTO*-coated glass substrates using the 'doctor blade' method to fabricate the capacitive sensors. The sensing performance was evaluated in a nitrogen-controlled chamber over a relative humidity (*RH*) range of 10% to 95%, with capacitance measurements recorded across a frequency range of 10 kHz to 1 MHz. **Results and discussion.** Among all tested compositions, the 4 wt.% *NGM*-doped *ZnO* sensor demonstrated the best performance, with a rapid response time of 4.0 s, a recovery time of 6.2 s, and excellent sensitivity. These improvements are attributed to enhanced surface conductivity and more active adsorption-desorption kinetics due to *NGM*. The developed sensors show strong potential for integration in real-time environmental monitoring systems, industrial automation, and smart home humidity control applications. The incorporation of nanographite into *ZnO* matrices significantly enhances humidity-sensing capabilities. The ZnO–NGM composite, particularly at 4 wt.% doping, offers a promising pathway for the development of next-generation, high-efficiency humidity sensors.

Introduction

Humidity sensors have significant applications in agriculture, food technology, medical diagnostics, and environmental monitoring due to the increasing need for real-time, accurate measurements in state-of-the-art intelligent systems. Low power consumption, rapid response, stability, and low cost are key requirements of contemporary sensors [1-2]. A research paper discusses a flexible humidity sensor that can sense minor changes in breath for medical use [3-4]. Similarly, another study presents highly sensitive humidity sensors constructed with carbon nanotube composites, emphasizing rapid response times suitable

* Corresponding author
Shirazi Muhammad Faizan, Ph.D. (Engineering)
Department of Electronic Engineering,
NED University of Engineering and Technology,
75270, University Road, Karachi, Pakistan
Tel.: +92-21-99261261-8 ext. 2215, **e-mail:** faizanshirazi@neduet.edu.pk

for various environments [5]. Another study showcases the efficacy of using encapsulated ionic liquids in nanostructured frameworks for enhanced humidity sensing capabilities, reinforcing the trend of leveraging novel materials for improved performance [6]. Self-powered and biocompatible sensors are increasingly under research, and graphene oxide-based humidity sensors promise energy-efficient, sensitive detection [7]. An *rGO:MoS₂*-based temperature-integrated humidity sensor proves the versatility of its applications in reality [8]. Research investigating TiO_2-SnS_2 heterostructures for use in humidity sensors emphasizes the advantages of nanoarchitectures in enhancing sensor performance [9-12].

Metal oxide humidity sensors, like *ZnO*, *TiO₂*, and *SnO₂*, are commonly researched for their stability and moisture sensitivity and measure humidity through capacitance or resistance changes after water adsorption [1-3]. These characteristics make *ZnO* an exceptionally versatile material for fabricating high-performance humidity sensors. Furthermore, the tunable electronic properties of *ZnO*, achieved through doping with various elements and precise nanostructuring, allow for fine-tuning of the sensor's performance to meet specific application requirements [13-14]. Nanographite material (*NGM*), which is green synthesized from orange and lemon peels, improves *ZnO*-based humidity sensors with enhanced charge transfer, adsorption ability, and stability, thereby supporting sustainable nanotechnology [10].

Recent studies emphasize the need for improvements in response times and recovery cycles in humidity sensors, highlighting that these parameters are critical for effective real-time applications [15-16]. A study conducted by *Ullah et al.* demonstrated that by integrating nanographite with metal oxides, the resulting sensor achieved significant reductions in response and recovery times, addressing previous limitations [17]. Furthermore, research by *Chaudhary et al.* emphasized the importance of utilizing innovative architectures and materials to enhance the sensor's overall performance metrics [18]. Moreover, the study by *Li et al.* outlined the effectiveness of doping *ZnO* with nanographite in improving the sensor's performance at various humidity levels, showcasing its potential for practical application [13]. The tunability of electronic properties through the introduction of nanographite provides researchers with new avenues for enhancing sensor reliability and efficiency, making them more suitable for integration into *IoT* and smart technology frameworks [14]. Despite the aforementioned studies, there is still a need for enhancement of zinc oxide-based nanosensors for lower response times.

Despite these advancements, there is still a clear need to develop *ZnO*-based humidity sensors with lower response times, improved stability, and environmentally friendly, scalable fabrication techniques. Specifically, the integration of *NGM* into *ZnO* using cost-effective and simple chemical methods remains relatively underexplored.

The present work aims to address these limitations by synthesizing *ZnO–NGM* nanocomposites via a low-cost chemical precipitation method. The nanocomposites are deposited onto fluorine-doped tin oxide (*FTO*) substrates using the doctor-blade technique to fabricate capacitive-type humidity sensors. The use of *NGM* is expected to improve the sensor's performance by enhancing electrical conductivity and water molecule interaction at the surface. Comprehensive characterization, including *UV–Vis* spectroscopy, *SEM*, *XRD*, and *FTIR*, was conducted to analyze the structural, optical, and chemical features of the material. Humidity sensing was evaluated through capacitance and impedance analysis in a nitrogen-controlled environment across *RH* levels from 10% to 95% [19]. Capacitance and impedance measurements assessed the humidity sensing capability of these synthesized sensors. The results contribute to the development of improved humidity nanosensors, with implications for environmental monitoring, healthcare, and industrial automation.

Investigation techniques

Materials and Methods

High-purity analytical-grade zinc acetate (*Zn(CH₃COO)₂*), ammonium hydrogen carbonate (*NH₄HCO₃*), nanographite material (*NGM*), ethanol (analytical grade), and ethyl cellulose were sourced from *BDH*, *Merck*, and *Sigma-Aldrich*. Deionized water was employed throughout the synthesis and washing to avoid ionic or particulate contamination. Fluorine-doped tin oxide (*FTO*) glass substrates were employed for

device fabrication. Copper and silver electrodes were used for device fabrication. Before application, all the substrates and components were properly cleaned with a *Liquinox* detergent solution (*Alconox Inc.*) and then rinsed with analytical-grade acetone (*Sigma-Aldrich*) to remove organic impurities and provide a clean surface free of contaminants.

### Synthesis of zinc oxide (ZnO) nanoparticles via chemical precipitation

10 ml of 1.5 mol/L zinc nitrate ($Zn(NO_3)_2$) was slowly added to 10 ml of 2.25 mol/L ammonium carbonate (($NH_4)_2CO_3$) solutions with magnetic stirring. A white $ZnCO_3$ precipitate confirmed successful synthesis [1].

The chemical reactions involved are:

$$Zn(NO_3)_2S + (NH_4)_2CO_3 \rightarrow ZnCO_3 \downarrow + 2\ NH_4NO_3$$
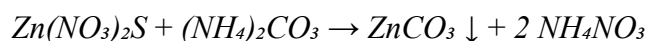
The precipitate was collected through vacuum filtration with an appropriate pore filter paper to remove liquid by-products and unreacted precursors. It was washed three times with deionized water. The high volatility of ethanol allowed for quicker drying, yielding a pure precipitate to be used in subsequent *ZnO* nanoparticles synthesis.

The $ZnCO_3$ was filtered and dried at 80°C to evaporate residual solvents without agglomeration, maintaining the nanostructure. The dried precursor powder was calcined at 550°C for 2 hours using a muffle furnace, promoting the thermal decomposition of $ZnCO_3$ to *ZnO*.

$$ZnCO_3 \rightarrow ZnO + CO_2$$
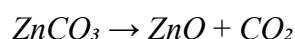
Doping of ZnO nanoparticles with nanographite (NGM)

Both *ZnO* and *NGM* were initially in powdered form. Both were dispersed separately in ethanol. The *NGM* suspension was then added dropwise to the *ZnO* solution with continuous stirring for 25 minutes to achieve good mixing. *ZnO* to *NGM* weight ratios were varied to obtain 99:1, 98:2, 97:3, 96:4, 95:5, and 90:10 composites. Next, 10 mL of ethanol was further added as a dispersant to facilitate dispersion and to lower surface tension. For the powder form, the paste was dried at 50–70 °C for 1–2 hours to prevent nanoparticle agglomeration and ensure equal *NGM* distribution.

Fabrication of the humidity sensor

FTO glass substrates were sequentially sonicated in detergent, deionized water, acetone, and ethanol to clean them for the best adhesion and consistent sensor performance. *ZnO* nanoparticles doped with *NGM* were combined with ethanol to produce a viscous paste appropriate for doctor-blading. The paste was cast on cleaned FTO substrates by the doctor-blade method and thermally treated at 150 °C for 1 hour for the improvement of film adhesion, evaporation of the residual solvents, and durability. Fig. 1 shows the *ZnO* doped with *NGM* paste on a *FTO* glass substrate. Figs. 1, *a* and 1, *b* show the *ZnO* doped with *NGM* paste on a *FTO* glass substrate.

For further stabilization of the film and to increase its stability, ethyl cellulose (2–10 wt %) was dissolved in ethanol with constant stirring to produce a uniform solution. This was added progressively into the *ZnO* doped *NGM* paste to achieve optimal coating. Incorporation of ethyl cellulose enhanced adhesion, surface smoothness, and mechanical strength to yield stable, uniform nanocomposite layers for humidity sensing [1, 30].

Results and Discussion

Structural and morphological analysis

The optical properties of the as-synthesized *ZnO* nanoparticles were investigated by *UV–Vis* spectroscopy. The absorption spectrum, shown in Fig. 2, shows a sharp and intense absorption edge at around 367 nm, which is consistent with the intrinsic bandgap transition of *ZnO*. The *UV–Vis* was performed using a *UV-*
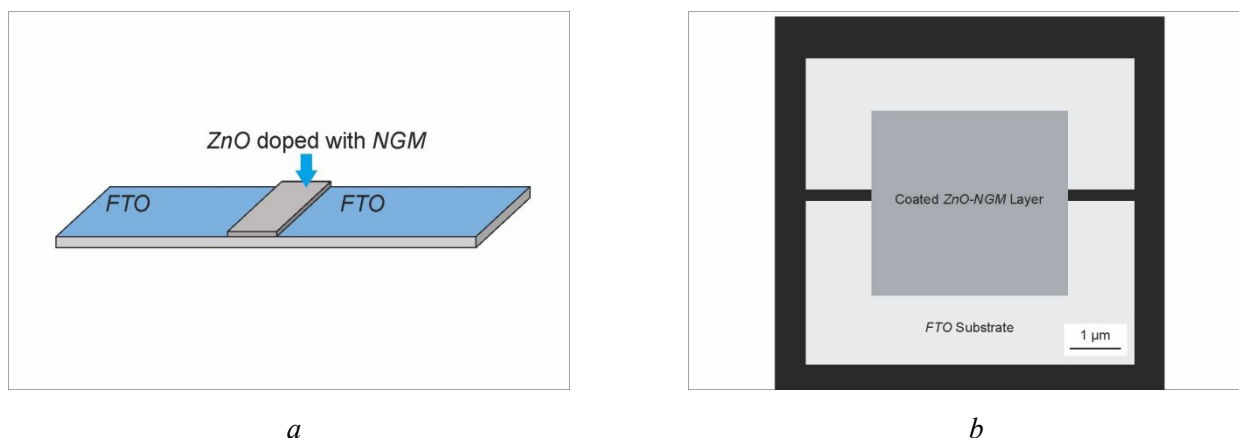
a

b

Fig. 1. (a) Side-view of *ZnO–NGM* paste on *FTO* substrate, (*b*) Top view showing surface morphology
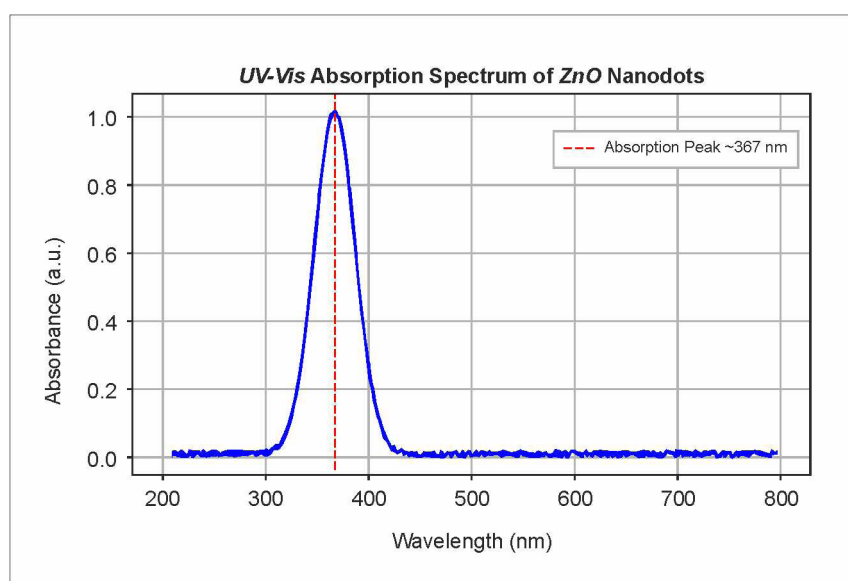

Fig. 2. UV–Vis absorption spectrum of as-synthesized *ZnO* nanoparticles exhibiting a narrow absorption peak at 367 nm, suggesting a direct bandgap transition and validating nanoscale crystallinity for optoelectronic and sensing purposes

1800 SHIMADZU. This peak is related to a direct bandgap energy of about 3.38 eV, which verifies the semiconducting nature of the *ZnO* nanostructures. The blue shift of the absorption edge from the bulk *ZnO* (~375 nm) as shown in Fig. 2 indicates a quantum confinement effect, a signature of the nanoscale size of the particles. The sharp and steep slope of the absorption also indicates the high crystallinity and purity of the as-synthesized *ZnO* nanoparticles. These optical characteristics render the material particularly apt for humidity sensing, *UV* photodetectors, and other optoelectronic uses, where there is a need for a fast and sensitive response to environmental stimuli.

SEM images (in Fig. 3) indicated well-distributed *ZnO* nanoparticles with well-defined morphology. Higher magnification images indicated well-dispersed particles with increased surface texture and observable agglomeration in certain areas. The scanning was performed using a *JEOL JSM-6490A* scanning electron microscope (*JEOL Ltd.*, Japan). The addition of *NGM* enhanced the surface roughness and uniformity of distribution. The increased roughness increases the number of active sites, which aids in better water molecule adsorption, which is essential for enhanced humidity sensing performance [3].

XRD patterns showed a well-crystallized hexagonal structure of *ZnO* (quartzite). Peak broadening and minor shifts were noted with increasing *NGM* concentration, which are signs of successful *NGM*
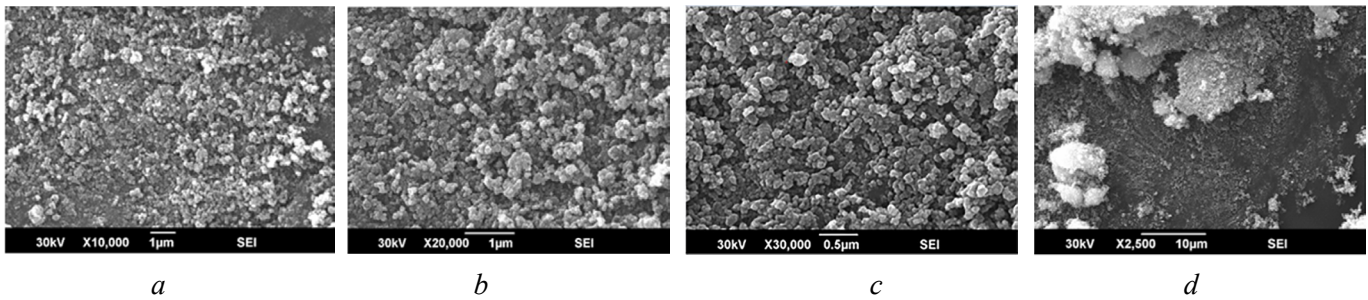
Fig. 3. Scanning electron microscopy (*SEM*) images of *ZnO* nanoparticles at different magnifications:
a – 10,000×; *b* – 20,000×; *c* – 30,000×; *d* – 2,500×

incorporation. These shifts are most likely due to lattice strain, resulting in smaller crystallite size and the creation of structural defects that increase surface area and water adsorption capacity [3].

Fig. 4 shows *XRD* patterns of different samples. Sample 1 (*B-3K953*) showed several peaks between 20° and 80° (2θ), with major peaks near 30°, 40°, and 50°, relating to *ZnO* and traces of impurities. Sample 2 (*B-3K954*) had sharper peaks, indicating better crystallinity. Sample 3 (*B-3K955*) had intermediate crystallinity. All the samples consisted of mostly the *ZnO* phase, while peak width and intensity variations were due to variations in crystallinity due to doping and processing conditions [3].

FTIR spectra verified the inclusion of *NGM* within the *ZnO* matrix Fig. 5. A typical *Zn–O* stretching vibration around 450 cm^{-1} ensured the presence of *ZnO*. Peaks around 1,570 cm^{-1} (*C=C*) and 1,730 cm^{-1} (*C=O*) ensured the occurrence of carbon-containing functional groups in *NGM*. A broad band around ~3,400 cm^{-1} indicated *O–H* stretching, due to hydroxyl groups, responsible for adsorption of water.

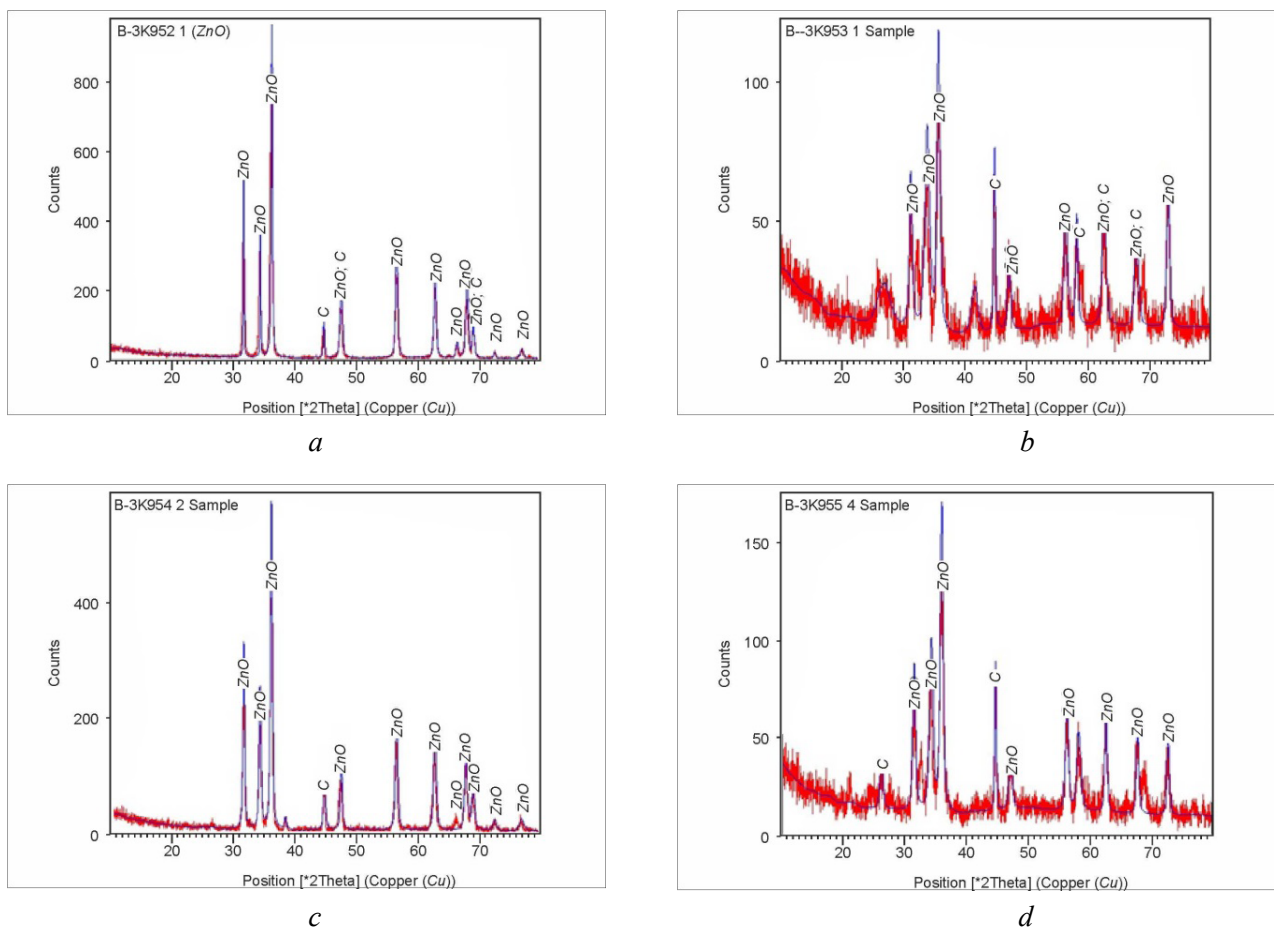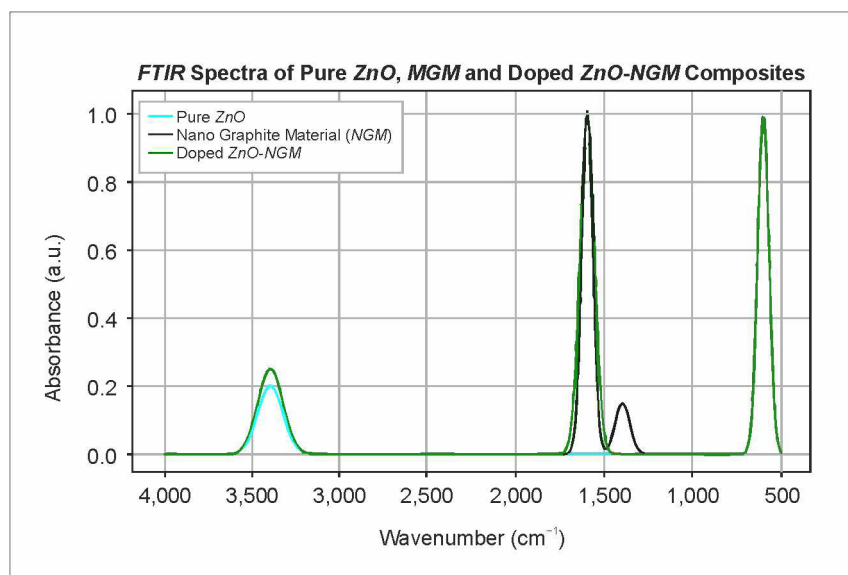*Fig. 4. XRD* patterns of (*a*) pure *ZnO*, (*b*) *ZnO–NGM* Sample 1, (*c*) Sample 2, and (*d*) Sample 3

Fig. 5. FTIR spectra of pure ZnO, nanographite material (NGM),
and NGM-doped ZnO composites

Doped *ZnO* showed characteristic *Zn–O* vibrations (400–600 cm^{-1}) and *O–H* stretching (~3,400 cm^{-1}). *NGM* spectra included *C=C* stretching (~1,600 cm^{-1}), *C–O* (~1,400 cm^{-1}), and *C–H* bending (~1,100–1,200 cm^{-1}), characteristic of sp²-hybridized carbon structures. Composites of *ZnO–NGM* showed shifted and intensified peaks, especially for *Zn–O* and *C=C*, indicating strong chemical bonding and successful doping. The broadened *O–H* peak indicated enhanced hydrogen bonding, which provided enhanced water affinity.

These microscopic and spectroscopic findings establish the successful integration of *NGM* into the *ZnO* structure. Increased surface area, lattice tension, and chemical functionalization enhance sensor performance and water adsorption. Decreased crystallite size and enhanced defect sites also enhance improved charge transport, which further increases the response rate and sensitivity of the humidity sensor.

The characteristic peaks of *ZnO*, *NGM*, and their composite indicate the presence of functional groups corresponding to *ZnO* vibrations and carbon-based materials. The shift in peak positions and intensity variations suggests successful doping of *NGM* into *ZnO*.

Electrical characterization and humidity sensing performance

To compare the electrical performance of the *ZnO–NGM* humidity sensors, a controlled humidity chamber was utilized. The sensor was positioned in a sealed chamber where humidity was accurately controlled from 10% to 90% *RH* using a dual-path nitrogen gas system. One path supplied nitrogen gas through a reservoir of distilled water to humidify it, while the other provided dry nitrogen to dehumidify it. The relative humidity was controlled by varying the flow rates of the two paths of nitrogen.

A digital hygrometer with ±0.8% *RH* accuracy was placed close to the sensor to continuously monitor *RH*, and the ambient temperature was held at 23 ± 1 °C. As shown in Fig. 6, the sensor was interfaced to a *Fluke PM6304/023* precision *LCR* meter with shielded terminals to reduce electrical noise. Automated data acquisition with real-time plotting and saving of capacitance values was carried out using a *Python*-based script. The capacitance of the sensor was recorded at 10 kHz, 20 kHz, 50 kHz, 80 kHz, 100 kHz, and 1 MHz frequencies under different humidity conditions.

The 2% *ZnO–NGM* sensor demonstrated a distinct monotonic increase in capacitance with RH. This was due to the adsorption of water molecules and increased dipolar polarization. The degree of doping made the sensor more sensitive than the pure *ZnO* because of the enhanced surface area and charge conduction pathways provided by the *NGM* flakes. The composite structure facilitated ionic conduction by adsorbed water layers and enhanced the dielectric constant via interfacial polarization. The response time was
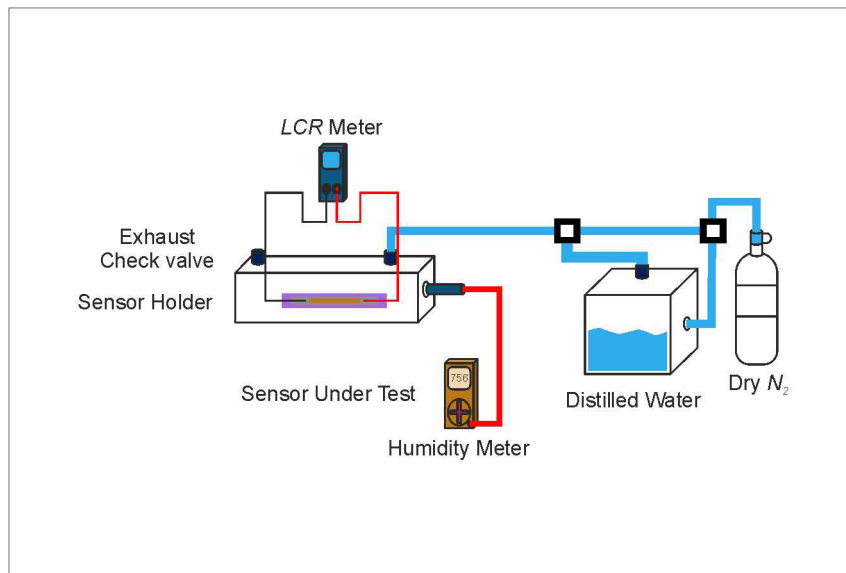
Fig. 6. Experimental setup for humidity sensing using an *LCR* meter
and a controlled chamber

4.5 seconds, and the recovery time was 6.9 seconds, reflecting efficient adsorption-desorption kinetics. As shown in Fig. 7, *a*, the capacitance-*RH* curve confirms moderate sensitivity and reliable humidity tracking at lower frequency ranges.

The 4% *ZnO–NGM* sensor exhibited well-balanced performance in sensitivity, response time, and recovery time. The capacitance rose steeply in the range of 10% to 60% *RH* and gradually at higher *RH*, with a good correlation between *RH* and capacitance. At lower frequencies (10–80 kHz), the sensor showed increased sensitivity as a result of improved dipole relaxation and ionic conduction, whereas at 1 MHz, the capacitance response became flattened as a result of polarization response time limitations. The response time was 4.0 s, and recovery time was 6.2 s, both of which were among the shortest recorded at all doping levels. As shown in Fig. 7, *b*, the capacitance-*RH* curve confirms moderate sensitivity and reliable humidity tracking at lower frequency ranges.

The 1% *ZnO–NGM* sensor had moderate capacitance sensitivity, response time, and recovery time. Capacitance increased with *RH* because of the dielectric polarization due to adsorbed water molecules. At lower frequencies (10 kHz and 50 kHz), the sensor was more sensitive, whereas at higher frequencies (1 MHz), the polarization response was restricted, leading to a flat capacitance curve. The response time was 4.8 seconds, and recovery time was 6.9 seconds, which provided a moderate improvement compared to the pure *ZnO*. As shown in Fig. 7, *c*, the capacitance-*RH* curve confirms moderate sensitivity and reliable humidity tracking at lower frequency ranges.

The 5% *ZnO–NGM* sensor exhibited high sensitivity to changing humidity levels, and the sensitivity was 53.9 pF/%*RH*. The capacitance rose sharply between 10% and 60% *RH* and gradually at higher *RH*. Although the sensor showed much higher sensitivity than with lower doping concentrations, the response and recovery times (4.2 and 6.6 seconds) were marginally slower as a result of partial agglomeration of the *NGM,* which lowered the number of active adsorption sites available. Despite the reduced kinetics, the sensor showed high sensitivity and was therefore appropriate for applications where sensitivity is more important than rapid response times. As shown in Fig. 7, *d*, the capacitance-*RH* curve confirms moderate sensitivity and reliable humidity tracking at lower frequency ranges.

The 10% *ZnO–NGM* sensor showed the highest capacitance sensitivity (62.1 pF/%*RH*) of all the doping levels, but its response time (6.0 s) and recovery time (8.0 s) were slower than those of the other sensors. The slower kinetics were mainly caused by the agglomeration of the *NGM* at this higher doping level, which restricted water molecule adsorption and desorption and also ionic mobility. Despite these limitations, the 10% doping level showed better sensitivity, and this is beneficial in many applications where sensitivity is important even at the cost of reduced response speed. As shown in Fig. 7, *e*, the capacitance-*RH* curve confirms moderate sensitivity and reliable humidity tracking at lower frequency ranges [31].
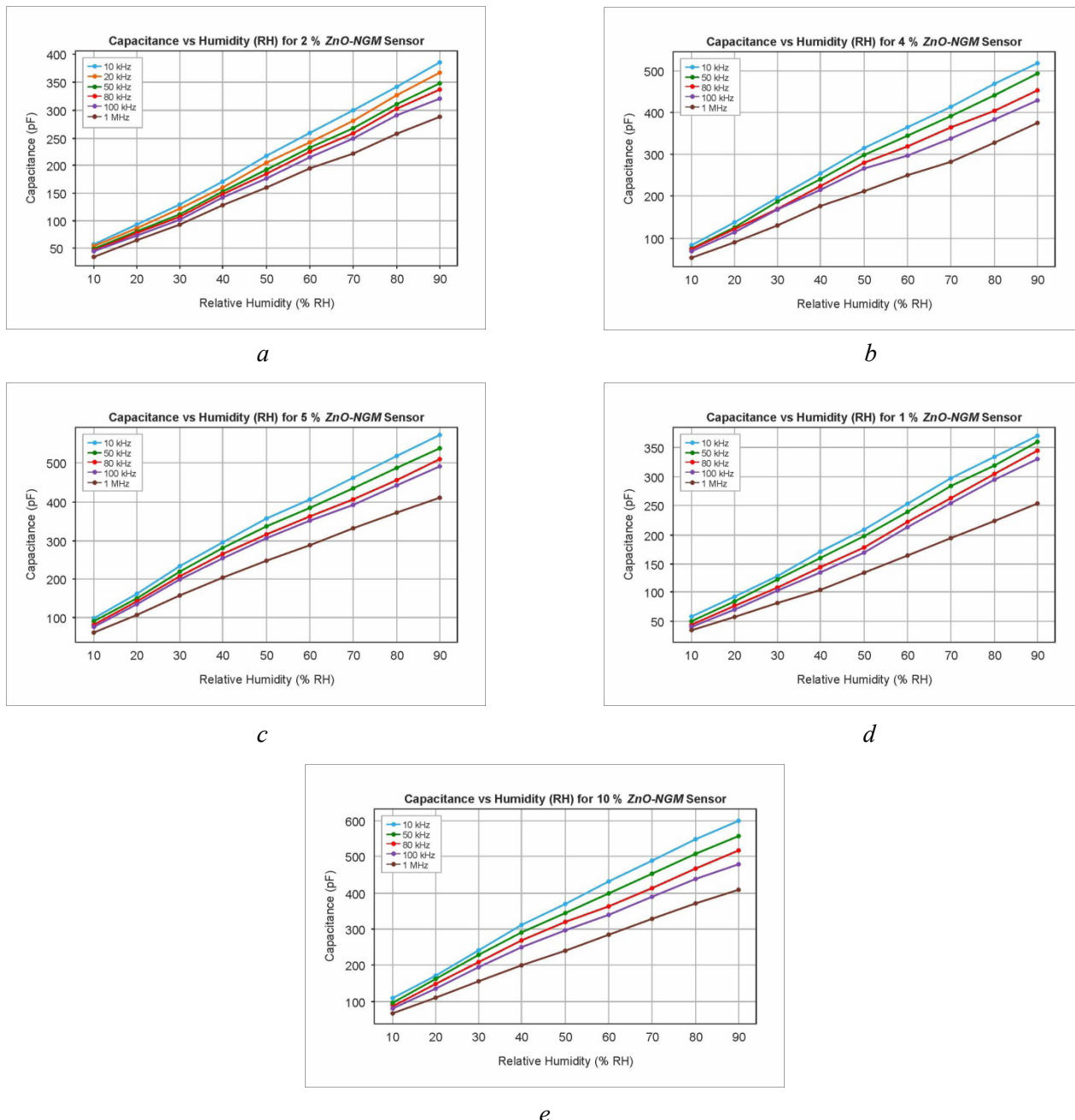
Fig. 7. Capacitance as a function of *RH* for *ZnO–NGM* sensors with (*a*) 2 wt.%, (*b*) 4 wt.%, (*c*) 1 wt.%, (*d*) 5 wt.%, and (*e*) 10 wt.% *NGM* doping

The dynamic behavior of the sensor was evaluated in terms of response and recovery time, which are defined as the time to achieve 90% of the maximum capacitance change when exposed to humidity and the time to recover to 10% of the initial value when moisture is removed, respectively (Table 1). The undoped *ZnO* had a response time of 5.0 s and a recovery time of 7.0 s. After doping, these values were significantly enhanced, and the 4% *ZnO–NGM* sensor realized an optimal trade-off: a quick response time of 4.0 s and a recovery time of 6.2 s. This is a characteristic of good water molecule adsorption–desorption kinetics facilitated by the synergy between *ZnO's* porous nature and *NGM's* charge transport ability.

At elevated *NGM* doping concentrations (≥5%), response and recovery times started to grow. For example, the 10% *ZnO–NGM* sensor had slower response (6.0 s) and recovery (8.0 s) times due to probable *NGM* agglomeration. Agglomeration decreases the number of active adsorption sites and inhibits water diffusion paths, thereby reducing sensing speed even though high capacitance sensitivity exists.

Capacitance variation with *RH* for different doping levels is shown in Fig. 8, *a*. While pure *ZnO* exhibited a baseline sensitivity of 18.5 pF/% *RH*, the introduction of *NGM* significantly enhanced the response.

**Effect of *NGM* doping on capacitance sensitivity, response time, and recovery time
of *ZnO*-based humidity sensors**

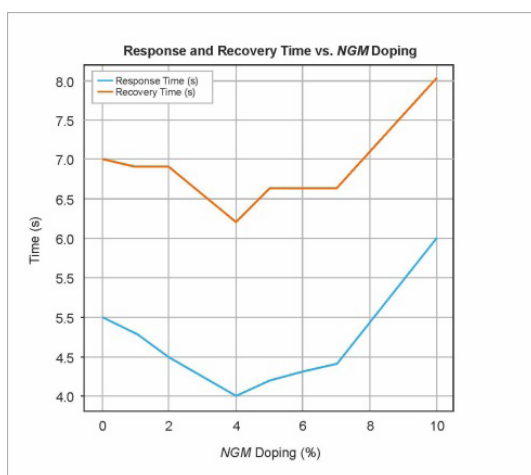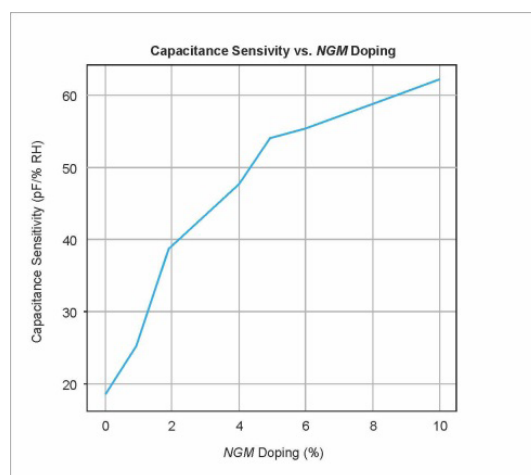| *NGM* Doping (%)	Capacitance sensitivity (pF/% RH)	Response time (s)	Recovery time (s)
0% (pure *ZnO*)	18.5	5	7
1 %	25.2	4.8	6.9
2 %	38.7	4.5	6.9
4 %	47.3	4.0	6.2
5 %	53.9	4.2	6.6
7 %	56.8	4.4	6.6
10 %	62.1	6	8

a

b

Fig. 8. (*a*) Response and recovery times as a function of *NGM* doping level; (*b*) Capacitance sensitivity
as a function of *NGM* doping level

Although 10% doping resulted in maximum sensitivity (62.1 pF/% *RH*), it came at the expense of slower kinetics. The 4% and 5% *ZnO-NGM* sensors presented the best compromise between high sensitivity and rapid response/recovery behavior, making them ideal candidates for real-time humidity detection.

ZnO-NGM-based humidity sensor response and recovery behavior was investigated to analyze real-time performance (Fig. 8, *b*). The best response (4.0 s) and recovery (6.2 s) times were obtained at 4% *ZnO–NGM*, due to the synergy between *ZnO's* high surface area and *NGM's* superior charge transport properties. For doping above 5%, performance decreased because *NGM* agglomeration decreased active adsorption sites and hampered electron mobility. At 10% doping, response and recovery times were elevated to 6.0 s and 8.0 s, respectively.

In general, controlled *NGM* doping greatly improves *ZnO* sensor performance, outperforming the drawbacks of conventional metal oxide sensors. The optimized *ZnO-NGM* composites surpass or match current sensors, showing great potential for use in environmental monitoring, industrial systems, and biomedical diagnostics. The cyclic sensing performance is indicated in Fig. 9, illustrating capacitance and *RH* levels against time over a period of 1,000 seconds. The capacitance (dotted red-blue line) closely follows the humidity (red squares), with evidence of synchronized and repeatable behavior.

The rapid slopes at times of humidity transition reflect rapid response and recovery behaviors. The regular periodic behavior supports sensor stability, repeatability, and suitability for dynamic environmental monitoring.
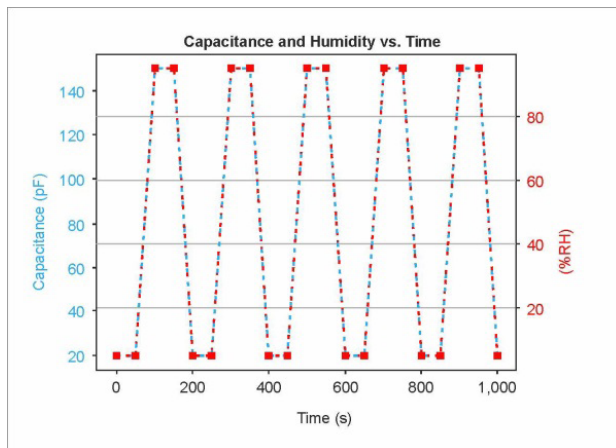
Fig. 9. Cyclic capacitance and humidity variation over 1,000 s, demonstrating sensor stability

Capacitive Sensitivity and Frequency Response

Capacitive sensitivity was greatly increased by *NGM* doping, reaching a peak of 65 a.u. for 5% NGM doping at 90% *RH* (Fig. 10, *c*). This is due to the high conductivity and high surface area of *NGM*, promoting increased charge storage and water molecule adsorption [8]. Doping concentrations higher than 5% caused decreased capacitance through agglomeration, limiting effective surface area and sites for adsorption.

Frequency-dependent measurements (Figs. 10, *a* and 10, *b*) identified that lower frequencies (<10 kHz) had more capacitance change, which is enhanced by stronger polarization. However, higher frequencies (>100 kHz) were less sensitive due to quicker charge carrier relaxation, restraining the capacity of water molecules to align with the electric field [9]. Fig. 7, *d* also verifies that at 5% doping, the sensor recorded high RH sensitivity over a range of frequencies, particularly at lower frequencies.
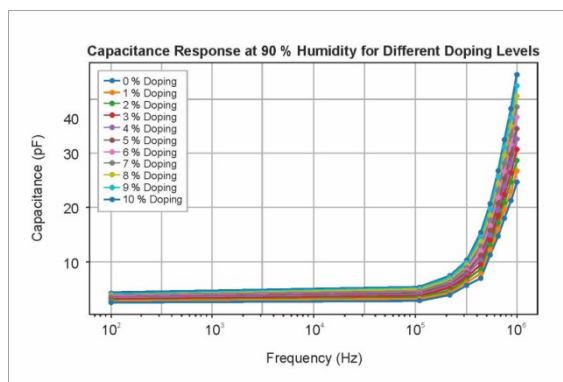
a
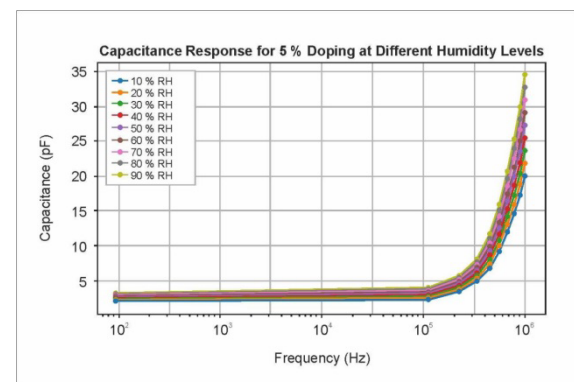
b
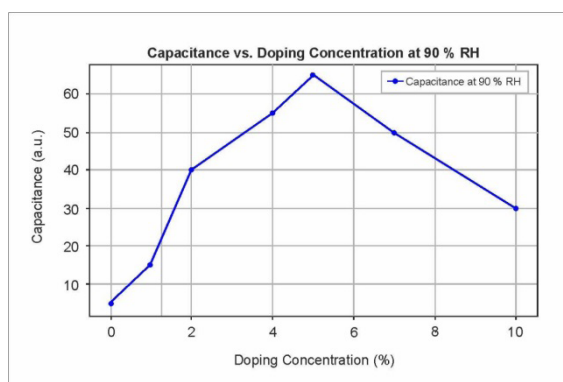
c
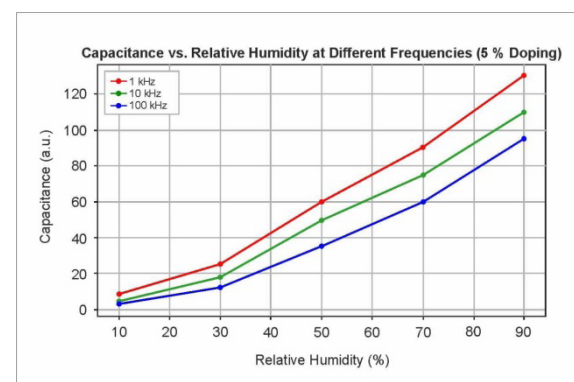
d

Fig. 10. (*a*) Capacitive response at 90% *RH*; (*b*) Response for 5 wt.% *NGM* doping; (*c*) Capacitance as a function of doping level at 90% *RH*; (*d*) Capacitance as a function of *RH* at different frequencies (5 wt.% *NGM* doping)

Electrode Influence on Sensor Performance

The influence of various electrode materials (*FTO*, silver, and copper) on sensor performance was assessed. *FTO* electrodes gave stable and reproducible responses, probably because of their chemical stability and strong adhesion to the sensing material. Silver electrodes improved sensitivity, probably because of their higher conductivity, which supports efficient charge transfer. Nevertheless, copper electrodes showed minor performance degradation with time, possibly because of oxidation effects, which can increase the contact resistance and lower the sensor sensitivity [32].

Comparison with existing sensors

Comparative studies between various humidity sensors emphasize the relative merits of *ZnO–NGM* sensors compared to multiple carbon-based and metal oxide-based materials. As an example, gram carbon quantum dot-based sensors have good sensitivity (178.6–254.86 pF/% *RH*) but less desirable response and recovery times (7.3–14.1 s) and therefore experience difficult detection at lower relative humidity (*RH*) concentrations. *PAA-MWCNT* composite sensors also register a notable resistance change (930 Ω) with humidity fluctuation but have very high response (680 s) and recovery (380 s) times, restricting their applicability. Graphene oxide (*GO*)-modified *PEDOT* sensors, though highly responsive to humidity (4.97% sensitivity at 97% RH), are characterized by sluggish response (31 s) and recovery (72 s). Other graphene-based sensors, including *Fe-GO* and *GO/WS₂* composites, offer modest performance but tend to have low sensitivity or high response/recovery times.

In order to put the performance of the *ZnO–NGM* humidity sensor prepared in the present research into perspective, its performance was compared to a vast array of recently published nanomaterial-based humidity sensors. Table 2 gives an overview of sensitivity, response time, recovery time, and some observations from past research work along with data from this research work.

The study shows that although some materials like gram carbon quantum dots have quite high sensitivity (178.6–254.86 pF/% *RH*), they have slow response and recovery times of up to 14.1 seconds, which restricts their use in fast-switching environments. Some designs, like the *PAA-MWCNT* composites, possess large resistance changes (930 Ω) but are weighed down by very long response (680 s) and recovery (380 s) times, making them unsuitable for real-time sensing.

Likewise, *GO*-modified *PEDOT* sensors exhibit a humidity sensitivity of 4.97% at 97% *RH* but with slower response (31 s) and recovery (72 s) cycles. *Fe–GO* and *GO/WS₂* sensors possess better speed but relatively lower sensitivity, particularly at lower *RH* values. Even *GO*-based sensors with abnormally high sensitivity (e.g., 37,800%) suffer from slow recovery times (~41 s) or are limited due to poor applicability in real-world situations because they are unstable at lower *RH*.

Conversely, *ZnO–NGM* sensors prepared in this work show a balanced and superior performance profile. The 5% *NGM*-doped *ZnO* sensor recorded a sensitivity of 53.9 pF/% *RH*, a response time of 4.2 s, and a recovery time of 6.6 s, outperforming many of the reported sensors with a significantly better dynamic response while retaining good sensitivity. At lower doping levels (e.g., 2% *NGM*), the sensor retained fast response (4.5 s) and recovery (6.9 s) times with a nominally lower sensitivity of 38.7 pF/% *RH*.

In addition, in contrast to most carbon-based sensors that exhibit scattered results across different *RH* levels, the *ZnO–NGM* sensors exhibited stable and reproducible performance within a broad *RH* range (10%–95%), rendering them feasible for application in real-time environmental or industrial monitoring systems. The fact that such sensors can also be made from inexpensive materials and using a facile doctor-blade method on *FTO* substrates further contributes to their practical benefits.

Structural and morphological analyses confirmed the successful incorporation of nanographite material (*NGM*) into the *ZnO* matrix. X-ray diffraction (*XRD*) patterns showed distinct peak shifts with increasing NGM content, indicating lattice strain and structural modification. Scanning electron microscopy (*SEM*) images revealed a uniform distribution of *NGM* within the *ZnO* matrix, resulting in increased surface roughness and the formation of additional active sites for water molecule adsorption. Fourier transform infrared (*FTIR*) spectroscopy further confirmed the presence of functional groups associated with humidity sensing, such as *O–H* stretching and *C=C* vibrations.

T a b l e 2

Comparison of recent nano humidity sensors

No.	Sensor Material	Sensitivity (pF/%RH or %)	Response Time (s)	Recovery Time (s)	Refer-ence	Key Observation
1	Gram Carbon Quantum Dots (*C-1*, *C-2*)	178.6–254.86	13.3 / 7.3	14.1 / 4.7	[33]	– High sensitivity; – Slow recovery
2	*PAA-MWCNT* (1:4 ratio)	930 Ом (resistance change)	680	380	[34]	– Excessively high response/recovery time
3	*GO*-modified *PEDOT*	4.97 % at 97 % RH	31	72	[35]	– Poor dynamic response
4	*MWCNT* in *NMP*	6.41	36	32	[36]	– Moderate performance
5	*SnO2–RGO*	146.53	102	"several seconds"	[37]	– Slow at high *RH*
6	*GO*	37,800 %	10.5	41	[38]	– Very high sensitivity; – Long recovery
7	*Fe–GO*	5.18	31	11	[39]	– Low sensitivity at low *RH*
8	*GO*	–9.5 пФ/% *RH*	5	–	[40]	– Good speed; – Limited range
9	*GO*/*WS2* Composite	Not specified	11.3	12.4	[41]	– Stable performance 25–95% *RH*
10	CNT@CPM (Chitosan-PAMAM	Not specified	<20	<20	[42]	– Fast; – No sensitivity data
11	**5% ZnO–NGM (this work)**	**53.9**	**4.2**	**6.6**	this work	– Best balance; – High sensitivity; – Fast response
12	**2% ZnO–NGM (this work)**	**38.7**	**4.5**	**6.9**	this work	– Slightly lower sensitivity; – Still fast

Electrical characterization demonstrated that *NGM* doping significantly enhanced sensor performance. Among the samples, the *ZnO* sensor doped with 2% *NGM* exhibited the most favorable dynamic response, with a response time of 4.5 seconds and a recovery time of 6.9 seconds. This improvement is attributed to enhanced charge transport properties and a greater number of available adsorption sites. However, at higher doping concentrations (above 5%), although sensitivity increased, the response and recovery times became longer. This behavior is likely due to agglomeration effects, which reduce the effective surface area and hinder rapid adsorption-desorption kinetics.

A comparison with previously reported humidity sensors highlights the advantages of *ZnO-NGM* nanocomposites. While many conventional sensors suffer from slow response and poor recovery, the optimized doping concentration in this study achieved a desirable balance between sensitivity and speed. These enhancements suggest that *NGM*-doped *ZnO* sensors are promising candidates for real-time humidity monitoring across various domains, including industrial process control, environmental sensing, and biomedical diagnostics.

Future work should focus on further optimizing the doping concentration to enhance performance without compromising long-term stability. Additionally, exploring alternative film deposition techniques and integrating the sensor onto flexible substrates could enable the development of wearable or portable humidity sensors for next-generation smart systems.

Conclusions

This work reports the effective synthesis of *ZnO* nanoparticles doped with nanographite material (*NGM*) for high-performance capacitive humidity sensing. *UV–Vis* spectroscopy verified a strong absorption peak at 367 nm, confirming the semiconductor nature and optical suitability of the *ZnO* structure. Structural (*XRD*) and morphological (*SEM*) analyses showed enhanced crystallinity and surface texture, while *NGM* doping significantly improved adsorption kinetics and charge transport. Among the different doping levels that were tested, the 4% *NGM*-doped *ZnO* sensor had the best sensitivity-speed balance with a fast response time of 4.0 s and recovery time of 6.2 s. While doping levels of 5% and above provided higher capacitance sensitivity, the response speed was reduced, possibly due to agglomeration and lower active surface area. The sensors also exhibited very good repeatability, negligible hysteresis, and robust performance over a broad frequency and humidity range (10–95% *RH*, 10 kHz–1 MHz).

References

1. Saqib M., Ali Khan S., Mutee Ur Rehman H.M., Yang Y., Kim S., Rehman M.M., Young Kim W. High-performance humidity sensor based on the graphene flower/zinc oxide composite. *Nanomaterials*, 2021, vol. 11 (1), p. 242. DOI: 10.3390/nano11010242.

2. Yang H., Ye Q., Zeng R., Zhang J., Yue L., Xu M., Qiu Z.-J., Wu D. Stable and fast-response capacitive humidity sensors based on a ZnO nanopowder/PVP-RGO multilayer. *Sensors*, 2017, vol. 17 (10), p. 2415. DOI: 10.3390/s17102415.

3. Ullah Z., Mustafa G.M., Raza A., Khalil A., Awadh Bahajjaj A.A., Batool R., Sonil N.I., Ali I., Nazar M.F. Facile assembly of flexible humidity sensors based on nanostructured graphite/zinc oxide-coated cellulose fibrous frameworks for human healthcare. *RSC Advances*, 2024, vol. 14 (50), pp. 37570–37579. DOI: 10.1039/D4RA05761A.

4. Sun Y., Gao X., Shiwei A., Fang H., Lu M., Yao D., Lu C. Hydrophobic multifunctional flexible sensors with a rapid humidity response for long-term respiratory monitoring. *ACS Sustainable Chemistry & Engineering*, 2023, vol. 11 (6), pp. 2375–2386. DOI: 10.1021/acssuschemeng.2c06162.

5. Ding S., Yin T., Zhang S., Yang D., Zhou H., Guo S., Li Q., Wang Y., Yang Y., Peng B., Yang R., Jiang Z. Fast-speed, highly sensitive, flexible humidity sensors based on a printable composite of carbon nanotubes and hydrophilic polymers. *Langmuir*, 2023, vol. 39 (4), pp. 1474–1481. DOI: 10.1021/acs.langmuir.2c02827.

6. Wu K., Miao X., Zhao H., Liu S., Fei T., Zhang T. Selective encapsulation of ionic liquids in UiO-66-NH$_2$ nanopores for enhanced humidity sensing. *ACS Applied Nano Materials*, 2023, vol. 6 (10), pp. 9050–9058. DOI: 10.1021/acsanm.3c01727.

7. Lei D., Zhang Q., Liu N., Su T., Wang L., Ren Z., Zhang Z., Su J., Gao Y. Self-powered graphene oxide humidity sensor based on potentiometric humidity transduction mechanism. *Advanced Functional Materials*, 2022, vol. 32 (10), p. 2107330. DOI: 10.1002/adfm.202107330.

8. Adib M.R., Lee Y., Kondalkar V.V., Kim S., Lee K. A highly sensitive and stable rGO: MoS2-based chemiresistive humidity sensor directly insertable to transformer insulating oil analyzed by customized electronic sensor interface. *ACS Sensors*, 2021, vol. 6 (3), pp. 1012–1021. DOI: 10.1021/acssensors.0c02219.

9. Yu W., Chen D., Li J., Zhang Z. TiO$_2$-SnS$_2$ nanoheterostructures for high-performance humidity sensor. *Crystals*, 2023, vol. 13 (3), p. 482. DOI: 10.3390/cryst13030482.

10. Baig M.F.W., Hasany S.F., Shirazi M.F. Green synthesis of nano graphite materials from lemon and orange peel: A sustainable approach for carbon-based materials. *Engineering Proceedings*, 2023, vol. 46 (1), p. 42. DOI: 10.3390/engproc2023046042.

11. Dare E., Adanu-Ogbole B., Oladoyinbo F., Makinde F., Uzosike A.O. Synthesis and characterization of silver–zinc oxide nanocomposites for humidity sensing. *Nano Select*, 2023, vol. 4 (4), pp. 255–262. DOI: 10.1002/nano.202200106.

12. Mahjoub M.A., Monier G., Robert-Goumet C., Réveret F., Echabaane M., Chaudanson D., Petit M., Bideux L., Gruzza B. Synthesis and study of stable and size-controlled ZnO–SiO$_2$ quantum dots: Application as a humidity sensor. *The Journal of Physical Chemistry C*, 2016, vol. 120 (21), pp. 11652–11662. DOI: 10.1021/acs.jpcc.6b00135.

13. Qian L., Fang C., Gui Y., Tian K., Guo H., Guo D., Guo X., Liu P. Heterojunctions of ZnO-nanorod-decorated WO$_3$ nanosheets coated with ZIF-71 for humidity-independent NO$_2$ sensing. *ACS Applied Nano Materials*, 2023, vol. 6 (14), pp. 13216–13226. DOI: 10.1021/acsanm.3c01955.

14. Ling T.Y., Pu S.H., Fishlock S.J., Han Y., Reynolds J.D., McBride J.W., Chong H.M.H. Sensing performance of nanocrystalline graphite-based humidity sensors. *IEEE Sensors Journal*, 2019, vol. 19 (14), pp. 5421–5428. DOI: 10.1109/JSEN.2019.2905719.

15. Wu J., Yin C., Zhou J., Li H., Liu Y., Shen Y., Garner S., Fu Y., Duan H. Ultrathin glass-based flexible, transparent, and ultrasensitive surface acoustic wave humidity sensor with ZnO nanowires and graphene quantum dots. *ACS Applied Materials & Interfaces*, 2020, vol. 12 (35), pp. 39817–39825. DOI: 10.1021/acsami.0c09962.

16. Dinç Zor Ş., Cankurtaran H. Impedimetric humidity sensor based on nanohybrid composite of conducting poly (diphenylamine sulfonic acid). *Journal of Sensors*, 2016, vol. 2016 (1), p. 5479092. DOI: 10.1155/2016/5479092.

17. Lin C., Zhang H., Zhang J., Chen C. Enhancement of the humidity sensing performance in Mg-doped hexagonal ZnO microspheres at room temperature. *Sensors*, 2019, vol. 19 (3), p. 519. DOI: 10.3390/s19030519.

18. Chaudhary P., Verma A., Chaudhary S., Kumar M., Lin M.-F., Huang Y.-C., Chen K.-L., Yadav B.C. Design of a humidity sensor for a PPE kit using a flexible paper substrate. *Langmuir*, 2024, vol. 40 (18), pp. 9602–9612. DOI: 10.1021/acs.langmuir.4c00366.

19. Agadi N.P., Teradal N.L., Manjunatha D.H., Seetharamappa J. Zinc oxide anchored porous reduced graphene oxide: Electrode material for sensing of ezetimibe. *Journal of The Electrochemical Society*, 2024, vol. 171 (3), p. 037513. DOI: 10.1149/1945-7111/ad2f78.

20. Hongsith N., Chansuriya S., Yatmontree B., Uai S. Capacitively coupled contactless conductivity detection (C4D) of ZnO nanostructures gas sensor by adding Au: Pd metal with response to ethanol and acetone vapor. *Journal of Physics: Conference Series*, 2023, vol. 2653 (1), p. 012062. DOI: 10.1088/1742-6596/2653/1/012062.

21. Luo N., Cai H., Li X., Guo M., Wang C., Wang X., Hu P., Cheng Z., Xu J. Non-crystal-RuO$_x$/crystalline-ZnO composites: controllable synthesis and high-performance toxic gas sensors. *Journal of Materials Chemistry A*, 2022, vol. 10 (28), pp. 15136–15145. DOI: 10.1039/D2TA02856E.

22. Saxena K., Kumar A., Chauhan N., Khanuja M., Malhotra B.D., Jain U. Electrochemical immunosensor for detection of H. pylori secretory protein VacA on g-C$_3$N$_4$/ZnO nanocomposite-modified Au electrode. *ACS Omega*, 2022, vol. 7 (36), pp. 32292–32301. DOI: 10.1021/acsomega.2c03627.

23. Dhahri R., Benamara M., Nassar K.I., Elkenany E.B., Al-Syadi A.M. Zinc oxide-based sensor prepared by modified sol–gel route for detection of low concentrations of ethanol, methanol, acetone, and formaldehyde. *Semiconductor Science and Technology*, 2024, vol. 39 (11), p. 115021. DOI: 10.1088/1361-6641/ad825e.

24. Hussain S., Hasany S., Ali S.U. Hematite decorated MWCNT nanohybrids: A facile synthesis. *Journal of the Chemical Society of Pakistan*, 2022, vol. 44 (5), pp. 480–489. DOI: 10.52568/001121/JCSP/44.05.2022.

25. Doroftei C., Leontie L. Porous nanostructured gadolinium aluminate for high-sensitivity humidity sensors. *Materials*, 2021, vol. 14 (22), p. 7102. DOI: 10.3390/ma14227102.

26. Zhang H., Liu L., Huang C., Liang S., Jiang G. Enhanced acetone gas sensing performance of ZnO polyhedrons decorated with LaFeO$_3$ nanoparticles. *Materials Research Express*, 2023, vol. 10 (9), p. 095902. DOI: 10.1088/2053-1591/acf6f8.

27. Zhang D., Pan W., Zhou L., Yu S. Room-temperature benzene sensing with Au-doped ZnO nanorods/ exfoliated WSe$_2$ nanosheets and density functional theory simulations. *ACS Applied Materials & Interfaces*, 2021, vol. 13 (28), pp. 33392–33403. DOI: 10.1021/acsami.1c03884.

28. Hosseini D., Donat F., Abdala P.M., Kim S.M., Kierzkowska A.M., Müller C.R. Reversible exsolution of dopant improves the performance of Ca$_2$Fe$_2$O$_5$ for chemical looping hydrogen production. *ACS Applied Materials & Interfaces*, 2019, vol. 11 (20), pp. 18276–18284. DOI: 10.1021/acsami.8b16732.

29. Fan W., Wang B., Gao R., Dimitrakopoulos G., Wang J., Xiao X., Ma L., Wu K., Yildiz B., Li J. Anodic shock-triggered exsolution of metal nanoparticles from perovskite oxide. *Journal of the American Chemical Society*, 2022, vol. 144 (17), pp. 7657–7666. DOI: 10.1021/jacs.1c12970.

30. Shah W., Khwaja R.W., Faraz S.M., Awan Z.H., Sayyad M.H. Photovoltaic and impedance analysis of dye-sensitized solar cells with counter electrodes of manganese dioxide and silver-doped manganese dioxide. *Engineering Proceedings*, 2023, vol. 46 (1), p. 31. DOI: 10.3390/engproc2023046031.

31. Zhang X., Maddipatla D., Bose A.K., Hajian S., Narakathu B.B., Williams J.D., Mitchell M.F., Atashbar M.Z. Printed carbon nanotubes-based flexible resistive humidity sensor. *IEEE Sensors Journal*, 2020, vol. 20 (21), pp. 12592–12601. DOI: 10.1109/JSEN.2020.3002951.

32. Al-Bonayan A.M., Althakafy J.T., Alorabi A.Q., Alamrani N.A., Aljuhani E.H., Alaysuy O., Al-Qahtani S.D., El-Metwaly N.M. Novel copper oxide-integrated carbon paste tirofiban voltammetric sensor. *ACS Omega*, 2023, vol. 8 (5), pp. 5042–5049. DOI: 10.1021/acsomega.2c07790.

33. Chaudhary P., Maurya D.K., Yadav S., Pandey A., Tripathi R.K., Yadav B.C. Ultrafast responsive humidity sensor based on roasted gram derived carbon quantum dots: experimental and theoretical study. *Sensors and Actuators B: Chemical*, 2021, vol. 329, p. 129116. DOI: 10.1016/j.snb.2020.129116.

34. Lee J., Cho D., Jeong Y. A resistive-type sensor based on flexible multi-walled carbon nanotubes and polyacrylic acid composite films. *Solid-State Electronics*, 2013, vol. 87, pp. 80–84. DOI: 10.1016/j.sse.2013.05.001.

35. Pang Y., Jian J., Tu T., Yang Z., Ling J., Li Y., Wang X., Qiao Y., Tian H., Yang Y., Ren T.-L. Wearable humidity sensor based on porous graphene network for respiration monitoring. *Biosensors and Bioelectronics*, 2018, vol. 116, pp. 123–129. DOI: 10.1016/j.bios.2018.05.038.

36. Kumar U., Yadav B.C. Development of humidity sensor using modified curved MWCNT based thin film with DFT calculations. *Sensors and Actuators B: Chemical*, 2019, vol. 288, pp. 399–407. DOI: 10.1016/j.snb.2019.03.016.

37. Zhang D., Chang H., Li P., Liu R., Xue Q. Fabrication and characterization of an ultrasensitive humidity sensor based on metal oxide/graphene hybrid nanocomposite. *Sensors and Actuators B: Chemical*, 2016, vol. 225, pp. 233–240. DOI: 10.1016/j.snb.2015.11.024.

38. Bi H., Yin K., Xie X., Ji J., Wan S., Sun L., Terrones M., Dresselhaus M.S. Ultrahigh humidity sensitivity of graphene oxide. *Scientific Reports*, 2013, vol. 3 (1), p. 2714. DOI: 10.1038/srep02714.

39. Kumar K., Kumar U., Singh M., Yadav B.C. Synthesis and characterizations of exohedral functionalized graphene oxide with iron nanoparticles for humidity detection. *Journal of Materials Science: Materials in Electronics*, 2019, vol. 30 (14), pp. 13013–13023. DOI: 10.1007/s10854-019-01663-9.

40. Zhao C.-L., Qin M., Li W.-H., Huang Q.-A. Enhanced performance of a CMOS interdigital capacitive humidity sensor by graphene oxide. *2011 16th International Solid-State Sensors, Actuators and Microsystems Conference*. IEEE, 2011, pp. 1954–1957. DOI: 10.1109/TRANSDUCERS.2011.5969243.

41. Wang G., Gao Q., Ke N., Si F., Wang J., Ding J., Zhang W., Fan X. Highly sensitive flexible humidity sensors with fast response and recovery times based on the composite of graphene oxide and WS 2 for detection of human breath and fingertip proximity. *Journal of Materials Chemistry C*, 2025, vol. 13 (10), pp. 4929–4937. DOI: 10.1039/D4TC05303F.

42. Kim H.-S., Kang J.-H., Hwang J.-Y., Shin U.S. Wearable CNTs-based humidity sensors with high sensitivity and flexibility for real-time multiple respiratory monitoring. *Nano Convergence*, 2022 , vol. 9 (1), p. 35. DOI: 10.1186/s40580-022-00326-6.

Conflicts of Interest

The authors declare no conflict of interest.

Obrabotka metallov -
Metal Working and Material Science

Journal homepage: http://journals.nstu.ru/obrabotka_metallov

Features of the structure of gradient layers «steel - Inconel - steel», obtained by laser direct metal deposition

Svetlana Dolgova [1, a], Alexandr Malikov [2, b], Alexander Golyshev [2, c], Aelita Nikulina [3, d,*]

[1] Novosibirsk semiconductor device plant Vostok, 60 Dachnaya st., Novosibirsk, 630082, Russian Federation
[2] Khristianovich Institute of Theoretical and Applied Mechanics SB RAS, 4/1 Institutskaya str., Novosibirsk, 630090, Russian Federation
[3] Novosibirsk State Technical University, 20 Prospekt K. Marksa, Novosibirsk, 630073, Russian Federation

[a] https://orcid.org/0000-0003-3918-273X, svetlanadolgova99@gmail.com; [b] https://orcid.org/0000-0003-1268-8546, smalik707@yandex.ru;
[c] https://orcid.org/0000-0002-4243-0602, alexgol@itam.nsc.ru; [d] https://orcid.org/0000-0001-9249-2273, a.nikulina@corp.nstu.ru

ARTICLE INFO

ABSTRACT

Introduction. Traditionally, the most common technology for producing parts from nickel alloys involves casting followed by heat treatment to achieve the required phase composition. Significant disadvantages of this method include the segregation of chemical elements, the presence of large undesirable inclusions such as *Laves* phase and eutectic structures, and the non-uniform distribution of strengthening phases throughout the workpiece cross-section. At the same time, many complex-shaped parts are assembled into a single combined structure using welding. An analysis of the hardening characteristics of nickel alloys and the products derived from them suggests that additive manufacturing techniques are a promising approach for fabricating such workpieces. The structure and phase composition of the material volumes formed via layer-by-layer deposition will differ significantly from those obtained by conventional methods. In the case of producing combined structures using additive methods, identifying the patterns of structure and phase composition formation becomes an even more complex challenge. Therefore, **the purpose of this work** is to identify the structural features of "steel - nickel alloy – steel" gradient layers fabricated by direct metal deposition. The study examines dissimilar joints produced using the "Welding and Surfacing Complex based on a Multi-Coordinate Arm and a Fiber Laser" at the S.A. Khristianovich Institute of Theoretical and Applied Mechanics of the Siberian Branch of the Russian Academy of Sciences, employing direct metal deposition technology. **Research methods.** A Carl Zeiss *Axio Imager A1m* light microscope and a Carl Zeiss *EVO 50 XVP* scanning electron microscope, equipped with an *INCA X-Act* energy-dispersive X-ray spectroscopy (*EDS*) attachment, were utilized for microstructural investigations of the fabricated layers. Phase composition analysis of the samples was performed using an *ARL X'TRA* X-ray diffractometer. Microhardness testing was conducted using a *Wolpert Group 402 MVD Vickers* hardness tester. **Results and discussion.** It was observed that the maximum layer height (up to 7 mm) was achieved when implementing the following parameters: 1,000 W laser power with a scanning speed of 35 mm/s, and 1,500 W laser power with a scanning speed of 15 mm/s. In the first case, minimal material mixing at the fusion boundary was noted. In all fabricated compositions, defects in the form of unmelted powder particles were observed, as well as cracks in the first steel layers. During the deposition of *Inconel 625* onto *316L* stainless steel, the transition zone exhibited solidification modes consistent with the formation of iron-based alloys, specifically *FA* (ferrite-austenite), *AF* (austenite-ferrite), and *A* (austenite) sequentially. When depositing *316L* stainless steel onto *Inconel 625*, the transition zone exhibited a solidification mode characterized by the formation of only the austenite phase. The microhardness values were found to be 230 ±15 HV for *316L* stainless steel and 298 ± 20 HV for *Inconel 625*.

* Corresponding author
Nikulina Aelita A., D.Sc. (Engineering), Professor
Novosibirsk State Technical University,
20 Prospekt K. Marksa,
630073, Novosibirsk, Russian Federation
Tel.: +7 383 346-11-71, **e-mail:** a.nikulina@corp.nstu.ru

Introduction

Nickel-based alloys are widely used for manufacturing critical components across various industries, including aerospace, power generation, petrochemical, and marine sectors. This widespread application is attributed to their combination of high corrosion resistance and mechanical strength at moderately elevated temperatures. The high strength of these alloys is achieved through a specific phase composition, which in turn is determined by the presence of particular alloying elements and the corresponding strengthening mechanisms [1–3].

Traditionally, the most common method for producing components from nickel alloys is casting, followed by heat treatment to form the desired phase structure [4]. However, this approach has several significant drawbacks. These include chemical element segregation, the presence of large undesirable *Laves* phase inclusions and eutectics [5, 6], as well as an uneven distribution of strengthening phases across the cross-section of the workpiece [7]. Moreover, many complex-shaped components are assembled into a single combined structure using welding techniques.

Additive manufacturing technologies present a promising alternative for producing nickel alloy components, as evidenced by analysis of strengthening mechanisms in these alloys and their manufactured parts [8–12]. This approach offers several key advantages: (1) it addresses the challenge of fabricating geometrically complex components; (2) the rapid cooling rates characteristic of additive processes minimize chemical segregation; (3) the layer-by-layer deposition induces repeated thermal cycling, which can promote *in situ* precipitation of strengthening phases during the build. Moreover, the ability to create hybrid structures reduces the consumption of expensive materials. As a result, the microstructure and phase composition of additively manufactured materials are anticipated to differ significantly from those produced via conventional methods.

Despite the growing interest in this topic in the scientific literature, a comprehensive understanding of the microstructural and phase characteristics of various alloys produced by additive technologies is still lacking. This is primarily due to the wide variability in processing methods and parameters used in different studies. Furthermore, in the case of hybrid structures produced via additive manufacturing, identifying the patterns of structure and phase formation becomes an even more complex task [13–15].

Consequently, the purpose of this work is to investigate the structural features of gradient layers in «steel – nickel alloy – steel» systems fabricated by direct laser deposition.

Research methods

Research materials

For sample fabrication, powders of *Inconel 625* nickel-based alloy (particle size: 50–70 μm) and *AISI 316L* stainless steel (particle size: 15–45 μm) were used (Fig. 1). A 50×50×5 mm plate made of *0.12 C-18 Cr-10 Ni-Ti* stainless steel served as the substrate. The chemical compositions of the initial materials are presented in Table 1.

Sample preparation

Dissimilar joints were fabricated at the Khristianovich Institute of Theoretical and Applied Mechanics SB RAS using a "Cladding and Welding Complex Based on a Multi-Axis Robotic Arm and a 3 kW Fiber Laser (IPG Photonics) with a Wavelength of 1.07 μm". Direct laser deposition (*DLD*) was employed as the processing method, where powder is delivered through a coaxial nozzle into a localized melt pool generated by laser radiation. The high scanning speed and rapid cooling rates inherent in this technique minimize thermal gradients and reduce the likelihood of secondary phase formation in the joint region. Argon served as the shielding gas. Detailed deposition parameters are provided in Table 2 [16].

The samples were fabricated in a unidirectional manner. Sequentially, four layers of each material were deposited in the order: steel – nickel alloy – steel. Each subsequent layer overlapped the previous layer by 50%, which was intended to ensure a smooth transition between the materials.
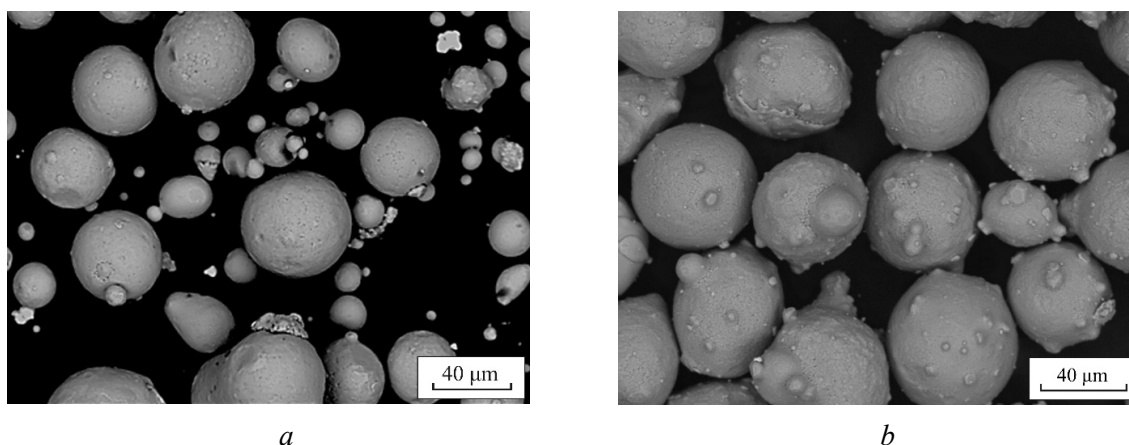
a   *b*

Fig. 1. Particles of *Inconel 625* (*a*) and *AISI 316L* (*b*) powders

T a b l e 1

Chemical composition of the materials

Material	Chemical element, wt.%								
	Fe	*Ni*	*Cr*	*C*	*Mo*	*Nb*	Ti	S	P
316L	*bal.*	8.84	18.69	0.03	2.50	-	0.71	0.013	0.015
Inconel 625	3.8	*bal.*	19.16	0.1	8.1	3.36	0.28	0.011	0.01
0.12 C-18 Cr-10 Ni-Ti	*bal.*	7.852	18.16	0.027	–	–	0.002	0.002	0.027

T a b l e 2

Deposition parameters for specimens

Mode	Power, W	Speed, mm/s	Consumption, g/min	Beam diameter, mm
1	1,000	35		
2	1,250	25	12	4,1
3	1,500	15		

Structural studies

Structural characterization was performed using an optical microscope *Carl Zeiss A1Z* and a scanning electron microscope (*SEM*) *Carl Zeiss EVO 50 XVP*. Sample preparation followed standard metallographic procedures, including grinding and polishing steps. To reveal the microstructure of the joints, electrolytic etching was carried out in a 10 % aqueous solution of oxalic acid.

The chemical composition in the joint zones between dissimilar materials was analyzed using energy-dispersive X-ray spectroscopy (*EDS*) with an *INCA X-Act* detector attached to the *SEM*.

Phase composition analysis was conducted on an *ARL X'TRA* X-ray diffractometer equipped with a *Mo Kα1/α2* radiation source ($\lambda = 0.7093$ Å), using a step size of $\Delta 2\theta = 0.03°$ and an acquisition time of 5 s per point.

Microhardness testing was carried out using a *Wolpert Group 402 MVD* Vickers hardness tester under a load of 100 g with a dwell time of 10 s applied to a diamond indenter.

Results and Discussion

An example of the fabricated hybrid structure is shown in Fig. 2. During deposition, a uniform wall was formed without visible surface cracks. The height of the built structures reached 7 mm for processing
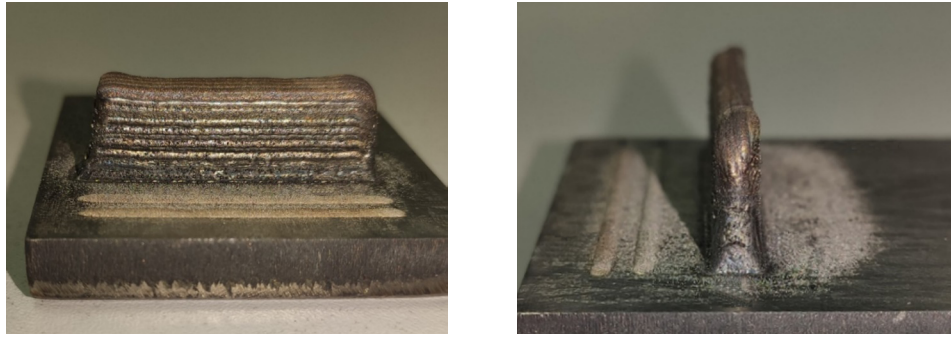
Fig. 2. Example of a fabricated specimen

modes 1 and 3, and 5 mm for mode 2. For microstructural analysis, the bimetallic specimen was sectioned along a plane perpendicular to the direction of layer growth.

The homogeneous layers produced from chromium-nickel steel or nickel-based alloy powder exhibit a characteristic dendritic microstructure with the formation of both equiaxed and columnar dendrites. At the interfaces between successive layers and near the boundaries of the deposited structure, where heat dissipation was more intense, columnar dendrites predominate. These dendrites are typically characterized by the presence of secondary arms (Fig. 3). At the edges of the deposited structures, regardless of the processing mode, spherical particles with diameters ranging from 25 to 40 µm were observed (Figs. 4, *a*, *b*). These are unmelted or partially melted particles of the original powder, which is a characteristic feature of the direct laser deposition (*DLD*) process [17, 18]. In addition, the formation of cracks was noted both at the interface between dissimilar materials (Fig. 4, *c*, *d*) and at the fusion boundaries between similar materials. This phenomenon is attributed to thermal stresses that arise during the formation of dissimilar gradient materials.
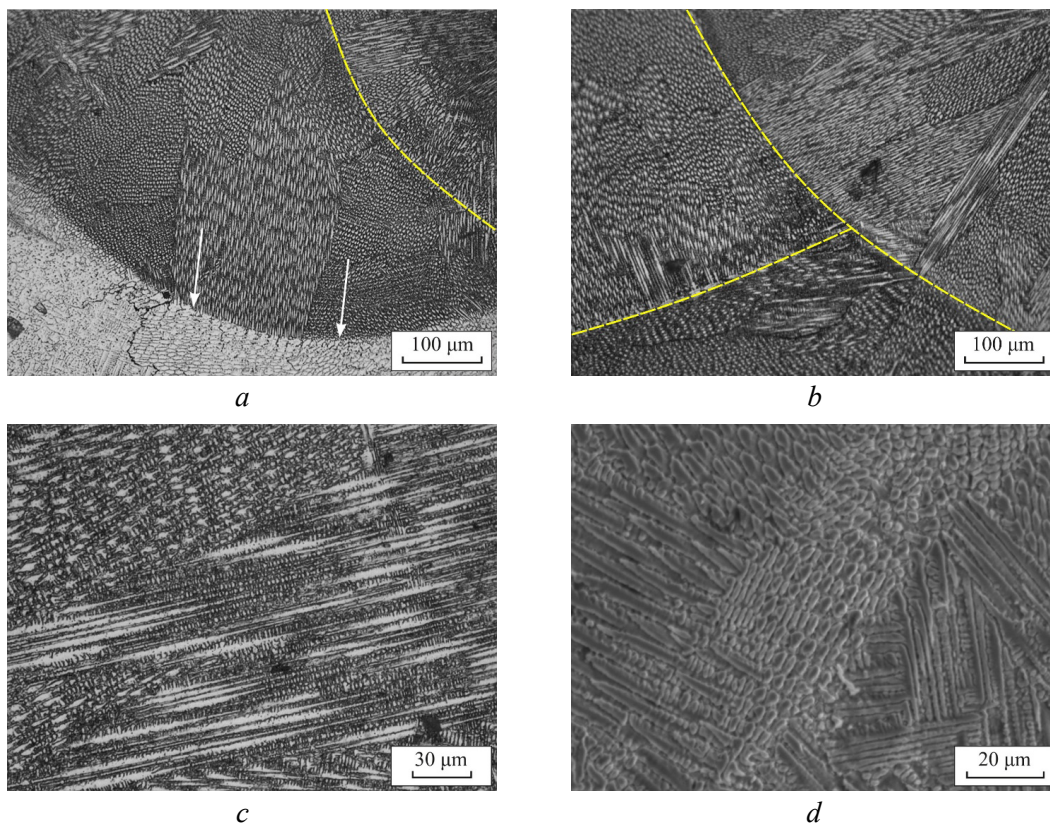

a

b

c

d

Fig. 3. Location of elongated dendrites:

a – transition layers boundary; *b* – dissimilar material interface; *c* – layer edge; *d* – secondary arms in elongated dendrites
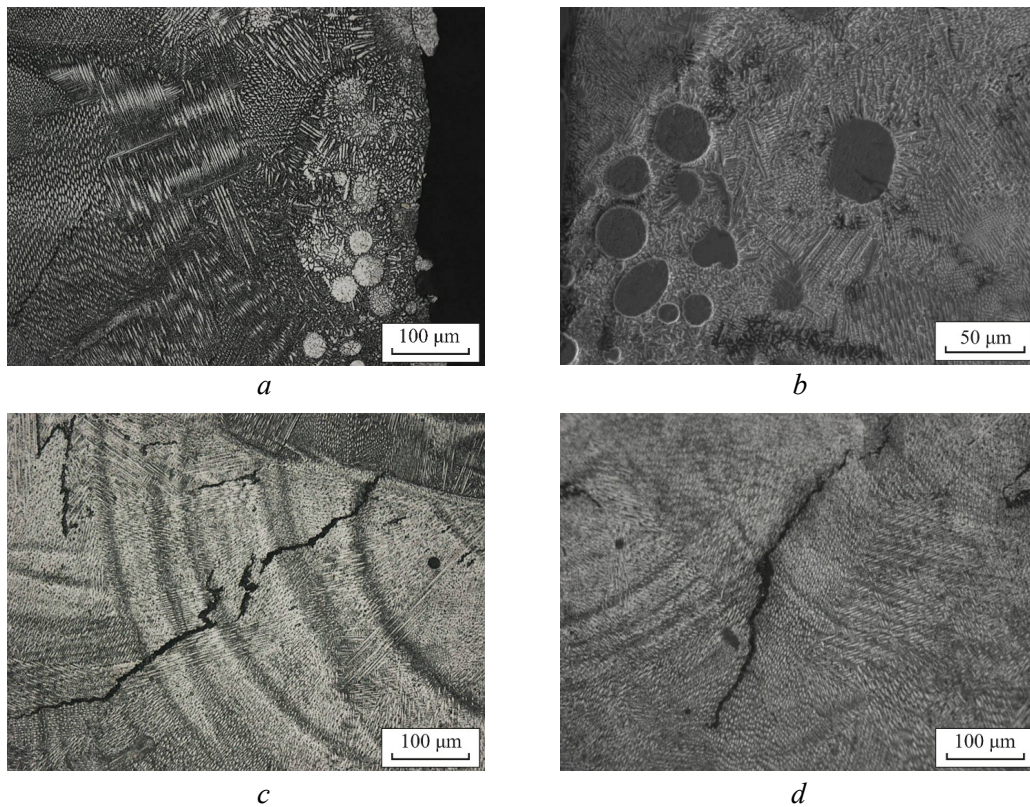
Fig. 4. Defects in fabricated materials: unmelted particles at layer boundaries in mode **1** (*a*)
and mode **2** (*b*); thermal cracks at the dissimilar material interface (*c*) and within the
homogeneous material (*d*)

The sequential deposition of four layers during material transitions resulted in the formation of smooth gradients between dissimilar materials. At the same time, a visible interface and mixing zones were observed for both material combinations (Figs. 5–7). The appearance of these zones may be attributed to the high melting rate, which can lead to the formation of an unstable melt pool [17, 19, 20]. Such zones were observed under all deposition modes; however, it was noted that with decreasing laser power, both the number and width of these regions were reduced.

In the case of *Inconel 625* deposited onto *316L* steel, the mixing zones exhibited sharper boundaries (Fig. 8, *a*) compared to those formed during deposition of austenitic steel onto the nickel-based alloy (Fig. 8, *b*).

Fig. 5.Cross-section of specimenfabricated using mode **1**:
a – general view; *b* – *Inconel 625 – 316L* stainless steel interface; *c* – mixing zones of nickel alloy and
steel; *d* – *316L* stainless steel – *Inconel 625* interface with mixing zone; *e* – clear interface region

Fig. 6. Cross-section of specimen fabricated using mode **2**:

a – general view; *b* – *Inconel 625* – *316L* stainless steel interface; *c* – mixing zones of nickel alloy and steel; *d* – *316L* stainless steel – *Inconel 625* interface; *e* – mixing zones of steel and nickel alloy
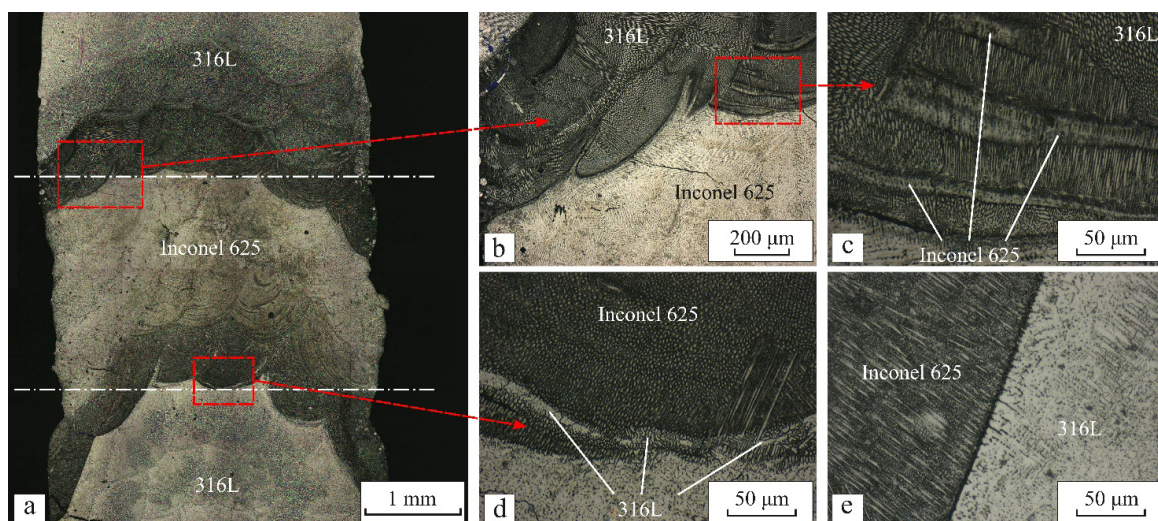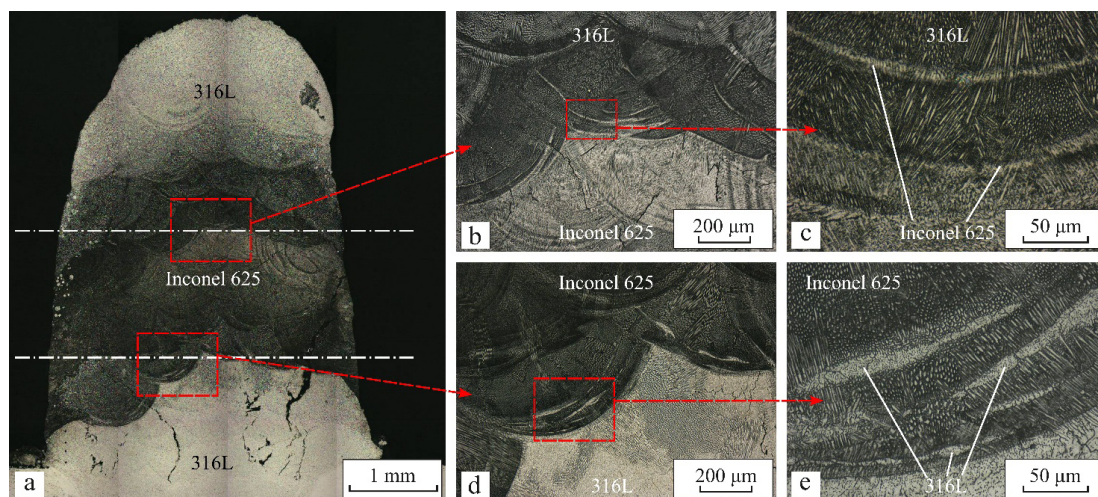

Fig. 7. Cross-section of specimen fabricated using mode **3**:

a – general view; *b* – *Inconel 625* – *316L* stainless steel interface; *c* – mixing zones of nickel alloy and steel; *d* – *316L* stainless steel – *Inconel 625* interface; *e* – mixing zones of steel and nickel alloy
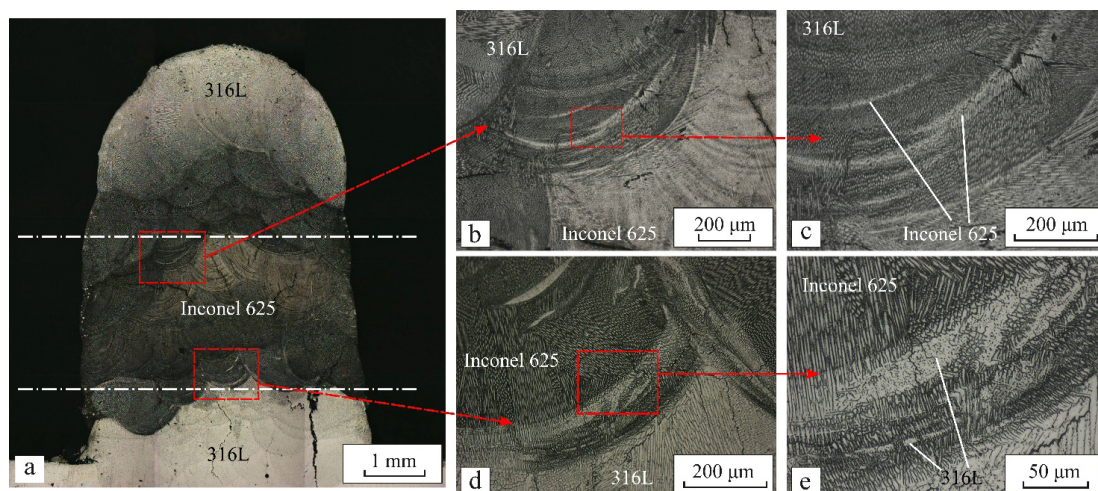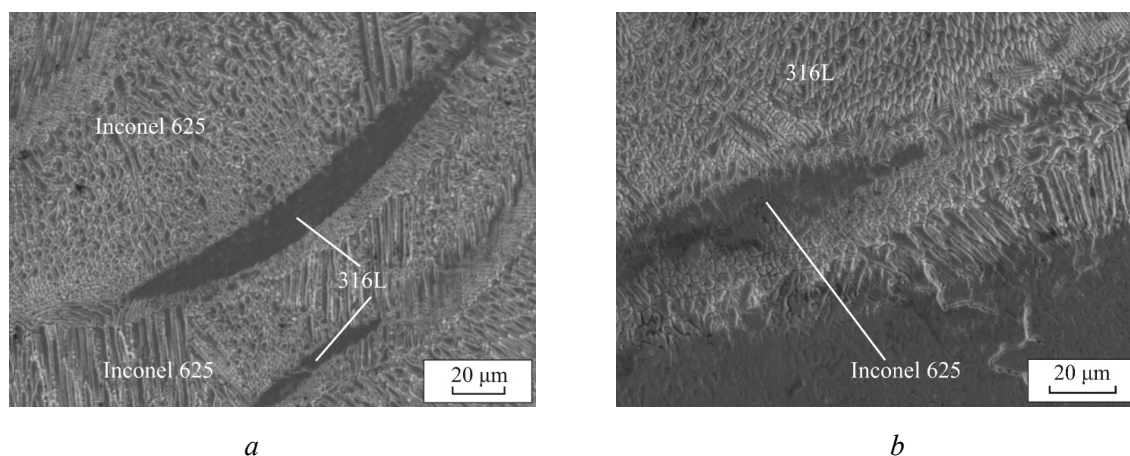

a

b

Fig. 8. Microstructure of mixed regions:

a – *Inconel 625* deposited on steel; *b* – *316L* stainless steel deposited on *Inconel 625*

Fig. 9 shows the distribution of chemical elements along a line positioned perpendicular to the transition zone in the case of nickel alloy deposition onto steel. In all cases, a wide transition zone is observed. As can be seen, under processing mode **1** (1,000 W, 35 mm/s), the concentrations of iron and nickel equilibrate within 50 μm from the visible fusion boundary between the dissimilar materials, already within the first deposited layer (Fig. 9, *a*). Under mode **2** (1,250 W, 25 mm/s), the concentrations of nickel and iron begin to equalize at a distance of 500–600 μm from the visible fusion line (Fig. 9, *b*). This region corresponds approximately to the boundary of the second deposited layer of the nickel alloy. In contrast, under mode **3** (1,500 W, 15 mm/s), the concentration equalization occurs significantly beyond the second nickel alloy layer and corresponds to a distance of 800–900 μm from the visible fusion boundary between the dissimilar materials (Fig. 9, *c*). In these transition regions, the nickel concentration is lower than that of the original nickel alloy and ranges between 35–45 wt. %. Below the visible fusion boundary, the steel regions retain their original composition, with a slightly elevated nickel content of up to 11 wt. %.
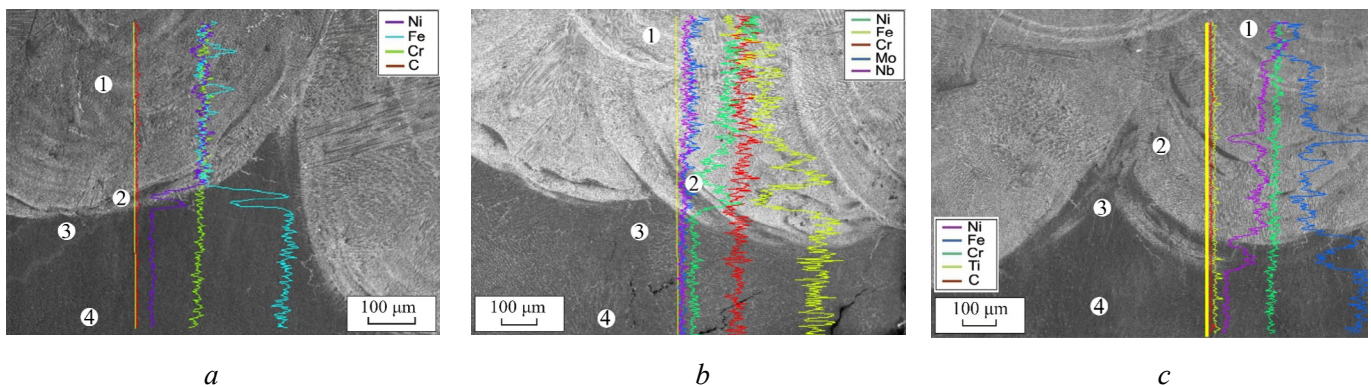

a *b* *c*

Fig. 9. Energy-dispersive X-ray spectroscopy (*EDS*) analysis results for the *316L* stainless steel –
Inconel 625 joint:
a – mode **1**; *b* – mode **2**; *c* – mode **3**

According to quantitative energy-dispersive X-ray spectroscopy (*EDS*) analysis, the zones of mechanical mixing of steel into the nickel alloy are characterized by reduced iron content and increased nickel content (Table 3). An increase in both distance from the fusion boundary and laser power promotes higher nickel content in these regions.

During the deposition of steel onto the nickel-based alloy, a wide transition zone and numerous regions of mechanical mixing were also observed (Fig. 10). The visible fusion boundary between the nickel alloy and steel is well-defined under the first two processing modes. Under mode **1** (1,000 W, 35 mm/s), the concentrations of iron and nickel begin to equilibrate within the first deposited layer of the nickel alloy at a distance of 300–400 μm from the visible fusion line, with the iron concentration starting to gradually increase within 50–100 μm beyond that point. Under mode **2** (1,250 W, 25 mm/s), the equalization of iron and nickel concentrations occurs at a distance of 600–700 μm from the visible fusion boundary between the dissimilar materials, corresponding to the level of the second deposited steel layer. Under mode **3** (1,500 W, 15 mm/s), the visible interface between the nickel alloy and steel becomes more diffuse, and the iron concentration exceeds that of nickel at the boundary of the second deposited steel layer, similarly to mode **2**. In this region, the iron concentration within the second deposited steel layer is in the range of 40–45 wt. %.

In the regions of the nickel alloy located below the visible fusion boundary, the chemical composition under mode **1** corresponds to that of the original alloy. However, for modes **2** and **3**, an elevated iron content and a slightly reduced nickel content were observed – 9 wt. % and 52 wt. %, respectively. The composition of the mechanical mixing zones, where nickel alloy is incorporated into the steel matrix, is characterized by an increased iron content and a correspondingly reduced nickel content compared to the original *Inconel 625* alloy (Table 4).

The varying ratio of chromium and nickel equivalents indicates the formation of zones with different phase compositions. According to established models of phase formation during welding of dissimilar

T a b l e 3

Chemical composition of mixing zones in the transition region when depositing *Inconel 625* on *316L* stainless steel

| Point	Chemical element, wt.%							
	Fe	*Ni*	*Cr*	*Ti*	*Mo*	*Nb*	*Si*	*Mn*
Mode **1**								
1	35.04	35.15	20.12	0.4	5.27	2.22	0.87	0.94
2	62.4	15.55	19.45	0.77	–	–	1.13	0.7
3	67.69	10.73	18.86	0.9	0.27	–	1.11	0.44
4	67.35	11.16	18.82	1.03	–	–	1.03	0.61
Mode **2**								
1	22.32	45.51	21.1	0.24	6.45	2.9	0.75	0.74
2	58.92	17.91	19.23	0.55	1.36	0.5	0.86	0.66
3	68.4	9.9	18.88	0.58	0.29	0.25	0.92	0.79
4	68.13	10.41	18.79	0.42	0.4	–	1.05	0.8
Mode **3**								
1	22.32	44.94	20.91	0.27	7.36	3.11	0.73	0.31
2	49.3	25.42	18.98	0.58	3.22	1.31	0.67	0.52
3	67.26	11.66	18.28	0.73	0.53	–	0.92	0.61
4	68.51	10.24	18.33	0.58	0.55	0.31	0.97	0.55
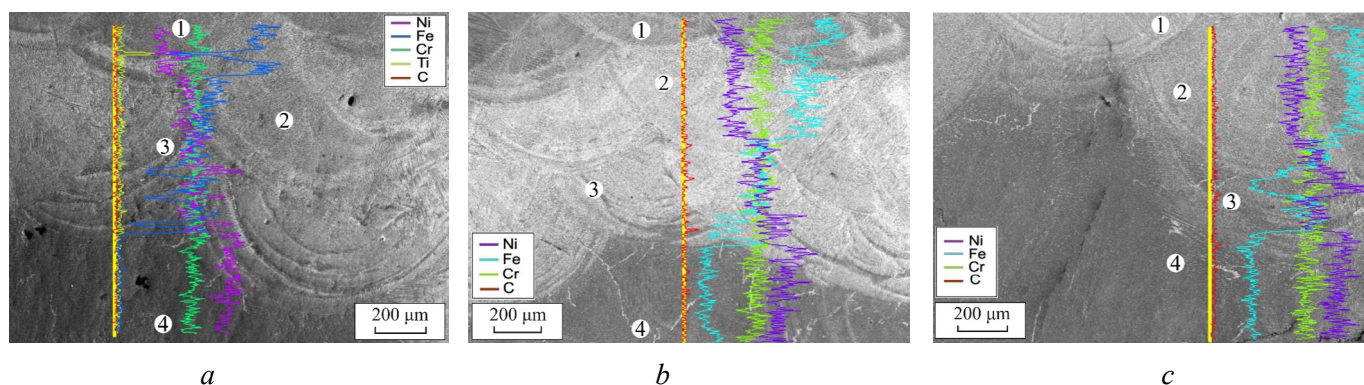
Fig. 10. Energy-dispersive X-ray spectroscopy (*EDS*) analysis results for the *Inconel 625 – 316L* stainless steel joint:

a– mode **1**; *b* – mode **2**; *c* – mode **3**

steels [21, 22], in the case of *Inconel 625* being deposited onto *316L* steel, the transition zone, where iron-based alloys form based on chemical composition, undergoes sequential solidification modes: *FA* (δ-*Fe* + γ-*Fe*), *AF* (γ-*Fe* + δ-*Fe*), and *A* (γ-*Fe*) (Fig. 11, regions **1**–**3**). Although nickel atoms have higher mobility in iron, the melting point of *316L* steel is slightly higher than that of the nickel alloy, resulting in a relatively narrow transition zone. At the same time, nickel diffusion is sufficiently intense, leading to changes in the chromium-to-nickel equivalent ratios in these areas. The formation of ferrite in the transition layers of the «steel – nickel alloy» system was confirmed by X-ray diffraction analysis (Fig. 12) and scanning electron microscopy (Fig. 13).

In regions **4**–**7** (Fig. 11), nickel-based alloys are formed. Regions **5** and **6** correspond to the original *Inconel 625* composition, while regions **4** and **7** are characterized by a reduced nickel content compared to the base alloy.

During deposition of steel onto the nickel alloy, the higher processing temperature leads to the formation of a wider transition zone. However, the nickel content in this zone remains relatively high, which ultimately

Table 4

Chemical composition of mixing zones in the transition region when depositing *316L* stainless steel on *Inconel 625*

| Point	Chemical element, wt.%								
	Fe	*Ni*	*Cr*	*Ti*	*Mo*	*Nb*	*Si*	*Mn*	*S*
Mode **1**									
1	51.74	23.78	20.09	0.54	1.44	0.79	0.78	0.54	0.31
2	47.39	26.05	19.71	0.51	3.36	1.43	0.85	0.7	–
3	19.11	46.48	21.12	0.17	7.88	3.64	1.02	0.6	–
4	0.7	61.09	22.37	–	10.26	4.44	0.74	0.34	–
Mode **2**									
1	55.01	20.76	19.36	0.61	2.07	1.06	0.8	0.32	–
2	45.64	27.86	20.07	0.47	3.2	1.35	0.93	0.48	–
3	22.81	44.47	21.05	0.29	6.66	3.5	0.76	0.47	–
4	7.79	55.57	22.15	–	9.54	3.82	0.83	0.3	–
Mode **3**									
1	43.8	29.34	20.31	0.5	2.81	1.35	0.82	0.51	–
2	38.89	31.86	20.1	0.42	4.76	2.35	0.96	0.67	–
3	14.44	50.49	21.76	0.17	7.34	3.65	0.95	0.66	0.53
4	8.57	55.79	21.17	0.11	9.14	3.83	0.84	0.56	–
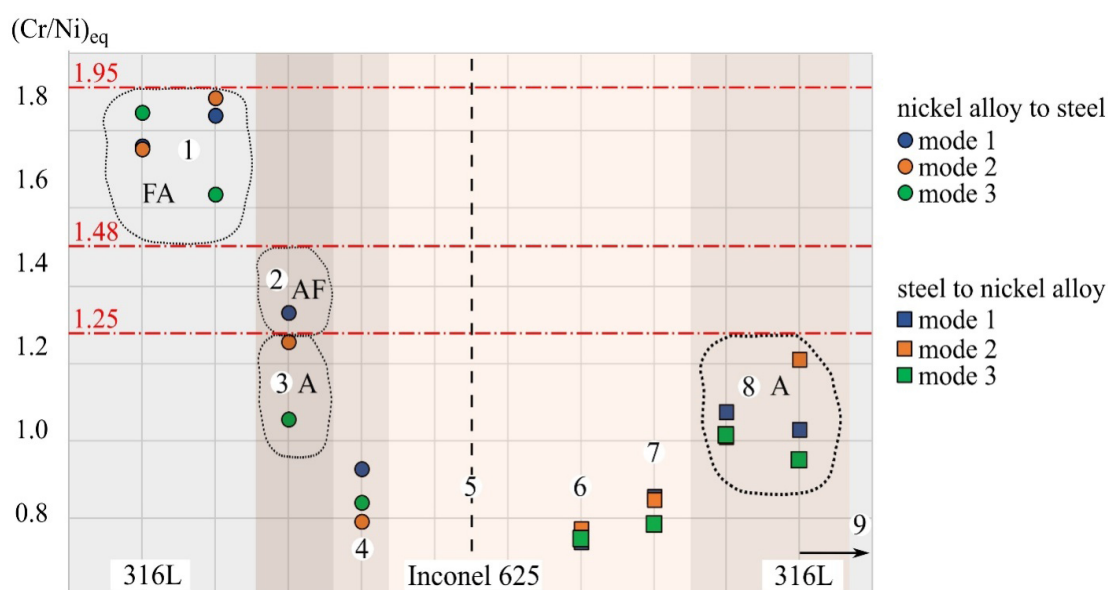
Fig. 11. Chromium and nickel equivalent ratios in different regions of the combined material. Solidification modes: *AF*, *FA* (austenite-ferrite); *A* (austenite)

results in the *A*-mode solidification regime (Fig. 11, region **8**). Region **9** corresponds to the chemical composition of the original *316L* stainless steel.

A sharp change in microhardness levels is observed across the gradient transition from steel to the nickel alloy (Fig. 14), which is typical for dissimilar material systems. At the same time, the differences in microhardness values between materials produced under different processing modes are relatively minor. It is worth noting that near the fusion boundary, the microhardness of *316L* steel deposited onto the nickel alloy is slightly higher than that of the steel layers onto which the nickel alloy was deposited. The average
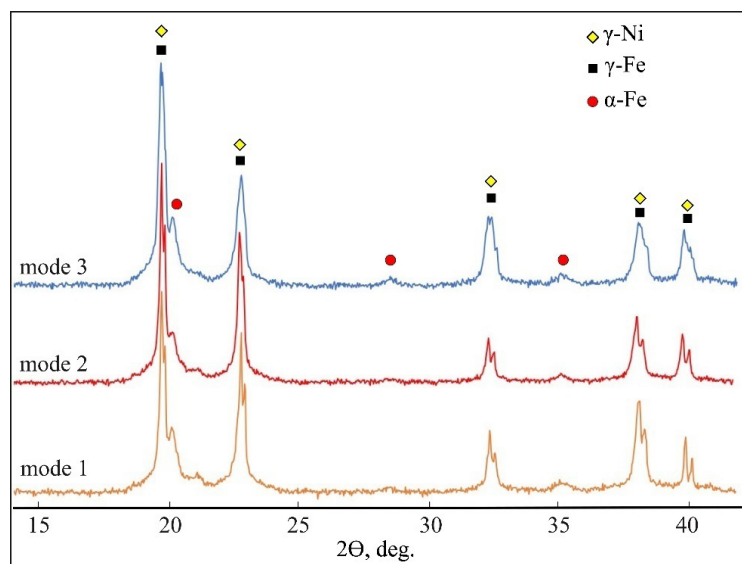
Fig. 12. X-Ray diffraction (*XRD*) patterns of heterogeneous compositions fabricatedusing different deposition modes
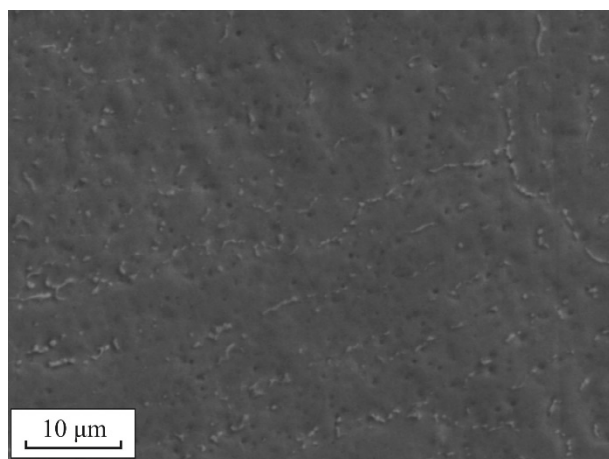

Fig. 13. Ferrite formed in the transition region during deposition of nickel alloy on steel
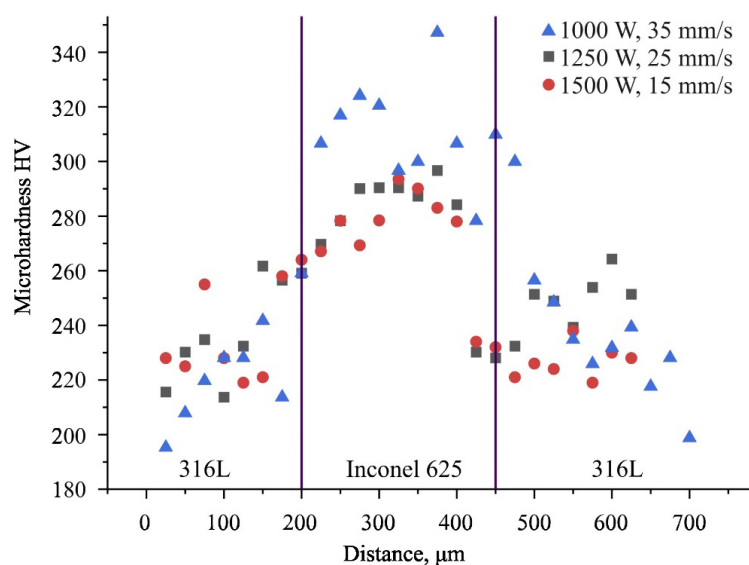

Fig. 14. Results of microhardness testing of the combined materials

microhardness for the steel regions in both cases is approximately 230 ± 15 HV, while for *Inconel 625* it is around 298 ± 20 HV.

Under the second and third processing modes, a slight decrease in the microhardness of the nickel alloy was observed, which can be attributed to higher heat input compared to mode **1**. These results are in good agreement with previously published data, regardless of the specific deposition method used [10, 11, 19].

Conclusoin

This study analyzed the structural features of gradient «*316L* steel – *Inconel 625* – *316L* steel» compositions fabricated *via* direct laser deposition. Results revealed that, during layer-by-layer fabrication of gradient structures comprising 12 layers, a maximum build height (up to 7 mm) was achieved under two distinct processing conditions: 1,000 W with a scanning speed of 35 mm/s, and 1,500 W with a scanning speed of 15 mm/s. Specifically, the former condition (1,000 W, 35 mm/s) resulted in minimal material mixing at the fusion boundary. All compositions exhibited a low density of defects, primarily in the form of unmelted powder particles located at the edges of the deposited structures. Cracking was most prevalent in the initial steel layers when employing higher laser power processing modes.

The chromium-to-nickel equivalent ratio correlated with the formation of mixing zones exhibiting distinct solidification modes and phase compositions. Specifically, deposition of *Inconel 625* onto *316L* steel resulted in a transition zone, characteristic of iron-based alloy compositions, exhibiting successive solidification modes: *FA* (ferrite–austenite), *AF* (austenite–ferrite), and *A* (austenite). Conversely, deposition of *316L* steel onto *Inconel 625* yielded a transition zone with exclusively austenite solidification. These phase identification results were confirmed by X-ray diffraction analysis. Scanning electron microscopy further confirmed the presence of ferrite in the interdendritic regions on the steel side.

Microhardness testing revealed minimal impact of deposition parameters on the average hardness of the materials. The microhardness of *316L* steel was consistently measured at 230 ± 15 HV, while that of *Inconel 625* averaged 298 ± 20 HV.

References

1. Zhang Y., Hu M., Cai Z., Han C., Li X., Huo X., Fan M., Rui S., Li K., Pan J. Effect of nickel-based filler metal types on creep properties of dissimilar metal welds between Inconel 617B and 10 % Cr martensitic steel. *Journal of Materials Research and Technology*, 2021, vol. 14, pp. 2289–2301. DOI: 10.1016/j.jmrt.2021.07.131.

2. Meng W., Zhang W., Zhang W., Yin X., Cui B. Fabrication of steel-Inconel functionally graded materials by laser melting deposition integrating with laser synchronous preheating. *Optics & Laser Technology*, 2020, vol. 131, p. 106451. DOI: 10.1016/j.optlastec.2020.106451.

3. Naffakh H., Shamanian M., Ashrafizadeh F. Dissimilar welding of AISI 310 austenitic stainless steel to nickel-based alloy Inconel 657. *Journal of Materials Processing Technology*, 2009, vol. 209 (7), pp. 3628–3639. DOI: 10.1016/j.jmatprotec.2008.08.019.

4. Reed R.C. *The superalloys: fundamentals and applications*. Cambridge, Cambridge university press, 2008. 363 p. ISBN 9780511541285. DOI: 10.1017/CBO9780511541285.

5. Knorovsky G.A., Cieslak M.J., Headley T.J., Romig A.D., Hammetter W.F. Inconel 718: A solidification diagram. *Metallurgical Transactions A*, 1989, vol. 20 (10), pp. 2149–2158. DOI: 10.1007/BF02650300.

6. Xie H., Yang K., Li F., Sun C., Yu Z. Investigation on the Laves phase formation during laser cladding of IN718 alloy by CA-FE. *Journal of Manufacturing Processes*, 2020, vol. 52, pp. 132–144. DOI: 10.1016/j.jmapro.2020.01.050.

7. Yang J., Zheng Q., Zhang H., Sun X., Guan H., Hu Z. Effects of heat treatments on the microstructure of IN792 alloy. *Materials Science and Engineering: A*, 2010, vol. 527 (4–5), pp. 1016–1021. DOI: 10.1016/j.msea.2009.10.026.

8. Rashkovets M.V. *Struktura i svoistva nikelevykh splavov, poluchennykh po additivnoi tekhnologii s ispol'zovaniem metoda pryamogo lazernogo vyrashchivaniya*. Diss. kand. tekhn. nauk [Structure and properties of nickel alloys obtained by additive technology using the direct laser deposition method. PhD, eng. sc. diss.]. Novosibirsk, 2022. 164 p.

9. Deshpande A. Additive manufacturing of nickel alloys. *Springer handbook of additive manufacturing*. Cham, Springer, 2023, pp. 655–669. ISBN 978-3-031-20751-8. DOI: 10.1007/978-3-031-20752-5_39.

10. Ahsan Md. R.U., Fan X., Seo G.-J., Ji C., Noakes M., Nycz A., Liaw P.K., Kim D.B. Microstructures and mechanical behavior of the bimetallic additively-manufactured structure (BAMS) of austenitic stainless steel and Inconel 625. *Journal of Materials Science & Technology*, 2021, vol. 74, pp. 176–188. DOI: 10.1016/j.jmst.2020.10.001.

11. Carroll B.E., Otis R.A., Borgonia J.P., Suh J., Dillon R.P., Shapiro A.A., Hofmann D.C., Liu Z.-K., Beese A.M. Functionally graded material of 304L stainless steel and Inconel 625 fabricated by directed energy deposition: Characterization and thermodynamic modeling. *Acta Materialia*, 2016, vol. 108, pp. 46–54. DOI: 10.1016/j.actamat.2016.02.019.

12. Li P., Gong Y., Xu Y., Qi Y., Sun Y., Zhang H. Inconel-steel functionally bimetal materials by hybrid directed energy deposition and thermal milling: Microstructure and mechanical properties. *Archives of Civil and Mechanical Engineering*, 2019, vol. 19 (3), pp. 820–831. DOI: 10.1016/j.acme.2019.03.002.

13. Tyagi S., Balla S.K., Manjaiah M., Aranas C. Microstructure and mechanical properties of stainless steel 316L-Inconel 625 bimetallic structure fabricated by laser wire direct energy deposition. *Journal of Materials Research and Technology*, 2024, vol. 33, pp. 8361–8371. DOI: 10.1016/j.jmrt.2024.11.130.

14. Ghanavati R., Naffakh-Moosavy H., Moradi M., Mazzucato F., Valente A., Bagherifard S., Saboori A. Design optimization for defect-free AISI 316 L/IN718 functionally graded materials produced by laser additive manufacturing. *Materials Characterization*, 2025, vol. 220, p. 114697. DOI: 10.1016/j.matchar.2024.114697.

15. Li Y., Koukolíková M., Džugan J., Brázda M. High temperature fracture behavior of 316L stainless steel-Inconel 718 functionally graded materials manufactured by directed energy deposition: Role of interface orientation and heat treatment. *Materials Science and Engineering: A*, 2024, vol. 898, p. 146389. DOI: 10.1016/j.msea.2024.146389.

16. Dolgova S.V., Malikov A.G., Golyshev A.A., Nikulina A.A. The effect of laser surfacing modes on the geometrical characteristics of the single laser tracks. *Obrabotka metallov (tekhnologiya, oborudovanie, instrumenty) = Metal Working and Material Science*, 2024, vol. 26, no. 2, pp. 57–70. DOI: 10.17212/1994-6309-2024-26.2-57-70.

17. Chen N., Khan H.A., Wan Z., Lippert J., Sun H., Shang S.-L., Liu Z.-K., Li J. Microstructural characteristics and crack formation in additively manufactured bimetal material of 316L stainless steel and Inconel 625. *Additive Manufacturing*, 2020, vol. 32, p. 101037. DOI: 10.1016/j.addma.2020.101037.

18. Everton S.K., Hirsch M., Stravroulakis P., Leach R.K., Clare A.T. Review of in-situ process monitoring and in-situ metrology for metal additive manufacturing. *Materials & Design*, 2016, vol. 95, pp. 431–445. DOI: 10.1016/j.matdes.2016.01.099.

19. Mei X., Wang X., Peng Y., Gu H., Zhong G., Yang S. Interfacial characterization and mechanical properties of 316L stainless steel/Inconel 718 manufactured by selective laser melting. *Material Science and Engineering: A*, 2019, vol. 758, pp. 185–191. DOI: 10.1016/j.msea.2019.05.011.

20. Villaret F., Boulnat X., Aubry P., Yano Y., Ohtsuka S., Fabrègue D., De Carlan Y. Laser Beam Direct Energy Deposition of graded austenitic-to-martensitic steel junctions compared to dissimilar Electron Beam welding. *Materials Science and Engineering: A*, 2021, vol. 824, p. 141794. DOI: 10.1016/j.msea.2021.141794.

21. Astafurov S., Astafurova E. Phase composition of austenitic stainless steels in additive manufacturing: A review. *Metals*, 2021, vol. 11 (7), p. 1052. DOI: 10.3390/met11071052.

22. Pouranvari M., Khorramifar M., Marashi S.P.H. Ferritic–austenitic stainless steels dissimilar resistance spot welds: metallurgical and failure characteristics. *Science and Technology of Welding and Joining*, 2016, vol. 21 (6), pp. 438–445. DOI: 10.1080/13621718.2015.1124491.

Conflicts of Interest

The authors declare no conflict of interest.

Obrabotka metallov –
Metal Working and Material Science

The influence of tungsten carbide particle size on the characteristics of metalloceramic WC/Fe-Ni-Al coatings

Alexander Burkov [a], Maxim Dvornik [b], Maria Kulik [c, *], Alexandra Bytsura [d]

Khabarovsk Federal Research Center FEB RAS, 153 Tihookeanskaya st., Khabarovsk, 680042, Russian Federation

[a] https://orcid.org/0000-0002-5636-4669, ✉ burkovalex@mail.ru; [b] https://orcid.org/0000-0002-1216-4438, ✉ maxxxx80@mail.ru;
[c] https://orcid.org/0000-0002-4857-1887, ✉ marijka80@mail.ru; [d] https://orcid.org/0009-0005-4750-7970, ✉ alex_btsr@mail.ru

ARTICLE INFO

ABSTRACT

Introduction. The granulometry (particle size distribution) of the starting powders significantly influences the hardness and strength of compacted tungsten carbide (*WC*) metalloceramic materials, but this effect has not been extensively studied in the context of *WC/Fe-Ni-Al* coatings. **The purpose of this work** is to investigate the influence of the granulometry of the starting *WC* powder introduced into the non-localized electrode on the kinetics of mass transfer, chemical composition, cross-sectional microstructure of *WC/Fe-Ni-Al* coatings, and their corrosion and tribological properties. **Methods.** *WC/Fe-Ni-Al* coatings were deposited on 45 steel substrates using the electrospark deposition (*ESD*) method with a non-localized electrode. The electrode comprised iron granules (Ø = 4 mm), *Ni* and *Al* powders, and *WC* powders with varying particle sizes. X-ray diffraction (*XRD*) analysis revealed that the coatings consisted of tungsten carbide, tungsten semicarbide (*W₂C*), intermetallic phases (*Al₈₆Fe₁₄*), ferronickel (*FeNi*), and body-centered cubic (*BCC*) phases (*AlNi, AlFe*). **Results and discussion.** It was determined that, with an increase in the *WC* powder particle size fraction in the electrode, the coating matrix composition became enriched with aluminum, while the iron concentration decreased from 60 to 30 at.%. The lowest values for hardness, wear resistance, and oxidation resistance were observed for the sample obtained using *WC* nanopowder. The microhardness of the coating surface ranged from 4.39 to 9.16 GPa. The oxidation resistance of the coated samples at 700 °C increased monotonically with increasing *WC* powder particle size. The study found that the use of *WC* powder with a particle size fraction of 20 to 40 μm resulted in the best performance in terms of hardness, wear resistance, and oxidation resistance of the *WC/Fe-Ni-Al* coatings at 700 °C. The application of these coatings increased the oxidation resistance of 45 steel by 11.6 times and wear resistance by 44 to 80 times, suggesting their potential for use in high-intensity applications.

Introduction

Recently, *NiAl* coatings have attracted attention due to their excellent resistance to high-temperature oxidation [1, 2]. The application of *NiAl* coatings in high-temperature environments has gained wide attention due to their ability to form a dense and stable Al_2O_3 scale [1]. It is known that the hardness, wear resistance, and compressive yield strength of *NiAl*-based alloys increase with an increase in iron content up to 20 at.% [3]. In the study [4], $Fe_{75}Ni_{15}Al_{10}$ and $Fe_{56}Ni_{14}Al_{30}$ coatings were obtained on the surface of low-carbon steel using the method of gas flame spraying of a mixture of iron, nickel, and aluminum powders. It has been shown that increasing the concentration of aluminum in *Fe-Ni-Al* coatings improves their oxidation resistance.

---
* Corresponding author
Kulik Maria A., Junior Researcher
Khabarovsk Federal Research Center FEB RAS,
153 Tihookeanskaya st.,
680042, Khabarovsk, Russian Federation
Tel.: +7 4212 22-69-56, **e-mail:** marijka80@mail.ru

At the same time, a cursory literature analysis shows that the wear resistance of *Fe-Ni-Al* composites is still significantly inferior to that of metalloceramic composites (*MMCs*). Therefore, reinforcing *Fe-Ni-Al* compositions with ceramic powder particles presents a promising strategy to significantly increase their hardness and wear resistance while maintaining high oxidation resistance.

Tungsten carbide (*WC*) is often considered as a reinforcing component of *MMCs* due to its high hardness and good wettability with metal melts [5–7]. The *Fe-Ni-Al* composition exhibits exceptionally high oxidation resistance but relatively poor wear resistance, while hard tungsten carbide is easily oxidized at high temperatures. Therefore, reinforcing the *Fe-Ni-Al* matrix with tungsten carbide allows for the creation of a *WC/Fe-Ni-Al* composite coating that combines high oxidation resistance and wear resistance.

According to a literature analysis, metalloceramic *WC/Fe-Ni-Al* coatings have previously been applied using techniques such as flame spraying [8], plasma-arc powder spraying [9], and electrospark deposition (*ESD*) [10]. Electrospark deposition (*ESD*) is a surface hardening technology that uses low-voltage, high-current electrical discharges to melt and transfer material from the working electrode to the substrate surface, significantly increasing the surface hardness and wear resistance. *ESD* technology offers notable advantages such as process simplicity, low cost, low residual stresses, and minimal substrate deformation, making it a highly effective method for producing coatings on metals and alloys [11]. The high temperature generated during the spark discharge process melts the electrode material, resulting in a uniform and dense coating, and the metallurgical bond ensures high adhesion of the coating to the substrate. The *ESD* method is employed in various applications: to improve the physical and chemical properties of metallic materials by applying refractory metals and their compounds; to expand the scope of application of composite materials by creating wear-resistant and oxidation-resistant layers on their surface; and to alter the chemical and phase composition of the surface in a controlled manner by processing in the presence of a reactive gas (e.g., nitriding of a titanium alloy) [12].

The use of a non-localized electrode (*NE*) for *ESD* facilitates the automation of the coating application process, including on curved parts, and enables the use of powders as the primary coating constituent [13]. In a previous study, *WC/Fe-Ni-Al* coatings with a high ceramic content were produced by the *ESDNE* method using a NE consisting of nickel and aluminum granules, and α*WC* powder with an average particle size of 1 μm [10]. In the field of compact *WC-Co* metalloceramic materials, the particle size of tungsten carbide has a significant effect on the hardness and strength of sintered products [14, 15]. However, the influence of the *WC* powder particle size on the properties of metalloceramic coatings has not been systematically investigated.

Aim of the study is to investigate the influence of the particle size distribution (granulometry) of the initial *WC* powder introduced into the non-localized electrode on the kinetics of mass transfer, chemical composition, cross-sectional structure of *WC/Fe-Ni-Al* coatings, and their corrosion and tribological properties.

To achieve the stated aim, the following ***tasks*** were accomplished:

– preparation of various tungsten carbide powder fractions via grinding in a planetary ball mill and sieve analysis;

– investigation of the influence of the particle size distribution of the initial tungsten carbide powder used in a non-localized electrode on mass transfer, composition, and structure of the coating;

– establishment of the relationship between the coating's structure and its properties: roughness, wettability, hardness, wear resistance, and oxidation resistance.

Methods

The working electrode for the *ESD* was a non-localized electrode consisting of iron granules and *Ni*, *Al* and *WC* powders (Table 1). Iron granules were obtained by cutting welding wire (*SV-08AA*) with a diameter of 4±0.1 mm into cylinders with a length of 4±0.5 mm. The tungsten carbide powder fractions ranged from 80 nm to 40 μm. The most dispersed fraction was nanostructured *WC* powder (99.95%) with an average particle diameter by volume ***D*** [4.3] of 0.8 μm, produced by *Hongwu* (China) (Fig. 1, *a, b*).

Composition of non-localized electrode and coating designations

Designation of coatings	Proportion of granules, vol.%	Proportion of Al powder, vol.%	Proportion of Ni powder, vol.%	Proportion of WC powder, vol.%	WC powder fraction, μm
WCn					$0.08 \leq WC \leq 0.1$
WC20	93.80	2.05	1.35	2.80	$1 \leq WC \leq 20$
WC40					$20 \leq WC \leq 40$

Fig. 1. SEM image of *WCn* fraction powder particles (a) and the results of its *BET* analysis (b);
integral distribution of *Ni, Al, WC20, WC40* powders (c) and X-ray diffraction patterns
of *WC* powders (d)

To prepare larger fractions, *WC* powder (*TU 6-09-03-360-78*) with particle size of $1 \leq WC \leq 40$ μm was used, which was separated through 40 μm and 20 μm s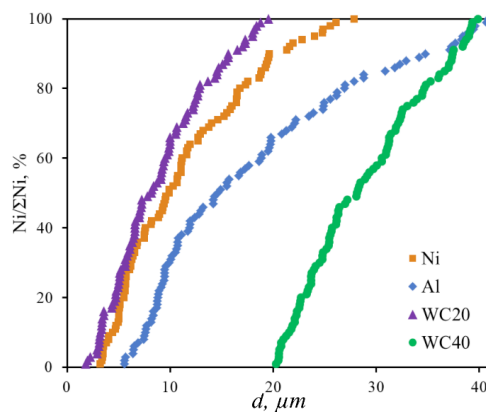ieves using a vibrating table. The particle diameter of the powders was measured using the arbitrary secant method according to *ASTM E112-12*. The average particle size of aluminum and nickel powders was 18.0±10.3 μm and 11.3±6.4 μm, respectively (Fig. 1, *c*). X-ray diffraction (*XRD*) patterns revealed that as the *WC* particle diameter decreased, a monotonic decrease in reflection intensity and an increase in reflection width were observed, consistent with the *Scherrer* equation (Fig. 1, *g*).

The substrate (cathode), made of grade 45 steel in the form of a cylinder (d = 12 mm and h = 10 mm), was immersed in a mixture of granules and powders with the end surface facing down. Thus, the coating was formed on the end and side surfaces of the substrate, with a total covered area of 2.88 cm^2. An *IMES-40* generator was used as a source of current pulses. The device settings were as follows: pulse duration – 100×10^{-6} s, frequency – 10^3 Hz, pulse current amplitude – 170 A at an open circuit voltage of 25 V.

The coatings were applied in an argon flow at a rate of 0.3 m^3/hour to protect the electrodes from oxidation. The total coating time for one sample was 10 minutes. A more detailed description of the laboratory setup for automatic coating application using the *ESDNE* method with powders is given in the study [16].

The weight gain of the substrate was measured on a laboratory scale (*Vibra HT120*) (10^{-4} g) every 120 s of *ESDNE* treatment. The phase composition of powders and prepared samples was studied by X-ray diffraction. For this purpose, a multifunctional X-ray diffractometer *DRON-7* (*NPP Burevestnik*, Russia) with *Cu-Kα* radiation (λ = 1.54056 Å) was used in this work. For metallographic examination of the microstructure and chemical microanalysis of samples with coatings, a scanning electron microscope *Vega 3 LMH* (*Tescan*, Czech Republic) equipped with a microanalyzer (*EDS*) X-max 80 (*Oxford Instruments*, UK) was used. The surface roughness of the coatings was measured using a *296* profilometer (*USSR*). For each sample, 10 roughness measurements were taken and average values were calculated. To determine wettability, the "sessile drop" method was used. A drop of distilled water was applied to the horizontal surface of the coating, and the contact angle with the surface at a temperature of 25 °C was determined from the drop profile [17]. For each sample, 5 measurements of wettability were performed, and average values were calculated. Microhardness was determined using the restored indentation method using a *PMT3-M* microhardness tester. Microhardness measurements were carried out using the Vickers method with a loading force of 1.96 N and an exposure time of 12 s. On each sample, 20 indentations were made, 20 measurements of the microhardness value were carried out, and the average values were calculated. Tests for the coefficient of friction and wear of samples were carried out using the "pin-on-disk" scheme [18–20] under a load of 25 N at speeds of 0.47 and 1.89 m/s for 10 minutes. Discs (*d* = 50 mm) made of high-speed *steel M45* (60 HRC) were used as the counterbody. For each sample, at least 4 measurements were made, the average data sets were calculated, and the average values of the friction coefficient were determined. To determine wear resistance, at least 6 measurements were taken for each sample. To study cyclic oxidation resistance, samples of *Steel 45* and samples with coatings that had a cubic shape with a 6 mm edge were used in the experiment. The samples were kept in a muffle furnace in cycles of ~6 hours at a temperature of 700 °C, and then placed in a desiccator to cool, and then weighed. The experiment was carried out for 100 hours.

Results and Discussion

When testing new compositions of non-localized electrodes, it is necessary to monitor the cathode weight gain during processing to establish the specific weight gain, as it characterizes the volume of material transferred to the substrate. Negative weight gain values indicate that a coating will not form. At the moments of voltage pulse application, electrical discharges occurred at the points of electrical contact between the granules and the substrate. This was accompanied by the transfer of metal from the melt pool of the granule to a pool on the surface of the substrate. Particles of *Ni*, *Al*, and *WC* powders located on the surface of the substrate or granules in the discharge impact area were wetted by the molten metal and incorporated into the melt pool on the substrate, forming a coating. With increasing processing time, the weight gain of the substrate gradually increased for all samples (Fig. 2, *a*). After 10 minutes of processing, the average values of the total specific weight gain of the cathode ranged from 2.74 to 4.76 mg/cm^2, with the *WC40* sample exhibiting the minimum value. The total weight gain values for the *WCn* and *WC20* samples were very close, whereas the weight gain rate for *W40* was noticeably lower. This may be due to the low specific surface area of large particles. The low surface area results in a lower specific surface free energy, which may not be sufficient for reliable particle attachment to the granule and cathode surfaces, potentially limiting the incorporation of such particles into the coating.

X-ray diffraction (*XRD*) analysis revealed that the structure of the coatings contains tungsten carbide (*WC*), tungsten subcarbide (*W$_2$C*), body-centered cubic (*BCC*) phases, an intermetallic compound (*Al$_{86}$Fe$_{14}$*), and an *FeNi* solid solution (Fig. 2, *b*). *BCC* phases may be represented by intermetallic compounds *AlNi*
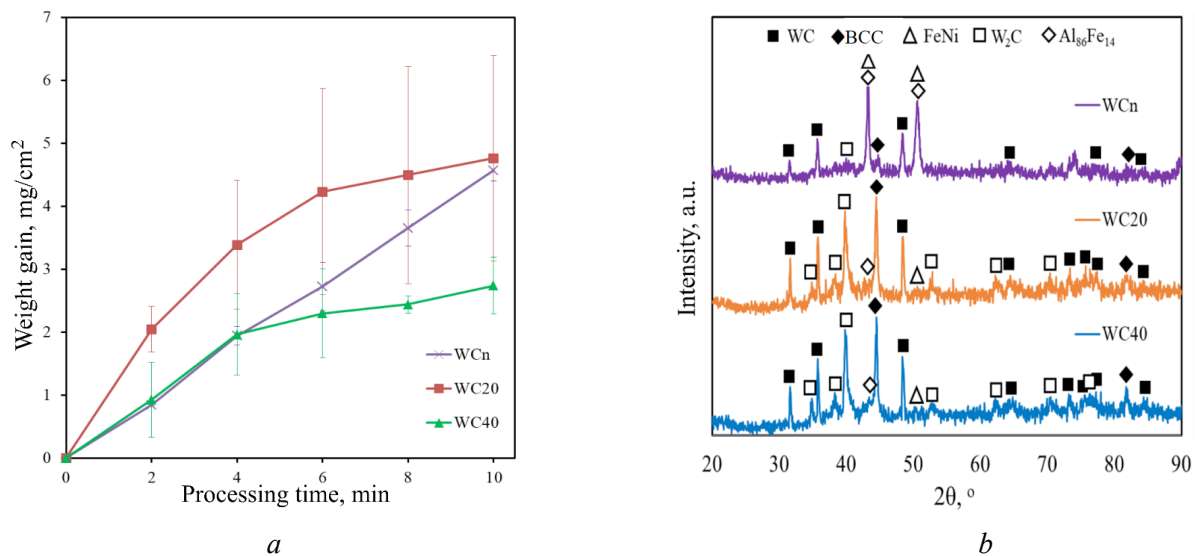
Fig. 2. Mass transfer of samples during coating deposition (*a*) and *XRD* analysis of the obtained coatings (*b*)

and *AlFe*, the reflections of which overlap on the 2θ scale. The W_2C phase formed as a result of tungsten carbide decarburization during interaction with molten iron in a melt pool, according to reaction 1:

$$2WC + 3Fe = W_2C + Fe_3C \qquad (1)$$

Thus, the prepared coatings exhibit a metalloceramic structure, where the metal binder is composed of aluminides and ferronickel, while tungsten carbides serve as reinforcing phases. The X-ray diffraction patterns of coatings obtained using micron-sized powders differ significantly from those obtained using nanopowders. Specifically, tungsten carbide (*WC*) is the most abundant phase in the *WC20* and *WC40* coatings, whereas ferronickel and the $Al_{86}Fe_{14}$ aluminide are present in higher concentrations in the *WCn* coating (Table 2). Furthermore, the concentration of the W_2C phase is lowest in the *WCn* coating compared to the other samples.

Table 2

Results of semi-quantitative phase analysis of coatings in accordance with Fig. 2, *b*

Samples	Concentration, vol.%				
	WC	*BCC*	W_2C	*FeNi*	$Al_{86}Fe_{14}$
WCn	19.5	20.5	3.9	40	16.1
WC20	32.3	23.6	20.9	15.6	7.5
WC40	31.0	28.4	30.0	6.4	4.6

Cross-sectional images of the *MMCs* coatings are shown in Fig. 3, *a–d*. The average coating thickness was very similar, ranging from 24.3 to 26.1 µm. The coating structure consists of a *Fe-Ni-Al* matrix and grains in the micron and submicron ranges. The *Wn* coating appears homogeneous without micron-sized inclusions (Fig. 3, *a*). At higher magnification, diamond-shaped crystallites with sizes ranging from 0.16 to 0.47 µm are observed in the *Wn* coating, uniformly distributed throughout the coating layer (Fig. 3, *b*). Given the low concentration of the W_2C phase in this coating (Fig. 2, *b*), it is reasonable to assume that the diamond-shaped crystallites are tungsten carbide. In the *W20* and *W40* coatings, both micron- and submicron-sized carbide grains are observed. Elemental mapping results reveal that the micron-sized inclusions are enriched in tungsten and carbon (Fig. 4). The difference in size and non-uniform distribution
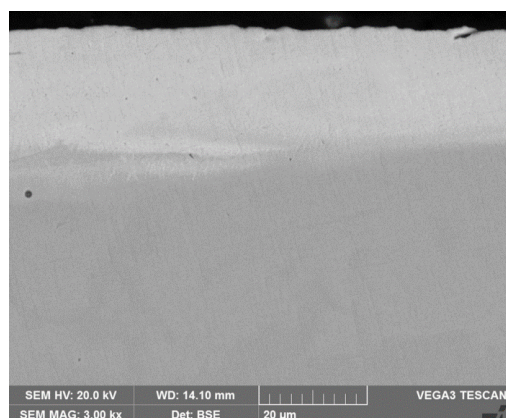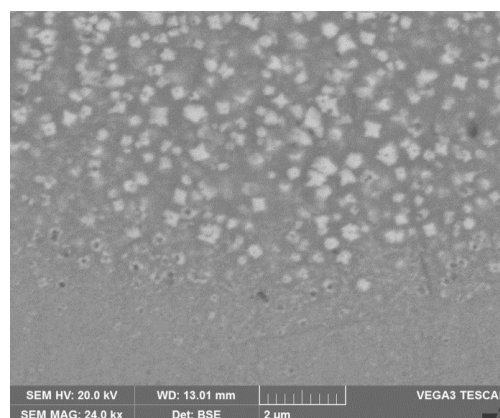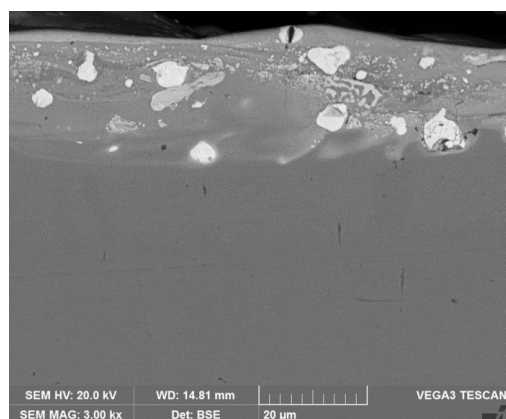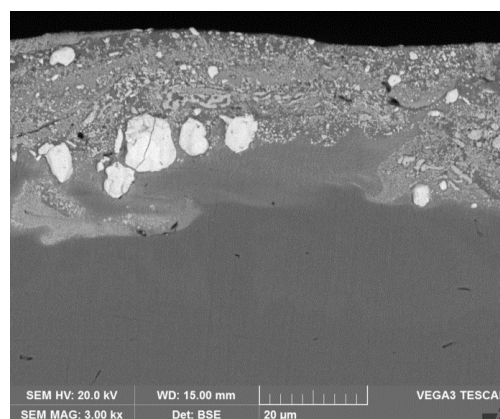
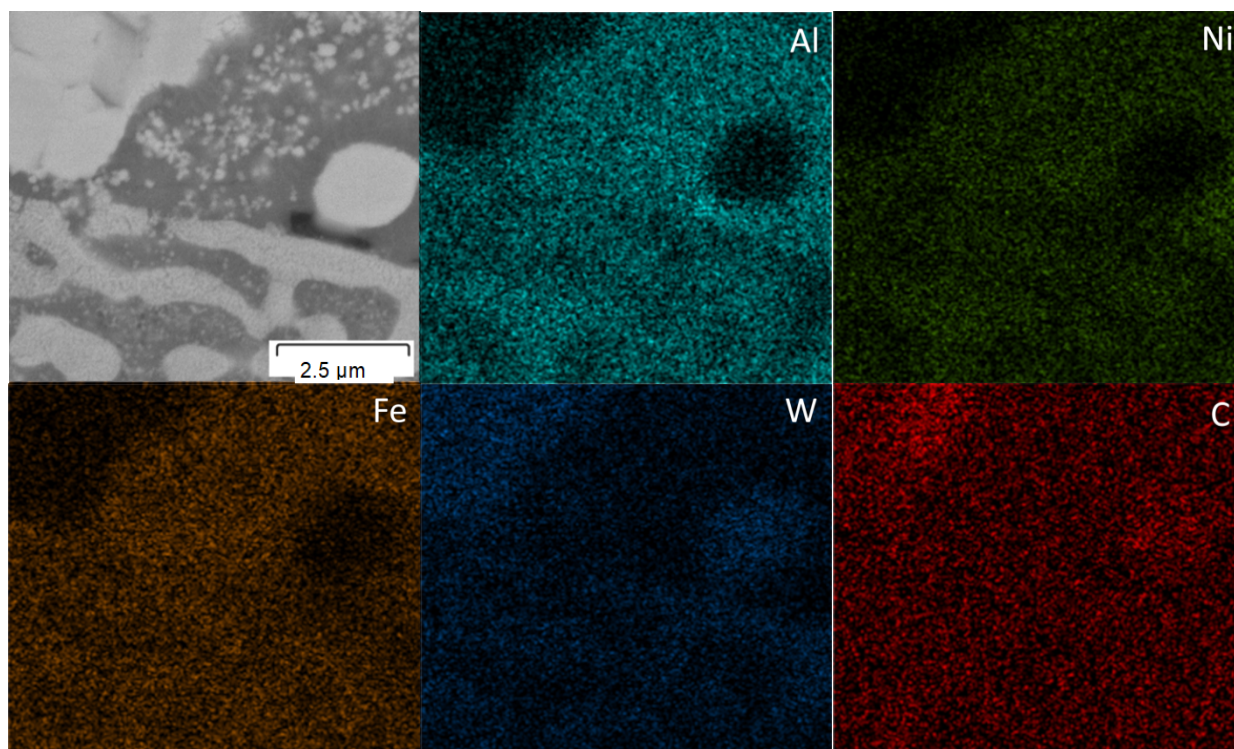*Fig. 3. SEM* images of the cross-section of coatings: *WCn* (*a*, *b*), *WC20* (*c*) and *WC40* (*d*)

Fig. 4. Mapping of the *WC20* coating area

of the white micron-sized inclusions in the *WC20* and *WC40* coatings suggest that they are original tungsten carbide WC particles. The cross-sectional images clearly show that the size of micron-sized *WC* inclusions increases with an increase in the *WC* powder fraction in the electrode. The diameter of the micron grains was smaller than the median particle diameter in the original *W20* and *W40* powders (Fig. 1, *c*, *d*). This suggests that the original powder particles were agglomerates of carbides, which disintegrated into fragments when wetted by the *Fe-Ni-Al* melt in the discharge pool and dissolved upon interaction with iron. The submicron inclusions in Fig. 4 likely formed via *WC* crystallization from the melt, as they resemble the diamond-shaped inclusions of the *WCn* sample, and reaction **1** is reversible. Micron inclusions could also act as *WC* crystallization centers, growing further during crystallization of the melt microbath after the discharge ceased. The distribution of aluminum, nickel, and iron is uniform, indicating a homogeneous composition of the coating matrix. The light grey areas in Fig. 4 are likely the result of tungsten carbide decarburization, as described in Eq. 1.

According to *EDS* analysis, the coatings contain tungsten, nickel, aluminum, and iron (Fig. 5, *a–c*). The source of iron is both the granules and the substrate. The concentration of elements remained relatively constant throughout the coating thickness. Fluctuations in tungsten concentration can be attributed to the presence of tungsten carbide grains in the path of the scanning electron beam. As the powder fraction size in the *NE* increased, the aluminum content in the coating matrix increased, while the iron (*Fe*) content decreased from 58 to 27 at.% (Fig. 5). The formation of the *ESD* coating inevitably involves the substrate as a source of iron. It is worth noting that the use of iron granules results in comparable iron concentrations in the coating to those obtained when using *Ni* and *Al* granules [10]. This can be explained by the fact
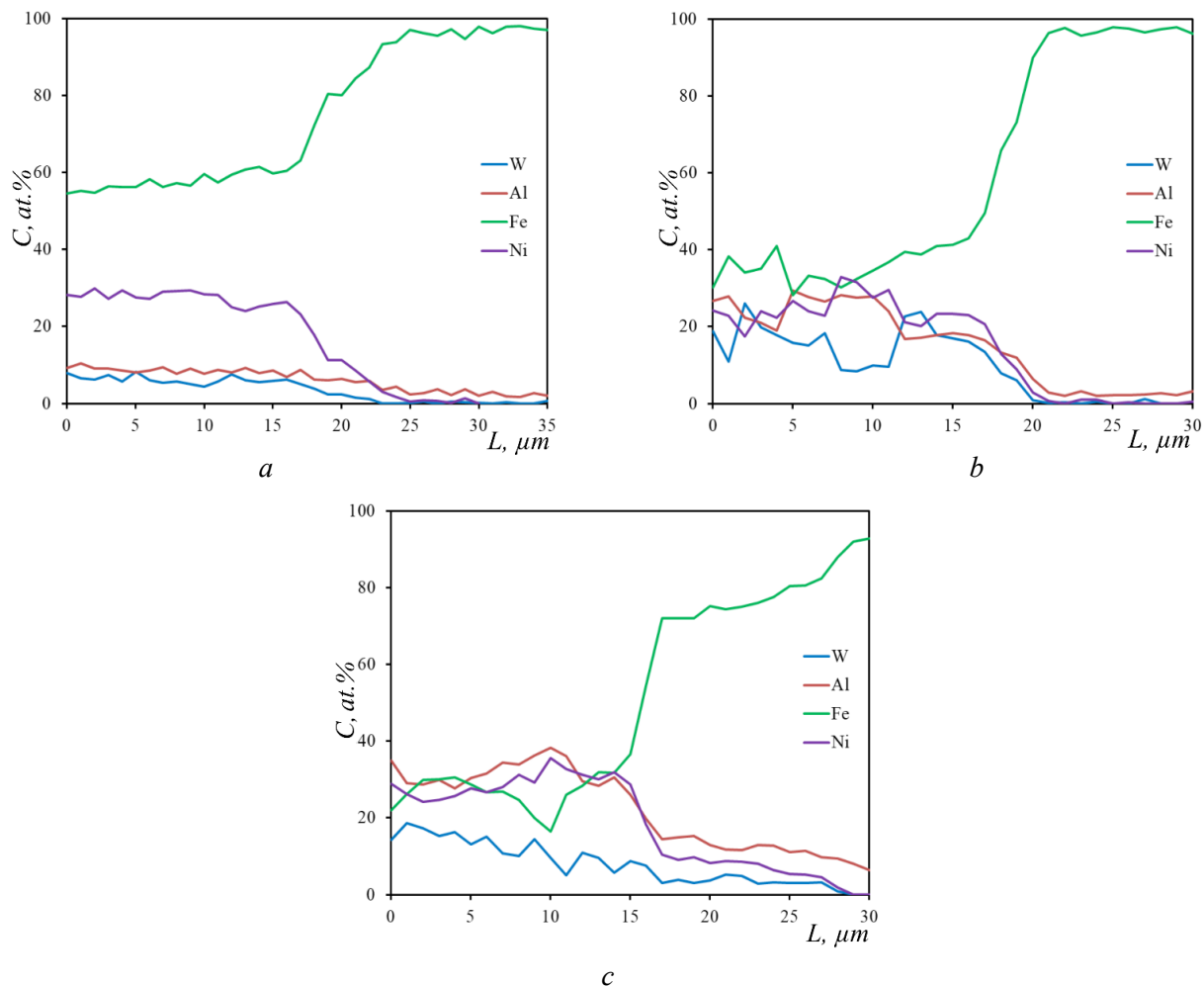

Fig. 5. Metal concentration distribution of across coating height, according to the results
of *EDS* analysis:

a – WCn; b – WC2; c – WC40

that powders participate much more intensively in the formation of coatings during *ESDNE* compared to compact electrodes (granules).

The surface roughness (*Ra*) of the coated samples ranged from 5.87 to 8.23 µm (Table 3). Furthermore, the contact angle with distilled water ranged from 77.7 to 83.6°, which is significantly higher than that of *Steel 45* (54.1±1.4°). Thus, the application of *WC/Fe-Ni-Al* coatings to components made of *Steel 45* will increase the hydrophobicity of their surface due to a reduction in surface free energy. This is expected to reduce the deposition of contaminants on the surface and, consequently, limit the development of corrosion on steel structures.

Table 3

Thickness, roughness and wettability of coatings

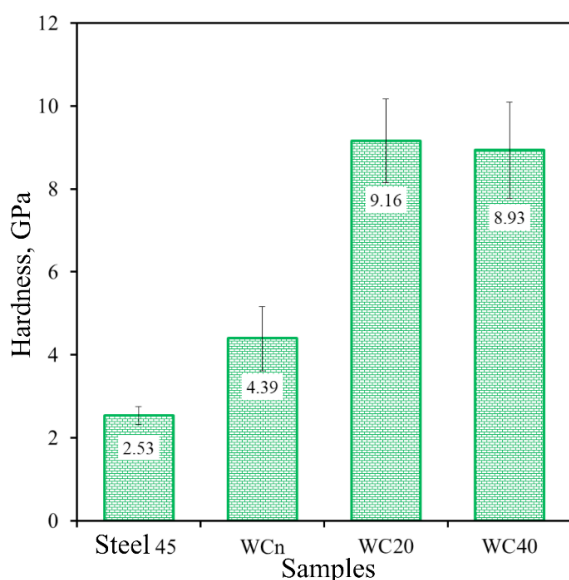| Characteristics	Sampels		
	WCn	*WC20*	*WC40*
Thickness, µm	25.19±5.78	24.35±5.68	26.13±6.10
Roughness, µm	8.23±2.17	6.73±0.89	5.87±0.94
Wettability, °	77.7±1.6	83.6±1.6	82.7±1.6

Fig. 6. Microhardness of the coating surface

The microhardness measurements on the coating surface revealed values ranging from 4.39 to 9.16 GPa, with the *WCn* sample exhibiting the minimum value and the *WC20* sample exhibiting the maximum (Fig. 6). Thus, the application of coatings allows for a 1.7 to 3.6-fold increase in the hardness of products made of *Steel 45*. The low hardness values of the sample obtained using tungsten carbide nanopowder can be attributed to the absence of large tungsten carbide inclusions in its composition. Moreover, this coating had the lowest content of the W_2C phase (30 GPa) [21]. The hardness of the *WC20* and *WC40* coatings was nearly identical, but significantly higher than that of *WCn* due to the higher content of the W_2C phase.

The results of friction tests on *WC/Fe-Ni-Al* coatings under a load of 25 N are shown in Fig. 7, *a*. During the initial 30 m of sliding, a sharp increase in friction force was observed, resulting from an increase in the contact area between the counter-surfaces due to running-in and smoothing out of roughness asperities. The friction coefficient curves of all coatings exhibited an ascending trend in the stable stage, while the friction force values of *Steel 45* fluctuated around a constant value. This can be attributed to the increased surface roughness of the coatings (Table 3). Analysis of the friction coefficient curves revealed that the friction force noise level was significantly lower for all samples with *WC/Fe-Ni-Al* coatings compared to *Steel 45*. The average friction coefficient values of the coatings (0.73–0.83) were 6–18% lower than those of uncoated *Steel 45* (0.88). This can be attributed to the anti-friction properties of WO_3, which forms during oxidative wear of tungsten carbide [22]. In conclusion, the use of the proposed *WC/Fe-Ni-Al* coatings allows for the reduction and stabilization of the friction coefficient of components made of *Steel 45*.

The wear resistance of the coatings was investigated at linear sliding speeds of 0.47 and 1.9 m/s under a load of 25 N. The wear rate of *WC/Fe-Ni-Al* coatings ranged from 0.61×10^{-6} to 10.91×10^{-6} mm³/Nm at a speed of 0.47 m/s and from 0.30×10^{-6} to 2.70×10^{-6} mm³/Nm at a speed of 1.89 m/s (Fig. 7, *b*). Therefore, the wear resistance of the developed coatings was 5 to 80 times greater than that of the
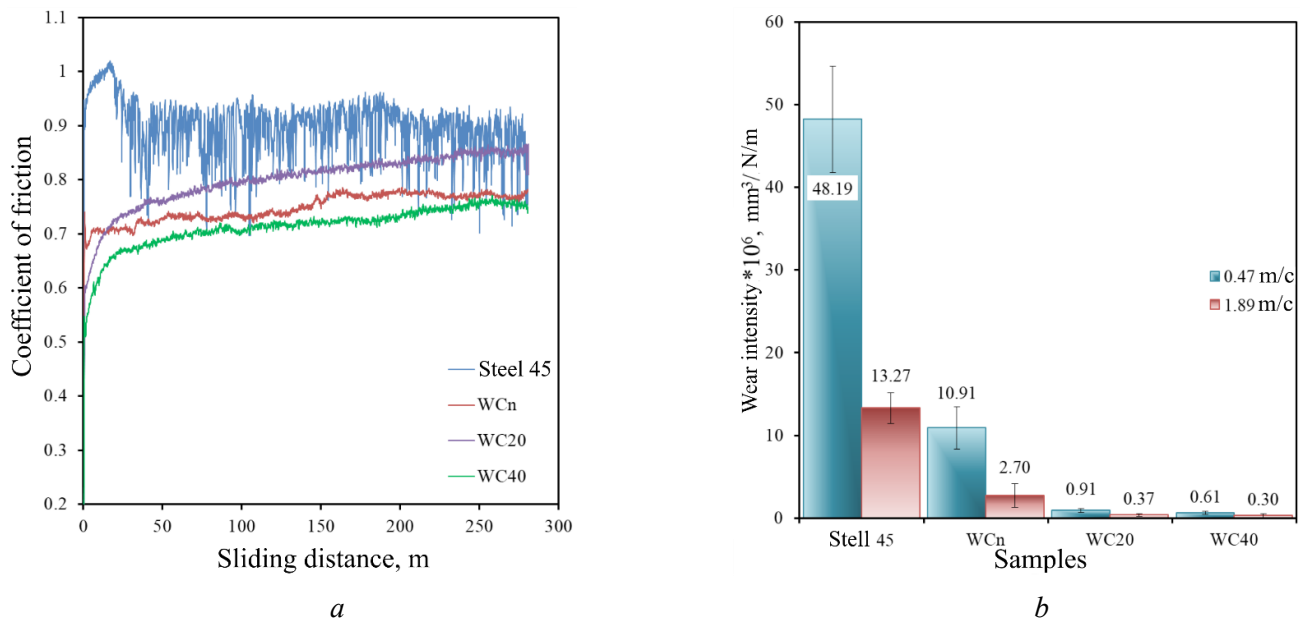
Fig. 7. Coefficient of friction at a sliding speed of 0.47 m/s and wear rate of coatings at 0.47 and 1.89 m/s

original *Steel 45*. At a sliding speed of 0.47 m/s, the wear of the samples was higher than at a higher speed (1.89 m/s). This can be attributed to the formation of a self-lubricating tribo-oxide layer, resulting from the high instantaneous temperature reached in the friction zone at the higher sliding speed [23, 24]. At both speeds, the *WCn* coating exhibited the lowest wear resistance, while the *WC40* coating exhibited the highest. The high wear resistance of the *WC40* coating can be attributed to the presence of large *WC* inclusions and areas with their accumulation, which prevented the counterbody from interacting with the abraded metal matrix of the coating.

Based on the weight gain plots of *WC/Fe-Ni-Al* coatings and *Steel 45* at 700 °C, after 100 hours of testing, the weight gain of coated samples ranged from 37.0 to 133.8 g/m^2, while that of uncoated *Steel 45* was 429.2 g/m^2 (Fig. 8, *a*). The weight gain of the coated samples increased with increasing powder dispersion, increasing by 2.6 times when transitioning from the *WC20* sample to the *WCn* sample. Thus, the results indicate that decreasing the diameter of tungsten carbide particles reduces the oxidation resistance of the *WC/Fe-Ni-Al* composition. This may be due to the increased decarburization of *WC* particles with an increase in their specific surface area, leading to a greater introduction of *W* and *C* elements into the
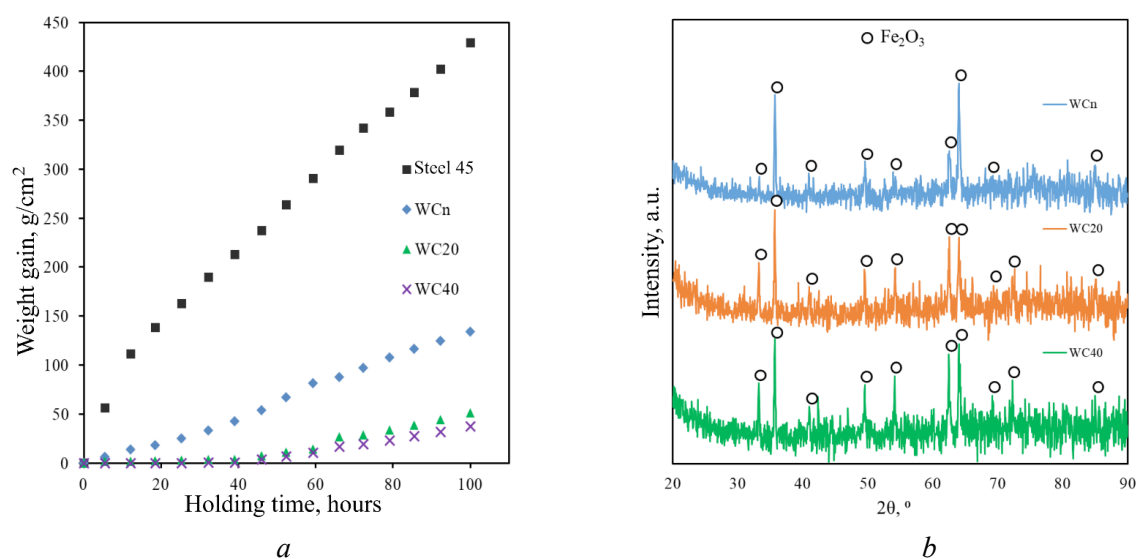

Fig. 8. Graphs of weight gain of *WC/Fe-Ni-Al* coatings and 45 steel over time at a temperature of 700 °C (*a*) and *XRD* patterns of coatings after oxidation resistance testing (*b*)

Fe-Ni-Al matrix, thereby reducing the barrier properties of the aluminum oxide layer formed during high-temperature oxidation. The weight gain during the oxidation resistance test results from the fixation of oxygen on the surface of the samples in the form of hematite Fe_2O_3 (Fig. 8, *b*). In general, the *WC20* and *WC40* composite coatings demonstrated high oxidation resistance at 700 °C. Their use allows for an 8.4 to 11.6-fold increase in the oxidation resistance of components made of *Steel 45*.

Conclusions

1. For the first time, the influence of tungsten carbide powder particle size distribution on the production of *WC/Fe-Ni-Al* metalloceramic coatings on *Steel 45* using electrospark deposition with a non-localized electrode was investigated. Tungsten carbide powder fractions of $1 \leq WC \leq 20$ μm and $20 \leq WC \leq 40$ μm were prepared via grinding in a planetary ball mill and subsequent sieve analysis.

2. The total weight gain values for samples *WCn* and *WC20* were similar, while the weight gain rate was noticeably lower for *W40*. X-ray diffraction analysis revealed that the deposited coatings consisted of tungsten carbide, tungsten subcarbide (W_2C), iron aluminide ($Al_{86}Fe_{14}$), ferronickel (*FeNi*), and *BCC* phases (*AlNi*, *AlFe*). It was shown that increasing the *WC* powder fraction size in the electrode resulted in enrichment of the coating matrix with aluminum, while the iron concentration decreased from 60 to 30 at.%. The coating structure corresponds to a metalloceramic composite.

3. The surface roughness of the coatings ranged from 5.87 to 8.23 μm, with a minimum value for the *WC40* sample. The contact angle of the coatings ranged from 77.7 to 83.6±1.6°, with the lowest value observed for the sample produced using tungsten carbide nanopowder.

4. The microhardness of the coating surface ranged from 4.39 to 9.16 GPa, with the lowest value observed for the sample produced using tungsten carbide nanopowder.

5. This study demonstrated that tungsten carbide particle fractions ranging from 20 to 40 μm provide the best wear resistance and oxidation resistance of *WC/Fe-N-Al* coatings at 700 °C. It was shown that the use of such coatings increases the oxidation resistance of *Steel 45* by up to 11.6 times and the wear resistance by 44 to 80 times.

References

1. Wang X., Liu Z., Cheng K., Li J., Ning H., Mao J. High-temperature corrosion characterization of Ni-Al laser cladding: The effect of Al content and Fe. *Journal of Thermal Spray Technology*, 2024, vol. 33 (5), pp. 1417–1439. DOI: 10.1007/s11666-024-01782-8.

2. Wang Z., Zhang J., Zhang F., Qi C. Study on the microstructure and properties of a laser cladding Fe–Ni–Al coating based on the invar effect. *Scientific Reports*, 2024, vol. 14 (1), p. 11685. DOI: 10.1038/s41598-024-62306-6.

3. Munroe P.R., George M., Baker I., Kennedy F.E. Microstructure, mechanical properties and wear of Ni–Al–Fe alloys. *Materials Science and Engineering: A*, 2002, vol. 325 (1–2), pp. 1–8. DOI: 10.1016/S0921-5093(01)01403-4.

4. Datu-Maki A.S.I., Ciswandi, Hermanto B., Saptari S.A., Sudiro T. Structure and oxidation resistance of flame sprayed Fe–Ni–Al coating. *Journal of Physics: Conference Series*, 2019, vol. 1204 (1), p. 012128. DOI: 10.1088/1742-6596/1204/1/012128.

5. Manikandan R., Ponnusamy P., Nanthakumar S., Gowrishankar A., Balambica V., Girimurugan R., Mayakannan S. Optimization and experimental investigation on AA6082/WC metal matrix composites by abrasive flow machining process. *Materials Today: Proceedings*, 2023. DOI: 10.1016/j.matpr.2023.03.274.

6. Alidokht S.A., Wu L., Bessette S., Chromik R.R. Microstructure and tribology of cold spray additively manufactured multimodal Ni-WC metal matrix composites. *Wear*, 2024, vol. 538, p. 205218. DOI: 10.1016/j.wear.2023.205218.

7. Liao Z., Huang X., Zhang F., Li Z., Chen S., Shan Q. Effect of WC mass fraction on the microstructure and frictional wear properties of WC/Fe matrix composites. *International Journal of Refractory Metals and Hard Materials*, 2023, vol. 114, p. 106265. DOI: 10.1016/j.ijrmhm.2023.106265.

8. Yuan J., Wang Q., Liu X., Lou S., Li Q., Wang Z. Microstructures and high-temperature wear behavior of NiAl/WC-Fex coatings on carbon steel by plasma cladding. *Journal of Alloys and Compounds*, 2020, vol. 842, p. 155850. DOI: 10.1016/j.jallcom.2020.155850.

9. Abreu-Castillo H.O., d'Oliveira A.S.C.M. Challenges of nanoparticle-reinforced NiAl-based coatings processed by in situ synthesis of the aluminide. *The International Journal of Advanced Manufacturing Technology*, 2024, vol. 134 (3–4), pp. 1547–1561. DOI: 10.1007/s00170-024-14162-x.

10. Burkov A.A. Use of Ni and Al granules and WC powder for electric spark deposition of metalloceramic coatings. *Izvestiya vysshikh uchebnykh zavedenii. Poroshkovaya metallurgiya i funktsional'nye pokrytiya = Powder Metallurgy and Functional Coatings*, 2025, vol. 19, no. 2, pp. 62–72. DOI: 10.17073/1997-308X-2025-2-62-72.

11. Barile C., Casavola C., Pappalettera G., Renna G. Advancements in electrospark deposition (ESD) technique: A short review. *Coatings*, 2022, vol. 12 (10), p. 1536. DOI: 10.3390/coatings12101536.

12. Nikolenko S.V., Verkhoturov A.D. *Novye elektrodnye materialy dlya elektroiskrovogo legirovaniya* [New electrode materials for electrospark alloing]. Vladivostok, Dal'nauka Publ., 2005. 219 p. ISBN 5-80444-0404-0.

13. Burkov A.A., Kulik M.A. Wear-resistant and anticorrosive coatings based on chrome carbide Cr_7C_3 obtained by electric spark deposition. *Protection of Metals and Physical Chemistry of Surfaces*, 2020, vol. 56, pp. 1217–1221. DOI: 10.1134/s2070205120060064.

14. Dvornik M., Mikhailenko E. The influence of the rotation frequency of a planetary ball mill on the limiting value of the specific surface area of the WC and Co nanopowders. *Advanced Powder Technology*, 2020, vol. 31 (9), pp. 3937–3946. DOI: 10.1016/j.apt.2020.07.033.

15. Dvornik M.I., Zaytsev A.V. Research of surfaces and interfaces increasing during planetary ball milling of nanostructured tungsten carbide/cobalt powder. *International Journal of Refractory Metals and Hard Materials*, 2013, vol. 36, pp. 271–277. DOI: 10.1016/j.ijrmhm.2012.10.004.

16. Burkov A.A. Production amorphous coatings by electrospark treatment of steel 1035 in a mixture of iron granules with CrMoWCBSi powder. *Obrabotka metallov (tekhnologiya, oborudovanie, instrumenty) = Metal Working and Material Science*, 2019, vol. 21, no. 4, pp. 19–30. DOI: 10.17212/1994-6309-2019-21.4-19-30. (In Russian).

17. Li Y.C., Zhang W.W., Wang Y., Zhang X.Y., Sun L.L. Effect of spray powder particle size on the bionic hydrophobic structures and corrosion performance of Fe-based amorphous metallic coatings. *Surface and Coatings Technology*, 2022, vol. 437, p. 128377. DOI: 10.1016/j.surfcoat.2022.128377.

18. Almond E.A., Gee M.G. Results from a UK interlaboratory project on dry sliding wear. *Wear*, 1987, vol. 120 (1), pp. 101–116. DOI: 10.1016/0043-1648(87)90136-0.

19. Kennedy F.E., Lu Y., Baker I. Contact temperatures and their influence on wear during pin-on-disk tribotesting. *Tribology International*, 2015, vol. 82, pp. 534–542. DOI: 10.1016/j.triboint.2013.10.022.

20. Nataraja M., Balakumar G., Santhosh N., Naik M.R. Characterization of wear rate of Al-12 wt% Si alloy based MMC reinforced with ZrO_2 particulates. *Materials Research Express*, 2024, vol. 11 (3), p. 036522. DOI: 10.1088/2053-1591/ad3468.

21. Chivavibul P., Watanabe M., Kuroda S. Effect of microstructure of HVOF-sprayed WC-Co coatings on their mechanical properties. *Thermal Spray*, 2007, p. 1212. DOI: 10.31399/asm.cp.itsc2007p0297.

22. Greenwood O.D., Moulzolf S.C., Blau P.J., Lad R.J. The influence of microstructure on tribological properties of WO3 thin films. *Wear*, 1999, vol. 232 (1), pp. 84–90. DOI: 10.1016/S0043-1648(99)00255-0.

23. Jayashree P., Turani S., Straffelini G. Effect of velocity and temperature on the dry sliding behavior of a SiC-Graphite composite against WC-CoCr and WC-FeCrAlY HVOF coatings. *Wear*, 2021, vol. 464, p. 203553. DOI: 10.1016/j.wear.2020.203553.

24. Ameen H.A., Hassan K.S., Mubarak E.M.M. Effect of loads, sliding speeds and times on the wear rate for different materials. *American Journal of Scientific and Industrial Research*, 2011, vol. 2 (1), pp. 99–106. DOI: 10.5251/ajsir.2011.2.1.99.106.

Conflicts of Interest

The authors declare no conflict of interest.

NSTU

NETI

Obrabotka metallov –
Metal Working and Material Science

Journal homepage: http://journals.nstu.ru/obrabotka_metallov

Investigation on the mechanical properties of stir-cast Al7075-T6-based nanocomposites with microstructural and fractographic surface analysis

Suhas Patil [1, a], Satish Chinchanikar [2, b, *]

[1] Department of Mechanical Engineering, Vishwakarma Institute of Information Technology, Affiliated to Savitribai Phule Pune University, Pune – 411048, India
[2] Department of Mechanical Engineering, Vishwakarma Institute of Technology, Affiliated to Savitribai Phule Pune University, Pune – 411037, India

[a] https://orcid.org/0000-0002-2965-1531, ✉ suhas.221p0007@viit.ac.in; [b] https://orcid.org/0000-0002-4175-3098, ✉ satish.chinchanikar@vit.edu

ARTICLE INFO

ABSTRACT

Introduction. Aluminum-based metal matrix composites (*MMCs*) have garnered considerable attention recently due to their enhanced mechanical properties, making them suitable for a wide range of industrial applications. While other methods exist for incorporating reinforcements into the base metal, stir casting is a particularly efficient process as it promotes a more uniform distribution of reinforcement particles throughout the matrix. *The purpose of this work*. It has been demonstrated that adding silicon carbide (*SiC*) reinforcements to alloys from the *7XXX* series enhances their fatigue strength. The impact of *SiC* reinforcements on the mechanical properties of *A356* composites, such as elongation, compressive strength, tensile strength, and hardness, has also been investigated. However, there is a need for more research on how hybrid reinforcement particles affect the mechanical properties of *Al7075-T6* alloy. **Methods.** Considering the broad application spectrum of aluminum matrix composites (*AMCs*) in the automotive and aerospace sectors, this study examines the influence of varying ratios of nano-sized *SiC* and graphene reinforcements on the hardness and tensile strength of stir-cast *Al7075-T6* aluminum alloy. The scanning electron microscopy — energy-dispersive X-ray spectroscopy (*SEM-EDS*) analysis of the composites' microstructural and fractographic surfaces is also included. The objectives of this work are to develop lightweight, high-performance hybrid metal matrix nanocomposite materials and to explore the feasibility of integrating graphene and *SiC* nanoparticles into *Al7075* alloy. Particular emphasis is placed on the discussion of the mechanical characteristics of these hybrid materials. **Results and discussion.** This study found that mechanical stirring improved the bonding, wetting, and cohesion between the reinforcements and matrix while reducing porosity. Compared to composites produced without stirring, stirred composites exhibited improved strength and toughness due to microstructural changes. The study suggests that appropriate mixing strategies can significantly impact the mechanical properties and surface morphology of *Al7075* nanocomposites. The results indicated that the hybrid reinforcement nanoparticles significantly improved both the hardness and tensile strength of the *Al7075-T6* alloy. Moreover, a distinct correlation between the ratio of silicon carbide to graphene nanoparticles and the mechanical properties of the specimens was observed. Specifically, an *Al7075* specimen reinforced with 0.5 wt.% graphene and 3 wt.% silicon carbide nanoparticles demonstrated superior hardness and tensile strength compared to unreinforced *Al7075* and other combinations of silicon carbide and graphene nanoparticles considered in this study. With a 0.5 wt.% graphene content and 1–3 wt.% *SiC* content, the *Al7075*-based nanocomposites consistently exhibited a well-defined grain structure with distinct, continuous grain boundaries. The resulting finely dispersed nanoparticles, ranging in size from 62.57 to 91.54 nm, facilitated effective load transfer, grain refinement, and impeded dislocation motion, leading to enhanced mechanical properties. An *Al7075*-based nanocomposite exhibited superior mechanical performance characterized by a dense, dimpled surface featuring uniform microvoids and minimal particle pull-out. This behavior was attributed to ductile fracture resulting from strong matrix-reinforcement bonding and efficient load transfer. Consistent with these observations, the study indicates that the mechanical behavior of hybrid *Al7075*-based nanocomposites is significantly influenced by the reinforcement ratio, particle size, and dispersion quality. This information is valuable for advanced industrial applications. The study further demonstrates that a balanced combination of graphene and silicon carbide nanoparticle reinforcements can enhance the mechanical properties of *Al7075*, emphasizing the need for further investigation into these synergistic effects.

Introduction

Hybrid metal matrix composites (*HMMCs*) are increasingly being utilized in the automotive and aerospace industries due to their exceptional properties, including low density, high stiffness, high specific strength, and a low coefficient of thermal expansion. Composite materials are categorized into two main

* **Corresponding author**
Satish Chinchanikar, Ph.D. (Engineering), Professor
Department of Mechanical Engineering,
Vishwakarma Institute of Information Technology,
Affiliated to Savitribai Phule Pune University, Pune – 411048, India
Tel.: 91-2026950401, **e-mail:** satish.chinchanikar@vit.edu

groups: matrix-based (metal, polymer, or ceramic) and reinforcement-based (particulate, fiber, or whisker). Currently, particulate metal matrix composites are widely adopted. These composites consist of a base metal (such as aluminum or magnesium) and reinforcement particles (such as silicon carbide (*SiC*), graphene (*C*), or boron carbide (B_4C), as well as natural materials like rock dust, eggshell, or jute).

Various methods are employed to incorporate reinforcements into the base metal; however, stir casting stands out as an effective technique, ensuring a uniform distribution of reinforcement particles throughout the base metal. Aluminum-based metal matrix composites (*Al-MMCs*) have garnered significant attention in recent years due to their improved mechanical properties, making them suitable for various industrial applications. The incorporation of reinforcement particles, such as silicon carbide (*SiC*) and graphene, has been shown to enhance the mechanical properties of metal matrix composites (*MMCs*). These *MMCs* have gained significant attention in recent years due to their improved mechanical and thermal properties [1].

A substantial enhancement in the material's mechanical properties is achieved by the addition of components such as graphene nanoplates (*GNPs*), boron nitride (*BN*), and vanadium carbide (*VC*), among others. For example, the hybrid *AA7075/GNPs+BN+VC* material exhibited superior hardness and compression strength due to the effective use of particle reinforcement [2]. Enhanced mechanical strength can also be achieved through the utilization of boride nanocrystals, such as hafnium diboride (HfB_2), which improve hardness and facilitate grain refinement [3].

Optimizing the microstructure of a material can be achieved by employing methods such as equal channel angular pressing (*ECAP*) and spark plasma sintering (*SPS*). This optimization, in turn, affects the yield strength and hardness of the material [4]. To attain optimal outcomes, it is necessary to refine grain size through hybridization and processing techniques. The enhanced grain boundary strengthening resulting from smaller grain sizes contributes to the improvement of the material's mechanical properties. Strong interfacial bonding between the matrix and reinforcements is crucial for efficient load transfer, directly influencing the mechanical performance of the composites.

Aluminum matrix composites (*AMCs*) have become increasingly popular due to the advantages they offer compared to monolithic aluminum alloys [5]. The mechanical and tribological properties of *AMCs* are influenced by several factors, including the processing methods, the type of reinforcement, the size, and the composition of the material [6]. Stir casting, friction stir processing, powder metallurgy, and spark plasma sintering are a few examples of the various manufacturing techniques available for *AMCs* [7].

Techniques such as stir casting, powder metallurgy, and friction stir processing are particularly significant in establishing a homogeneous distribution of reinforcements throughout the material. Friction stir processing effectively reduces grain size, with reductions of up to 10.3 times compared to the base alloy. This technique utilizes friction to stir the material, enhancing its mechanical properties. During friction stir processing, the uniform distribution of hybrid reinforcement particles contributes to an increase in both the hardness and compression strength of the resulting composites [2].

Powder metallurgy techniques, such as mechanical alloying and hot pressing, are used to enhance the compressive strength, elongation to failure, and microhardness of composites. Researchers have found that hot pressing yields superior mechanical properties for *AA2024*/multi-walled carbon nanotube (*MWCNT*) composites compared to other techniques, as it facilitates uniform *MWCNT* dispersion and improved connectivity across interfacial surfaces [8].

Stir casting is a cost-effective method but faces challenges with agglomeration during production. Powder metallurgy is also considered a successful approach for creating hybrid aluminum nanocomposites [5]. Nanocomposites produced via stir casting exhibit enhanced hardness and a lower wear rate. This technique enables the creation of a dense microstructure with minimal porosity, leading to improved mechanical properties in the composite [9].

Silicon carbide (*SiC*) and boron carbide (B_4C) are two examples of established materials used as reinforcements. Powders derived from agricultural waste, such as rice husk ash and coconut shell ash, can also be effectively employed. The use of these reinforcements enhances characteristics such as compressive strength, hardness, and wear resistance [10]. The incorporation of B_4C and *SiC* reinforcements into *Al6061* composites has been shown to affect mechanical properties, including hardness, tensile strength, and impact energy [11].

The addition of *SiC* reinforcements to *7XXX* series alloys has been shown to improve fatigue strength [12]. The incorporation of Al_2O_3 reinforcements into scrap aluminum alloy wheels affects porosity, hardness, ultimate tensile strength, and ultimate compressive strength [13-15]. Researchers have reviewed the effect of mixed nanoparticles in base fluids on the properties of nanofluids and machining characteristics, suggesting that nanoparticle size and concentration significantly influence nanofluid effectiveness [16-19]. Research has also explored the effect of *SiC* reinforcements on the mechanical properties of *A356* composites, including hardness, tensile strength, compressive strength, and elongation [20]. However, the effects of hybrid reinforcement particles on *Al7075-T6* alloy remain largely unexplored.

Silicon carbide and graphene offer varying benefits as reinforcement materials: *SiC* is ideal for enhancing hardness and tensile strength, while graphene excels in lightweight, high-strength applications. This study aims to investigate the influence of varying proportions of nanosized *SiC* and graphene (*Gr*) on the hardness and tensile strength of *Al7075-T6* alloy, prepared using the stir casting method. The study also examines the microstructural and fracture surface analysis of the composites using scanning electron microscopy (*SEM*) and energy-dispersive X-ray spectroscopy (*EDX*).

This research aims to create lightweight, high-performance hybrid metal matrix nanocomposite materials and explore the potential of combining *SiC* and *Gr* nanoparticles with *Al7075*, with a focus on characterizing the mechanical properties of these hybrid materials.

Materials and Design

Aluminum matrix composites (*AMCs*) reinforced with silicon carbide (*SiC*) and graphene are favored for aerospace and automotive applications due to their enhanced mechanical and tribological properties [21]. Graphene's high strength-to-weight ratio can improve property enhancement, although its poor wettability and tendency to aggregate can be limiting factors [22]. Stir casting and other methods are employed to achieve a homogeneous reinforcement distribution, which enhances the mechanical properties of *Al7075* composites [23]. In this study, *Al7075-T6* serves as the matrix material, while silicon carbide (30-50 nm) and graphene (5-10 nm) are used as reinforcements. Reinforcement materials influence the mechanical and physical properties of composites. *SiC* and graphene are preferred reinforcements for engineering applications due to their distinctive characteristics.

Silicon carbide, known for its hardness, thermal conductivity, and resistance to corrosion and chemical attack, is well-suited for high-temperature environments and enhances durability. With a density of 3.22 g/cm³ and a hardness of 2450 BHN, silicon carbide is a rigid, robust material ideal for wear-resistant applications. Graphene, with a low density of 2.2 g/cm³ and a hardness of 110 BHN, is well-suited for strong, lightweight components. Despite its lower hardness compared to SiC, graphene can be used to create flexible, high-strength composites. Graphene's tensile strength of 130 GPa surpasses that of most materials, benefiting advanced composites that require a high strength-to-weight ratio.

The mechanical properties of the cast specimens were characterized using hardness tests (*ASTM* E10) and tensile tests (*ASTM-B557*). Hardness was measured using a *Brinell* hardness tester. Tensile tests were performed on a universal testing machine (*UTM*). Scanning electron microscopy (*SEM*) was used to analyze the particle distribution patterns in the composites. Energy dispersive X-ray spectroscopy (*EDS*) was used to identify the elements present in the specimens. *SEM* and *EDS* were performed using a *JEOL JSM-IT200* model.

The experimental setup for preparing *Al7075*-based nanocomposites with varying reinforcements is depicted in Fig. 1. Initially, *Al7075-T6* ingots weighing 1.5 kg each were obtained. These ingots were then placed in a crucible within the stir casting furnace. The molten metal was heated to 750 °C and maintained at that temperature for 120 minutes. Magnesium powder (1 wt.%) was added to the molten metal to prevent oxidation. Varying combinations of graphene and silicon carbide reinforcements were then introduced into the molten metal. Before introduction, these reinforcements were preheated for 5-7 minutes.

A mechanical stirrer was used to ensure uniform dispersion of reinforcements in the molten metal for fifteen minutes. The slurry that formed on the surface of the molten metal was gradually removed to

Fig. 1. Preparation of *Al7075* specimens with varying reinforcements by stir casting

ensure sound cast specimens. Specimens with a diameter of 20 mm and a length of 250 mm were obtained. The mold was preheated for 5-7 minutes prior to pouring the molten metal to facilitate deoxidation. The chemical composition of *Al7075* is presented in Table 1. Table 2 describes the different specimens prepared with varying reinforcements using stir casting.

Hardness was measured using a *Brinell* hardness tester according to *ASTM E10*. A load of 187.50 kg was applied to the specimen using a 2.5 mm steel ball indenter for a dwell time of 20 seconds. To assess the uniform distribution of hybrid reinforcements, hardness values were measured at two different locations on the cast specimen. Tensile behavior of the nanocomposites was investigated by manufacturing and testing specimens in accordance with *ASTM B557*. Before testing in the *UTM*, the test specimen was machined according to the standard.

Table 1

Chemical composition of *Al7075-T6* alloy

Element	*Si*	*Fe*	*Cu*	*Mn*	*Mg*	*Cr*	*Ni*	*Zn*	*Ti*	*Zr*	*Al*
wt.%	0.10	0.23	1.48	0.07	2.11	0.22	0.01	5.29	0.07	0.02	Balance

Table 2

Al7075 nanocomposites prepared with varying reinforcements

Specimen	Reinforcement
S1	Unreinforced *Al7075* alloy
S2	*Al7075* + 0.5% *SiC* + 0.1 % graphene
S3	*Al7075* + 0.5% *SiC* + 0.2 % graphene
S4	*Al7075* + 0.5% *SiC* + 0.3 % graphene
S5	*Al7075* + 0.5% graphene + 1 % *SiC*
S6	*Al7075* + 0.5% graphene + 2 % *SiC*
S7	*Al7075* + 0.5% graphene + 3 % *SiC*
S8	*Al7075* + 1 % graphene + 2 % *SiC*
S9	*Al7075* + 1 % graphene + 4 % *SiC*

Results and Discussion

This section presents the effects of varying ratios of nanosized *SiC* and graphene reinforcements on the hardness and tensile strength of *Al7075-T6* aluminum alloy produced via stir casting, considering the widespread use of aluminum matrix composites (*AMCs*) in aerospace and automotive applications. The microstructural and fracture surface analysis of the composites, conducted using *SEM-EDX* analysis, is also presented.

This research aims to develop lightweight, high-performance hybrid metal matrix nanocomposite materials and explore the potential of combining *SiC* and graphene nanoparticles with *Al7075* alloy, focusing on characterizing the mechanical properties of these hybrid materials.

The following aspects will be addressed:

– The influence of varying proportions of nanosized *SiC* and graphene on the hardness and tensile strength of *Al7075-T6* alloy;

– The microstructure and fracture surface morphology of *Al7075-T6* nanocomposites, investigated using *SEM-EDX* analysis;

– Key findings of the study and directions for further research.

Mechanical properties of Al7075-T6 nanocomposites

This subsection discusses the mechanical properties - hardness and tensile strength – of both unreinforced and reinforced *Al7075-T6* nanocomposite specimens prepared using stir casting. As shown in Table 2, a total of eight different *Al7075-T6* nanocomposite specimens were fabricated via stir casting, with varying silicon carbide (*SiC*) and graphene nanoparticle reinforcements. The mechanical properties – hardness and tensile strength – were measured and compared between the unreinforced and differently reinforced *Al7075-T6* nanocomposites. Fig. 2 illustrates the hardness and tensile strength of both unreinforced and reinforced *Al7075-T6* nanocomposites.

As illustrated in Fig. 2, the addition of graphene and *SiC* reinforcements to *Al7075* significantly increases the material's tensile strength and hardness, resulting in a considerable improvement in overall strength. Specimen **1**, representing the unreinforced *Al7075* material, exhibits a tensile strength of 89.47 MPa and a *Brinell* hardness number (BHN) of 84.3. Increasing the graphene percentage from 0.1% to 0.3% in Specimens **2** through **4**, while maintaining a constant 0.5% *SiC* reinforcement, results in a gradual increase in hardness (101.40-107.5 BHN) and tensile strength (117.68-141.82 MPa). Furthermore, increasing the

Fig. 2. Hardness and tensile strength of *Al7075-T6* nanocomposites

SiC percentage from 1% to 3% in Specimens **5** through **7**, while maintaining a constant 0.5% graphene reinforcement, leads to a significant improvement in tensile strength (151.55-156.62 MPa) and hardness (132.60-163.40 BHN).

Fig. 2 demonstrates that reinforced *Al7075-T6* nanocomposites exhibit greater hardness and tensile strength compared to the unreinforced *Al7075* specimen. Furthermore, these properties increase with higher concentrations of *SiC* and graphene nanoparticle reinforcements. However, the increase in these properties, particularly hardness, appears more pronounced with *SiC* reinforcement compared to graphene reinforcement in the *Al7075-T6* alloy. With a constant 1% graphene reinforcement, tensile strength decreases when *SiC* reinforcement exceeds 2%.

Increasing the *SiC* percentage from 2% to 4% in *Al7075*-based nanocomposites, while maintaining a constant 1% graphene reinforcement (Specimens **8** and **9**), results in a significant decrease in tensile strength (120.24-126.16 MPa) compared to the increase in hardness (145.16-163.40 BHN). The decrease
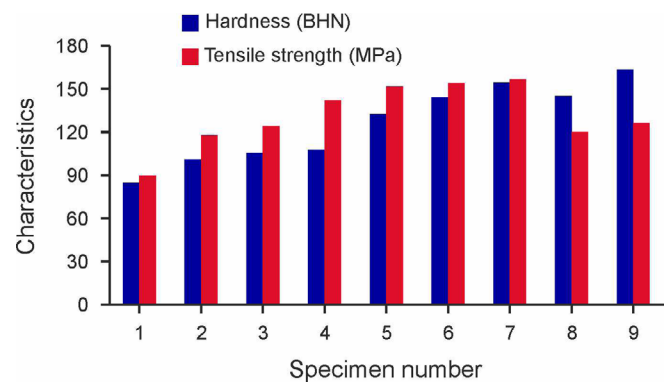
in tensile strength for the *Al7075* nanocomposite when reinforced beyond 2% *SiC* with a constant 1% graphene proportion may be attributed to increased brittleness in the nanocomposite, resulting from stress concentrations caused by the *SiC* particles. This study underscores the importance of balancing hardness and tensile strength in nanocomposites to achieve the desired properties, highlighting the need for careful consideration of reinforcement material selection. It is crucial for researchers to carefully optimize reinforcement percentages to balance strength and hardness in *Al7075*-based nanocomposites.

When properly combined, graphene and silicon carbide reinforcements can synergistically enhance mechanical properties. This study indicates that Specimen **7**, composed of *Al7075*, 0.5% graphene, and 3% *SiC*, exhibits an excellent balance between tensile strength (156.62 MPa) and hardness (155.52 BHN), representing an optimal combination of these characteristics. The enhanced mechanical strength resulting from the addition of *SiC* and graphene to the *Al7075-T6* nanocomposite may be attributed to *SiC's* hardness and modulus, which facilitate load transfer, grain refinement, and dislocation impediment. Furthermore, graphene's high tensile strength and large surface area improve interfacial bonding and inhibit cracking. Differential thermal expansion between the reinforcements and the matrix generates dislocation networks that impede plastic deformation. Consequently, *SiC* and graphene enhance the composite's tensile strength, hardness, and wear resistance.

The test results demonstrate that the hybrid nanocomposites possess higher tensile strength and hardness than the unreinforced *Al7075* alloy, and these properties increase with the hybrid reinforcement ratio. The correlation between mechanical properties and the homogeneous dispersion of nano reinforcements, which inhibits dislocation movement, reduces porosity, and minimizes nanoparticle agglomeration, is explored in the subsequent subsection focusing on the microstructural and fracture surface analysis of *Al7075*-based nanocomposites.

The microstructural and fracture surface analysis of nanocomposites

The superior tensile strength (156.62 MPa) and hardness (155.52 BHN) observed for Specimen **7** among the prepared nanocomposites can be elucidated through microstructural and fracture surface analysis. Fig. 3 presents *SEM* images of the fracture surfaces of Specimen **7** (*Al7075* + 0.5% *Gr* + 3% *SiC*) after tensile testing. Figs. 3, *a* through 3, *d* display *SEM* images of the fracture surfaces at increasing magnification levels. These images reveal the microstructural traits and features of the fracture surfaces at various scales.

The *SEM* analysis provides valuable insights into the material's failure mechanisms and fracture propagation characteristics. A dense, dimpled surface with homogeneous microvoids and minimal particle pull-out is observed, indicative of ductile fracture with strong matrix-reinforcement bonding and efficient load transfer. The presence of fine, uniformly distributed dimples suggests that *SiC* particles served as solidification nucleation sites, while graphene blunted crack tips and impeded dislocation movement.

SEM images of the fracture surfaces of Specimen **8** (*Al7075* + 1% *Gr* + 2% *SiC*) are shown in Figs. 4, *a* through 4, *d* at increasing magnification levels. The fracture surfaces exhibit non-uniform dimples with mixed-mode characteristics, indicating interfacial decohesion and reinforcement particle pull-out. Increased graphene concentration may weaken matrix-reinforcement bonding due to graphene agglomeration and reduced wettability. Stress concentrations caused by microstructural discontinuities can lead to premature cracking, potentially explaining why Specimen **8** exhibits lower tensile strength and hardness compared to Specimen **7** despite having a higher overall reinforcement content.

This study observed that *Al7075* nanocomposites prepared with stirring exhibit a more uniform and homogeneous surface compared to those prepared without stirring. Scanning electron micrographs reveal distinct surface morphologies for composites prepared with and without stirring. Fig. 5, *a* depicts the unstirred composite's flat, featureless surface characterized by scattered particles, non-uniform reinforcement distribution, and agglomerates. This non-uniformity indicates inadequate matrix-reinforcement particle dispersion resulting from insufficient mechanical mixing during fabrication. Visible voids and poor interfacial bonding suggest weak matrix-reinforcement interaction, which can negatively impact composite mechanical performance. Fig. 5, *b* displays the stirred composite's smooth, homogeneous surface. Visible striations and consistent fine particle dispersion suggest that stirring enhances mixing and reinforcement
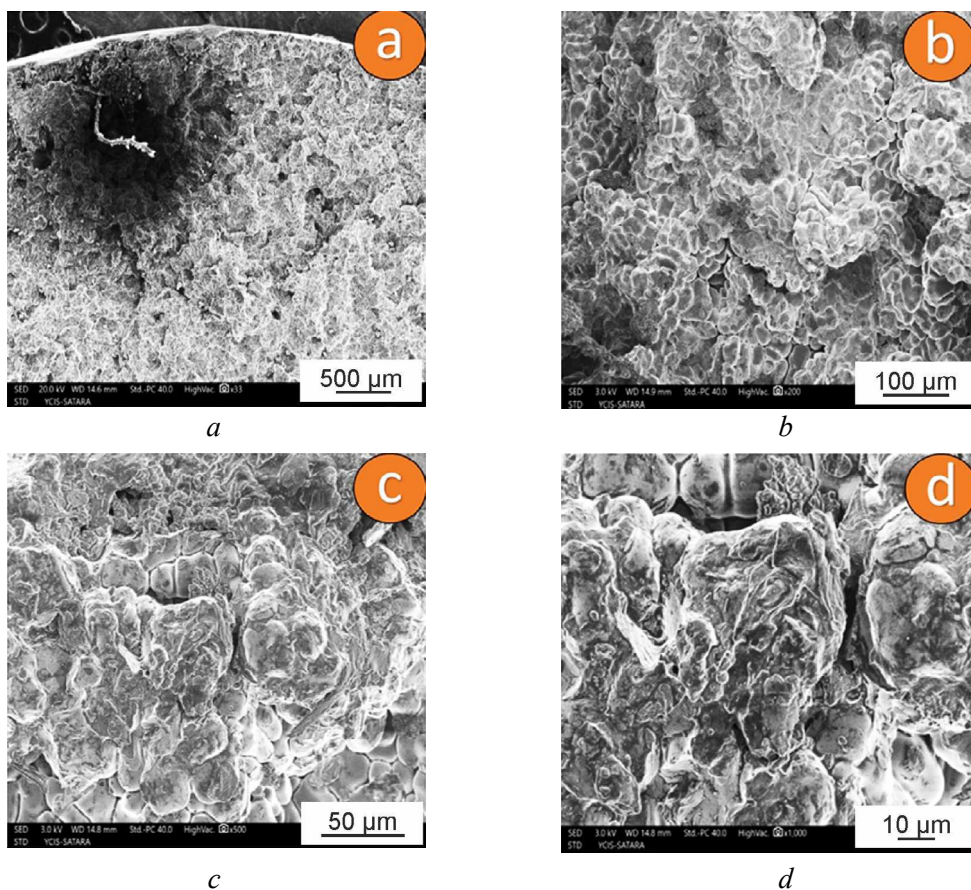
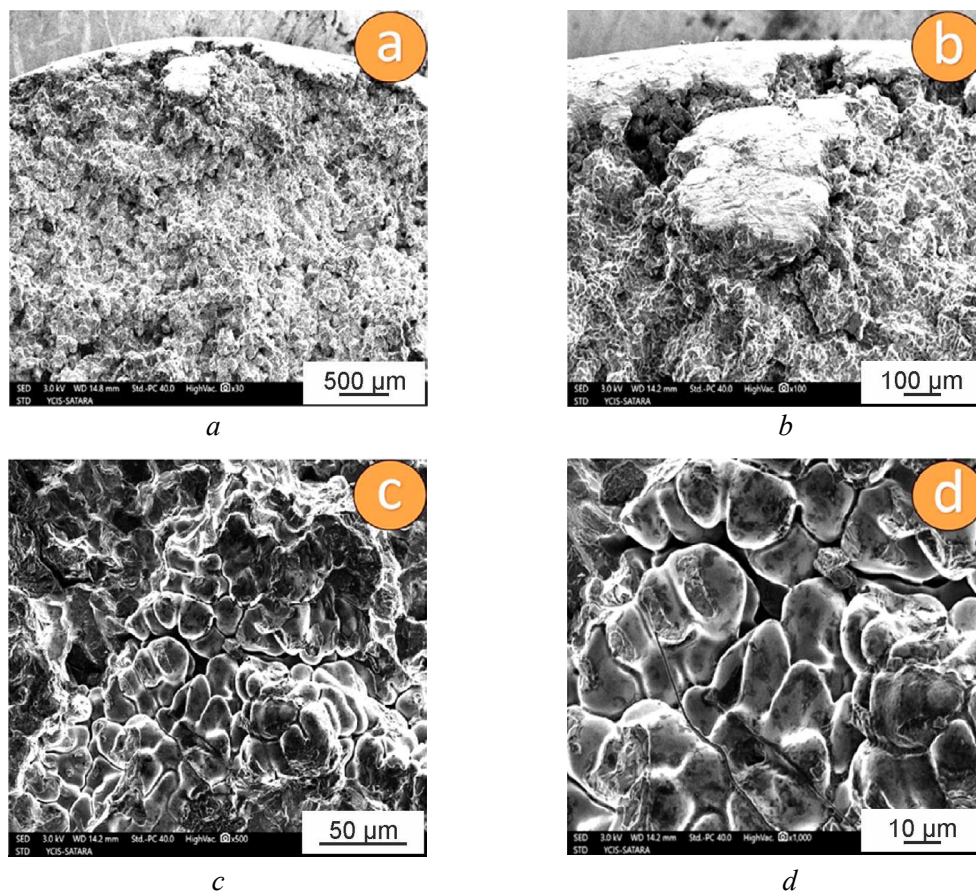*Fig. 3.* *SEM* images of fractured surfaces after tensile testing for Specimen 7

Fig. 4. *SEM* images of fractured surfaces after tensile testing for Specimen 8

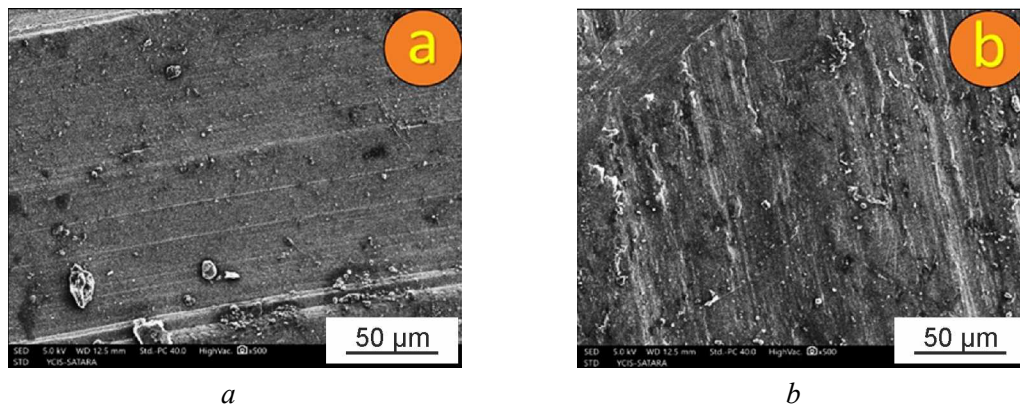*a*   *b*

Fig. 5. Surface images without (*a*) and with (*b*) stirring for Specimen 7

distribution. Mechanical stirring reduces porosity and improves bonding, wetting, and cohesion between the matrix and reinforcements. These microstructural alterations likely contribute to the superior strength and toughness of stirred composites compared to unstirred ones. The study highlights that the implementation of appropriate mixing techniques can significantly influence the surface morphology and mechanical properties of *Al7075* nanocomposites.

Energy dispersive X-ray spectroscopy (*EDX*) analysis in this study confirms the homogeneous distribution of *SiC* and graphene nanoparticles within the aluminum matrix. Figs. 6 and 7 present the elemental analyses of Specimens **7** (*Al7075* + 0.5% graphene + 3% *SiC*) and **8** (*Al7075* + 1% graphene + + 2% *SiC*), respectively. The *EDX* analysis confirms the presence of *SiC* nanoparticles within the aluminum
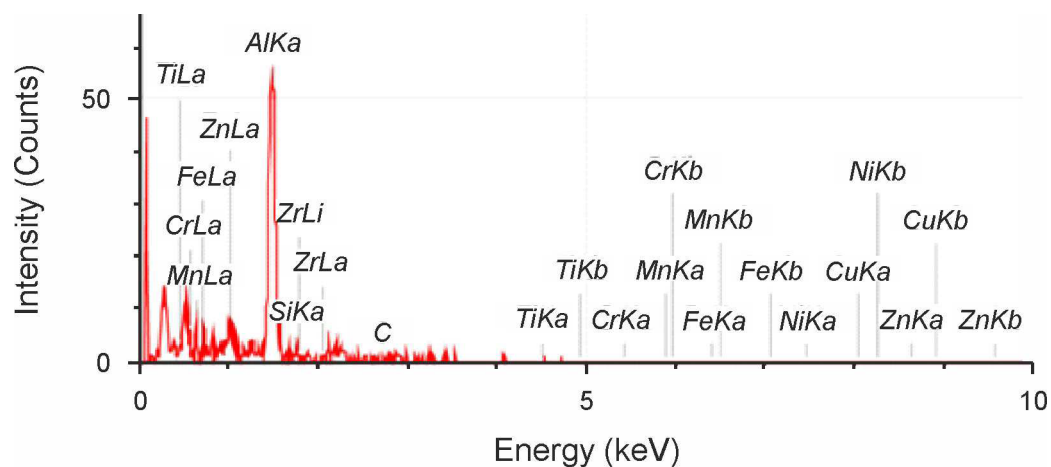

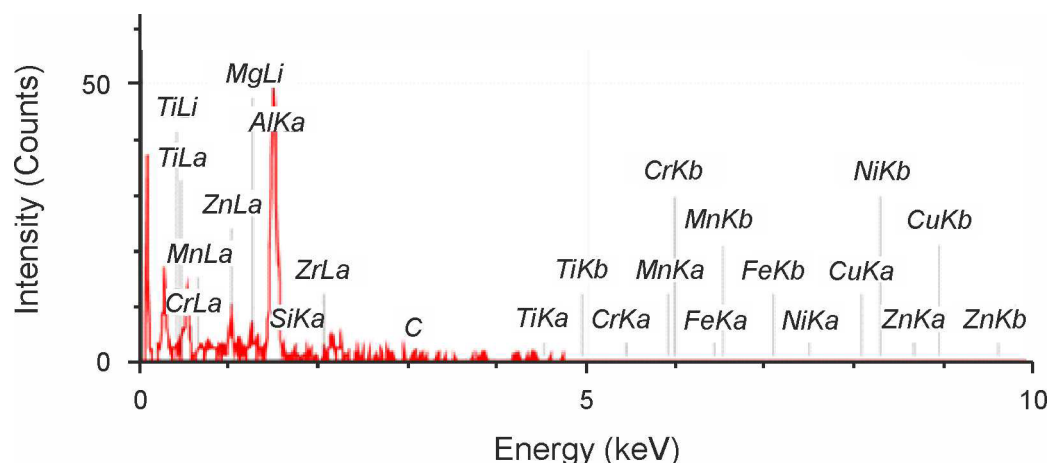*Fig. 6.* Elemental analysis of Specimen 7 (*Al7075* + 0.5 % graphene + 3 % *SiC*)

Fig. 7. Elemental analysis of Specimen 8 (*Al7075* + 1% graphene + 2% *SiC*)

matrix, indicated by the detection of carbon, silicon, and aluminum. Furthermore, the *EDX* results clearly demonstrate the presence of graphene nanoparticles in the aluminum matrix, with carbon peaks observed in both specimens. The dispersion of *SiC* and graphene nanoparticles throughout the aluminum matrix highlights their potential to enhance the mechanical properties of the composite material.

Energy dispersive X-ray spectroscopy (*EDX*) analyzes the elemental composition of the *Al7075*-based nanocomposites. Figs. 6 and 7 show a dominant aluminum signal in the *EDX* spectra, confirming that the matrix material is primarily aluminum. The presence of titanium (*Ti*) and zirconium (*Zr*) peaks suggests their role in mechanical optimization as reinforcing elements. Silicon (*Si*) may be present as intermetallic compounds or ceramics. Trace peaks of iron (*Fe*), manganese (*Mn*), chromium (*Cr*), nickel (*Ni*), copper (*Cu*), and zinc (*Zn*) indicate the presence of a multi-elemental alloying system designed to improve strength, wear resistance, and corrosion resistance. While *EDX* has limited sensitivity to light elements like carbon, a minor carbon peak near 2 keV suggests the presence of graphene or graphitic carbon structures. Even at low concentrations, graphene's high tensile strength and large surface area contribute to enhanced structural and functional performance of the composite. Overall, the *EDX* results demonstrate the successful incorporation of both micro- and nano-scale reinforcements into the aluminum matrix, highlighting its suitability for advanced structural applications.

Fig. 7 illustrates the elemental distribution within the eighth composite specimen. The prominent *AlKα* signal at 1.5 keV confirms aluminum as the primary matrix material. The presence of a strong *MgKα* peak indicates the addition of magnesium to enhance the strength-to-weight ratio and improve corrosion resistance. Peaks corresponding to titanium (*TiLα*, *TiKα*), zirconium (*ZrLα*), and silicon (*SiKα*) suggest the presence of reinforcing phases that contribute to mechanical and thermal stability. Transition metals such as chromium (*Cr*), manganese (*Mn*), iron (*Fe*), nickel (*Ni*), copper (*Cu*), and zinc (*Zn*) are detected across a wide energy range, particularly between 5 and 9 keV, suggesting their role as alloying elements or secondary reinforcements. These constituents can enhance the composite's hardness, wear resistance, and multifunctionality. Variations in magnesium content between spectra suggest a compositional design modification. Overall, the spectrum depicts a complex multi-phase aluminum-based composite system with tailored elemental additions for improved structural and functional performance.

Fig. 8 presents optical micrographs illustrating the microstructures of Specimen **7** (*Al7075* + 0.5% graphene + 3% *SiC*) and Specimen **8** (*Al7075* + 1% graphene + 2% *SiC*). Both specimens were fabricated with different combinations of graphene and *SiC*. Specimen **7** (Fig. 8, *a*) exhibits a consistently polished grain structure with well-defined, continuous grain boundaries. The absence of porosity or clustering suggests enhanced interfacial bonding, while the presence of fine grains indicates effective nucleation facilitated by properly dispersed *SiC* particles.

High-resolution *SEM* images reveal the nanoscale reinforcement particle size and dispersion within the composite matrix. The presence of fine particles ranging from 62.57 to 91.54 nm indicates a well-
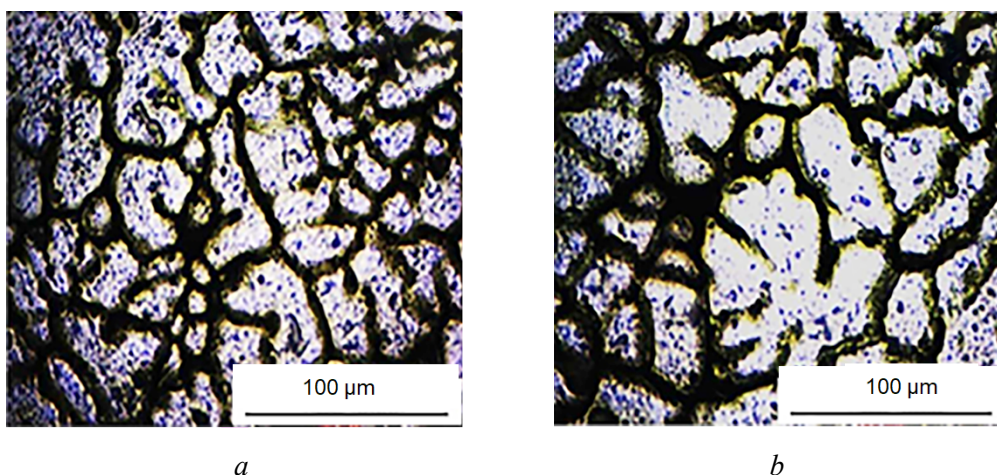

a   *b*

Fig. 8. Microstructure observed for (*a*) Specimen 7, (*b*) Specimen 8

distributed reinforcing phase in Fig. 8, *a*. Due to their higher surface area-to-volume ratio, these nanoscale particles exhibit strong bonding with the matrix, thereby improving mechanical properties. Effective load transfer, grain refinement, and impediment of dislocation motion contribute to increased hardness, tensile strength, and wear resistance. These microstructural observations corroborate the superior hardness (155.52 BHN) and tensile strength (156.62 MPa) observed for Specimen **7**.

Conversely, Fig. 8, *b* depicts a coarser particle distribution ranging from 90.49 to 116.9 nm for Specimen **8**. Coarser and irregular grains with less distinct grain boundaries are apparent. The clustered structure and larger particle size suggest agglomeration, often resulting from inadequate mixing or thermodynamic instability during processing. Agglomerated particles concentrate stress and degrade matrix-reinforcement interaction, limiting load transfer. The reduced grain boundary density and uniformity lead to decreased dislocation impediment, which correlates with the diminished mechanical properties observed for Specimen **8**.

This comparative microstructure analysis demonstrates that reinforcement percentage, particle size, and dispersion quality are key determinants of the mechanical behavior of hybrid *Al7075*-based nanocomposites. The study provides valuable insights for the development of advanced materials with enhanced performance for various industrial applications.

Conclusions

This research investigated the effects of varying ratios of nanosized *SiC* and graphene reinforcements on the hardness and tensile strength of *Al7075-T6* aluminum alloy produced via stir casting, considering the widespread use of aluminum matrix composites (*AMCs*) in aerospace and automotive applications. The microstructural and fracture surface analysis of the composites was also performed using *SEM-EDX*. This study aimed to develop lightweight, high-performance hybrid metal matrix nanocomposite materials and explore the potential of combining graphene and *SiC* nanoparticles with *Al7075* alloy, with particular attention given to characterizing the mechanical properties of these hybrid materials. The following conclusions can be drawn from this work:

– An *Al7075*-based nanocomposite with a 0.5 wt.% graphene and 3 wt.% *SiC* composition exhibited a tensile strength of 156.62 MPa and a hardness of 155.52 BHN. *SiC* nanoparticles were found to be most effective in hardening metal matrix composites, while graphene contributed to enhancing the tensile strength of the nanocomposites.

– Mechanical stirring effectively reduced porosity and improved bonding, wetting, and cohesion between the matrix and reinforcements. The resulting microstructural changes led to superior strength and toughness in stirred composites compared to unstirred composites. The use of appropriate mixing techniques significantly influenced the surface morphology and mechanical properties of *Al7075* nanocomposites.

– *Al7075*-based nanocomposites with 1 wt.% graphene and 2 wt.% *SiC* content exhibited decreased mechanical properties, which correlated with reduced dislocation obstruction due to decreased grain boundary density and uniformity.

– *Al7075*-based nanocomposites with 0.5 wt.% graphene and 1-3 wt.% *SiC* content displayed a uniformly polished grain structure with distinct and continuous grain boundaries. The fine-polished nanoparticles produced, ranging in size from 62.57 to 91.54 nm, demonstrated superior mechanical characteristics through efficient load transfer, grain refinement, and dislocation motion impediment.

– *Al7075*-based nanocomposites with a dense, dimpled surface, homogeneous microvoids, and minimal particle pull-out exhibited superior mechanical properties. This was attributed to ductile fracture with strong matrix-reinforcement bonding and effective load transfer.

– Reinforcement percentage, particle size, and dispersion quality significantly influence the mechanical behavior of hybrid *Al7075*-based nanocomposites, providing valuable insights for advanced industrial applications.

References

1. Ajithkumar J.P., Xavior M.A. Cutting force and surface roughness analysis during turning of Al 7075 based hybrid composites. *Procedia Manufacturing*, 2019, vol. 30, pp. 180–187. DOI: 10.1016/j.promfg.2019.02.026.

2. Khoshaim A.B., Moustafa E.B., Alazwari M.A., Taha M.A. An investigation of the mechanical, thermal and electrical properties of an AA7075 alloy reinforced with hybrid ceramic nanoparticles using friction stir processing. *Superalloys*, 2023, vol. 13 (1), p. 124. DOI: 10.3390/met13010124.

3. Ma B., Gómez-Recio I., Mazerolles L., Mazeran P.-E., Sanchez C., Delalande S., Portehault D. Ultrasound-assisted liquid-phase synthesis and mechanical properties of aluminum matrix nanocomposites incorporating boride nanocrystals. *Small*, 2021, vol. 18 (4), p. 2104091. DOI: 10.1002/SMLL.202104091.

4. Lacour-Gogny-Goubert A., Doquet V., Novelli M., Tanguy A., Hallais S., Bourgon J., Villeroy B., Arruffat-Massion R. Microstructure, mechanical properties, and thermal stability of Al-Al$_2$O$_3$ nanocomposites consolidated by ECAP or SPS from milled powders. *Metals*, 2023, vol. 13 (5), p. 825. DOI: 10.3390/met13050825.

5. Ujah C.O., Kallon D.V.V. Trends in aluminium matrix composite development. *Crystals*, 2022, vol. 12 (10), p. 1357. DOI: 10.3390/cryst12101357.

6. Lakshmikanthan A., Angadi S., Malik V., Saxena K.K., Prakash C., Dixit S., Mohammed K.A. Mechanical and tribological properties of aluminum-based metal-matrix composites. *Materials*, 2022, vol. 15 (17), p. 6111. DOI: 10.3390/ma15176111.

7. Aynalem G.F. Processing methods and mechanical properties of aluminium matrix composites. *Advances in Materials Science and Engineering*, 2020, vol. 2020 (1), p. 3765791. DOI: 10.1155/2020/3765791.

8. Stergioudi F., Prospathopoulos A., Farazas A., Tsirogiannis E.-Ch., Michailidis N. Mechanical properties of AA2024 aluminum/MWCNTs nanocomposites produced using different powder metallurgy methods. *Metals*, 2022, vol. 12 (8), p. 1315. DOI: 10.3390/met12081315.

9. Shivalingaiah K., Nagarajaiah V., Selvan C., Kariappa S., Chandrashekarappa N., Lakshmikanthan A., Chandrashekarappa M., Linul E.E. Stir casting process analysis and optimization for better properties in Al-MWCNT-GR-based hybrid composites. *Metals*, 2022, vol. 12 (8), p. 1297. DOI: 10.3390/met12081297.

10. Ratna Kumar G.E.V., Senthil Kumar K., Ranga Babu J.A. A review on fabrication and mechanical characterization of particulate reinforced Al-7075 metal matrix composites/hybrid composites. *Journal of Advanced Research in Applied Sciences and Engineering Technology*, 2023, vol. 34 (2), pp. 62–71. DOI: 10.37934/araset.34.2.6271.

11. Poovazhagan L., Kalaichelvan K., Rajadurai A., Senthilvelan V. Characterization of hybrid silicon carbide and boron carbide nanoparticles-reinforced aluminum alloy composites. *Procedia Engineering*, 2013, vol. 64, pp. 681–689. DOI: 10.1016/j.proeng.2013.09.143.

12. Alam Md. T., Ansari A.H., Arif S., Alam Md. N. Mechanical properties and morphology of aluminium metal matrix nanocomposites-stir cast products. *Advances in Materials and Processing Technologies*, 2017, vol. 3 (4), pp. 600–615. DOI: 10.1080/2374068X.2017.1350543.

13. Patil S.P., Kore S.S., Chinchanikar S.S., Waware S.Y. Characterization and machinability studies of aluminium-based hybrid metal matrix composites – A critical review. *Journal of Advanced Research in Fluid Mechanics and Thermal Sciences*, 2023, vol. 101 (2), pp. 137–163. DOI: 10.37934/arfmts.101.2.137163.

14. Waware S.Y., Kore S.S., Patil S.P. Heat transfer enhancement in tubular heat exchanger with jet impingement: A review. *Journal of Advanced Research in Fluid Mechanics and Thermal Sciences*, 2023, vol. 101 (2), pp. 8–25. DOI: 10.37934/arfmts.101.2.825.

15. Waware S.Y., Kore S.S., Kurhade A.S., Patil S.P. Innovative heat transfer enhancement in tubular heat exchanger: An experimental investigation with minijet impingement. *Journal of Advanced Research in Fluid Mechanics and Thermal Sciences*, 2024, vol. 116 (2), pp. 51–58. DOI: 10.37934/arfmts.116.2.5158.

16. Kulkarni P., Chinchanikar S. A review on machining of nickel-based superalloys using nanofluids under minimum quantity lubrication (NFMQL). *Journal of the Institution of Engineers (India): Series C*, 2023, vol. 104 (1), pp. 183–199. DOI: 10.1007/s40032-022-00905-w.

17. Chinchanikar S., Kore S.S., Hujare P. A review on nanofluids in minimum quantity lubrication machining. *Journal of Manufacturing Processes*, 2021, vol. 68, pp. 56–70. DOI: 10.1016/j.jmapro.2021.05.028.

18. Kulkarni P., Chinchanikar S. Machining effects and multi-objective optimization in Inconel 718 turning with unitary and hybrid nanofluids under MQL. *Frattura ed Integrità Strutturale*, 2024, vol. 18 (68), pp. 222–241. DOI: 10.3221/IGF-ESIS.68.15.

19. Kulkarni P., Chinchanikar S. Machinability of Inconel 718 using unitary and hybrid nanofluids under minimum quantity lubrication. *Advances in Materials and Processing Technologies*, 2024, vol. 11 (1), pp. 421–449. DOI: 10.1080/2374068X.2024.2307103.

20. Patil S.P., Ghadage K.L., Bhave S.V. Machinability studies of aluminium-based hybrid metal matrix composites – A critical review. *International Journal of Advanced Research in Science, Communication and Technology*, 2023, vol. 3 (1), pp. 94–99. DOI: 10.48175/IJARSCT-9014.

21. Alam M., Ya H., Azeem M., Mustapha M., Yusuf M., Masood F., Marode R., Sapuan S., Ansari A. Advancements in aluminum matrix composites reinforced with carbides and graphene: A comprehensive review. *Nanotechnology Reviews*, 2023, vol. 12 (1), p. 20230111. DOI: 10.1515/ntrev-2023-0111.

22. Md Ali A., Omar M.Z., Hashim H., Salleh M.S., Mohamed I.F. Recent development in graphene-reinforced aluminium matrix composite: A review. *Reviews on Advanced Materials Science*, 2021, vol. 60 (1), pp. 801–817. DOI: 10.1515/rams-2021-0062.

23. Sambathkumar M., Gukendran R., Mohanraj T., Karupannasamy D.K., Natarajan N., Christopher D.S. A systematic review on the mechanical, tribological, and corrosion properties of Al 7075 metal matrix composites fabricated through stir casting process. *Advances in Materials Science and Engineering*, 2023, spec. iss., p. 5442809. DOI: 10.1155/2023/5442809.

Conflicts of Interest

The authors declare no conflict of interest.

ОБРАБОТКА МЕТАЛЛОВ

ТЕХНОЛОГИЯ ОБОРУДОВАНИЕ ИНСТРУМЕНТЫ

НАУЧНО-ТЕХНИЧЕСКИЙ И ПРОИЗВОДСТВЕННЫЙ ЖУРНАЛ

«Обработка металлов (технология • оборудование • инструменты)» – рецензируемый научно-технический и производственный журнал, издающийся с 1999 года с периодичностью 4 раза в год.

В журнале публикуются в основном результаты оригинальных фундаментальных, прикладных и поисковых научных исследований и аспирантских работ. Значительное внимание уделяется публикациям обзорных, проблемных и дискуссионных работ по актуальным вопросам машиностроения, материаловедения и современной металлургии. Научно-технические статьи, направленные в адрес журнала, проходят рецензирование и редактирование. *Публикация статей бесплатная.*

Журнал предназначен для профессорско-преподавательского состава и научных работников высших учебных заведений и научно-исследовательских институтов, инженерно-технических работников производственных предприятий и проектных организаций.

Присутствуют разделы: **«Технология»**, **«Оборудование»**, **«Инструменты»**, **«Материаловедение»**, **«Научно-техническая информация»** и др.

Журнал «Обработка металлов (технология • оборудование • инструменты)» индексируется в крупнейших в мире реферативно-библиографических и наукометрических базах данных *Web of Science* и *Scopus*.

Полный текст журнала «Обработка металлов (технология • оборудование • инструменты)» можно найти в базах данных компании EBSCO Publishing на платформе EBSCOhost. EBSCO Publishing является ведущим мировым агрегатором научных и популярных изданий, а также электронных и аудиокниг.

Журнал входит в «Перечень ведущих рецензируемых научных журналов и изданий, в которых должны быть опубликованы основные научные результаты диссертаций на соискание ученых степеней доктора и кандидата наук».

Правила представления статей для публикации и другая информация о журнале размещены на сайте научного издания:

http://journals.nstu.ru/obrabotka_metallov

630073, г. Новосибирск, проспект К. Маркса, 20, корп. 5, к. 137 ВЦ

+7 (383) 346-17-75

metal_working@mail.ru
metal_working@corp.nstu.ru

НОВОСИБИРСК

ОБРАБОТКА
МЕТАЛЛОВ

ТЕХНОЛОГИЯ
ОБОРУДОВАНИЕ
ИНСТРУМЕНТЫ